Experimental proof of principle of the Neutrino Tagging at NA62

Bianca de Martino

NNT/NL : 2020AIXM0001/001ED000

THÈSE DE DOCTORAT

Soutenue à Aix-Marseille Université
le 10 novembre 2023 par

Bianca DE MARTINO

Experimental proof of principle of the Neutrino Tagging at NA62

Discipline
Physique et Sciences de la Matière

Spécialité
Physique des Particules et Astroparticules

École doctorale
ED 352 PHYSIQUE ET SCIENCES DE LA MATIERE

Laboratoire/Partenaires de recherche
CPPM
IN2P3
CERN
NA62 Collaboration

Composition du jury

Anselmo MEREGAGLIA LP2I - Bordeaux	Rapporteur
Marie-Hélène SCHUNE IJCLab CNRS/Université Paris Saclay	Rapporteure
Andrea CONTU INFN Cagliari	Examinateur
Sandrine EMERY CEA Saclay	Examinatrice
Christinel DIACONU CNRS/CPPM	Président du jury
Jürgen BRÜNNER CNRS/CPPM	Directeur de thèse
Mathieu PERRIN-TERRIN CNRS/CPPM	Co-Directeur de thèse

Affidavit

Je soussigné, Bianca De Martino, déclare par la présente que le travail présenté dans ce manuscrit est mon propre travail, réalisé sous la direction scientifique de Mathieu Perrin-Terrin et Jurgen Brunner, dans le respect des principes d'honnêteté, d'intégrité et de responsabilité inhérents à la mission de recherche. Les travaux de recherche et la rédaction de ce manuscrit ont été réalisés dans le respect à la fois de la charte nationale de déontologie des métiers de la recherche et de la charte d'Aix-Marseille Université relative à la lutte contre le plagiat.
Ce travail n'a pas été précédemment soumis en France ou à l'étranger dans une version identique ou similaire à un organisme examinateur.

Fait à Marseille le 08/09/2023

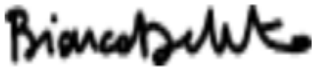

Acknowledgements

I apologize in advance to the reader if this section results verbose and at times cheesy, but I must recognize and acknowledge the contribution of all the people that contributed, directly or indirectly, to the success of this thesis.
In the first place, I would like to thank the many members of the NA62 collaboration that have helped, one way or another, to the good outcome of this project. You helped build the foundation of knowledge, and acquire the skills and the know-how that I am going to need in the next steps of my career. I would like to thank, in particular, Rado and Evgueni for the many suggestions and inputs they offered during the analysis phase and during the signal selection building, and for their patience in their explanations when answering to my many questions. I would also like to mention the big help I got from many members of the collaboration during the data taking periods. The year I first took part in the data taking of such a big experiment, I was disoriented and overwhelmed with the amount of information I felt needed to be learned. In particular, thanks to Roberto, Alina and especially to Michele: during my GigaTracKer on-call expert shifts at CERN your help and the "brutal force" training you offered me have been crucial in order to not literally fry the detector!
Then, it is important to thank the people that I have seen almost every day – except from the covid periods – and that have dealt with my crises, my stress, and that have overall made the entire PhD feel lighter and more pleasurable. I accept the risk that from the next lines it will become clear that all that I did during this PhD was having coffee breaks.
First, I would like to thank a couple of people at the CPPM who have handled my bureaucracy issues with infinite patience: merci Brigitte et Catherine!
A big thank you also goes to the fellow PhD students I shared the office with: Marie, Renan and Gaia. Without you, my PhD would have surely felt lonelier. Gaia, your banana bread, the coffee breaks together, and the evenings spent in Noailles looking for the best homemade mahjouba shop have been a blessing! Gaia and Jacopo have been my reference for the first two years, showing me that even though the PhD can feel so hard at times, it is surely worth finishing.
Another person who has changed for the better how the PhD *felt* like doing is Vijay: I am glad that science allowed me to meet such a patient, caring person. Thank you for all the lunches together at CROUS, commenting on the tasteless food (made better from your Indian spices), and sharing bits and pieces of our experience.
Many other colleagues from the lab deserve to be mentioned in this section. I would like to thank, in particular, Chiara, that with her many advices has helped me navigate through these three years. Damiano and Simone, despite having arrived only during my third and last year, have brightened my long last-year-of-PhD work days at the lab, and also deserve acknownledging here.

Finally, in this acknowledgement section, I would like to thank my supervisors, Jurgen and Mathieu. Mathieu is, in particular, the mind behind the idea of this project, and has mentored and guided me from day 0. Our collaboration started while I was pursuing my master's degree. After a few short term projects and an internship, we started working on the neutrino tagging for this thesis work. During these years, he consistently demonstrated patience, a kind but firm demeanour, and he has always made time to assist me and to address my (always many) questions. At times, working together so closely for four consecutive years, both for him and me, presented its challenges, which, in my humble opinion, is perfectly normal. There have been times when a firmer encouragement was needed to boost my motivation, and a few occasions in which a "sink or swim" approach was used. I admit that those instances have been at times particularly challenging to get through, but in the end I recognize they have productive and formative. So thank you, Mathieu, for being a great teacher and mentor; thank you for your tireless guidance and for setting such a high standard for what it means to be a scientist and researcher. I believe we can both agree that this collaboration has been exceptionally fruitful and rewarding, and that we even had some fun in the process.

This project would probably have felt very different without the support from the many friends external to the lab, and the few family members, who have always been there to cheer on me, never doubting me. Il faut donc remercier mon groupe d'amis de Marseille (ou pas), rencontrés par hasard en salle d'escalade un des premiers jours de mon stage M1. Merci à PH, Estelle, Bruno, Thibault, Jenna: merci pour les soirées, pour les mille aventures, pour l'amour et le bonheur (et bien parfois aussi le chagrin) que nous avons partagés, pour les centaines de kilomètres parcourus sur le chemin de Compostelle, pour la musique qui n'a jamais manqué entre nous, pour m'avoir toujours poussée et soutenue, toujours dans la compréhension et l'acceptation de mes limites, pour m'avoir aussi soutenue dans mes nombreux intérêts. Merci à Lou de n'avoir jamais arrêté de croire en moi et de m'avoir rappelé à chaque fois que j'étais capable de m'en sortir. Vous avez été l'âme de ces trois ans, et je sais que notre chemin ensemble n'est pas fini.

Grazie anche ai miei amici di Torino che, nonostante la distanza fisica, non hanno mai smesso di sostenermi: grazie a Cecilia e Cristian, I pomeriggi con voi sono appuntamenti fissi ogni volta che torno a Torino.

Come potrebbe mancare un ringraziamento speciale alla persona che più di tutte mi é stata vicina, ogni singolo giorno, sopportando le mie incertezze, cercando di cancellare le mie insicurezze, supportandomi in ogni progetto – professionale e non – e avendo cieca fiducia nelle mie capacitá ma soprattutto nella mia determinazione! Grazie Ettore; insieme abbiamo scalato, letteralmente e figurativamente, intere montagne: a volte facili e piacevoli, altre volte sgradevoli e faticose. Mi hai sempre mostrato che ció che conta é avere un ottimo belayer, fidato, capace di prendere le tue cadute senza strappi eccessivi, e che sappia spronarti nelle parti piú dure delle vie! Sono convinta che davanti (o sopra?) di noi ci sia ancora molta strada da percorrere insieme. Ho menzionato prima l'importanza della mia famiglia. Durante questi tre anni ci sono stati dei momenti difficili a livello personale, e sono cosí contenta di avervi avuto vicini (o quasi, a poche centinaia di km di distanza) nel superarli insieme. Grazie alla mia nonna Melania, che mi aspetta sempre a Coggiola, e

che anche se non capisce davvero cosa faccio di lavoro, mi ascolta sempre parlarne col viso amorevole. Grazie ai miei fratelli, Davide e Matteo, per la complicitá, le risate, le litigate, e per aver sempre e senza nessun dubbio creduto nelle mie capacitá. Grazie alla mia mamma, che da sempre mi fornisce ogni mezzo nelle sue possibilitá per riuscire a fare ció che desidero fare (e su cui, talvolta, mi intestardisco). Sei da sempre un punto di riferimento, e la casa a cui tornare. Hai saputo credere in me in ogni istante, da sempre, e tenermi testa, e aiutarmi a rimettere in carreggiata dopo ogni errore. Mi rendo conto che mancano le parole per esprimere la mia gratitudine verso di voi. Finally, I would like to thank Naky, my big potato dog, that has been my official serotonin provider for the past 2 years. Thank you for reminding me every day that, even though life can sometimes be very scary, it is always worth being brave and getting out in the world, because you never know when (and where!) you will find some soft green grass to roll into and some friends to play with.

I have undoubtedly forgotten to include someone, and I hope you won't be offended - there are just so many people that have given me advices, or even just listened to me, that it would be impossible to include everyone.

I would like to conclude this Acknowledgements section with a broader consideration. In my opinion, no professional project exists in isolation; it's not just about the work itself. We all need the support, affection, motivation, guidance, and love that our friends, family and colleagues can provide. Moreover, we need the resources and opportunities to be in a position where we can pursue our professional goals. I feel this has been especially true for me. During these years, but also during the formative years in which I got a degree in Physics and started this PhD, I have been actively supported and motivated by many people – teachers, friends, family. These people have been able to give me the resources, whether they be intellectual, material, or emotional, that have enabled me to reach the point I'm at right now – that is, specifically, writing the acknowledgements of my thesis on the flight on my way back from Japan, with my thesis manuscript almost finished, with some tears in my eyes and with the heart full of joy.

I consider myself incredibly lucky, grateful and privileged to have benefited from your mentorship, support and affection, and to have achieved what feels like a significant professional milestone. Here's to all of you, and I hope each of you experiences the same joy and fulfilment. I promise that I will find ways to give back in the future.

Résumé

Abstract

Ce travail de thèse s'inscrit dans le cadre de la physique des neutrinos aux accélérateurs. Dans ce contexte, une technique innovante est proposée, qui permettra de réduire significativement les incertitudes systématiques liées aux études des oscillations des neutrinos: la technique du neutrino tagging. Cette technique propose d'instrumenter une ligne de faisceau de neutrinos avec des détecteurs en silicium, afin de reconstruire cinématiquement les propriétés de chaque neutrino du faisceau produits dans les désintégrations $\pi^{\pm} \to \mu^{\pm}\overset{(-)}{\nu}_{\mu}$, $K^{\pm} \to \mu^{\pm}\overset{(-)}{\nu}_{\mu}$. Le flux initial de neutrinos est donc précisement déterminé et l'énergie individuelle des neutrinos est reconstruite avec une résolution meilleure que 1%. De plus, grâce aux coincidences temporelles et angulaires, les neutrinos reconstruits cinématiquement par les trajectographes peuvent être associés individuellement aux neutrinos interagissant dans le détecteur de neutrinos. La mesure précise de leurs propriétés peut donc être utilisée pour des analyses de physique (par exemple, des oscillations, des sections efficaces). L'objectif principal de ce travail est de démontrer la faisabilité de la technique du neutrino tagging. La preuve de principe de cette méthode a été réalisée en utilisant l'expérience NA62 au CERN comme expérience de physique de neutrinos en miniature: son intense faisceau de kaons chargés produit des neutrinos lors de leur désintégration en $K^+ \to \mu^+\nu_{\mu}$, ses spectromètres reconstruisent les propriétés des particules chargées, et son calorimètre électromagnétique sert de détecteur de neutrinos. La mise en œuvre de la technique du neutrino tagging dans le cadre d'une expérience de neutrinos à longue ligne de base est décrite en détail, de même que l'analyse en aveugle effectuée sur les données de NA62. Au terme de l'analyse, deux candidats neutrinos taggués ont été observés, démontrant ainsi la faisabilité de cette technique. Enfin, l'analyse des données provenant d'un test sur faisceau effectué sur des modules basés sur la technologie du GigaTracKer de NA62, visant à étudier la résolution temporelle dans les détecteurs en pixels de silicium, est présentée.

Cadre théorique : physique des neutrinos et oscillations

Ce travail de thèse concerne la preuve de principe d'une nouvelle technique pour les expériences de neutrinos basées sur des accélérateurs. Depuis la première détection du neutrino, qui s'est réalisée dans les années 50 par Cowan et Reines, la physique des particules a développé une nouvelle branche qui concerne la physique des neutrinos. Les neutrinos sont, dans le modèle standard, des fermions électriquement neutres, n'interagissant qu'à

travers l'interaction faible avec la matière. Les neutrinos se présentent sous forme de doublets de saveurs avec leur lepton correspondant, ce qui signifie qu'il existe trois espèces de neutrinos : ν_e, ν_μ et ν_τ. Les neutrinos peuvent interagir avec la matière via deux canaux : le premier canal d'interaction est le courant neutre (CN), où l'interaction se produit par l'échange d'un boson Z^0 et l'émission d'un neutrino de la même saveur que celui entrant. Le deuxième canal d'interaction est le courant chargé (CC), qui se produit par l'échange d'un boson $W^\pm$; l'état final inclut un lepton chargé de la même saveur que le neutrino entrant. Les interactions CC sont le principal canal de détection des neutrinos, car un état final chargé est facilement détectable. Dans cette thèse, on se concentrera sur les interactions de neutrinos CC dans la plage d'énergie de 1 à 100 GeV.
Le canal d'interaction CC principal utilisé dans ce travail est la diffusion inélastique profonde (DIS) des neutrinos, qui se produit à des énergies supérieures à 5 GeV. Dans ce régime d'énergie, les neutrinos interagissent avec les quarks à l'intérieur des atomes, produisant un lepton chargé et un système hadronique, se manifestant sous forme d'une gerbe hadronique, comme le montre la figure Figure 1.

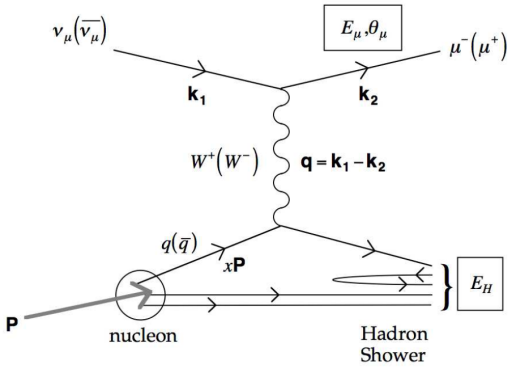

Figure 1.: Diagramme de Feynman pour un processus de DIS de neutrinos CC. Le diagramme est reproduit à partir de [41].

Oscillations des neutrinos

Les neutrinos sont produits par l'interaction faible sous forme d'états de saveur propres (états ayant une saveur définie), qui ne sont pas identiques aux états propres de masse (états ayant une masse définie). En conséquence, chaque état propre de saveur peut être exprimé comme une combinaison linéaire d'états propres de masse. On peut utiliser cette combinaison linéaire dans une équation de Schrödinger dépendante du temps; la solution d'une telle équation est une onde plane, ce qui permet d'écrire les coefficients de la combinaison linéaire des états propres de masse :

$$|\nu_\alpha(x,t)\rangle = \sum_\beta \sum_i U_{\beta i} U^* \alpha i e^{-i\phi_i t} |\nu\beta(0,0)\rangle. \tag{0.1}$$

Il est important de remarquer que les états propres de saveur sont un mélange des états propres de masse: un neutrino d'une saveur initiale donnée peut être détecté, après

propagation, dans une autre saveur. De plus, si les états ont des masses différentes, alors la phase entre les états change avec la distance par rapport à la source. La probabilité de détecter un neutrino de saveur α après un temps t, ayant généré un neutrino de saveur β à $t = 0$ est:

$$P(\nu_\alpha(0,0) \to \nu_\beta(x,t)) = \sum_i \sum_j U_{\alpha i} U^*_{\beta i} U^*_{\alpha j} U_{\beta j} e^{i(\phi_j - \phi_i)t} \tag{0.2}$$

$P(\nu_\alpha \to \nu_\beta)$ est appelée *probabilité d'oscillation* ou *probabilité de transition*. La différence de phase $\phi_j - \phi_i$, en tenant compte que les neutrinos sont des particules dans la limite ultra-relativiste, peut être écrite comme :

$$\phi_j - \phi_i = L\left(\frac{m_j^2}{E_j^2} - \frac{m_i^2}{E_i^2}\right) = \frac{\Delta m^2 L}{2E} \tag{0.3}$$

où $\Delta m^2 = m_j^2 - m_i^2$ et $E_i = E_j = E$ est l'énergie du neutrino. La probabilité d'oscillation dans Equation 0.2 peut donc être écrite comme :

$$P(\nu_\alpha(0,0) \to \nu_\beta(x,t)) = P(\nu_\alpha \to \nu_\beta) = \sum_i \sum_j U_{\alpha i} U_{\beta i} U^{\alpha j} U_{\beta j} e^{\frac{\Delta m^2_{ij} L}{2E}} \tag{0.4}$$

De nombreux paramètres de cette probabilité d'oscillation à trois saveurs sont encore inconnus ou connus avec de grandes incertitudes comme $\sin^2\theta_{23}$ ou l'octant de θ_{23}. De plus, la phase de violation de CP δ_{CP} est toujours inconnue. Plusieurs expériences sont actuellement en construction pour mesurer ces paramètres, telles que DUNE et T2HK.

Neutrino tagging

L'étude et la mesure des paramètres d'oscillation ont lieu dans des expériences appelées *long baseline neutrinos experiments* (LBNEs). Les expériences de neutrinos aux LBNEs observent les oscillations de neutrinos qui se produisent sur des distances de l'ordre de $\mathcal{O}(100 - 1000)$ km; leur conception et leur configuration reposent sur des faisceaux de neutrinos très intenses, dont l'énergie est ajustée pour maximiser la probabilité d'oscillation. Ils exploitent généralement des faisceaux de neutrinos créés à partir de désintégrations hadroniques telles que $\pi^\pm \to \mu^\pm \overset{(-)}{\nu}_\mu$. Les propriétés du faisceau de neutrinos comme son spectre en énergie sont mesurées avant les oscillations par un *near detector*. Le faisceau traverse ensuite la Terre sur des centaines ou des milliers de kilomètres pour atteindre le *far detector*, qui mesure les propriétés du faisceau de neutrinos et son spectre après les oscillations. Un schéma de la ligne de faisceau généralement utilisée dans les LBNE est présenté dans la figure Figure 2. Les mesures dans ces installations expérimentales sont généralement affectées par de grandes incertitudes systématiques, principalement en raison de l'incertitude sur l'échelle d'énergie des neutrinos, et de l'angle solide différent couvert par le détecteur proche et le détecteur lointain, ce qui entraîne une différence substantielle dans le spectre mesuré.
Un nouveau paradigme pour les LBNE est proposé dans ce projet, appelé *neutrino tagging*. La technique du neutrino tagging consiste à exploiter le processus de production des

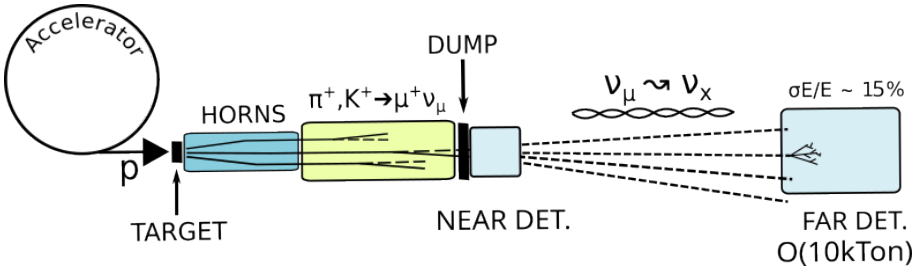

Figure 2.: Représentation schématique annotée (non à l'échelle) de la ligne de faisceau d'une LBNE classique.

neutrinos pour reconstruire cinématiquement les propriétés de chaque neutrino lors de leur production. Cette technique est mise en œuvre en équipant la ligne de faisceau d'une expérience de neutrinos basée sur un accélérateur, avec des capteurs en silicium, pour former des spectromètres de faisceau. Ces spectromètres de faisceau permettent de déduire précisément l'impulsion des neutrinos produits dans la désintégration $\pi^{\pm} \rightarrow \mu^{\pm}\nu_{\mu}$ en mesurant celles du pion et du muon. La technique du neutrino tagging consiste ensuite à établir une association unique entre le neutrino reconstruit cinématiquement et le neutrino interagissant dans le détecteur de neutrinos, en se basant sur des informations temporelles et angulaires provenant à la fois du spectromètre à faisceau et du détecteur de neutrinos. En ce qui concerne la mise en œuvre de cette technique, les limitations technologiques ont empêché de la développer jusqu'aux récents progrès dans la technologie des capteurs en silicium. La principale limitation à la mise en œuvre de cette technique a été le taux de particules prohibitif au niveau du spectromètre à faisceau. Pour référence, l'expérience DUNE va fournir un taux de particules instantané après la cible de l'ordre de $\mathcal{O}(10^{18})$ π/s, en supposant un π^+ produit par proton incident. Les récents développements dans les technologies des détecteurs en silicium ont permis de produire des trajectographes capables de résister à un taux de particules instantané de l'ordre de $\mathcal{O}(10^6)$ $particules/s/mm^2$, comme le démontre le GigaTracKer, le spectromètre à faisceau de l'expérience NA62 [53]. Les projets en cours visent à développer des capteurs pour la jouvance du HL-LHC: les capteurs envisagés doivent être capables de fonctionner à des flux de l'ordre de $\mathcal{O}(10^7)$ $particules/s/mm^2$ [108] (le GigaTracKer de NA62 résiste à un taux instantané de $\mathcal{O}(10^6)$ $particules/s/mm^2$ [53]). Pour qu'un spectromètre à faisceau en silicium puisse fonctionner dans une LBNE, il est donc nécessaire d'adapter la configuration de la ligne de faisceau habituellement employée.

Le tagging nécessite en effet de faire fonctionner l'accélérateur en mode d'extraction lente, où les particules sont extraites en salves de quelques secondes au lieu de quelques microsecondes. Cette modification seule réduit le taux de particules projeté au niveau du spectromètre à faisceau de 5 à 6 ordres de grandeur. L'utilisation de cornes pour la collimation des π est incompatible avec l'extraction lente, car le chauffage Joule provenant des longues impulsions de courant dans le conducteur du corne peut compromettre irrémédiablement le dispositif [37]. Par conséquent, ils doivent être remplacés par un dispositif de focalisation statique; la collaboration ENUBET [106] a récemment démontré que des ensembles de quadrupôles

peuvent atteindre des performances de focalisation compatibles avec celles d'un corne à bande étroite.
De plus, la mise en place d'une sélection en fonction de l'impulsion pour éliminer les particules moins énergétiques réduirait le taux de pions à un niveau acceptable pour le spectromètre à faisceau, le réduisant de 1 à 2 ordres de grandeur, donnant un taux d'hadrons secondaires instantané de $\mathcal{O}(10^6 - 10^7)$ $particules/s/mm^2$.
La technique du neutrino tagging apporterait d'importants avantages aux expériences de neutrinos basées sur un accélérateur, car elle permet la reconstruction de presque tous les neutrinos dans le faisceau et permet de poursuivre chaque neutrino interagissant jusqu'à sa production. Les avantages sont détaillés dans [88], et les principaux sont les suivants :

- Amélioration de la mesure du flux : la reconstruction de tous les neutrinos dans le faisceau est utile pour déterminer la composition du flux de neutrinos en termes d'énergie, de saveur et de chiralité.
- Amélioration de la mesure de l'énergie : la résolution en énergie sur l'énergie manquante des neutrinos est de l'ordre de $\mathcal{O}(0.1 - 1)\%$. Pour comparaison, les détecteurs de neutrinos avancés tels que DUNE ou HK ont une résolution en énergie de 10 à 15% ([47], [92]).
- Amélioration du rejet des bruits de fond : réduction des bruits de fond des ν_e non oscillés, car les ν_e interagissant non oscillés ne coïncident pas avec un ν_μ étiqueté.

L'analyse présentée dans ce document se concentre sur la démonstration de la faisabilité de la technique d'étiquetage dans l'expérience NA62.

L'éxperience NA62

L'expérience NA62, illustrée dans la figure Figure 3a, est une expérience à cible fixe conçue pour reconstruire les kaons chargés et leurs particules filles, lorsque les kaons se désintègrent en vol. En particulier, le but principal de NA62 est de mesurer le rapport de désintégration de la désintégration super rare $K^+ \to \pi^+\nu\nu$, qui est, selon le Modèle Standard, $(8.5 \pm 1.0) \cdot 10^{-11}$. Un faisceau de protons primaires de 400 GeV/c est extrait du SPS du CERN et est dirigé vers la cible en béryllium T10 en salves d'une durée effective de trois secondes. Le faisceau d'hadrons secondaires à haute intensité, est dérivé de la cible T10 avec une impulsion nominale de 75 GeV/c et est composé à 70% de π^+, 23% de protons et 6% de K^+. NA62 est composé de plusieurs sous-détecteurs, en particulier:

- le KTAG, un compteur Cherenkov différentiel dédié à l'identification des kaons dans le faisceau ;
- le GigaTracKer (GTK), le spectromètre à faisceau, composé de capteurs en silicium à pixels. Ce détecteur a une résolution temporelle de 130 ps et une résolution sur la mesure de l'impulsion de 0,2% ;

- le spectromètre STRAW, composé de quatre chambres de *straw tubes* avec un fil central à l'intérieur qui détecte les paires électron-ion formées après le passage des particules. Ce détecteur permet de reconstruire l'impulsion et la direction des particules produites dans la désintegration des kaons.
- le détecteur RICH (Ring Imaging CHerenkov), qui sert à l'identification des particules;
- un calorimètre électromagnétique à krypton liquide (LKr), qui est un cryostat rempli de 9000 l de krypton à 120 K. Il détecte les MIP (Minimum Ionizing Particles) et les gerbes électromagnétiques et hadroniques;
- les calorimètres hadroniques Shashlik MUV1 et MUV2, qui détectent les gerbes hadroniques et les MIP ;
- le MUV3, constitué de scintillateurs, placés après une tonne de fer, qui sert à identifier les muons.

Grâce à ces sous-détecteurs, il est possible d'utiliser l'expérience NA62 pour détecter les événements $K^+ \to \mu^+\nu_\mu$ avec l'interaction du neutrino dans le calorimètre, démontrant ainsi la faisabilité de la technique du tagging des neutrinos.

Étude de faisabilité du neutrino tagging

Tagging à NA62

Le faisceau de kaons à haute intensité de NA62 et ses détecteurs peuvent être exploités pour démontrer la faisabilité de la technique d'étiquetage des neutrinos. En effet, comme les kaons K^+ se désintègrent principalement en $K^+ \to \mu^+\nu_\mu$(appelé $K\mu\nu$ par la suite), ils produisent naturellement un faisceau de neutrinos. L'énergie moyenne de ces neutrinos est d'environ 40 GeV. Dans la gamme d'énergie de NA62, la section efficace des neutrinos est dominée par le processus de diffusion inélastique profonde (DIS). Dans ce régime, l'identification des interactions NC au niveau du déclencheur n'est pas possible, car leur signature expérimentale ne consiste qu'en une gerbe hadronique dans le LKr[56]. Cependant, l'interaction CC des neutrinos induit la production d'une gerbe hadronique et d'un lepton chargé de saveur correspondante (μ^-) dans le processus DIS, comme illustré dans le diagramme de la figure Figure 1.4 [51]. La présence à la fois d'une gerbe hadronique dans le LKr et d'un μ^- dans l'état final peut être efficacement exploitée dans une stratégie de déclenchement comprenant le MUV3. Pour qu'une telle stratégie fonctionne, le μ^- créé dans l'interaction neutrino doit être à l'intérieur de l'acceptance géométrique du MUV3. L'angle entre la direction du μ^- et l'axe identifié par la direction du neutrino dépend de la fraction d'énergie d'interaction prise par le μ^- (également appelée inélasticité de l'interaction). Les grandes valeurs d'inélasticité correspondent à de petits angles.

Topologie de l'événement

La signature de la désintégration $K\mu\nu$ pour laquelle le neutrino a interagi, appelé en ce qui suit $K\mu\nu*$, est une seule trace de muon jusqu'au LKr, avec une gerbe hadronique

apparaissant dans le LKr et les MUVs à des positions cohérentes avec celles extrapolées du neutrino, ainsi que deux muons bien séparés dans le détecteur MUV3, comme illustré dans la figure Figure 3. Les principales caractéristiques de ce type d'événement sont la masse manquante au carré $m^2_{\text{miss}} = (P_K - P_{\mu^+})^2$, où P_K et P_{μ^+} sont les quadri-impulsions du K^+ et du μ^+, et la distance entre le cluster LKr associé à l'interaction du neutrino et la position extrapolée du neutrino au plan frontal du LKr, notée $d_{\text{LKr}\nu}$. Le bruit de fond provient de deux sources. La première source de bruit de fond consiste en des $K\mu\nu$ avec de l'activité supplémentaire fortuite dans le LKr, les MUV1/2 et les MUV3, appelée par la suite *désintégrations superposées* $K\mu\nu$. La deuxième source de bruit de fond provient d'autres désintégrations du K^+ (comme $K^+ \to \pi^+\pi^0$ et $K^+ \to \pi^+\pi^+\pi^-$) avec une activité fortuite dans les calorimètres et dans les MUV3, et avec un μ^+ mal identifié. Un tel bruit de fond est désigné dans la suite sous le nom de *désintégrations mal reconstruites du* K^+ .

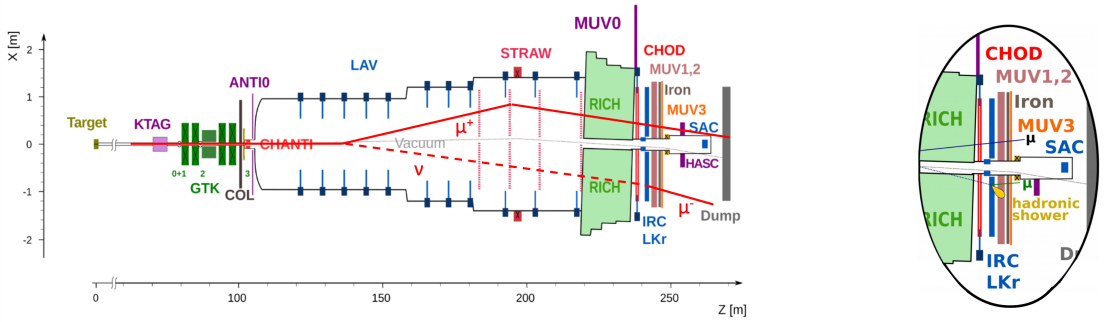

(a) (b)

Figure 3.: Schéma de la désintégration $K\mu\nu*$ superposé à la vue topologique schématique de l'expérience NA62 (4.1a) et un zoom sur les sous-détecteurs qui contribuent à détecter l'interaction du neutrino (4.1b).

L'analyse a été faite en l'aveugle. La topologie de l'événement signal permet de définir des régions de l'espace des phases principalement peuplées par le signal ou le bruit de fond. La sélection des événements est optimisée en utilisant les données dans les régions de bruit de fond et les données simulées du signal. Le contenu de la région du signal pour les données est gardé masqué pendant le développement de l'analyse pour éviter tout biais potentiel. La région du signal est définie comme $|m^2_{\text{miss}}| < 0.006\,\text{GeV}^2/\text{c}^4$ et $d_{\text{LKr}\nu} < 60\,\text{mm}$. Le premier critère garantit que les candidats sont effectivement des désintégrations $K\mu\nu$ et le deuxième impose que le dépôt d'énergie dans le LKr provienne de l'interaction du neutrino provenant du processus $K\mu\nu*$. La taille de la région du signal est choisie pour correspondre à la résolution expérimentale sur ces deux paramètres. Le bruit de fond provenant des désintégrations superposées $K\mu\nu$ est étudié sur les bandes latérales de la région du signal $d_{\text{LKr}\nu}$, tandis que le bruit de fond provenant des désintégrations mal reconstruites des kaons est étudié sur les bandes latérales de la région du signal m^2_{miss}. La contamination de bruit de fond dans la région du signal est évaluée à l'aide d'une méthode basée sur les données séparément pour les deux sources de bruit de fond. Le nombre attendu d'événements du signal peut être estimé grâce aux éléments suivants :

- le nombre de désintégrations efficaces de K^+ dans une région donnée, N_K
- le taux de branchement de la désintégration $K\mu\nu$, $\mathcal{B}(K^+ \to \mu^+\nu_\mu)$
- la probabilité d'interaction d'un neutrino d'une énergie donnée dans le LKr, $P_{int,LKr}$
- l'efficacité de détection et de reconstruction d'un événement de neutrino étiqueté, $\epsilon_{K\mu\nu*}$.

Le nombre attendu d'événements étiquetés dans une région donnée peut donc être écrit comme :

$$N^{exp}_{K\mu\nu*} = N_K \cdot \mathcal{B}(K^+ \to \mu^+\nu_\mu) \cdot Pint, LKr \cdot \epsilon_{K\mu\nu*} \tag{0.5}$$

L'efficacité $\epsilon_{K\mu\nu*}$ prend en compte plusieurs effets, tels que les acceptances géométriques et cinématiques, la définition de la région de désintégration et les critères de sélection pour identifier la désintégration $K\mu\nu$ étiquetée. La probabilité d'interaction $P_{int,LKr}$, qui peut être calculée avec le calcul simple dans Equation 4.1, peut être estimée plus précisément grâce aux échantillons MC. Un échantillon de désintégrations $K\mu\nu$ standard, appelé échantillon de normalisation, fournit une estimation du nombre total de désintégrations efficaces de K^+ (N_K) dans une région fiduciale donnée :

$$N_K = \frac{N_{K\mu\nu}}{\epsilon_{K\mu\nu} \cdot \mathcal{B}(K^+ \to \mu^+\nu_\mu)}, \tag{0.6}$$

où $N_{K\mu\nu}$ est le nombre d'événements de normalisation $K\mu\nu$ dans la région choisie, $\epsilon_{K\mu\nu}$ est l'efficacité pour sélectionner les événements de normalisation $K\mu\nu$, et $\mathcal{B}(K^+ \to \mu^+\nu_\mu)$ est le taux de branchement de la désintégration $K\mu\nu$. L'échantillon de signal et de normalisation partagent la même sélection d'événements (sélection commune) jusqu'au point où les topologies des événements de normalisation et de signal divergent en raison de l'interaction du neutrino. Au niveau de la prise de donnée, une stratégie de déclenchement a été développée pour sélectionner les désintégrations de kaons à une seule trace, avec un dépôt d'énergie dans le LKr d'au moins 5 GeV et avec un candidat MUV3 associé.

Analyse experimentale

La sélection des événements est divisée en deux étapes: une sélection commune au signal et à la normalisation, appelée ci-après "sélection commune" et abrégée CS, suivie de la sélection du signal pour identifier l'interaction du neutrino.

Selection commune

La sélection commune pour la désintégration $K\mu\nu$ nécessite l'identification d'une particule chargée comme un μ^+; le μ^+ doit se trouver à l'intérieur de l'acceptance des détecteurs et pas trop près du faisceau. De plus, le neutrino, reconstruit à l'aide de la cinématique de la désintégration doit se trouver dans l'acceptance du LKr, pas trop près du tube à faisceau et bien séparé du μ^+.

Sélection du signal

Quelques exigences supplémentaires pour la sélection du signal sont nécessaires pour la reconstruction et l'identification de l'activité associée au neutrino dans les détecteurs et pour le rejet du bruit de fond. La sélection du signal se déroule en quatre étapes :

- **Association de l'interaction**: association de l'activité de l'interaction du neutrino dans les sous-détecteurs pertinents. L'activité du neutrino devrait apparaître dans le LKr, en raison de la gerbe hadronique créée dans l'interaction. La gerbe hadronique devrait se poursuivre à travers le calorimètre hadronique MUV1, laissant un dépôt d'énergie. L'interaction du neutrino CC génère également un muon négativement chargé. Le μ^- serait détecté par le détecteur MUV3 et devrait également laisser un dépôt d'énergie MIP dans MUV1 et MUV2.

- **Rejet de l'activité supplémentaire**: conditions pour rejeter le bruit de fond des désintégrations tardives du K^+ et des π^+ du faisceau se désintégrant tardivement dans la ligne de faisceau, en phase avec l'événement $K\mu\nu$. Les événements sont rejetés s'ils présentent la présence d'activité en phase avec la trace μ^+ dans les régions internes des calorimètres LKr, MUV1 et MUV2. De plus, le nombre de coups dans le KTAG, dans une fenêtre temporelle de 8 ns par rapport au temps de détection du RICH, doit être inférieur à 50.

- **Exigences en énergie**: L'interaction du neutrino est identifiée en utilisant le dépôt d'énergie de la gerbe hadronique dans les calorimètres. Des exigences minimales en énergie dans le LKr et MUV1 et 2 ainsi que la conservation de l'énergie sont requises.

- **Topologie de l'interaction** : La dernière partie de la sélection se base sur des critères liés à la topologie de la désintégration du K^+ et de l'interaction du neutrino, visible dans Figure 4. Les signaux dans le LKr et le MUV1 doivent provenir du même objet (la gerbe hadronique) et donc être suffisement proche l'un de l'autre. Une sélection similaire est appliquée aux signaux dans le MUV2 et le MUV3, permettant ainsi d'assurer qu'ils proviennent du même objet (μ^-).

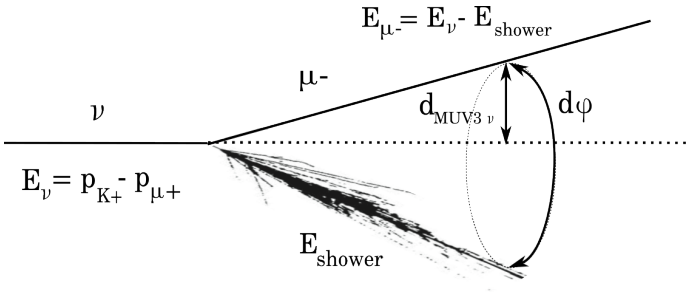

Figure 4.: Topologie de l'interaction du ν_μ.

Nombre d'événements attendus et observés

Bruit de Fond

Le nombre des événements de bruit de fond dans la région du signal est estimé à l'aide d'une méthode basée sur les données, en ajustant les distributions des données sur les bandes latérales de m^2_{miss} et de $d_{\text{LKr}\nu}$, et en calculant l'intégrale des fonctions d'ajustement dans la région de signal. Les résultats sont :

- $\mathbf{N^{exp}_{bkg}(OV\ K\mu\nu) = 0.04 \pm 0.02_{stat} \pm 0.01_{syst}}$.
- $\mathbf{N^{exp}_{bkg}(Mis - reco\ K^+) = 0.0014 \pm 0.0007_{stat} \pm 0.0002_{syst}}$.

Signal

Le nombre d'événements du signal attendu dans la région de signal peut être calculé avec l'Equation 0.5, simplifiée avec les termes communs de normalisation. Le résultat est :

$$N^{exp}_{\text{signal}} = 0.228 \pm 0.014_{stat} \pm 0.011_{syst}$$

En supposant que le nombre d'événements attendus suit une distribution de Poisson, il est possible de calculer la probabilité d'avoir 0, 1 ou 2 événements dans la région de signal pour un nombre total d'événements $\mathbf{N^{exp}_{events} = 0.2694}$:

- pour 0 événements de donnée p = 0.7638
- pour 1 événement de donnée p = 0.2058
- pour 2 événements de donnée p = 0.0277.

Après avoir révélé le contenu de la région de signal, deux événements sont trouvés, dont l'activité est montrée sur la Figure 6a pour l'événement A et sur la Figure 6b pour l'événement B. Notez que l'activité dans MUV2 et 3 est due au μ^- créé dans l'interaction ν; c'est pourquoi on s'attend à ce que cette activité soit légèrement désalignée par rapport à la trajectoire du neutrino.

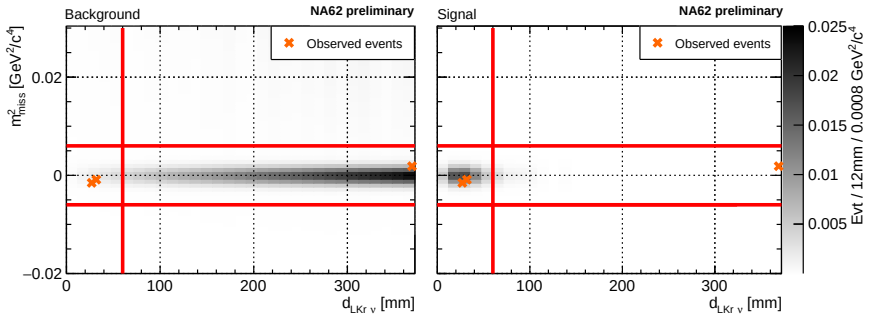

Figure 5.: Nombre d'événements attendus pour le bruit de fond (à gauche) et le signal (à droite). L'échelle de gris reflète le nombre d'événements attendus par bin de $0.0008\,\text{GeV}^2/\text{c}^4 \times 12\,\text{mm}$. Les lignes rouges représentent les coupures qui définissent la région de signal. Les marqueurs orange en forme de croix représentent les événements trouvés à l'intérieur de la région de signal et dans les bandes latérales après avoir regardé dans la région du signal.

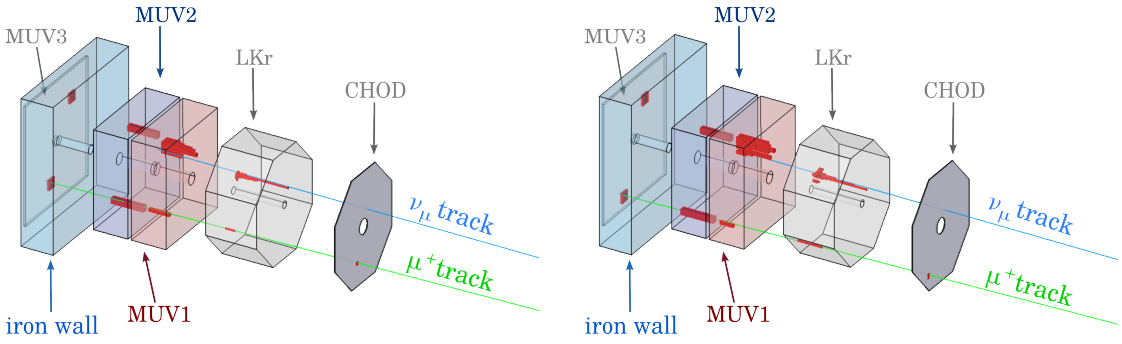

(a) (b)

Figure 6.: Représentation graphique del'événement A (6a) et de l'événement B (6b). La ligne verte est la trace du μ^+; la ligne bleue représente la trajectoire du neutrino reconstruite à partir du K^+ et du μ^+. Les boîtes rouges représentent l'activité dans le détecteur. Pour le LKr, MUV1 et 2, la longueur de la boîte est le dépôt d'énergie normalisé dans chaque cellule.

Étude de résolution temporelle d'un trajectographe en silicone

Dans le cadre du neutrino tagging et de sa mise en œuvre dans une expérience sur les neutrinos à grande échelle, il est important d'étudier la résolution temporelle des trajectographes à pixels en silicium et des facteurs qui l'influencent. Pour ce but, les données d'un beam test réalisé en 2017 au CERN SPS avec un télescope constitué de modules individuels de TDCPix, le circuit intégré de lecture du NA62 GigaTracKer, ont été analysées. Les résultats montrent qu'un type de capteur, le n-on-p, fonctionne nettement mieux que l'autre (p-on-n); cependant, en raison de contributions supplémentaires à la résolution temporelle nominale, il était impossible de quantifier la contribution à la résolution temporelle due à l'effet du weighting field, un effet qui dépend de la géométrie du capteur.

Conclusions

La technique du neutrino tagging présente un grand potentiel lorsqu'elle est appliquée aux expériences sur les neutrinos visant à mesurer les oscillations. Jusqu'à présent, il n'a pas été possible d'utiliser cette technique, principalement en raison de limitations technologiques. Ce travail de thèse visait à démontrer la faisabilité de la technique du tagging des neutrinos en utilisant les données d'une expérience existante, NA62. NA62 présente certaines caractéristiques désirables: un faisceau d'hadrons chargés intense, qui produit naturellement un faisceau de neutrinos, deux spectromètres, des calorimètres et un détecteur à muons. De plus, l'expérience offre la possibilité de déclencher sur les états finals de l'interaction. Ces caractéristiques ont permis de réaliser une démonstration de principe, dans laquelle l'analyse a été effectuée en maintenant la région de signal masquée.

En ouvrant la région de signal, deux événements ont été trouvés. Ces deux événements sont les premiers candidats neutrinos taggués de l'histoire.

Abstract

This thesis work objectives belong to the framework of neutrino physics at accelerators. In this context, an innovative technique is proposed, that will substantially reduce the systematic uncertainties linked to the neutrino oscillation studies: the neutrino tagging technique. The neutrino tagging technique proposes to instrument a neutrino beam line with silicon trackers to kinematically reconstruct properties of individual beam neutrinos produced in $\pi^{\pm} \to \mu^{\pm}\overset{(-)}{\nu}_{\mu}$, $K^{\pm} \to \mu^{\pm}\overset{(-)}{\nu}_{\mu}$ decays. As a result, the initial neutrino flux is precisely determined and the individual neutrino energy can be reconstructed with a resolution better than 1%. Moreover, based on time and angular coincidence, the neutrinos kinematically reconstructed by the trackers can be individually associated to the neutrinos interacting in the neutrino detector, such that the precise measurement of their properties can be used for physics analyses (e.g. oscillations, cross-section). The main aim of this work is to demonstrate the feasibility of the neutrino tagging technique. The proof of principle of the neutrino tagging method has been performed using the NA62 experiment at CERN as a miniature neutrino experiment: its intense kaon beam copiously produces neutrinos when decaying as $K^+ \to \mu^+\nu_{\mu}$, its spectrometers act as tagger for the charged particles, and its electromagnetic calorimeter serves as neutrino detector. The implementation of the neutrino tagging at a Long Baseline Neutrino Experiment is described in detail, as well as the blind analysis performed on NA62 data. Two tagged neutrino candidates are found in the signal region, proving the feasibility of this technique. Finally, the data analysis on the data from a test beam performed on modules based on the NA62 GigaTracKer technology, aimed to study the time resolution budget in silicon pixel detectors, is presented.

Contents

List of Figures

List of Tables

1. Neutrino physics: history and present knowledge

Summary

Neutrinos are the most elusive elementary particles in the Standard Model, despite them being the second most abundant particles in the universe. Their discovery and detection mark important points in the history of Physics, and it is worth reviewing the steps that lead to today knowledge to have a better understanding of the context of this thesis work, whose broad scope is the neutrino physics at accelerator based experiments.

1.1. History of neutrino physics

The history of neutrino discovery and science begins in the early 20th century with the observation of the energy spectrum of the β-decay by James Chadwick in 1914. Such process consist in the decay of a nucleus of a certain element of atomic number Z, into a nucleus of atomic number Z+1, with the emission of an electron, as detailed in Equation 1.1.

$$X_Z \rightarrow Y_{Z+1} + e^- \tag{1.1}$$

This is a two body process; the outgoing atom has a smaller mass than the parent atom, therefore the energy difference between the two atoms can, in principle, be precisely calculated, and was expected to be carried entirely by the electron. The emitted electrons' energy spectrum was thus expected to be discrete, and centered at the value corresponding

to the energy difference between the two atoms. Instead, it was found that the energy spectrum of the emitted electron was continuous, and had as end point the expected energy [35]. The same result was confirmed by others [102]. The spectrum of the emitted electron energy is shown in Figure 1.1.

Such discovery was extremely puzzling for physicists at that time, as it hinted to the

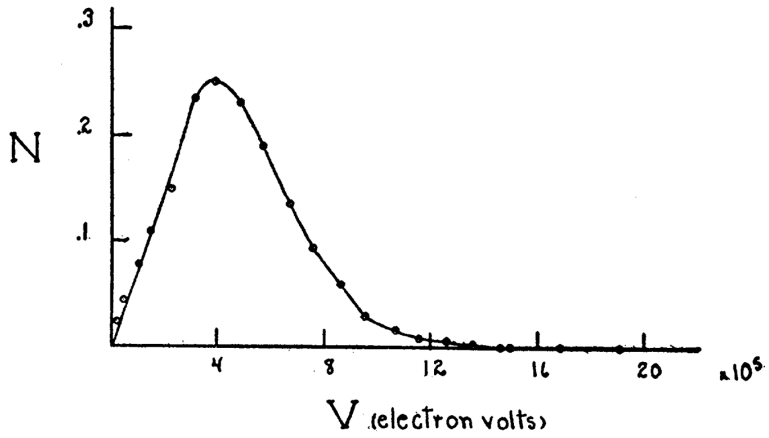

Figure 1.1.: Energy spectrum of the emitted electron in a β decay experiment. From [102].

violation of energy conservation. In 1930, in an open letter [84] addressed to Lise Meitner and Hans Geiger, and to the attendees of the nuclear physics conference in Tübingen, Wolfgang Pauli proposed a solution: the shape of the β spectrum could be due to the presence of a third invisible particle. Such a particle must be electrically neutral, so he called it the "neutron". He also predicted that this particle had spin 1/2, and very light mass, so that it was impossible to detect. As a result, the continuous β spectrum was reconsidered under the three body approach:

$$X_Z \rightarrow Y_{Z+1} + e^- + \nu \tag{1.2}$$

where ν is the neutrino.

Enrico Fermi, a few years later, developed and wrote a theory about the new particle proposed by Pauli, which he called "neutrino" [50] (after Chadwick's discovery of the particle known today as neutron [36]). The cross section of the neutrino was estimated to be $\sigma > 10^{-44}\,\mathrm{cm}^2$ by H. Bethe and R. Peierls [24]. At this point, the challenge became the experimental discovery of the neutrino.

1.1.1. The first neutrino detection

In the early 50's nuclear fission was perfectioned; since the nuclear fission is a neutrino-producing mechanism, physicist Frederick Reines, who was involved in nuclear weapon tests, thought of exploiting the atomic bomb to detect neutrinos. Together with Clyde Cowan, they developed a neutrino detector, that consisted of two water tanks that also

contained cadmium chloride, layered with three liquid scintillating detectors. Due to the evident difficulties of operating such a detector nearby an atomic bomb explosion, the two physicist decided to place it deep underground close to one of the Savannah River Plant reactors in the US. Thanks to the inverse β-decay for cadmium, shown in Equation 1.3, that produces a positron and a neutron from the interaction between an antineutrino and a proton, Cowan and Reines were able to detect neutrino signals for the very first time. In order to do that, they looked for the coincidence of the two signals: the annihilation of the positron produced in the inverse beta decay, shown in Equation 1.4, and the neutrino capture by a Cadmium nucleus, shown in Equation 1.5. The Cadmium nucleus indeed becomes excited and emits de-excitation photons.

$$\overline{\nu} + p \rightarrow e^+ + n \tag{1.3}$$

$$e^+ + e^- \rightarrow 2\gamma \tag{1.4}$$

$$n + {}^{108}\mathrm{Cd}^+ \rightarrow {}^{109}\mathrm{Cd}^* \rightarrow {}^{109}\mathrm{Cd}^+ + \gamma \tag{1.5}$$

They observed about 3 events per hour, and they were able to calculate a cross section of $6 \cdot 10^{-20}$ barn ($6\ 10^{-44}\,\mathrm{cm}^2$) [94], which was compatible with the predicted cross section. For the discovery of the neutrino, Reines was awarded the Nobel Prize in Physic in 1995, unfortunately after Cowan passed away.

1.1.2. Neutrino species

After Reines' and Cowan's experiment, neutrino physics knew rapid progress that led to new questions. One of the first questions was to understand if the neutrinos produced together with electrons and muons are equal. To answer this question, in 1962, Leon Lederman, Melvin Schwartz and Jack Steinberger designed the first neutrino beam experiment. At the Brookhaven National Laboratory (BNL), a proton beam was directed to a beryllium target, producing pions that decay in muons and neutrinos. By blocking the muons with a thick iron shield, the resulting beam was entirely made of muon-associated neutrinos. This was the first neutrino beam in history. A fraction of the neutrinos then interacted in a 10 ton aluminium spark chamber. Since pions decay primarily into muons ($\sim 100\%$ branching fraction), this setup allowed to test if the neutrinos produced together with a muon were different from neutrinos produced together with an electron. Indeed, if muon- and electron-associated neutrinos would be identical, muon and electron tracks would be observed in equal number. They observed 29 muons, and 6 electrons that were compatible with backgrounds [42], thus confirming that there were at least two neutrino species. Lederman, Schwartz and Steinberger received the Nobel Prize in 1988 for "the neutrino beam method and the demonstration of the doublet structure of the leptons through the discovery of the muon neutrino".
The discovery of the τ lepton at the SLAC e^+e^- accelerator in 1975 [86] led to the search for a third neutrino species, the ν_τ, as an implication of flavor theory. The ν_τ was finally detected by the DONUT experiment at the Fermilab Tevatron in 2000 [66]. To obtain this experimental result, a beam composed primarily of ν_τ particles was employed. These

particles originated mainly from the decay of τ leptons, which in turn were generated by the decay of D_S mesons produced through the collision of 800 GeV protons with a tungsten beam dump. τ leptons resulting from ν_τ scatterings were detected thanks to a nuclear emulsion, where a characteristic kinked track was visible. At the neutrino energies in the DONUT experiment ($\mathcal{O}(100)$ GeV), the τ lepton typically decays within 2 mm of its creation to a single charged daughter (86% branching fraction). Thus, the signature of the τ is a track with a kink, signifying a decay characterized by a large transverse momentum. A total of four such events were detected, which was consistent with the theoretical predictions. After the ν_τ discovery, all the leptons in the standard model seemed to have a corresponding neutrino; the question that naturally arises is whether there are more than three leptons generations. The answer to this question was brought by the four LEP experiment studying the Z decay width. The Z boson can decay into charged particles and particles that are invisible at accelerators, such as neutrinos. By measuring the total Z boson decay width, and subtracting from the Z width the measurable contributions from the charged particles, one can obtain the width of the "invisible" particles contributions. Under the assumption that the invisible width comes from $Z \to \nu\overline{\nu}$, and that each neutrino species contributes equally to such width, it is possible to measure the number of neutrino species contributing to this process. The obtained result is compatible with the fact that there are only three species that couple to the Z boson.

1.2. Neutrinos in the Standard Model

The interactions among elementary particles through three fundamental forces are described by the Standard Model (SM), which is a comprehensive framework extensively discussed in [17]. The modelization and mathematical description of the three fundamental interaction forces -electromagnetic, strong and weak - is based on the Quantum Field Theory (QFT), and, to date, has been experimentally verified.
In the SM, particles are divided into bosons and fermions. Fermions have non-integer 1/2 spin and obey Pauli exclusion principle; boson, also known as "force carriers", have integer spin and are the mediators of the interactions between particles. The experimental discovery of the three neutrino species is in agreement with what is called "weak interaction doublets", meaning that neutrino and leptons come in pairs and have same flavour, namely e, μ or τ. Neutrinos are electrically neutral particles, that do not have color charge; hence they can only interact with matter via the weak interaction, mediated by the $W^\pm$ and the Z bosons.

1.2.1. Neutrino interactions in matter

In matter, neutrinos can interact via two channels, leaving neutrinos in the final state. Neutrinos can interact either via neutral (NC) or charged current (CC) processes. The NC interaction proceeds through the exchange of a Z^0 boson and the emission of a neutrino of the same flavour as the incoming one[56]. In the CC interaction, which occurs through

the exchange of a $W^{\pm}$ boson, the final state lepton is the charged partner of the incoming flavour. An extensive and detailed description of the neutrino interactions can be found in [51]. The CC interactions are the main channel of neutrinos detection, as a charged final state is easily detectable, while the NC interaction often constitute a background in neutrinos experiments. This section will focus on the CC neutrino interactions in the energy range 1-100 GeV.
Figure 1.3 shows the ratio between the (anti)neutrino cross section and its energy as function of the incoming (anti)neutrino energy.

Charged Current Quasi-Elastic processes (CCQE)
This interaction channel is dominant for neutrinos energies up to 2 GeV. In CCQE, neutrinos elastically scatter off nucleons, liberating one or more nucleons from the target. In the case of a neutrino interacting, the target neutron is converted to a proton. In the case of an antineutrino that scatters, the target proton is converted to a neutron:

$$\begin{aligned} \nu_l n &\rightarrow l^- p \\ \overline{\nu}_l p &\rightarrow l^+ p \end{aligned} \tag{1.6}$$

Such process becomes increasingly less probable at higher energies due to the fact that the 4-momentum transfer increases, making it increasingly difficult for the target nucleon to remain intact.
The CCQE process is relevant in neutrinos experiments because its two-body kinematic process allows to precisely determine the neutrino energy, crucial for oscillation studies.

Resonance production (RES)
Neutrinos can excite the target nucleon to a resonance state. In this case, the interaction is inelastic; this mechanism is dominant for neutrino energies from 2 to 5 GeV; it typically happens when the center of mass energy is larger than the mass of a delta baryon ($1232\,\mathrm{MeV/c^2}$). The resonance state quickly decays, resulting in nucleon with a single pion production [51], as shown in Figure 1.2. The single pion production can occur for both neutron and protons as targets; there are three (for both neutrino and antineutrino) possible charged current resonant single pion reaction channels:

$$\begin{aligned} \nu_l p &\rightarrow l^- p\, \pi^+ \\ \nu_l n &\rightarrow l^- p\, \pi^0 \\ \nu_l n &\rightarrow l^- n\, \pi^+ \end{aligned} \tag{1.7}$$

where the charged lepton of corresponding flavour is produced in the resonance. Resonance production is most significant in the transition region between QE and Deep Inelastic Scattering (see next paragraph) dominance, above which it decreases like QE.

Deep Inelastic Scattering (DIS)
At neutrino energies from 5 GeV, the main interaction channel is Deep Inelastic Scattering

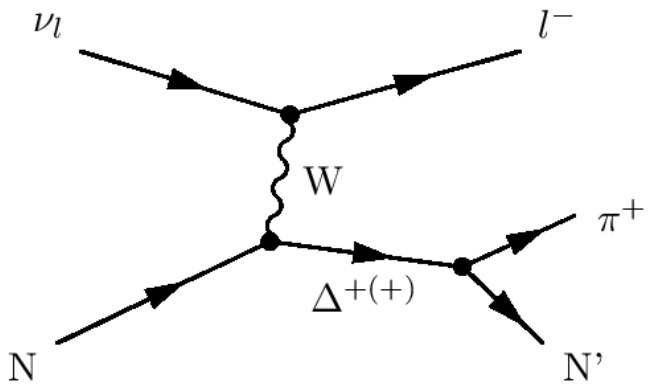

Figure 1.2.: Feynman diagram for a CC neutrino RES process. Diagram is reproduced from [101].

(DIS). In this regime, the neutrino can resolve the individual quark constituents of the nucleon. The neutrino can scatter off the quarks of a nucleon via the exchange of a charged virtual W boson, producing a lepton and a hadronic system in the final state. The hadronic system manifests as the creation of a hadronic shower:

$$\nu_l N \to l^- X \tag{1.8}$$

where X is the hadronic system. A Feynmann diagram of a DIS is shown in Figure 1.4. DIS processes can be described with three dimensionless variables: the inelasticity y, the 4-momentum transfer Q^2, and the Bjorken scaling variable x. These three kinematic variables are defined with the following relations:

$$Q^2 = -q^2 = (p_\nu - p_l)^2 \tag{1.9}$$

$$y = \frac{p_p \cdot q}{p_p \cdot p_\nu} \tag{1.10}$$

$$x = \frac{Q^2}{2p_p \cdot q} \tag{1.11}$$

where p_p, p_ν and p_l are respectively the 4-momenta of the scattered quark, of the incoming neutrino and of the outgoing lepton. In practice, the experiments do not directly measure 4-momenta, but these three Lorentz-invariant parameter can be easily reconstructed using the observables in a given experiment. The inelasticity y can be derived as:

$$y = \frac{E_{had}}{E_\nu} \tag{1.12}$$

where E_{had} is the energy of the hadronic shower and E_ν is the energy of the incoming neutrino. The inelasticity variable clearly reflects the kinetic energy of the outgoing hadronic system. The Bjorken scaling variable can be expressed as a function of the inelasticity as:

$$x = \frac{Q^2}{2M_N E_{had}} = \frac{Q^2}{2M_N E_\nu y} \tag{1.13}$$

where M_N is the mass of the nucleon. Lastly, the 4-momentum transfer Q^2 can be written as:

$$Q^2 = -m_l^2 + 2E_\nu(E_l - p_l \cos\theta_l) \tag{1.14}$$

where m_l, E_l, p_l and θ_l are the mass, energy, 4-momentum and scattering angle, with respect to the incoming neutrino, of the outgoing charged lepton.

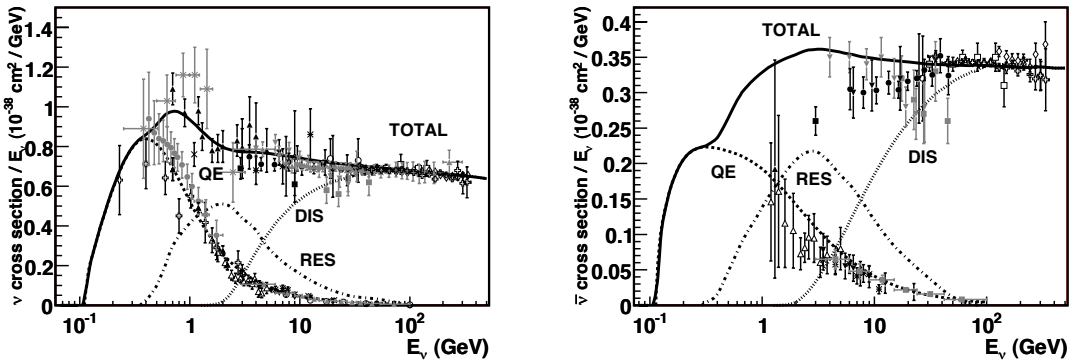

(a) (b)

Figure 1.3.: Total neutrino (1.3a) and antineutrino (1.3b) per nucleon CC cross-sections divided by neutrino energy and plotted as a function of energy [51].

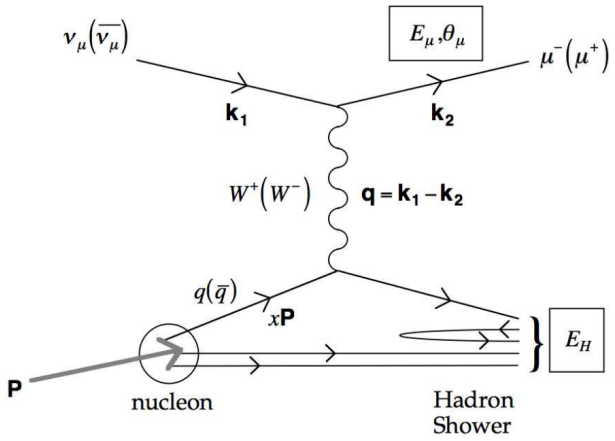

Figure 1.4.: Feynman diagram for a CC neutrino DIS process. Diagram is reproduced from [41].

1.2.2. Neutrinos properties: helicity and CP symmetry

Experimental observations have made it possible to determine the properties of neutrinos in the SM. In particular, their helicity and their symmetry under Parity and Charge Conjugation transformations have been tested from the late 50's.

The chirality is an intrinsic quantum property of the particle, that refers to how a particle's quantum mechanical wave function behaves when a particle is rotated. To visualize this concept, one can say that it translates into the particle's wave function not being superimposed on its image in a mirror.

The helicity of a particle, on the other hand, is the projection of a particle's spin onto its

momentum. Left-handed particles have spins in the opposite direction of their momentum, or left helicity; the opposite stands for right-handed particles. For msssless particles, helicity and chirality are the same; on the other hand, for massive particles, the chirality and the helicity no longer correspond. A Parity (P) transformation is the flip in the sign of the spatial coordinates, and it corresponds to a point reflection; parity conservation means that, under a parity transformation, the properties of a particle - such as right- or left- handedness - do not change. Lee and Yang were questioning P conservation in weak interaction [68], when Wu carried out an experiment to test such property in weak interactions, recording the helicity of the $\overline{\nu}_e$ produced in the Cobalt 60 β decay [111]. Wu showed that the helicity of the $\overline{\nu}_e$ was always right-handed; hence, parity is not conserved in weak interactions. The main discovery of such experiment was that **neutrinos are always left-handed** and **antineutrinos are always right-handed**. Such result was confirmed for ν_μ and $\overline{\nu}_\mu$ by measuring the muon's helicity from a beam of $\pi^\pm \to \mu^\pm + (\nu_\mu/\overline{\nu}_\mu)$ [19]. The non-conservation of parity for neutrinos and anti-neutrinos was extremely puzzling for the physicist in the 60's; more experiments were carried out to test the neutrino properties under the combined Charge Conjugation and Parity transformations.

The Charge Conjugation (C) operator transforms a particle into its own antiparticle. If applied to the neutrino, the Charge Conjugation operator would give a left-handed antineutrino, which does not occur; this grants the non conservation of the Charge Conjugation in weak interactions.

However, by combining the C and the P operators, the new Charge-Parity operator (CP) should in principle be conserved in the weak interactions, since it turns a left-handed neutrino to a right-handed antineutrino. CP conservation means that the laws of physics should be the same if a particle is interchanged with its antiparticle (C-symmetry) while its spatial coordinates are inverted. It has been shown in [38], with an experiment that used K^0 mesons that decay into pions, that the CP symmetry is not conserved in weak interactions in the quark sector. The K^0 mesons evolve as the coherent superposition, in equal proportions at the time of production, of two CP eigenstates, one CP-odd and one CP-even. The former, that has a very short lifetime, decays into two pions; the latter, with a lifetime about five times larger, decays into three pions. Such difference in the lifetime allows for a clean separation of the two eigenstates when far away from the K^0 producing target [62]. In 1964, at the end of a beam of about 17 m, Christenson, Cronin, Fitch and Turlay observed for the first time a significant number of two pions decays (roughly 1/500), providing the first evidence for CP violation in the quark sector.

CP violation was demonstrated by Sakharov in 1967 [100] to be one of the three necessary conditions for baryogenesis. Investigating CP violation in the leptonic sector could provide new hints to solve this fundamental enigma.

1.3. Neutrino Oscillations

1.3.1. Solar neutrinos problem

One of the most abundant sources of electron neutrinos is the Sun, which creates its energy via nuclear fusion. In the late 1960s, R. Davis and J. Bahcall set up an experiment located in the Homestake mine in South Dakota to measure electron neutrino emissions from the sun and compare it to the flux predicted by Bahcall et al. [64]. The detection method exploited the electron capture decay $^{37}\mathrm{Ar} + e^- \rightarrow \mathrm{Cl} + \nu_e$. Davis et al. found that the measured flux was about three times smaller than the predicted flux [45]. Such discrepancy is known as the "Solar Neutrinos Problem", and triggered the questions and research that lead to the discovery of neutrinos oscillations phenomenon. The same results were reproduced later in the 1990s by other experiments such as Kamiokande [59], SAGE [1] and GALLEX [29], and in 2002 the Sudbury Neutrino Observatory (SNO) collaboration performed and published a measurement of the solar neutrino flux independent of any solar model assumptions [13].
Already at the time of the Homestake experiment results, Bruno Pontecorvo suggested an explanation for this anomaly. He developed a theory of neutrino-antineutrino oscillations similar to the known oscillations in the quark sector [89] and a theory of lepton number violation [90] which predicted that neutrinos can change their flavor as they propagate, similarly to quarks ($\nu \leftrightarrow \overline{\nu}$). Hence, the observed reduction in the flux of electron neutrinos detected on Earth can be accounted for by the fact that a portion of the initially emitted electron neutrinos from the Sun undergo oscillations, transforming into different flavor states as they travel from sun to Earth. The SNO experiment confirmed this hypothesis by measuring both the electron neutrino and the total neutrino flux from the sun. The electron neutrino flux was indeed about a third than the total neutrino flux [13], providing strong evidence that part of the ν_e's change their flavor into ν_μ and ν_τ.
Such flavor changing mechanism is what is now known as *neutrinos oscillations*.

1.3.2. Atmospheric neutrinos

Another strong evidence for neutrino oscillations came from the Super Kamiokande experiment, that aimed to measure the flux of atmospheric muon neutrinos and electron neutrinos. Atmospheric neutrinos are produced by the cosmic ray interaction with the Earth atmosphere. Such interaction creates hadronic showers, mostly made of pions that can decay in flight producing (anti)muons and (anti)neutrinos:

$$\pi^{\pm} \rightarrow \mu^{\pm} + \overset{(-)}{\nu}_{\mu}$$

$$\mu^{\pm} \rightarrow e^{\pm} + \overset{(-)}{\nu}_{\mu} + \overset{(-)}{\nu}_{e}.$$

The flux of $\overset{(-)}{\nu}_{\mu}$ is hence expected to be twice the flux of ν_e; such hypothesis was confirmed by experiments targeting high energy neutrinos ([40]). However, the Super-Kamiokande experiment measured equal fluxes for the two neutrino species [52]. This result was confirmed by other experiments (IBM [23]). The main difference between the experiments that did measure the expected flux ratio and those that did not, lies in the targeted energy range

and in the baseline between the neutrino production point and the detection. The Super-Kamiokande Cherenkov detector is able to distinguish down-going neutrinos (originating from hadronic showers in the atmosphere right above the detector) from up-going neutrinos (originating from showers in the atmosphere on the other side of the Earth), as shown in Figure 1.5a. The former travel $\mathcal{O}(10^2)$ km before encountering the detector, while the latter travel $\mathcal{O}(10^4)$ km before reaching the detector. The major new feature introduced by Super-Kamiokande was the zenith angle distribution. In particular, Super-Kamiokande measured a zenith angle dependent depletion of muon neutrinos coming from below the horizon ($cos(\theta) = -1$); such depletion seemed to have a dependence on the ratio between L, the baseline travelled by the ν, and E_ν. the neutrino energy. Such depletion is shown in Figure 1.5b. These results were compared to the extension to Pontecorvo's theory of neutrino oscillation, proposed by Ziro Maki, Masami Nakagawa and Shoichi Sakata in 1962 [74], that broadened the theory to flavor oscillations. The Super-Kamiokande results were in agreement with this scenario, and provided the first evidence, in 1998, of neutrinos oscillations. Takaaki Kajita of the Super-Kamiokande Collaboration was awarded the 2015 Nobel Prize in physics, along with Arthur B. McDonald of the SNO Collaboration.

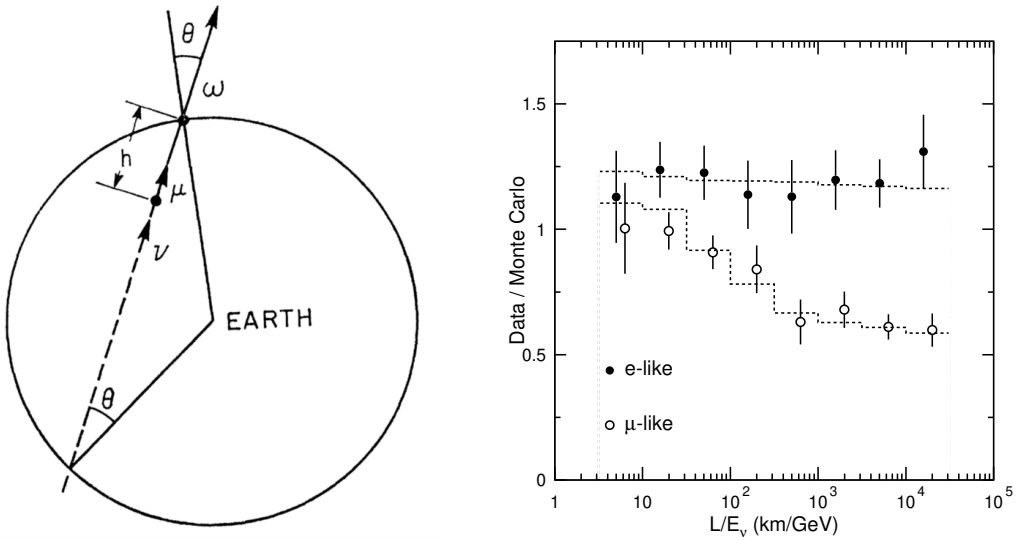

(a) (b)

Figure 1.5.: 1.5a: Atmospheric neutrino detection technique based on upgoing neutrinos. Upgoing neutrinos that arrive at Earth with an angle θ with respect to the normal to the Earth surface. The ν_μ, after the CC interaction, produces a μ that flies on the same direction. h represents the distance between the interaction and the detection point. 1.5b: ratio of data to Monte-Carlo prediction assuming no neutrino oscillations, for ν_μ and ν_e atmospheric neutrino events seen by Super-Kamiokande. From [52].

1.3.3. Oscillation theory

Neutrinos are produced as flavour eigenstates in the weak interaction: $|\nu_\alpha\rangle$ with $\alpha = e, \mu, \tau$, which are the same as that of the other lepton in their doublet. However, as with the

quarks and the CKM matrix that describes the probability of a transition from a quark of flavour x to a quark to flavour y, it is possible that the flavour eigenstates (states with definite flavour) are not identical to the mass eigenstates $|\nu_i\rangle$ (states which have definite mass). This means that each flavour eigenstate can be expressed as a linear combination of mass eigenstates:

$$|\nu_\alpha\rangle = \sum_i U^*_{\alpha i}|\nu_i\rangle, \tag{1.15}$$

where the leptonic mixing matrix U is known as the PMNS matrix (Pontecorvo-Maki-Nakagawa-Sakata). Equation 1.15 can be inverted as:

$$|\nu_i\rangle = \sum_i U_{\alpha i}|\nu_\alpha\rangle \tag{1.16}$$

U is a 3x3 unitary matrix; for a 3-flavor picture, the flavour eigenstates can be written as:

$$\begin{pmatrix}\nu_e\\ \nu_\mu\\ \nu_\tau\end{pmatrix} = \begin{pmatrix}U^*_{e1} & U^*_{e2} & U^*_{e3}\\ U^*_{\mu 1} & U^*_{\mu 2} & U^*_{\mu 3}\\ U^*_{\tau 1} & U^*_{\tau 2} & U^*_{\tau 3}\end{pmatrix} \cdot \begin{pmatrix}\nu_1\\ \nu_2\\ \nu_3\end{pmatrix} \tag{1.17}$$

In vacuum, the mass eigenstates created at t = 0 and x = 0 propagate in time and space according to the time-dependent Schroedinger equation with no potentials (using $c = \hbar = 1$):

$$i\frac{\mathrm{d}}{\mathrm{d}t}|\nu_i(x,t)\rangle = \mathcal{H}|\nu_i(x,t)\rangle = -\frac{1}{2m_i}\frac{\partial^2}{\partial x^2}|\nu_i(x,t)\rangle \tag{1.18}$$

The solution to this equation is a plane-wave:

$$|\nu_i(x,t)\rangle = e^{-i(E_i t - p_i x)}|\nu_i\rangle = e^{-i\phi_i}|\nu_i\rangle \tag{1.19}$$

where $E_i = \sqrt{p_i^2 + m_i^2}$ is the particle energy, p_i is the 4-momentum of the neutrino mass state and x is the 4-space vector. By using in Equation 1.15 the solution in Equation 1.19, one can obtain:

$$|\nu_\alpha\rangle = \sum_i U^*_{\alpha i} e^{i\phi_i}|\nu_i\rangle. \tag{1.20}$$

By combining Equation 1.16 and Equation 1.20 it is possible to obtain the time evolution of the flavor eigenstate $|\nu_\alpha(x,t)\rangle$ as function of the initial flavor state $|\nu_\beta(0,0)\rangle$:

$$|\nu_\alpha(x,t)\rangle = \sum_\beta \sum_i U_{\beta i} U^*_{\alpha i} e^{-i\phi_i t}|\nu_\beta(0,0)\rangle. \tag{1.21}$$

It is important to notice that Equation 1.21 shows us that if U is not a diagonal matrix, meaning that the flavor eigenstates are mixed to mass eigenstates, then a neutrino of a given initial flavor can be detected, after propagation, in another flavor. Moreover, if the states have different masses, then the phase between the states will change with distance from the source. It is now possible to calculate the transition amplitude for detecting a neutrino of flavor β after a time t having generated a neutrino of flavor α at t=0, x=0, which is:

$$\mathcal{A}(\nu_\alpha(0,0) \to \nu_\beta(x,t)) = \langle\nu_\beta(x,t)|\nu_\alpha(0,0)\rangle \tag{1.22}$$

and the probability for detecting a neutrino of flavor α after a time t having generated a neutrino of flavor β at t=0, that is the squared modulus of such amplitude:

$$\begin{aligned} P(\nu_\alpha(0,0) \to \nu_\beta(x,t)) &= |A(\nu_\alpha(0,0) \to \nu_\beta(x,t))|^2 \\ &= \left|\sum_i U_{\alpha i} U^*_{\beta i} e^{-i\phi_i}\right|^2 \\ &= \sum_i U_{\alpha i} e^{i\phi_i} U^*_{\beta i} \sum_j U^*_{\alpha j} e^{-i\phi_j} U_{\beta j} \\ &= \sum_i \sum_j U_{\alpha i} U^*_{\beta i} U^*_{\alpha j} U_{\beta j} e^{i(\phi_j - \phi_i)t} \end{aligned} \tag{1.23}$$

$P(\nu_\alpha \to \nu_\beta)$ is called *oscillation* or *transition probability*. The phase difference $\phi_j - \phi_i$ can be written as:

$$\phi_j - \phi_i = (E_j - E_i)t - (p_j - p_i)x \tag{1.24}$$

given that $\phi_i = E_i t p_i x$. It is possible to simplify Equation 1.23 taking into account that the neutrinos are highly relativistic, then $t = x = L$ where L is the travelled distance between the neutrino source and the neutrino detector, often referred to as *baseline*, and $p_i = \sqrt{E_i^2 - m_i^2} = E_i\sqrt{1 - \frac{m_i^2}{E_i^2}} \simeq E_i(1 - \frac{m_i^2}{E_i^2})$. Hence,

$$\phi_j - \phi_i = L\left(\frac{m_j^2}{E_j^2} - \frac{m_i^2}{E_i^2}\right) = \frac{\Delta m^2 L}{2E} \tag{1.25}$$

where $\Delta m^2 = m_j^2 - m_i^2$ and $E_i = E_j = E$ is the neutrino energy. The oscillation probability in Equation 1.23 can hence be written as:

$$P(\nu_\alpha(0,0) \to \nu_\beta(x,t)) = P(\nu_\alpha \to \nu_\beta) = \sum_i \sum_j U_{\alpha i} U^*_{\beta i} U^*_{\alpha j} U_{\beta j} e^{\frac{\Delta m^2_{ij} L}{2E}}. \tag{1.26}$$

Equation 1.26 clearly indicates that the oscillation probability and mechanism only depends on the squared mass difference, and not on the individual neutrino masses. Neutrino flavour and mass states are mixed and a coherent superposition of mass states is created at the weak vertex. This coherent superposition reflects the fact that it is not possible to experimentally resolve the single mass states created at the vertex. Equation 1.26 can be expressed in terms of the real and imaginary components of the matrix product:

$$\begin{aligned} P(\nu_\alpha \to \nu_\beta) = \delta_{\alpha\beta} &- 4\sum_{i>j} \mathfrak{Re}(U_{\alpha i} U^*_{\beta i} U^*_{\alpha j} U_{\beta j}) \sin^2\left(\frac{\Delta m^2_{ij} L}{4E}\right) \\ &+ 2\sum_{i>j} \mathfrak{Im}(U_{\alpha i} U^*_{\beta i} U^*_{\alpha j} U_{\beta j}) \sin\left(\frac{\Delta m^2_{ij} L}{2E}\right). \end{aligned} \tag{1.27}$$

A few observation can be made from this formula:

- in order for oscillations to occur, there must be mixing and the masses must be unequal. If the masses eigenvalues were equal, and in particular if they were null, the oscillation probability would be zero;

- the unitarity of U grants the conservation of the total neutrino flux, but the composition of said flux changes;
- if mass states and flavour states are mixed, there will always be a probability of flavour change; however, if it was possible to resolve the mass states at the production vertex, the probability of flavour change would not oscillate;
- the oscillation probability depends on L/E, which is the ratio between the distance of production and detection point of the neutrino and its energy.

The U matrix, or PMNS matrix, is usually expressed by 3 rotation matrices and a complex phase:

$$U = \begin{pmatrix} 1 & 0 & 0 \\ 0 & c_{23} & s_{23} \\ 0 & -s_{23} & c_{23} \end{pmatrix} \begin{pmatrix} c_{13} & 0 & s_{13}e^{-i\delta_{CP}} \\ 0 & 1 & 0 \\ -s_{13}e^{-i\delta_{CP}} & 0 & c_{13} \end{pmatrix} \begin{pmatrix} c_{12} & s_{12} & 0 \\ -s_{12} & c_{12} & 0 \\ 0 & 0 & 1 \end{pmatrix} \begin{pmatrix} e^{i\alpha_1/2} & 0 & 0 \\ 0 & e^{i\alpha_2/2} & 0 \\ 0 & 0 & 1 \end{pmatrix} \tag{1.28}$$

where $c_{ij} = cos(\theta_{ij}$ and $s_{ij} = sin(\theta_{ij})$. The PNMS matrix is parametrized by the three mixing angles θ_{ij}, and by three complex phases δ_{CP}, α_1 and α_2. Observations:

- the first matrix is called the "23 sector" or "atmospheric sector", because the θ_{23} angle regulates most of the atmospheric neutrinos oscillation
- the second matrix is called the "13 sector" or "reactor sector"
- the third matrix is called the "cross-mixing sector" or "solar sector" as the θ_{12} angle influences most of the solar neutrino oscillations.
- the fourth matrix has physical consequences only if neutrino are Majorana particles - meaning that neutrinos are their own antiparticle. Even in the case of Majorana neutrinos, it would not affect neutrino oscillation, since the Majorana phases cancel out when the U matrix is squared.
- the non zero diagonal terms result in neutrinos created in mass eigenstates superposition.

The present knowledge of the oscillations parameters, obtained with a global fit from SuperKamiokande, Gallex, GNO, SAGE, SNO and Borexino is reported in Table 1.1.

CP symmetry in neutrinos oscillations

It is interesting to discuss how the P, C symmetries affect the neutrino oscillations. As mentioned earlier in this section, the weak interaction violates the P and C symmetries singularly, and it violates the CP symmetry in the quark sector. The oscillation probability

for antineutrinos can be optained by applying the CP operator to the oscillation probability in Equation 1.27:

$$P(\overline{\nu}_\alpha \to \overline{\nu}_\beta) = \delta_{\alpha\beta} - 4\sum_{i>j} \mathfrak{Re}(U_{\alpha i}U^*_{\beta i}U^*_{\alpha j}U_{\beta j}) \sin^2\left(\frac{\Delta m^2_{ij}L}{4E}\right) - 2\sum_{i>j} \mathfrak{Im}(U_{\alpha i}U^*_{\beta i}U^*_{\alpha j}U_{\beta j}) \sin\left(\frac{\Delta m^2_{ij}L}{2E}\right). \tag{1.29}$$

Equation 1.27 and Equation 1.29 are identical but for their complex parts which are opposite of one another. The only difference between Equation 1.27 and Equation 1.29 is a sign before the imaginary part. If the PMNS matrix is complex, meaning that $\delta_{CP} \neq 0, \pi$, it implies that $P(\overline{\nu}_\alpha \to \overline{\nu}_\beta) \neq P(\nu_\alpha \to \nu_\beta)$. The difference between the two oscillation probabilities for neutrinos and antineutrinos can be expressed as [110]:

$$P(\nu_\alpha \to \nu_\beta) - P(\overline{\nu}_\alpha \to \overline{\nu}_\beta) = \Delta P_{\alpha\beta} = \pm 16 J \sin\left(\frac{\Delta m^2_{21}L}{4E}\right) \sin\left(\frac{\Delta m^2_{31}L}{4E}\right) \sin\left(\frac{\Delta m^2_{32}L}{4E}\right), \quad J \equiv \mathrm{Im}\left[U_{\beta 1}U^*_{\alpha 1}U^*_{\beta 2}U_{\alpha 2}\right] \tag{1.30}$$

The quantity J in Equation 1.30 is a measure of CP violating phase δ_{CP} of the PMNS matrix. Using the standard parametrization of the PMNS matrix, one can define J as:

$$J = \frac{1}{8}\cos\theta_{13}\sin 2\theta_{12}\sin 2\theta_{13}\sin 2\theta_{23}\sin\delta_{CP} \tag{1.31}$$

The definition of J, called *Jarlskog invariant*, shows that CP violation in neutrino oscillations can happen only if all three mixing angles θ_{ij} are different from zero and the δ_{CP} phase is different from 0 and π. It is also important to note that, from Equation 1.30, the CP violation effects are non-zero only in appearance channels ($\beta \neq \alpha$), and it is zero in disappearance channels ($\beta = \alpha$). From Equation 1.30 and the values of Δm^2_{ij} from Table 1.1, it is possible to deduce that the effect of CP violation is proportional to $\sin\left(\frac{\Delta m^2_{ij}L}{4E}\right)$. Being $\Delta m^2_{31} \simeq \Delta m^2_{32} << \Delta m^2_{21}$, the oscillation frequency in the 31 and 32 channels is larger, and it averages out in the region where the CP violating effect is appreciable [21]. Hence, the CP violating effect can be observed in experiments that can observe the oscillations governed by Δm^2_{21}; these experiments compare $P(\nu_\mu \to \nu_e)$ to $P(\overline{\nu}_\mu \to \overline{\nu}_e)$ and they involve long baselines (several hundreds of km) so that the L/E ratio is large enough that the variable $\Delta P_{\alpha\beta}$ is non-zero. However, in such type of experiment, neutrinos typically propagate in matter - the Earth - which creates an asymmetry in the oscillations of neutrinos and antineutrinos, as explained in Section 1.3.4. The effects of the CP violation and of the oscillations in matter need to be disentangled, which is non-trivial but a crucial point in knowledge of neutrinos physics. A measurement of value of $\delta_{CP} \neq 0, \pi$ would indeed provide the first evidence of CP violation in the lepton sector.

1.3.4. Oscillations in matter and consequences of matter effect

Neutrino oscillations arise from a phase difference between the wavepackets of the three mass eigenstates, caused by the fact that wavepackets with different masses propagate with

different velocities. Neutrinos can propagate and interact in matter, and this affects the oscillations, that in matter are described differently. This effect is known as the MSW or matter effect [110]. The matter effect introduces a potential V in the hamiltonian, that induces a phase difference. For neutrinos oscillating in a potential V, the phase difference depends on the total energy of the mass eigenstate, as the interaction with matter can be different for the three flavor eigenstates. Indeed, neutrinos can interact via NC or CC interactions, as shown in Section 1.2.1. Neutral current interactions do not affect the oscillation probability; however, charged current interaction affect only electron neutrinos, since stable matter is made of electrons. Such effect can be added in the oscillation probability derivation through an additional potential term in the interaction Hamiltonian:

$$V_{CC} = \pm\sqrt{2}G_F n_e \tag{1.32}$$

where G_F is the Fermi constant and n_e is the average electron density of the medium. This term is positive for ν_e and negative for $\overline{\nu}_e$. A detailed description of the matter effect is beyond the scope of this work, and can be found in many resources, such as [54]. The main consequences of the oscillations in matters are discussed briefly.

In vacuum, oscillations are sensitive only to the absolute value of the mass differences; however, when neutrinos propagate in matter, the oscillations become sensitive to the sign of the mass splitting term Δm_{ij}. The matter effect introduces an additional term in the oscillation probability of Equation 1.23, proportional to $sin(\Delta m^2_{31} L/4E_\nu)$, that has the potential to resolve the sign of the mass difference. Indeed, despite having established that ν_1 is lighter than ν_2[9], it has still not been determined whether ν_3 is the heaviest (NH or NO, standing for normal neutrino mass hierarchy or ordering) or the lightest (inverted neutrino mass hierarchy or ordering, IH or IO) of the mass eigestates. A schematic representation of the possible neutrino mass hierarchies is shown in Figure 1.7.

The consequence of the matter effect is thus that, the larger the amount of matter traversed by the neutrinos, the larger the term sensitive to the mass hierarchy. For this reason, long baseline experiments in which the neutrinos propagate in matter for very long distances are the most sensitive to resolving the neutrino mass hierarchy.

However, the matter effect also introduces an asymmetry in the oscillation probability of neutrinos and antineutrinos. Indeed, neutrinos and antineutrinos interaction are differentiated in matter by the sign of the V_{CC} potential. The experimental challenge that long baseline experiments face is hence to disentangle the CP violating effects from the matter effect, as both induce neutrino-antineutrino asymmetry. Figure 1.6 shows $P(\nu_\mu \to \nu_e)$ and $P(\overline{\nu}_\mu \to \overline{\nu}_e)$ oscillation probability, as a function of the neutrino energy, for different values of δ_{CP} in degrees, for oscillations in vacuum (1.6a) and in matter (1.6b).

1.4. Current knowledge and future experiments

Since the discovery of neutrino oscillations, most of the parameters involved have been measured with different degrees of accuracy, and they are reported in Table 1.1. At present, the values of all mixing angles and squared-mass differences from solar and reactor

		Normal Ordering (best fit)		Inverted Ordering ($\Delta\chi^2 = 2.7$)	
		bfp $\pm 1\sigma$	3σ range	bfp $\pm 1\sigma$	3σ range
without SK atmospheric data	$\sin^2\theta_{12}$	$0.304^{+0.013}_{-0.012}$	$0.269 \to 0.343$	$0.304^{+0.013}_{-0.012}$	$0.269 \to 0.343$
	$\theta_{12}/^\circ$	$33.44^{+0.78}_{-0.75}$	$31.27 \to 35.86$	$33.45^{+0.78}_{-0.75}$	$31.27 \to 35.87$
	$\sin^2\theta_{23}$	$0.570^{+0.018}_{-0.024}$	$0.407 \to 0.618$	$0.575^{+0.017}_{-0.021}$	$0.411 \to 0.621$
	$\theta_{23}/^\circ$	$49.0^{+1.1}_{-1.4}$	$39.6 \to 51.8$	$49.3^{+1.0}_{-1.2}$	$39.9 \to 52.0$
	$\sin^2\theta_{13}$	$0.02221^{+0.00068}_{-0.00062}$	$0.02034 \to 0.02430$	$0.02240^{+0.00062}_{-0.00062}$	$0.02053 \to 0.02436$
	$\theta_{13}/^\circ$	$8.57^{+0.13}_{-0.12}$	$8.20 \to 8.97$	$8.61^{+0.12}_{-0.12}$	$8.24 \to 8.98$
	$\delta_{\rm CP}/^\circ$	195^{+51}_{-25}	$107 \to 403$	286^{+27}_{-32}	$192 \to 360$
	$\frac{\Delta m^2_{21}}{10^{-5}eV^2}$	$7.42^{+0.21}_{-0.20}$	$6.82 \to 8.04$	$7.42^{+0.21}_{-0.20}$	$6.82 \to 8.04$
	$\frac{\Delta m^2_{3\ell}}{10^{-3}eV^2}$	$+2.514^{+0.028}_{-0.027}$	$+2.431 \to +2.598$	$-2.497^{+0.028}_{-0.028}$	$-2.583 \to -2.412$
		Normal Ordering (best fit)		Inverted Ordering ($\Delta\chi^2 = 7.1$)	
		bfp $\pm 1\sigma$	3σ range	bfp $\pm 1\sigma$	3σ range
with SK atmospheric data	$\sin^2\theta_{12}$	$0.304^{+0.012}_{-0.012}$	$0.269 \to 0.343$	$0.304^{+0.013}_{-0.012}$	$0.269 \to 0.343$
	$\theta_{12}/^\circ$	$33.44^{+0.77}_{-0.74}$	$31.27 \to 35.86$	$33.45^{+0.78}_{-0.75}$	$31.27 \to 35.87$
	$\sin^2\theta_{23}$	$0.573^{+0.016}_{-0.020}$	$0.415 \to 0.616$	$0.575^{+0.016}_{-0.019}$	$0.419 \to 0.617$
	$\theta_{23}/^\circ$	$49.2^{+0.9}_{-1.2}$	$40.1 \to 51.7$	$49.3^{+0.9}_{-1.1}$	$40.3 \to 51.8$
	$\sin^2\theta_{13}$	$0.02219^{+0.00062}_{-0.00063}$	$0.02032 \to 0.02410$	$0.02238^{+0.00063}_{-0.00062}$	$0.02052 \to 0.02428$
	$\theta_{13}/^\circ$	$8.57^{+0.12}_{-0.12}$	$8.20 \to 8.93$	$8.60^{+0.12}_{-0.12}$	$8.24 \to 8.96$
	$\delta_{\rm CP}/^\circ$	197^{+27}_{-24}	$120 \to 369$	282^{+26}_{-30}	$193 \to 352$
	$\frac{\Delta m^2_{21}}{10^{-5}eV^2}$	$7.42^{+0.21}_{-0.20}$	$6.82 \to 8.04$	$7.42^{+0.21}_{-0.20}$	$6.82 \to 8.04$
	$\frac{\Delta m^2_{3\ell}}{10^{-3}eV^2}$	$+2.517^{+0.026}_{-0.028}$	$+2.435 \to +2.598$	$-2.498^{+0.028}_{-0.028}$	$-2.581 \to -2.414$

Table 1.1.: Three-flavor oscillation parameters from our fit to global data. The numbers in the 1st (2nd) column are obtained assuming NO (IO), *i.e.*, relative to the respective local minimum. Note that $\Delta m^2_{3\ell} \equiv \Delta m^2_{31} > 0$ for NO and $\Delta m^2_{3\ell} \equiv \Delta m^2_{32} < 0$ for IO. The results shown in the upper (lower) table are without (with) adding the tabulated SK-atm $\Delta\chi^2$. From [48].

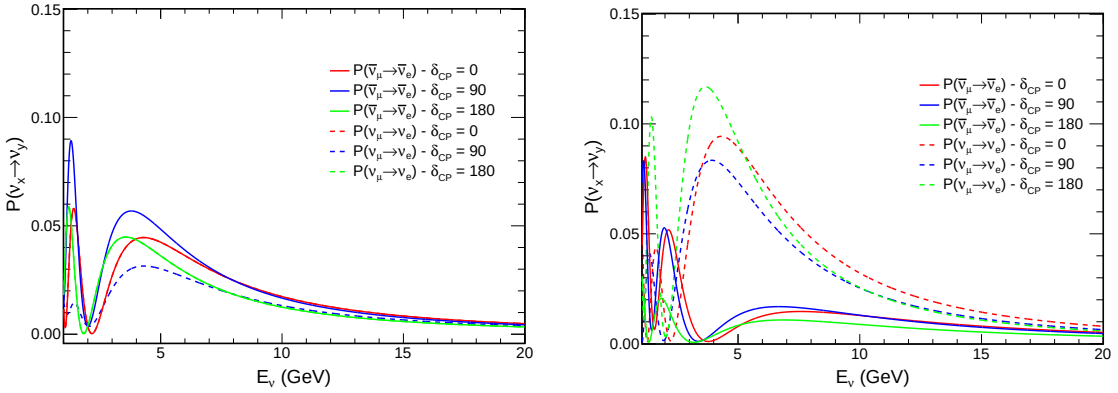

(a) (b)

Figure 1.6.: Oscillation probability for CP-effect sensitive channel $\overset{(-)}{\nu}_{\mu} \rightarrow \overset{(-)}{\nu}_{e}$ as function of the neutrino energy in vacuum (1.6a) and in matter (1.6b) for a baseline of 2000 km and for different values of δ_{CP}, reported in degrees in the legend. The oscillation probabilities are computed with the OscProb software package using the oscillation parameters in Table 1.1.

parameters in the 3 neutrinos oscillation scheme can be extracted from global fits of available data with a precision better than 15%. The atmospheric parameters, and in particular $\sin^2\theta_{23}$ have the largest remaining uncertainty - the octant of θ_{23} , i.e. whether it is smaller or larger than $\pi/4$, is still unknown. Moreover, the CP violating phase δ_{CP} is still undetermined. The current generation of experiments (NOvA, T2K, and Super-Kamiokande) is unlikely to obtain the statistical threshold to access these parameters. The next generation of neutrino experiments (DUNE, Hyper-Kamiokande) should reach the statistical threshold; hence they aim to improve the precision on the measurements of known parameters, and to measure the yet unknown parameters θ_{23}-octant and δ_{CP}, and to resolve the neutrino mass ordering. The JUNO experiment, under construction, is building a 35 m diameter detector at a distance of 53 km from the reactor cores of the Yangjiang and Taishan nuclear power plants in Kaiping, South China, and will have an unique sensitivity to the solar oscillation parameters Δm^2_{21}, Δm^2_{32}, and $sin^2\theta_{12}$ among the next generation experiments. Furthermore, neutrino telescopes such as IceCube and KM3NeT are expected to provide important contributions to the measurement of the unknown parameters. In particular, the goals of KM3NeT (whose infrastructure is described in more details in the following section) are measuring the neutrino mass ordering and identifying high-energy neutrino sources in the Universe [46].

1.4.1. KM3NeT

KM3NeT (KM3-scale Neutrino Telescope) [9] is a research infrastructure that manages the under-water neutrino telescopes currently being deployed in the Mediterranean Sea. It includes two sites, that are meant to target neutrinos of different energies. Both sites use the same technology; the principle is to instrument a large volume of seawater with modules of

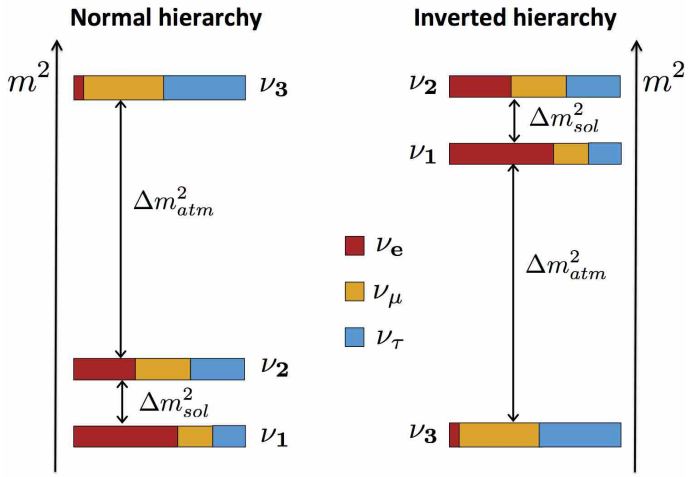

Figure 1.7.: Scheme of the two distinct neutrino mass hierarchies. The colour code indicates the fraction of each flavour (e, μ, τ) present in each of the mass eigenstates (ν_1, ν_2, ν_3). From [9].

photomultipliers. The photomultipliers are arranged into Digital Optical Modules (DOM), visible in Figure 1.10b, that are pressure-resistant spheres hosting 31 PMTs each, with their electronics and calibration devices. The DOMs are organized in strings anchored to the seabed, and kept vertical by a submarine buoy. The strings are connected to junction boxes that provide connections for power and data transmission. Both sites will be equipped of 115 strings, also called Detection Units (DUs).
As many neutrino detectors, KM3NeT uses Cherenkov light of charged secondary particles created in a neutrino interaction to detect neutrinos. Thanks to the arrival time of the Cherenkov photons and the positions of the fired photosensors, the direction and energy of the incoming neutrino can be reconstructed. Indeed, charged particles passing through a medium with a velocity larger than the speed of light in said medium, emit Cherenkov radiation. The Cherenkov light is emitted with an angle θ_C and that forms a conical light front, as shown in Figure 1.8. The opening angle of the cone depends on the particle velocity and on the refraction index of the medium, as shown in Equation 1.33:

$$\theta_C = \frac{1}{\beta n} \tag{1.33}$$

where $\beta = \frac{v}{c} = \frac{p}{\gamma mc}$ is the velocity of the particle and n is the refraction index of the medium. From the characteristics of the Cherenkov light detected by the modules, it is thus possible to reconstruct the energy, direction (spatial resolution of the sensors ($\sim 10\,\text{mm}$), arrival time ($\mathcal{O}(1)$ ns time resolution) and flavour of the particle. Indeed, muons of the energy up to few tens of GeV behave as minimum ionizing particles (MIP), which means that they lose a minimal amount of energy while propagating in a medium, and they mostly propagate in straight lines. For this reason, muons are identified in water Cherenkov detectors as straight tracks. On the other hand, electrons lose energy mostly via brehmsstrahlung for the same energies; this means that the particle radiates photons while propagating in the medium,

that in turn can interact with matter, producing more electron/positron pairs of lower energy. Thus they create a cascade of electromagnetic process (electromagnetic shower), identified by Cherenkov detectors as burst of light, opposed to the tracks formed by the muons. The different signature of the two particles events ("track-like", caused by muons produced in CC interactions of ν_μ or ν_τ, or "shower-like", caused by electrons produced in CC interactions of ν_e or ν_τ) allow identifying the flavor of the incoming lepton, as shown in Figure 1.9. The two KM3NeT sites under construction are called KM3NeT/ARCA and KM3NeT/ORCA; they differ in size, arrangement of the photomultipliers and foreseen objective.

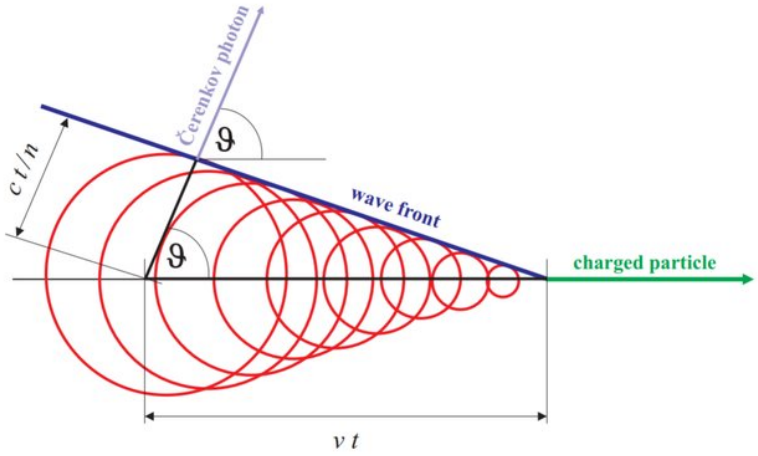

Figure 1.8.: from [60].

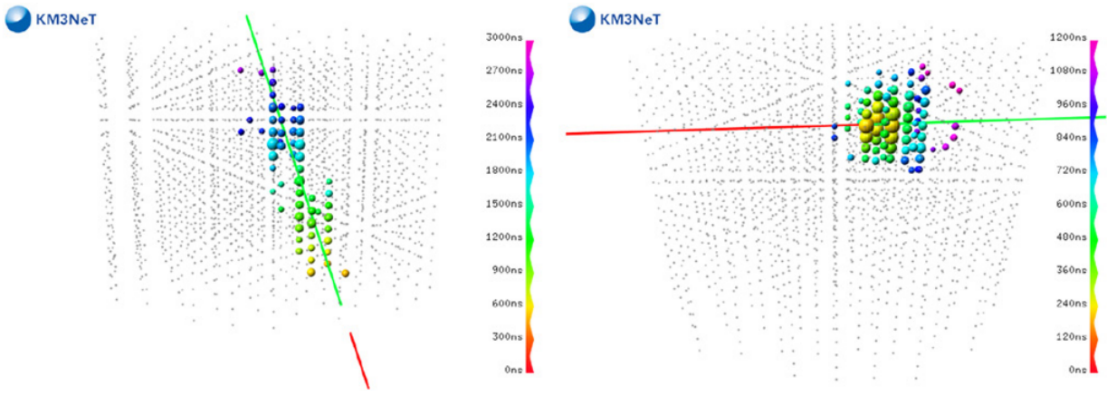

Figure 1.9.: Event displays for a simulated ν_μ CC event (left) and a contained ν_μ NC event (right). the incoming neutrino is indicated by the red line, and the outgoing lepton (muon or neutrino) by the green line. The colour scale gives the hit times with respect to the time of the neutrino interaction.From [9].

ARCA (Astroparticle Research with Cosmics in the Abyss) is located offshore Capo Passero, Italy, at a depth of 3500 m underwater in the Mediterranean Sea. It is the bigger detector with a sparser configuration, aiming at detecting high-energy cosmic neutrino sources (in

(a) (b) (c)

Figure 1.10.: 1.10a: Schematic of the layout of the completed KM3NeT/ORCA site, from [16]. 1.10b: a DOM being calibrated, photo taken in the CPPM assembly lab. 1.10c: photo of a launch vehicle deployment that exploits the unfurling of the string, taken in the CPPM assembly lab.

the range of TeV/PeV).
KM3NeT/ORCA is located 40 km offshore Toulon, France, in a depth of about 2450 m underwater in the Mediterranean Sea, providing a vast medium for detecting neutrino interactions. The design of the KM3NeT/ORCA is based on instrumenting 2200 200 200 m^3 of seawater with modules of photomultipliers. The DOMs are arranged in string arrays of 18, with a vertical separation of 9 m. The main objective for ORCA is the determination of the mass hierarchy of neutrinos and improving the uncertainties on atmospheric neutrino mixing parameters thanks to the detection of neutrinos of energies of the order of a few GeV.
ORCA is expected to play an important role for the neutrino tagging technique, as will be explained in Chapter 2.

2. Neutrino Tagging

Summary

The discovery of neutrino oscillations has brought a lot of attention to neutrino physics. The research in the last three decades has focused on the measurement of the oscillation parameters: the mixing angles θ_{12}, θ_{23} and θ_{13}, the two mass splittings Δm^2_{12} and Δm^2_{32}, the neutrino mass hierarchy, and the CP violating phase δ_{CP}. The precision measurements of these parameters constitute the physics program of many modern experiments.

As partially shown in Chapter 1, neutrinos experiments can exploit two sources of neutrinos: either natural, such as the Sun, the cosmic rays interacting in the atmosphere, relics from Big Bang, supernovae and other galactic and extra-galactic processes; or artificial, which is the case of nuclear reactors and particle accelerators. Experiments exploiting artificial sources of neutrinos are best suited for precision measurement of the oscillation parameters, as it is relatively simple to tune the distance between the neutrino source and the neutrino detector. This is crucial because, as shown in Section 1.3.3, the oscillation probability depends on the ratio between the baseline L (the distance between the production and the detection point) and on the neutrino energy E. In particular, many accelerator based experiments have been designed and built in the last two decades; they are particularly convenient as the neutrino beam that can be produced at accelerators can be focussed and directed to facilities for the detection of the neutrinos after oscillation. Accelerator based experiments can exploit long or short baselines. Experiments that study standard neutrino oscillations are called Long Baseline Neutrino Experiments (LBNE), because the neutrinos have to oscillate over long distances ($\mathcal{O}(100 - 1000)$ km), as shown previously. Short Baseline Neutrino Experiments (SBNE), on the other hand, focus on the measurement

of neutrino cross sections and on the search for non-standard oscillation patterns. Both type of experiments often exploit neutrino beams of energy of the order of a few GeV, and they use a near detector (ND), to characterize the initial neutrino flux, and a far detector (FD), that aims to detect the neutrinos after propagating hundreds of kilometers through Earth. Because of the very small cross-section of neutrinos, the detectors used in these experiments are usually very large and instrument very large volumes of matter ($\mathcal{O}(10^4)$ ton for Super-Kamiokande and DUNE, for example); in addition, very intense neutrino beams are employed. The focus of this thesis work is the Neutrino Tagging technique and its potential implementation at a LBNE; the following sections will focus on the description of LBNE.

2.1. Long Baseline Neutrino Experiments

Long Baseline Neutrino Experiments observe neutrino oscillations that occur over distances of $\mathcal{O}(100)$ km; their design and setup relies on well tuned neutrino beams, whose energy is tuned to maximize the oscillation probability. The first generation of LBNE appeared in 1999 and included K2K experiment [14], that exploited a neutrino beam from the KEK accelerator to the Super-Kamiokande detector, both located in Japan, for a baseline of 250 km; and the MINOS experiment (2005-2012) [8] that used a beam from the NuMI neutrino beam produced at Fermilab (Illinois, US), with a baseline of 735 km. These experiments aimed to confirm and measure the mixing angles and the mass splittings by searching for neutrino disappearance. The second generation of LBNE's, including T2K [2] (sending a neutrino beam from Tokai accelerator facility in Japan to the Super-Kamiokande detector), OPERA [104] (neutrino beam produced at CERN in Switzerland, far detector located at Gran Sasso in Italy) and NOνA [44] (sending a neutrino beam from Fermilab to its far detector in Minnesota), focus on detecting neutrino appearance through the $\nu_\mu \to \nu_e$ channel. After measuring such phenomenon, T2K physics program shifted towards comparing the rate of ν_e and $\overline{\nu}_e$ appearance, which provides sensitivity to the CP violation in lepton sector. The next generation of LBNE, such as DUNE [6] (whose beam produced at Fermilab is sent to its far detector at Sanford Lab in South Dakota) and T2HK [71] are being constructed to provide measurements of the neutrino mass hierarchy and of the amount of CP violation in neutrino sector thanks to the $\nu_\mu \to \nu_e$ and $\overline{\nu}_\mu \to \overline{\nu}_e$ channels. In addition, the possibility to perform LBNE using a neutrino beam produced by the U70 accelerator in Protvino, Russia to KM3NeT/ORCA was discussed in detail in [16]. Such an experiment is referred to as P2O and would have a baseline of 2595 km corresponding to an energy at the first oscillation maximum of around 5 GeV, as shown in Figure 2.1. Thanks to a beam power corresponding to $2.23 \cdot 10^{14}$ proton per pulse, the expected pions rate should be $\mathcal{O}(10^{12})$ particles/s. Unfortunately, the geopolitical developments of recent history prevent from implementing such beamline and utilizing the U70 accelerator; however, other options to send a neutrino beam to KM3NeT/ORCA are foreseeable, for example using a neutrino beam produced at CERN [87], [20]. The next sections are dedicated to a general description of the experimental setup of a LBNE.

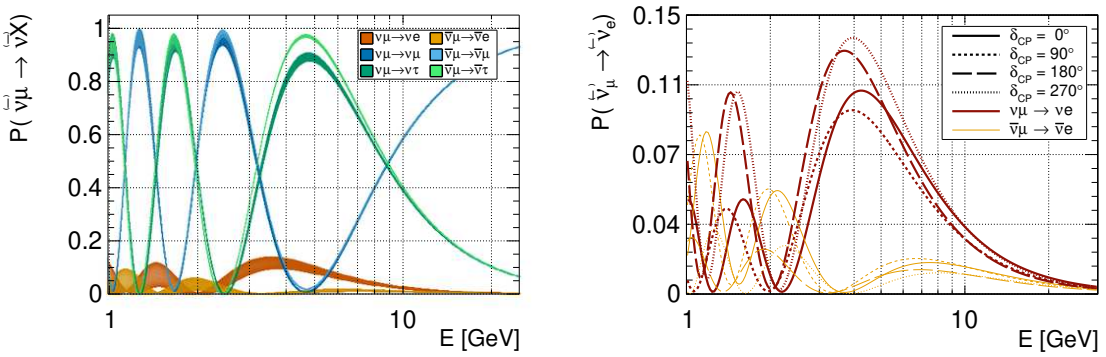

(a) (b)

Figure 2.1.: 2.1a: Probabilities for ν_μ's (dark colour scatter plots) and $\overline{\nu_\mu}$'s (light colour scatter plots) to oscillate to each neutrino flavours as function of the neutrino energy and for all possible values of δ_{CP}, for a baseline of 2595 km. 2.1b: Probabilities for a ν_μ's (dark red thick lines) and $\overline{\nu_\mu}$'s (yellow thin lines) to oscillate to the electron neutrino flavour as a function of the neutrino energy, for a baseline of 2595 km. The probabilities for different δ_{CP} values are shown with different line styles. From [88].

2.1.1. Neutrino beamline

Neutrino beams are usually obtained from very intense hadron beams, typically from $\pi^\pm \to \mu^\pm \overset{(-)}{\nu}_\mu$ that decay in flight [67]. The hadron beams are produced by impinging high energy protons into a stationary target. The idea of producing a neutrino beam from hadron decays arose very early in the 1960s with the experiment, mentioned in Section 1.2.2, performed by Lederman, Schwartz and Steinberger. Compared to modern experiments, the hadron beam of such experiment was lacking two important elements, the proton extraction and the beam focussing.

The proton extraction is usually performed with short spills lasting $\mathcal{O}(10^{-5})$s. The short beam pulses from single-turn extractions are one of the advantages of accelerator neutrino experiments, as the experiments (provided it has fast enough electronics) can close its trigger acceptance around a small "gate" period around the accelerator pulse, reducing false triggers of cosmic ray muons. Because of the low neutrino cross section, the neutrino beams have to be very intense, thus they require large amounts of protons delivered to the target. From the target, a beam of secondary particles is produced - mostly pions and kaons of both charge. Such secondary beam must be collimated in order to increase the neutrino flux to the detectors on axis with the beam line. Magnetic pulsed horns, shown in Figure 2.2 are conventionally used to focus the secondary hadron beam in a neutrino beamline [6], [67]. This kind of device was first proposed by S. van der Meer in 1961 [76] and, since then, have been employed by all wide-band neutrino beams at the GeV scale. A horn is composed of conductor sheets on which a current flows in the longitudinal direction during the proton extraction, producing a strong magnetic field of toroidal shape. Their role is not only to focus the beam, but also to de-focus the particles of unwanted charge, enhancing the ν_μ ($\overline{\nu}_\mu$) purity of the beam and reducing the background of $\overline{\nu}_\mu$ (ν_μ)

produced by the negatively (positively) charged hadrons. Either neutrino-enhanced or antineutrino-enhanced beams are created by operating the focusing horns in forward or reverse current configurations, respectively. This feature is crucial for experiments that aim at measuring the CP violating phase in neutrinos oscillations, as for this measurement both neutrinos and antineutrinos appearance/disappearance rates need to be available.

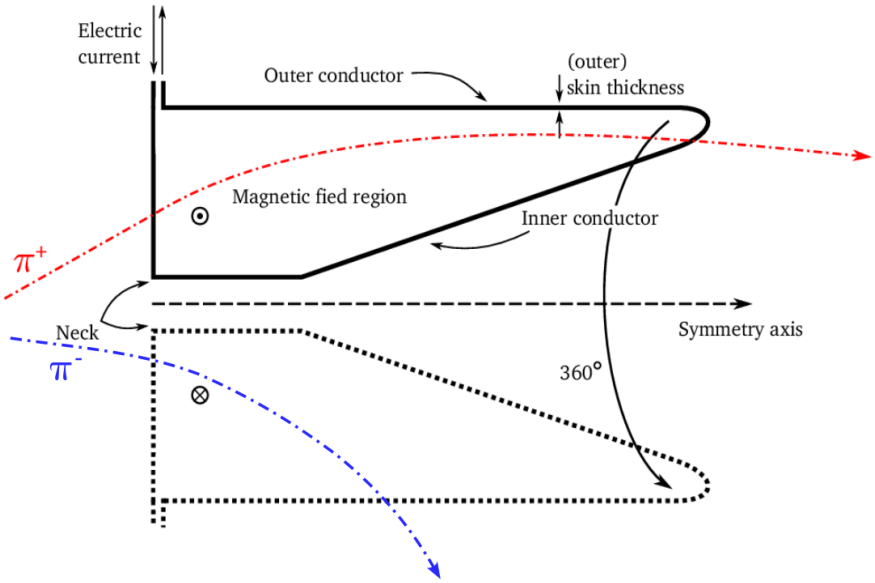

Figure 2.2.: Schematic view of a magnetic horn: the device is axially symmetric and focuses particles of a given sign in both the transverse dimensions. The unwanted sign charge on the other hand gets bent out of the beam line. The symmetry axis is also the target and beam axis. Adapted from [37].

The focussed hadron beam then enters a decay volume, in which the secondary hadrons decay and form a neutrino beam. The main decay channels for mesons produced in secondary beams and their branching fractions are summarized in Table 2.1. At the end of the decay volume, a beam dump is usually placed to stop all particles except for muons and neutrinos; the muons are then usually detected with a muon monitor to constrain the neutrino flux.

The direction of the neutrino beam is chosen depending on the requirements of each experiment. Many experiments (such as T2K) employ the "off-axis" technique, meaning that the neutrino beam is purposely directed at a small angle away from the far detector. The reasoning behind this lies from the primary source of beam neutrinos, the $\pi^+ \rightarrow \mu^+\nu_\mu$ decay: for a pion decaying in the decay tunnel, the energy of the produced neutrino, E_ν, depends on the angle of emission and can be written as:

$$E_\nu = \frac{m_\pi^2 - m_\mu^2}{2(E_\pi - p_\pi cos\theta)} \tag{2.1}$$

where m_π and m_μ are the masses of the pion and of the muon, p_π is the pion's momentum

Particle	Decay Products	Branching Fraction (%)
π^+	$\rightarrow \mu^+\nu_\mu$	99.9877
	$\rightarrow e^+\nu_e$	1.23×10^{-4}
K^+	$\rightarrow \mu^+\nu_\mu$	63.55
	$\rightarrow \pi^0\mu^+\nu_\mu$	3.353
	$\rightarrow \pi^0 e^+\nu_e$	5.07
K^0_L	$\rightarrow \pi^-\mu^+\nu_\mu$	27.04
	$\rightarrow \pi^- e^+\nu_e$	40.55
μ^+	$\rightarrow e^+\bar{\nu}_\mu\nu_e$	100

Table 2.1.: Main neutrino-producing decay modes and their branching ratio in percentage. Decay modes for $\bar{\nu}_\mu$ and $\bar{\nu}_e$ are omitted in this table. The π^-, K^- and μ^- modes are charge conjugates of the π^+, K^+ and μ^+ modes, respectively. Taken from [3].

and θ is the direction of the neutrino with respect to the pion. The maximum value of neutrino energy is obtained for $\theta = 0$ and its value is $E_\nu \approx 0.43 p_\pi$. Equation 2.1 is plotted in Figure 2.3 for different decay angles, and it shows that the neutrino's energy dependency on the pion's energy disappear for off-axis neutrinos. Using the off-axis technique in a LBNE thus provides a narrow band neutrino spectrum even from a large band pion spectrum.
The beamline ends with a near detector, that serves to monitor the initial neutrino beam.

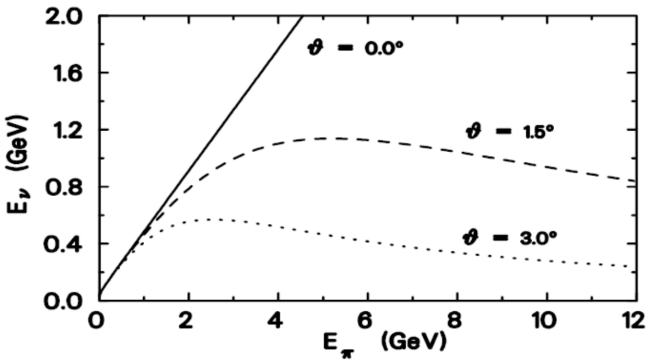

Figure 2.3.: Neutrino energy from pion decay as a function of pion energy, for several choices of decay angle between the neutrino and pion direction. From [22].

2.1.2. Near Detector

In LBNE, near detectors (ND) play a crucial role in the characterization of the initial neutrino flux. ND are usually placed close to the neutrino beam production point ($\mathcal{O}(100)$ m), contrary to the far detector, described in Section 2.1.3 that is placed thousands of km away. Their main functions are:

- characterizing the intensity, flavour composition and energy spectrum of the neutrino

beam, prior to modification by oscillations;

- reducing systematic uncertainties by measuring event rates, kinematics, and cross sections.

The two detectors measure different energy spectra, and such difference depends primarily on the different solid angles subtended by the detectors (see Figure 2.5). In addition, the significant acceptance differences between the near and far detectors are a function of the energy of the pion (hence neutrino), as is indicated schematically in Figure 2.4. High energy pions tend to live longer and decay in the decay volume; on the other hand, soft pions tend to enter the decay volume with different angular divergences, even in the case of a beam focussed with horns. Furthermore, even high energy pions can have an angle with respect to the beam nominal axis, that would result in neutrinos that are able to get at an angle to the near detector, but unable to get to the far detector. Only pions emitted with angles close to 0 can produce neutrinos reaching the far detector. Such effect is another source of significant differences in the spectra of near and far detectors.

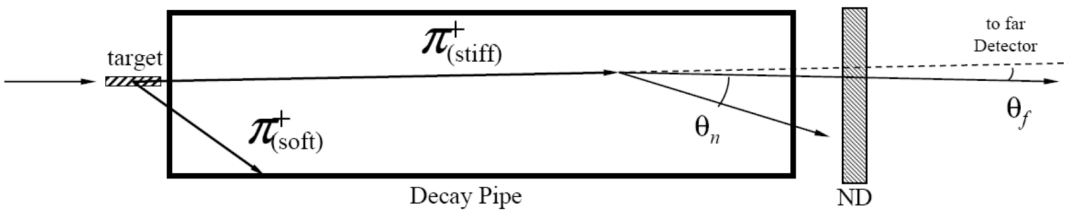

Figure 2.4.: Not-to-scale demonstration of the solid angle differences in a two-detector neutrino experiment. From [67].

2.1.3. Far Detector

Far detectors are large neutrino detectors, strategically positioned at a $\mathcal{O}(100-1000)$ km from the neutrino source, in order to have a large L/E ratio, allowing to access the CP-violating phase. DR are typically high granularity detectors, made of technologies such as liquid argon time projection chambers (LArTPCs [6]), scintillator-based detectors, or water Cherenkov detectors [2], which allow for precise reconstruction of neutrino interactions.In general, their primary purpose is to measure the neutrino flux after oscillations, providing information about their energy and flavour.
Far detectors are designed to maximize the detection efficiency and minimize background noise. Most far detectors in long baseline neutrino experiments are typically shielded from atmospheric muons and from other sources of neutrinos to minimize background and enhance the sensitivity of the measurements. The background sources can include atmospheric neutrinos, neutrinos from cosmic ray interactions in the atmosphere, and neutrinos from nearby nuclear reactors or nuclear power plants. Several shielding strategies are employed:

- Underground locations: far detectors are often located deep underground to shield them from cosmic ray interactions and atmospheric neutrinos. The overburden of rock or other shielding materials helps reduce the flux of these background neutrinos. An example of underground located FD is Super-K, located 1000 m underground.
- Active Shielding: Far detectors may incorporate active shielding components to further reduce background. These can include layers of shielding materials, such as water or liquid scintillator, surrounding the detector volume to absorb or veto cosmic ray-induced particles and external neutrino interactions, as is done in DUNE [5].
- Veto Systems: Veto systems can be implemented to identify and reject background events. These systems are typically placed around the detector and consist of additional detectors that can detect and distinguish background particles from the desired neutrino interactions.

Far detectors employ different detection techniques depending on the specific technology used. In LArTPCs, for example, the detector is filled with liquid argon, which acts as both the target for neutrino interactions and the detection medium. Neutrinos can interact with an Ar atom, ionizing the argon atoms. The electrons within the detector drift towards readout planes, where they produce signals. This allows for the precise reconstruction of neutrino interactions and the identification of different particles. In water Cherenkov detectors such as Super-Kamiokande, the detection medium is ultrapure water. When a neutrino interacts with the water, it produces charged particles that move faster than the speed of light in water, emitting a cone of light known as Cherenkov radiation. Photomultiplier tubes (PMTs) are used to detect this faint light, allowing for the reconstruction of particle tracks and, in turn, the measurement of the neutrino energy and direction. Scintillator-based detectors exploit scintillating materials and photomultiplier tubes that are also used in this case to detect the scintillation light. The time and intensity of the light pulses provide information about the energy and type of particles produced in the neutrino interactions, as explained in Section 1.4.1. A sketch of the beamline typically employed in LBNE is found in Figure 2.5.

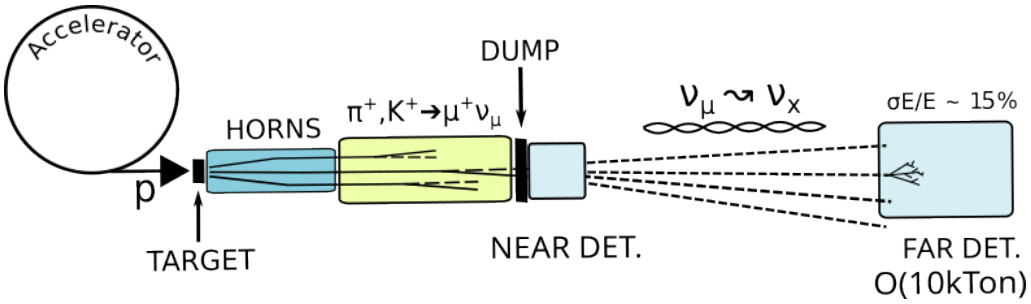

Figure 2.5.: Annotated not-to-scale schematic representation of the beamline of a classic LBNE.

2.1.4. Limitations of accelerator based neutrinos experiments

The landscape of existing and future LBNE is vast and holds exciting promises for precision measurements of oscillation parameters; however, the results obtained from LBNE are affected by large systematic uncertainties. Such systematics mostly arise from the fact that the oscillation studies heavily rely on the measurement of the neutrino flux at the Near and Far detectors. The measured neutrino event rate is affected by several factors, namely the initial neutrino flux (the number of created ν_μ, ν_e and ν_τ), the neutrino energy, the neutrino interaction cross-section with the Near Detector (indicating the likelihood of neutrino interaction), the detector efficiency (reflecting the detector's ability to reconstruct the neutrino event), and lastly, the oscillation probability (determining the survival of initial ν_μ or the appearance of ν_e), as shown in Equation 2.2 [61]:

$$\begin{aligned} N^{ND}_{\nu_\alpha}(E_\nu) &= \Phi^{ND}_{\nu_\alpha}(E_\nu) \times \epsilon^{ND}(E_\nu) \times \sigma^{ND}_{\nu_\alpha}(E_\nu) \\ N^{FD}_{\nu_\beta}(E_\nu) &= \Phi^{FD}_{\nu_\beta}(E_\nu) \times \epsilon^{FD}(E_\nu) \times \sigma^{FD}_{\nu_\beta}(E_\nu) \times P(\nu_\alpha \to \nu_\beta)(E_\nu) \end{aligned} \tag{2.2}$$

where $N^{ND}(N^{FD})$ is the rate at the Near (Far) Detector, Φ is the expected flux of (anti)neutrinos of flavour α (β), ϵ is the efficiency to detect the (anti)neutrino that depends on the (anti)neutrino energy E_ν, σ is the energy dependent cross section for a (anti)neutrino of flavour α (β) and $P(\nu_\alpha \to \nu_\beta)(E_\nu)$ is the oscillation probability from flavour α to flavour β as function of the energy. The flux, efficiency and cross-section terms are sources of systematic uncertainties which affect the outcome of the event rate measurement. In particular, the knowledge of the neutrino flux (i.e. the range of available neutrino energies and the rate of neutrinos produced) and the neutrino interaction cross-section (i.e. what the interaction probability is and how it changes as a function of neutrino energy) represent two of the largest sources of systematic uncertainty in the measurement of neutrino oscillation parameters. Such systematic uncertainty is reduced to some extent by the presence of the ND, that measures the initial neutrino flux. However, the spectrum measurements of the initial flux must be corrected by two factors: the effect of the expected oscillation probabilities, and the solid angle. Indeed, as the ND and FD are separated by potentially thousands of kilometers, they cover very different solid angles [67], [88], requiring to correct the measured fluxes; nonetheless, these corrections are not trivial. The neutrino cross section depends on the energy, which in turn depends on the neutrino direction. In addition, the neutrino energy reconstruction at LBNE relies on the Near and Far detectors; typically, such detectors have uncertainties on the reconstructed energy of $\mathcal{O}(20\%)$ [47] and have energy scales uncertainties. An example of systematic uncertainties at LBNE is shown in Table 2.2.

In order to reduce the systematic uncertainties of the neutrino cross section measurements, new approaches are being studied; this is the case of the ENUBET (Enhanced NeUtrino BEams from kaon Tagging) project [77], that proposes to instrument the decay tunnel of a $K^+ \to \pi^0 e^+ \nu_e$, in order to monitor the neutrino-associated lepton production at a single particle level. With this approach, ENUBET has demonstrated that it is possible to measure the ν_e cross section with a precision of 1%, with the help of an offline fit for particle identification.

Source of Uncertainty	ν_e $\delta N/N$	ν_μ $\delta N/N$
Flux	3.7%	3.6%
cross-section	5.1%	4.0%
Flux+cross-section		
(w/o ND280 Constraint)	11.3%	10.8%
(w/ ND280 Constraint)	4.2%	2.9%
Other	3.5%	4.2%
All		
(w/o ND280 Constraint)	12.7%	12.0%
(w/ ND280 Constraint)	6.8%	5.1%

Table 2.2.: Sources of the systematic uncertainty on the predicted neutrino event rates at Super-Kamiokande in T2K oscillation analyses [4]. The effect of the near detector (ND280) constraint on the flux and cross-section is particularly visible. The line (Other) reports the effect of Final State Interactions and Secondary Interactions. From [54].

2.2. Neutrino tagging: a new option for LBNE

It was described in Section 2.1.4 that the neutrino oscillations measurements uncertainties at LBNE are dominated by systematic effects. In this context, the neutrino tagging technique presents as an interesting option. The neutrino tagging technique consists in exploiting the neutrino production process to kinematically reconstruct the properties of each neutrino at its production. This approach requires equipping the beam line of an accelerator based neutrino experiment with silicon trackers. Such trackers allow reconstructing the properties of the neutrinos produced in the $\pi^{\pm} \to \mu^{\pm}\nu_\mu$ decay based on the kinematics of incoming and outgoing particles.
The option of equipping an accelerator based neutrino experiment with a tagged neutrino beam has been thought of already in the late 70s [91]. However, the implementation of such technique has been set back by technological limitations until the recent advancements in silicon sensor technology. The primary limitation to the implementation of this technique has been the prohibitive particle rate at the tracker, $\mathcal{O}(10^{13})$ particles/s/mm^2.

2.2.1. Conceptual description

In a tagged neutrino beamline, some silicon trackers station would be equipped along the hadron beamline and decay volume. Such trackers would detect and reconstruct the properties of all the charged incoming and outgoing particles of a $\pi^{\pm} \to \mu^{\pm}\overset{(-)}{\nu}_\mu$ decays. The reconstruction of charged pions and muons taking part in the two body decays enables accessing the beam neutrino properties:

- the neutrino energy can be precisely reconstructed thanks to energy and momentum conservation requirements;

- the neutrino direction can be precisely determined with kinematic considerations and momentum conservation requirements;
- the flavour of the neutrino must be muonic, as it is associated with a $\mu^{\pm}$;
- the chirality of the neutrino can be inferred because it must be opposed to the one of the outgoing lepton and incoming pion or kaon.

If used in a LBNE, the neutrinos produced in the pions decay propagate oscillating for thousands of kilometers, and can be detected at the far detector. Based on timing and angular information, each neutrino interacting at the FD - called *interacting* neutrino - can be uniquely associated to a neutrino reconstructed by the tracker - called in the following the *tagged* neutrino. Such association allows exploiting the precise information available on the tagged neutrino for oscillation studies.

2.3. Neutrino tagging experimental setup

The present section focuses on the beam rate and on the technique that can be employed to make it sustainable for the tracker; the DUNE experiment will be used as a reference for the discussion. The DUNE experiments beam line is expected to deliver $1.1 \cdot 10^{21}$ protons on target (POT) per year [47]. This roughly corresponds to an instantaneous particle rate after the target of $\mathcal{O}(10^{18})$ particles/s. It is possible to do a rough computation of the pion rate after the focussing devices, that amounts to $\mathcal{O}(10^{13})$ particles/s/mm^2, assuming one π^+ produced per incident proton. Such high rate of the secondary hadron beams after the target and after focussing at LBNE's has always been the main limiting factor for implementing the tagging technique, ruling out the possibility to perform the tagging at an existing LBNE. Recent developments in silicon tracker technologies have enabled the production of trackers that can withstand an instantaneous particle rate of $\mathcal{O}(10^6)$ particles/s/mm^2, as demonstrated by the NA62 GigaTracKer [53]. Moreover, ongoing projects aim at developing sensors for the HL-LHC upgrade. These detectors should be capable of operating at fluxes ten times larger than what the NA62 GigaTracKer can withstand, of the order of $\mathcal{O}(10^7)$ particles/s/mm^2 [108]. The particle rate that the tracker can sustain is 6 order of magnitude smaller than the nominal DUNE's particle rate. In order for a silicon tracker to be able to function in a LBNE, it is hence necessary to adapt the beam line setup conventionally employed, which, as a consequence, rules out the possibility to use the tagging at experiments already under construction, such DUNE or T2HK.

2.3.1. Beamline

As mentioned in Section 2.1.1, the classic LBNE utilize short spills of the order of 10 μs, allowing a shorter trigger time window that reduces the false triggers from cosmic ray muons. Moreover, short spills enable the use of magnetic horns as focussing devices. Assuming that the next generation of silicon trackers for HL-LHC will be able to withstand

an instantaneous rate of $\mathcal{O}(10^7)$ particles/s/mm^2, hence implementing a tagged neutrino beam would rule out the use of fast extraction. The tagging indeed requires operating the accelerator in slow extraction mode, where particles are extracted in spills lasting a few seconds. This modification alone decreases the projected particle rate at the tracker by 5 or 6 orders of magnitude. The use of magnetic horns for π collimation is incompatible with slow extraction, as the Joule heating from the long current pulses in the horn conductor can compromise the device beyond repair [37]. Hence, they must be replaced by a static focussing device. Recently the ENUBET collaboration [106] demonstrated that quadrupole sets can achieve focussing performances compatible with the ones of a horn for a narrow band beam. Furthermore, implementing a narrow band beam would bring the pion rate to an acceptable level for the tracker, reducing it by 1 to 2 orders of magnitude, giving an instantaneous secondary hadron rate of $\mathcal{O}(10^6 - 10^7)$ particles/s/mm^2. It is shown in Figure 2.6 that the typical pion spectrum falls very fast and the low energy part of the spectrum can safely be removed. Indeed, these low energy pions would yield neutrinos of even lower energies (since $E_\nu < 0.43 \cdot E_\pi$). The energy cut would be set below the energy of the first oscillation maximum. The momentum selection of the secondary beam can be done using a dipole magnet and a collimator. Additionally, since quadrupoles can be arranged to focus both π^+ and π^-, it is possible to produce a beam composed of both polarities and of both neutrinos and antineutrinos. Such feature, despite it being considered troublesome for classic beamlines, is an advantage in a tagged beamline, where the chirality of each beam neutrino can be determined at its production. The secondary hadron beam can be effectively separated into two polarities using a dipole magnet. This separation causes the negatively charged particles to deviate in the opposite direction compared to the positively charged particles. The beam in each polarity branch is realigned to be parallel to its initial trajectory by a dipole magnet with magnetic field opposite to the first one. The characteristics of each individual particle can be accurately measured by employing pairs of tracker stations positioned after the dipole. Finally, by employing a corresponding arrangement of magnets in the reverse order, the beam particles are restored to a trajectory aligned with their initial paths. The configuration of the four magnets constitutes an achromat. One more pair of tracking devices can be placed after the second dipole. The two tracking devices pairs enable momentum measurement, as the displacement between the trajectory after and in-between the achromat scales with the particle rigidity (that is the ratio between the momentum of the particle and its charge). The pions of both polarity then enter a decay volume about 100 m long; at the end of the decay pipe, a dipole magnet with two sets of tracking stations, one after and one before the magnet, allow measuring the outgoing muons' direction, electric charge and momentum. The tracker stations together with the dipoles will be referred to as spectrometers.

Since the muons from pions decaying before the decay volume cannot be reconstructed, the portion of the beamline before the decay volume needs to be as short as possible; likewise, the beam dump must be placed right after the last dipole to prevent more untrackable decays.

Under these considerations, the classic LBNE beamline can be modified to accommodate a set of quadrupoles for the focussing, the achromat and the trackers station; an example

of a tagged beamline is represented in Figure 2.7. Assuming the beam is spread over a surface of integrated over a surface of $\mathcal{O}(0.1)\,\mathrm{m}^2$, the tracker devices can sustain a pion rate of $\mathcal{O}(10^{12})$ particles/s. The neutrino rate at the end of the beamline is $\mathcal{O}(10^{11})$ particles/s, assuming $\mathcal{O}(10^{12})\,\pi$/s, 10% of pions decaying and being the beampipe $\mathcal{O}(100)$ m long.

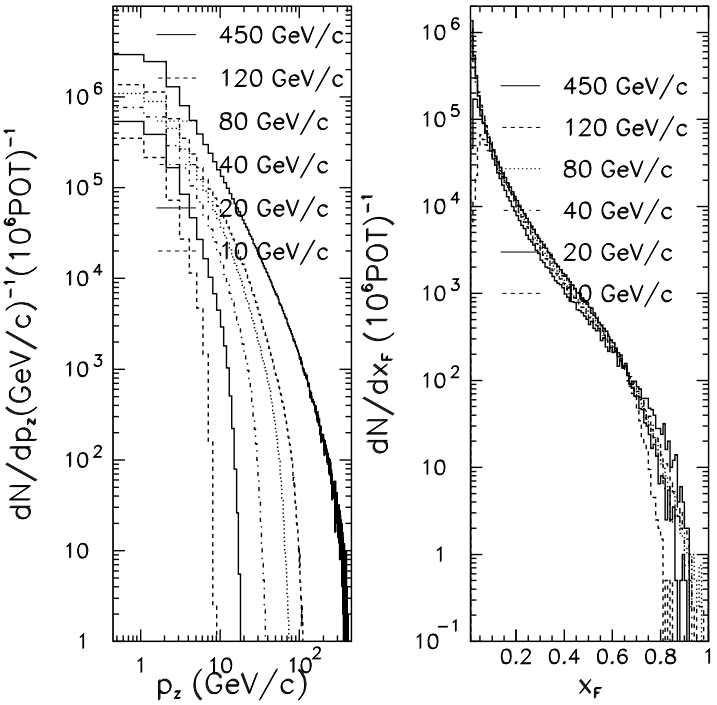

Figure 2.6.: Simulated calculations of (left) p_T (transverse momentum component) spectra of π^+ produced in p + C collisions at various incident proton momenta p_0; (right) p_T spectra of π^+ produced in 120 GeV/c p + C collisions for various values of $x_F \approx p_z/p_0$. Taken from [85].

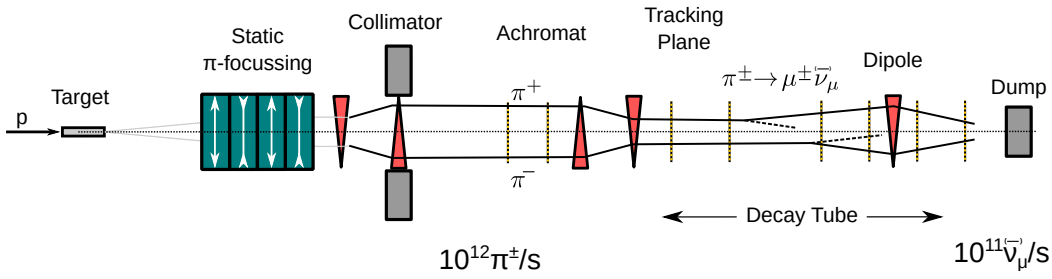

Figure 2.7.: Schematic of a possible beam line enabling neutrino tagging. Blue rectangles represent quadrupoles, red triangles dipoles and vertical dotted lines correspond to tracking planes. From [88].

2.3.2. Tagged and Interacting neutrino pairing

The tagging technique relies on the ability to perform an unambiguous pairing between the tagged and the interacting neutrino. Such association is performed based on timing and angular coincidences.

The tagged neutrinos have a very precise timestamp; this is due to the fact that each tracker device has a time resolution of $\mathcal{O}(10)$ ps. However, the neutrino detector has a much worse time resolution, $\mathcal{O}(10)$ ns [9]. In a 10 ns time window and with an instantaneous neutrino rate of $\mathcal{O}(10^{11})\,\nu$/s, $\mathcal{O}(10^3)$ tagged neutrino coincide in time with an interacting neutrino. This number can be further reduced thanks to angular coincidences between the tagged and the interacting neutrino. The resolution of the interacting neutrino position depends on the type of neutrino detector, and it ranges from meters to millimeters according to the density of the instrument. In general, one can assume the angular resolution (being the direction of the interacting neutrino the ratio between the transverse position of the neutrino interaction to the baseline) to be better than $\mathcal{O}(10)$ μrad. The angular resolution of the tagged neutrino, on the other hand, depends on the performances of the beam spectrometer. For example, the NA62 GigaTracKer has 0.2% momentum resolution; moreover, the resolution on the position of the tagged neutrinos is affected by the fact that the charged particles crossing the trackers devices undergo Coulomb scattering. In particular, the $\pi^{\pm}$'s direction is impacted by the Coulomb scattering in the last tracking plane that they encounter, while the $\mu^{\pm}$'s direction is affected by Coulomb scattering in the last plane they encounter, as shown in Figure 2.8. The scattering angle depends on the quantity of material crossed by the particle, and to assess the effect of the multiple Coulomb scattering one can assume the thickness of the NA62 GigaTracKer, that is of 0.5% of a radiation length. If $\theta_{ik} = \theta_{i+k} - \theta_i$ is the scattering angle after crossing a number k of devices, its distribution is a Gaussian peaked at zero and with a standard deviation given by:

$$\sigma_{\theta ik} = \frac{13.6MeV}{p\beta c}\sqrt{\frac{x}{X_0}}\left[1 + 0.038\ln\left(\frac{x}{X_0}\right)\right] \tag{2.3}$$

where x is the traversed distance in the material, X_0 the radiation length of the material, p is the particle momentum in MeV/c, βc is its velocity [11].

On average, the angular resolution on the tagged neutrino ranges between 0.1 and 1 mrad, being best for ν_μ produced by high momentum $\pi^{\pm}$s.Being the angular resolution of the beam spectrometer worse than the one of the neutrino detector, the angular association between tagged and interacting neutrino is affected by the angular resolution of the tagged neutrino.

To be able to determine whether unambiguous pairing between the tagged and the interacting neutrino is possible, it is necessary to compare the angular resolution to the angular divergence of the neutrino beam. The larger the angular divergence, the smaller the pile-up (i.e. the smaller is the number of accidentally matched tagged neutrinos). It is hence conservative to assume a perfectly focussed pions beams, with the divergence of the

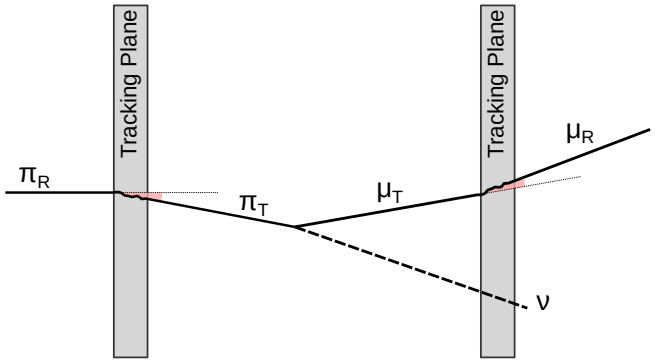

Figure 2.8.: Schematic representation of the multiple Coulomb scattering that affect the reconstruction of pions and muons. From [88]

neutrinos arising only from the decay. Such divergence is for the neutrino beam about $\frac{1}{\gamma}$ where $\gamma = \frac{E_\pi}{m_\pi}$ is the pions' Lorentz boost. Assuming a 15 GeV pion beam and knowing the charged pion's mass is ~ 140 MeV, the Lorentz boost is $\gamma \sim 100$, hence the beam divergence is $\mathcal{O}(0.01)$ rad $= \mathcal{O}(10)$ mrad. If the interacting neutrinos are distributed on a disk that is the base of a cone of 10 mrad apex angle, the radius of such disk is $r_D = L \tan\theta_D$ where theta is θ_D =10 mrad and L is the baseline of the experiment. The same reasoning can be applied to the angular resolution of the interacting neutrino: it identifies a thinner cone of apex angle $\theta_d = 0.1$ mrad, that translates in the capability to resolve a disk of radius $r_d = L \tan\theta_d$. A schematic representation of the geometry of the problem can be found in Figure 2.9. For small angles $\theta << 1$ rad, it is valid the approximation $\tan\theta \sim \theta$, hence the area of a disk of radius $r = L \tan\theta \sim L\theta$ is proportional to θ^2. The number of accidentally matched tagged neutrinos is thus reduced by a factor $\left(\frac{0.1}{10}\right)^2 = 10^4$ that corresponds to the ratio between the areas of the two disks subtended by the two cones. Hence, if the number of potential tagged neutrino matches was 10^3 for any given interacting neutrino, thanks to the angular resolution of the tracker and with the conservative hypothesis of a beam divergence due only to the decay, the number of accidentally matched tagged neutrinos reduces to 0.1. This means that in 90% of the cases, it is possible to perform an unambiguous match between the tagged and the interacting neutrino. The remaining 10% of events will have to be discarded for physics analyses.

The main source of background of mis-associated tagged neutrino in such a setup are non-reconstructed tagged neutrino. A tagged neutrino can not be reconstructed by the beam spectrometer if it originates from a pion decaying early in the beamline. One can assume that fraction of interacting neutrinos from early decays is $\mathcal{O}(1\%)$, depending on the length of the decay tube, hence the probability for a mis-tagged event is $\mathcal{O}(0.1\%)$. Thus, the unambiguous matching under these conservative hypothesis is possible, using the new trackers developed for HL-LHC; neutrino tagging is feasible with a beam of $10^{11}\nu_\mu/s$.

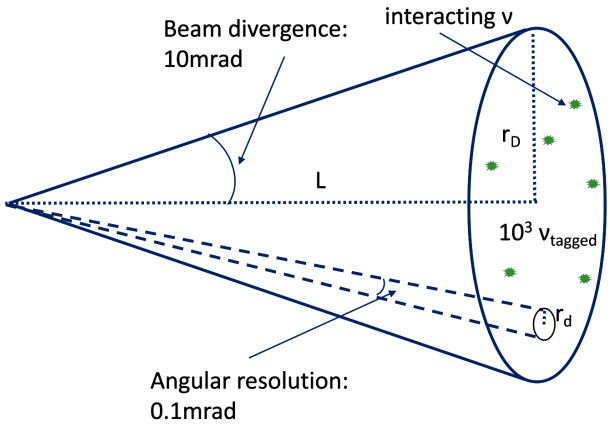

Figure 2.9.: Schematic not-to-scale representation of the geometry of the beam divergence and of the angular resolution on the tagged neutrino. r_D and r_d are the radii respectively of the cone of θ_D =10 mrad aperture angle and of the cone of θ_d = 0.1 mrad aperture angle and L represents the baseline of the tagged experiment.

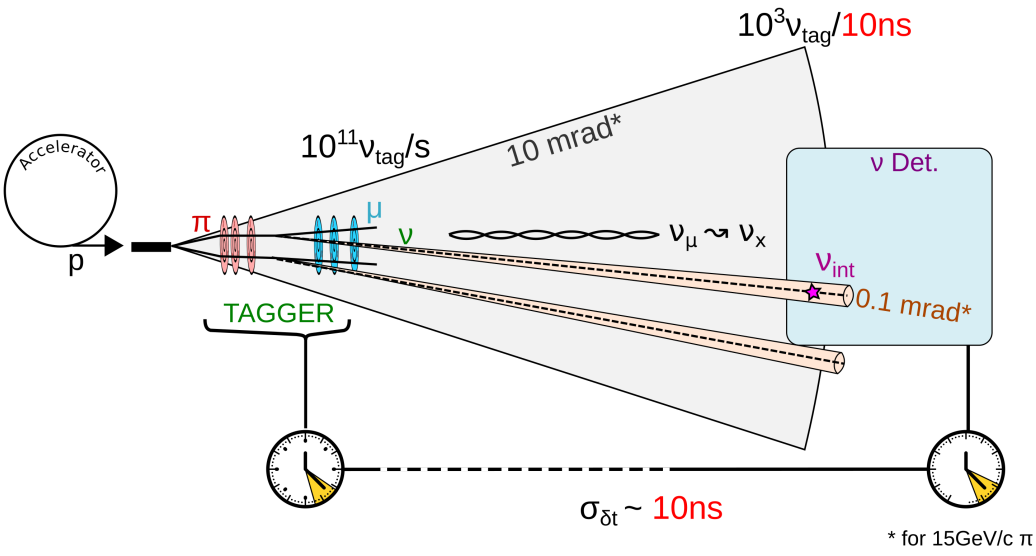

Figure 2.10.: Schematic not-to-scale representation of the beamline and of the unambiguous matching procedure for a tagged experiment.

2.3.3. Benefits of Neutrino Tagging at a LBNE

Implementing the tagging at a LBNE can bring significant advantages that can drastically reduce the systematic uncertainties and provide more precise measurements. The three main advantages of a tagged experiment are:

- it allows to reconstruct almost all the neutrinos in the beam;
- it allows to track each beam neutrino from the production to the detection;

- the interacting neutrinos' properties are precisely reconstructed thanks to the fact that it is matched to a tagged neutrino reconstructed by the beam spectrometer, that exploits the decay kinematics.

These three advantages can significantly improve the precision of the physics analysis. The expected benefits [88] are described in the following paragraphs.

Improved flux measurements

With the neutrino tagging technique, the initial flux is completely characterized thanks to decay kinematics, event by event. Each neutrino's energy, flavour and chirality is known at the production, and the neutrino rate can be precisely derived at any distance from the neutrino production thanks to geometrical considerations, as the momentum and direction of each beam neutrino can be derived kinematically from the properties of the beam charged particles. As mentioned in Section 2.1.4, the neutrino flux in classic LBNE is known on average, and is only known in the two checkpoints, the near and the far detector. To compare the two fluxes, non trivial corrections need to be applied because the two detectors cover very different solid angles. However, in a tagged neutrino beam, it is possible to predict which beam neutrinos may reach the far detector , and these corrections are not needed. This means that it enables eliminating one of the main sources of systematic uncertainties in oscillation measurements.

Improved energy resolution

The energy resolution of each beam neutrino is reconstructed by the beam spectrometer from the decay kinematics, instead of being reconstructed by the neutrino detector as the energy of the interacting neutrino. Considering an on-axis tagged LBNE, the neutrino energy E_ν is given by Equation 2.1 and is $E_\nu = 0.43 \cdot E_\pi$. Being in the ultrarelativistic limit, the resolution on the beam pions' energy corresponds to the pions' momentum resolution; a beam spectrometer has a momentum resolution of order $\mathcal{O}(0.1 - 1)\%$ for pions of momenta of $)(1 - 10)$ GeV/c [53]. Such resolution is, as mentioned in Section 2.3.2, dominated by the angular resolution of the tracker, i.e. dominated by the multiple Coulomb scattering that pions and muons undergo when crossing the trackers planes, whose uncertainty is in Equation 2.3. The neutrino's energy resolution is hence expected to range between 0.2% and 0.6%, and is independent of the pions' momentum. On the other hand, in classic LBNE, the neutrinos' energy reconstruction relies completely on the neutrino detector, where is much more challenging as it has to take into account neutrino interaction models, that induce a systematic uncertainty, leading to an energy resolution one order of magnitude worse.

Background suppression

One of the main background sources in LBNE looking for the appearance of $\overset{(-)}{\nu}_\mu \rightarrow \overset{(-)}{\nu}_e$ comes from non-oscillated $\overset{(-)}{\nu}_e$ components [12]. In a tagged experiment, such background is drastically reduced [72]: the non-oscillated interacting $\overset{(-)}{\nu}_e$ do not coincide with any tagged $\overset{(-)}{\nu}_\mu$ and are discarded.

Improved knowledge on beam neutrinos properties
Since the neutrino energy is reconstructed by the tracker with a resolution 10 times better than with a neutrino detector, it becomes possible to understand the process undergone by the neutrino in the interaction by comparing the energy reconstructed by the neutrino detector to the one provided by the beam spectrometer. This allows to recognize NC interactions, that release a smaller energy than CC interactions. NC interaction are typically considered background in classic oscillations experiments, as their spectrum and rate is independent of neutrino oscillations: in NC, the incoming neutrino flavor is uncorrelated with the final state particles and cannot thus be measured. In a tagged experiment, neutrinos interacting via NC can be recognized and isolated. In addition, it would also be possible to isolate a sample of ν_τ, as the energy released by their CC interaction is also smaller due to the τ decaying into electron and two neutrinos.
Moreover, the chirality of each neutrino can be determined thanks to the charged particles associated to the tracker. This enables the possibility to run with the two pions polarities at the same time, increasing by a factor two the statistics and reducing the systematic uncertainties on the measurements of the CP-violating effects.
Finally, the event-by-event beam knowledge and the better energy resolution allows performing precise cross-section measurements.

2.3.4. Neutrino Tagging at SBNE

A Short Baseline Neutrino Experiment with a tagged beam is also conceivable. Such experiments would allow measuring the ν_e and ν_μ cross sections with a precision below 1%. The ν_e cross section can be measured with the use of a tagged secondary charged kaon beam. Thanks to the tagging, it is possible to compare the number of $K^+ \to \pi^0 e^+ \nu_e$ (also called Ke3), obtained from the number of $K^+ \to \mu^+ \nu_\mu$ decays (precisely measured thanks to the tagging) corrected by the branching fractions of the two decays and by the geometrical acceptances, to the number of ν_es from the Ke3 interacting at the Far Detector. The two corrections to get the number of $K^+ \to \pi^0 e^+ \nu_e$ are simple and straightforward; the main limitation of this method is the precision on the branching fractions. In addition, the $K^+ \to \mu^+ \nu_\mu$ decays are identified by a full kinematical reconstruction; it is hence a very solid and clean method, that is immune to background.
Furthermore, a tagged neutrino beam enables measuring the ν_μ cross section with unprecedented precision. Employing a $\pi^\pm \to \mu^\pm \overset{(-)}{\nu}_\mu$ beam that is fully reconstructed thanks to the tagging, it is possible to precisely count the number of decays and to compare that to the number of interacting ν_μ at the Far Detector. Since the neutrino energy is precisely reconstructed on an event-by-event basis thanks to the kinematic of the decay, the tagging at SBNE enables the measurement of the ν_μ differential cross section.
In addition, as the energies of the neutrinos are precisely known thanks to the kinematic reconstruction, it is possible to compare the energy reconstructed by the neutrino detector with the one known from the tracker. This allows improving and validating the interaction models used to do the energy reconstruction at the far detectors.

2.4. Neutrino tagging feasibility

It has been shown in the previous sections that the neutrino tagging technique can bring significant improvements to the oscillation precision measurements, and that it is in principle feasible under the hypothesis of a slowly extracted hadron beam and of a new generation silicon tracker technology. The timing information from the trackers and from the interaction at the neutrino detector is combined with the interacting neutrino position knowledge, provided from the neutrino detector, and the spatial details on the neutrino direction, provided by the tracker. Such information enables a one-to-one match between the neutrino kinematically reconstructed by the tracker (the "tagged" neutrino), and the neutrinos interacting at the neutrino detector.
The tagging technique feasibility can be proven using the data from the NA62 experiment. The NA62 experiment can indeed be exploited a miniature tagged experiment, thanks to its slowly-extracted and intense hadron beam, its state-of-the-art beam spectrometers and a liquid Krypton calorimeter acting as neutrino detector. The characteristics of the NA62 experiment are detailed in Chapter 3; the details of the analysis of the feasibility study of the neutrino tagging technique and the challenges it presented are described in Chapter 4.

3. The NA62 experiment

Summary

NA62, schematically shown in Figure 3.1, is a fixed-target experiment located at the CERN north areaNA62's 400 GeV beam is extracted from the CERN Super Proton Synchrotron (SPS). The NA62 main goal is the study of the rare kaon decay $K^+ \to \pi^+\nu\bar{\nu}$, aiming to first provide unequivocal evidence of its existence, and then measure its branching ratio at a precision of order 10%, testing the SM prediction of $\mathcal{B}(K^+ \to \pi^+\nu\bar{\nu})_{SM}) = (8.4\pm1.0)\times10^{-11}$. The NA62 experiment was designed and built to meet the challenges of such goal. The features of the NA62 experiment that are desirable for the tagging proof of principle are:

- its high intensity kaon beam with 1% momentum spread;
- its high resolution tracking system for the kaons and the daughter particles downstream;
- particle identification detectors ;
- an efficient veto system for photons and muons.

The total length of the experiment is 270 m, from the beryllium target producing the secondary beam to the beam dump. The entire experiment is placed in an underground facility or cavern; the first 42 m of the beamline are dedicated to the momentum selection and the focussing of the beam. An *upstream* section follows this first beam section, that includes detectors measuring the beam particles properties. The charged kaons decay region

is defined between 102 and 180 m and it is contained in a vacuum tank, that also contains two downstream detectors, the LAV and the STRAW. The detectors dedicated to the detection of the K^+ decay products are placed in a 150 m long *downstream* section, starting from 121 m from the target. The NA62 experiment and its many components are described in detail in the following sections.

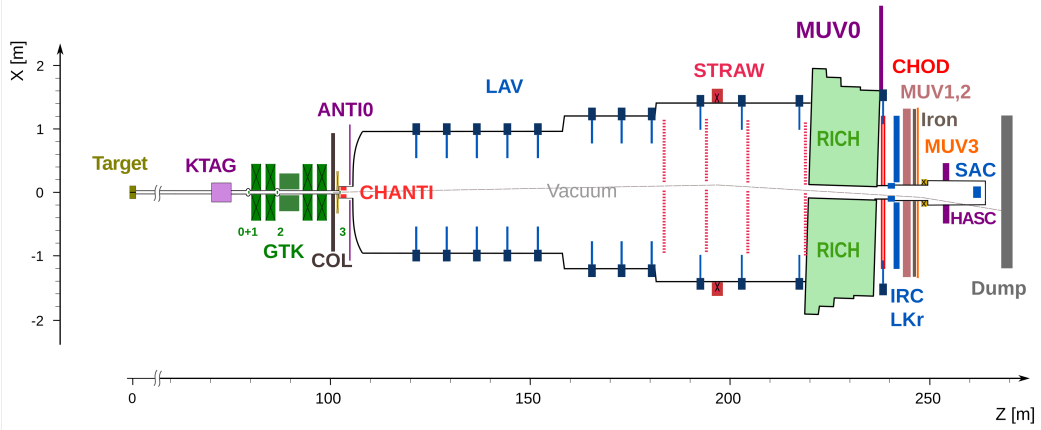

Figure 3.1.

3.1. The NA62 beamline

The 400 GeV/c proton beam from the CERN SPS is extracted in spills of 3 s effective duration to the T10 target, (400 mm long, 2 mm diameter beryllium) located in a tunnel connecting the SPS to the underground experimental hall target. From the target, a secondary beam (K12) is produced and directed in the underground facility where the experiment detectors are located. A copper collimator is placed after the T10 target with a 15 mm diameter hole. Then, a set of three quadrupole magnets with a large solid angle acceptance ($\pm$ 2.7 mrad horizontally and $\pm$ 1.5 mrad vertically) collects particles at 75 GeV/c central momentum. After the quadrupoles, a momentum selection is performed by an achromat made of four dipole magnets, shown in Figure 3.2a in A1. The first pair of dipole magnets displaces the beam, and the second one returns it to its initial trajectory performing a momentum selection of the beam particles. Such design is favourable for sweeping away muon background and low momentum particles. In between the dipole magnets, the beam passes through a set of graduated movable holes in two large, motorized and water-cooled metal blocks, TAX1 and TAX2, that serve to perform a momentum selection while acting at the same time as a beam dump for the remaining protons beam and unwanted secondary particles. The taxes are also an additional security measure during the data taking: the holes can be completely closed for safety when there are workers in the experimental hall. The K12 beam line has a length of 101.3 m up to the final collimators (C6, C7 in Figure 3.2a). Another quadrupoles triplet is placed after the achromat to re-focus the beam and make it parallel in the horizontal plane. In between the second set of quadrupoles, two collimators (C1, C2) change the vertical and horizontal acceptance of the

beam while removing the unwanted particles and another collimator (C3) absorbs positrons whose momentum have been degraded by a tungsten "radiator" placed between TAX1 and TAX2. After the C3 collimator, the beam passes through a 40 mm diameter bore, made by iron plates, located between the poles of a 2 m long dipole (B3), whose vertical field around the beam sweep aside muons of both signs.
The beam then encounters the first detector of the beamline, the KTAG, made of a Cherenkov differential counter (CEDAR), about 70 m downstream of the target. Such detector serves to identify the kaons in the beam, and to be effective, it requires the beam to be parallel to the z axis with minimal angular divergence. This is ensured via two other quadrupoles (Q7 and Q8) placed before the entrance of the beam in the KTAG, while two additional quadrupole magnets (Q9, Q10) follow the KTAG, refocussing the beam before the upstream spectrometer achromat system for momentum measurement is reached. Two collimators (C4, C5) absorb the particles in the tails of the beam. Upstream and downstream the KTAG, the beam parameters, i.e. its mean and standard deviation, are measured by two pairs of filament scintillating counters, FISC1,3 and FISC2,4. The beam reaches at this point a first spectromter.
At CEDAR, during the spill duration, the particle rate in the NA62 secondary hadron beam is 750 MHz, of which 6% is from K^+, 70% is made of π^+, and 23% from protons. The K^+ component has nominal momentum of 75 GeV/c and a 1% momentum spread. The beam spectrometer, the GigaTracKer (GTK), is composed of stations of silicon pixel detectors, three during the Run1 of the experiment (from 2015 up to 2018 included) and four since the beginning of the Run2 (from 2021 onward), and an achromat, placed between the first and the last tracker stations. Such achromat (A2) is made by four C-shaped dipole magnets and vertically deflects the beam by -60 mm; muons are also de-focussed thanks to a scraper magnet (SCR1). The beam is returned to its nominal direction after the momentum measurement. During 2018 an additional fixed collimator was added to the beamline (TCX) after GTK3, which further blocks particles arising from upstream decays together with the final collimators C6 and C7. From 2021, a 4th GTK station (GTK0) has been placed upstream next to GTK1 to increase the detector efficiency and reduce the upstream background. A schematic of the Run1 beam spectrometer is shown in Figure 3.2b.
A final dipole magnet, TRIM5, provides a deflection of 1.2 mrad in the horizontal direction, compensating the displacement provided by the MNP33 magnet placed further downstream. Since 2021, in addition, a hodoscope (ANTI0) has been installed mainly to reduce the muon halo background present in dump mode searches. Beam particles then enter into the decay region, contained in the vacuum tank, that starts at z = 104.2 m and ends at z = 219.6 m. The schematic of the beam spectrometer setup from 2021 is shown in Figure 3.3.
Downstream the beam spectrometer, the MNP33 magnet, positioned in between pairs of tracking detector forming the downstream spectrometer, induces a kick of 270 MeV/c deflecting the 75 GeV/c beam particles by -3.6 mrad in the vertical direction. Such deflection, combined with the previous one of 1.2 mrad, is such that the not-decayed beam particles pass through the center of LKr calorimeter and other downstream detectors, as shown in Figure 3.4. The vacuum tank that delimits the decay region contains eleven Large Angle Veto (LAV) detectors, four spectrometer (STRAW) chambers and the MNP33 magnet.

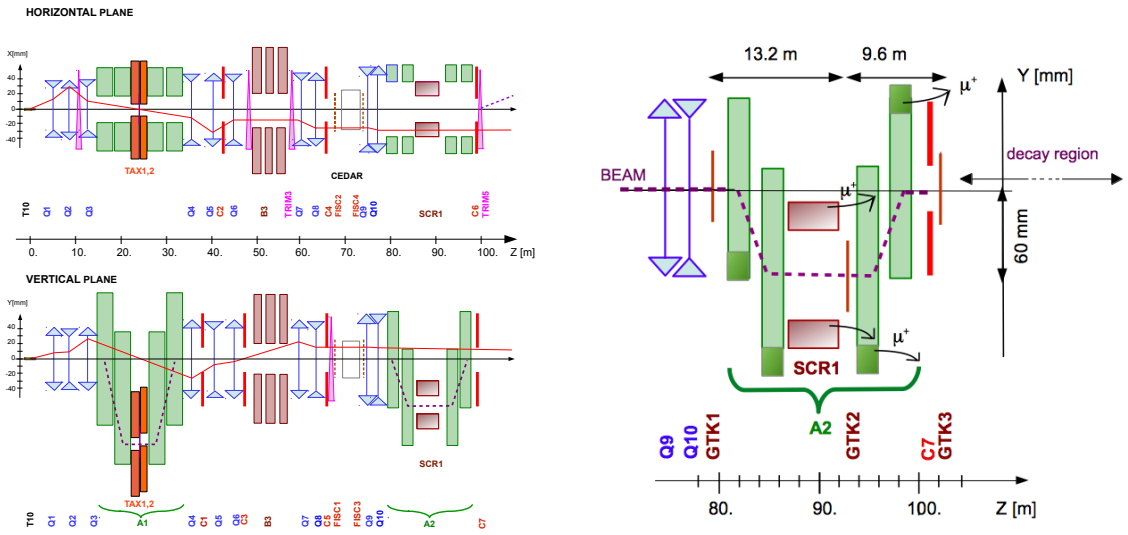

(a) (b)

Figure 3.2.: 3.2a: Upstream region from T10 target to decay volume with both horizontal and vertical views, for Run1. In each view, the solid line corresponds to the trajectory of a particle leaving the target from the centre at nominal momentum and at the angle indicated. The dashed line indicates the trajectory of an initially on-axis 75 GeV/c momentum particle. 3.2b: Schematic description of the beam spectrometer in the second achromat (A2). Muons are swept away by the scraper SCR1. From [81].

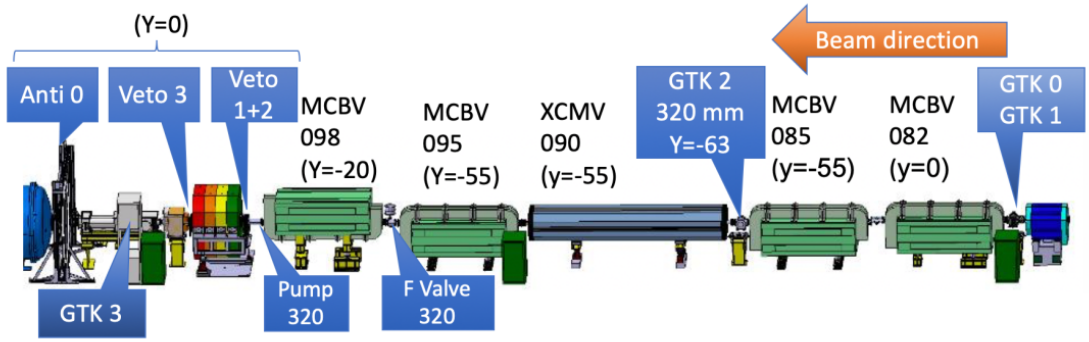

Figure 3.3.: Schematic layout of the Run2 achromat and beam line. From [34].

After the end of the vacuum tank, the remaining beam particles are contained in a beam pipe that follows the beam trajectory passing in the center of the other downstream detectors. Being the remaining beam uninteresting, it is guided towards the end of the cavern hall without further interaction, and is finally deflected towards negative X through a further angle of -13.2 mrad by a dipole magnet (BEND), that deflects charged beam particles away from the Small Angle Calorimeter (SAC) veto detector, towards a beam dump composed of iron surrounded by concrete where it is absorbed.

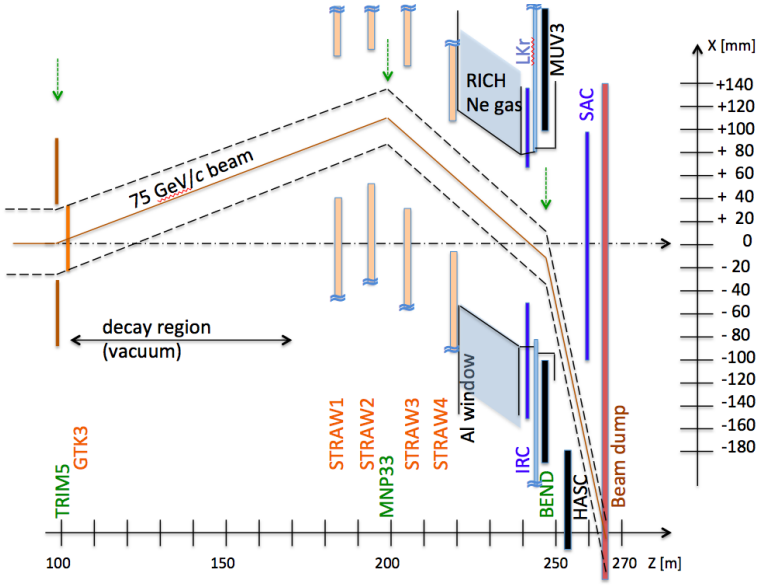

Figure 3.4.: Downstream region in the x,z plane from decay volume entry to beam dump.

3.2. NA62 subdetectors

3.2.1. KTAG

Kaons make up just 6% of the NA62 beam; a K^+ identification system early in the beamline is crucial to any physics analysis. The CEDAR/KTAG system is a fast kaon tagging apparatus . It is formed by a ChErenkov Differential counters with Achromatic Ring (CEDAR), designed at CERN in the 70's to provide separation for protons, pions and kaons extracted from the CERN SPS [27], coupled to a specially designed photon detection and readout KTAG detector module that can sustain the 45 MHz kaon rate. The NA62 CEDAR is a cylindrical gas vessel of length 7 m and diameter 60 cm, providing a surface of 0.93 m^2, filled with nitrogen (N2) (hydrogen H2 at 3.9 bar since early 2023 [58]) at 1.75 bar at room temperature, that corresponds to $3.5 \cdot 10^{-2} X_0$ of material in the path of the beam. The CEDAR has a diaphragm of fixed central radius and an adjustable annular aperture so that the beam particles produce Cherenkov light when passing in the vessel. The Cherenkov photons' emission angle θ_C depends on the velocity of the particle and on the refraction index of the medium (cf. Equation 1.33). Since the particles forming NA62's beam all have a momentum of 75 GeV/c, the velocity will be different for each particle species as it depends on its mass. In turn, this leads to different Cherenkov photon emission angles. The Cherenkov photons are reflected by a mirror and pass through an optic system made of lenses, an annular diaphragm and a chromatic corrector. The width of the diaphragm can be modified; by adjusting the gas pressure and the width of the diaphragm. These modifications allow controlling the refractive index, enabling the selection of the desired particles (K^+) by letting their Cherenkov light cone pass through the diaphragm. The Cherenkov light passing through the annular diaphragm is focussed to the exit of the vessel through eight quartz windows, that steer it into eight spherical mirrors. Such

mirrors reflect the Cherenkov light radially into eight arrays of 48 photomultiplier tubes (PMTs) [57]. The time coincidence between at least 5 sectors of the detector ensures the presence of a K^+. A schematic of the NA62 CEDAR/KTAG system is shown in Figure 3.5. The K^+ time resolution is 70 ps, the K+ identification probability is 98% when requiring coincident signals in at least five KTAG sectors with a pion misidentification estimated (at low intensity) to be $\mathcal{O}(10^{-4}$ with nitrogen gas.

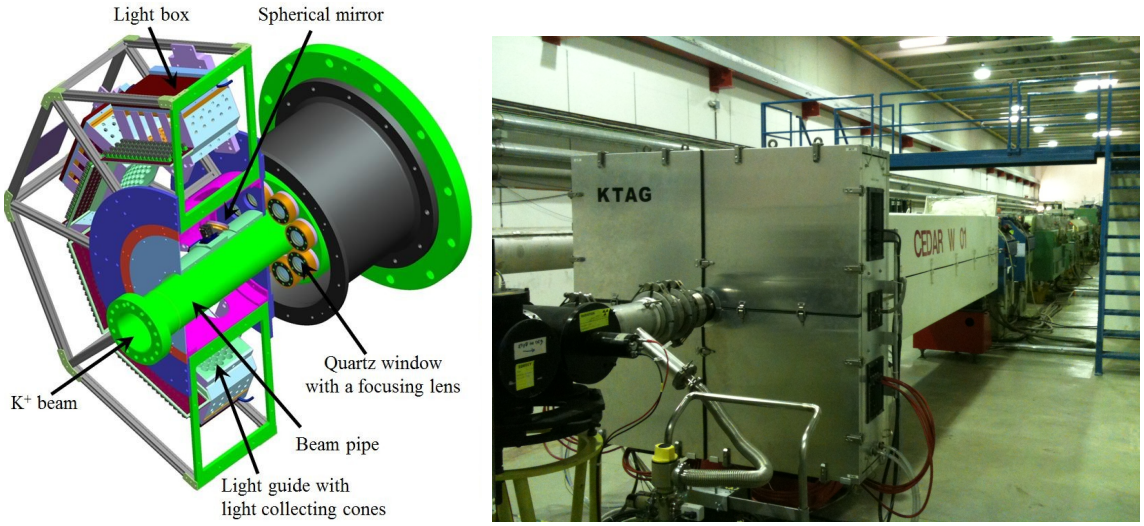

(a) (b)

Figure 3.5.: 3.5a: scheme of the KTAG, from [55]. 3.5b: Cedar vessel with the readout KTAG; photo taken in the NA62 experimental hall.

3.2.2. GigaTracKer (GTK)

The GigaTracker is a silicon pixel detector and the beam spectrometer of the NA62 experiment; it is designed to sustain a particle rate of 750 MHz and to have a minimal material budget to reduce scattering. The GTK technology is a milestone in the development of planar time tagging silicon pixel detectors. Its function is to measure the momentum, direction and time of arrival of the beam particles. In particular, it was designed to respect the following requirements:

- a track momentum resolution of 0.2%;
- a hit time resolution better than 200 ps to unambiguously reconstruct the beam tracks;
- sustain a yearly fluence of 4.5 10^{14} 1MeVn$_{eq}$/cm^2/200days

The GigaTracker is made of four stations (since 2021; before 2021 there were three stations), perpendicular to the beam and placed in vacuum, installed around four dipole magnets arranged as an achromat.

The particle momentum is measured thanks to the vertical displacement of the trajectory in the second station. The hits in the four stations allow reconstructing an upstream beam track, with a precision of 0.2% on the momentum measurement, an angular resolution of 16 µrad and a track time resolution of 65 ps (hit time resolution of 130 ps). The sensor is a 200 µm thick, 60.8 × 27 mm silicon sensor. The sensor is segmented in 180000 pixels of 300 × 300 µm^2, read out by an application-specific integrated circuit (ASIC) called TDCPix, where TDC stands for time-to-digital converter. Each GTK station, one of them being shown in Figure 3.6, is read out by two rows of five chips, that perform the time stamping of the hits. These chips have been designed using 130 nm CMOS technology. The material budget, given by thickness of the read-out chips (100 µm), the thickness of the sensor (200 µm) and the 210 µm of the cooling system plus the support, is $\sim 0.5\% X_0$ i.e. 500 µm of Si. The power consumption of the chips, due to the time stamping, is about 4 W per chip; active cooling is hence required. Moreover, the GTK is located in a harsh radiation environment, having to sustain the full nominal beam intensity (750 MHz), corresponding to rate in the central region of the sensor of 1.5 MHz/mm^2). The detector must hence be radiation hard; the ageing effects due to radiation damage are minimized thanks to the cooling system that pumps the cooling liquid C_6F_{14} through 150 parallel micro channels etched on the silicon wafer (cooling plate) bonded to the silicon sensors. The cooling liquid circulates in the micro-channels at a pressure of 3 bar with a flow of 2 g/s/station, and the temperature can be controlled in a range between -25 to 0 C°. The integration of the cooling system is done through a *carrier card*, which also provides mechanical support for the cooling assembly. The detector is powered by ten 1.2 V "analogue" lines and ten 1.2 V "digital" lines, two per each of the ten chips. Furthermore, 2.5 V, 3.3 V and 5 V lines are needed for the carrier card. All these channels are interlocked with the readout chips temperature sensors: in case of cooling or vacuum failure, this interlocks protect the system from damage. A 5.3 V non-interlocked line powers the temperature interlock logic. The low voltages power supplies (CAEN A3009) are installed in the cavern, next to the detector. High voltage power supplies (CAEN A1821) are installed in surface.

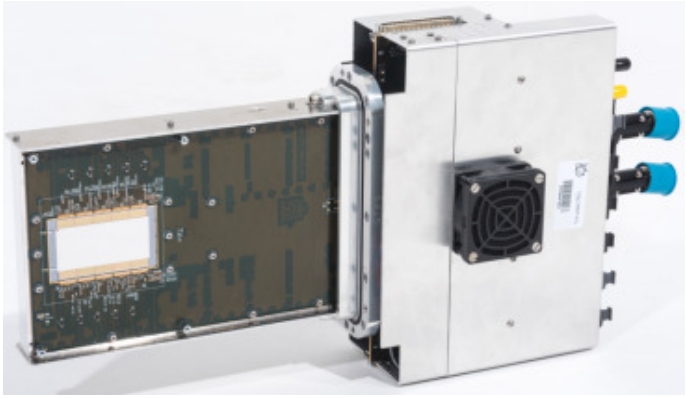

Figure 3.6.: A module of the GigaTracker detector on the sensor side. From [81].

3.2.3. CHarged ANTI-coincidence detector (CHANTI)

Despite the small material budget of the GTK, the particles crossing it can still undergo inelastic interactions. The particles interacting in the first two (up to 2018) or three (from 2021) GTK stations are swept away by the magnets; the CHANTI (Charged Anti-coincidence) detector's purpose is to provides rejection of the high transverse momentum particles that interacted inelastically with the last GTK station material: particles resulting from inelastic interactions in GTK3 can enter the acceptance of the downstream detector and are a source of background for NA62's analyses. The CHANTI is made by six stations (each with two perpendicular "x" and "y" layers) of scintillator bars, located in the same vacuum vessel of GTK3, with an area of 300x300 mm^2. A central aperture of 95x65 mm^2 allows the passage of the beam. The CHANTI provides hermetic coverage for particles originating from GTK3 from 49 mrad to to 1.34 rad [81]. The detection efficiency is measured to be at least 99% [81]; the spatial resolution is 2.5 mm and the time resolution 830 ps.

3.2.4. ANTI0

The Anti0 hodoscope has been added to the experiment for the Run2, and has been designed to reduce the background present in the hidden sector searches done in "beam-dump mode", where the TAXes holes are completely closed and the target moved away from the beam, so that the beam can impinge directly on the Cu of the TAXes [78].
The detector consists of two planes of scintillating tiles readout by silicon photo-multipliers, it was commissioned during 2021, and it was installed just in front of the Decay Volume [43].

3.2.5. Straw Spectrometer (STRAW)

The STRAW spectrometer provides the momentum and direction measurements for particles produced in K^+ decays in the decay volume. The STRAW is positioned ~ 20 m after the end of the decay tube (180 m) and extends for 35 m along the beam line. It consists of four chambers (one shown in Figure 3.7a) made each of two modules that contain each two layers (views) of straw tubes, and a large aperture dipole magnet (MNP33) positioned at the middle, between two pairs of chambers, which provides a magnetic field of 0.9 Tm. Since its function is to provide precise momentum and direction measurements, its design must be oriented towards a minimization of the multiple scattering, which is obtained by using light material for the chambers and by installing them in the vacuum tank. The total amount of material in the spectrometer corresponds to 1.8% X_0. Detection happens thanks to the creation of electron-ion pairs consequently to the passage of a particle. The pairs drift to opposite electrodes, inducing charge on the central wire. The electric field intensity consequently grows leading to an avalanche (multiplication) process, that creates a macroscopic current pulse on the anode wire which is read out. The time to drift to the anode wire enables deriving the radial position from the wire; the position of a particle is derived by combining information from other straw tubes. Each chamber is indeed

composed of four layers (views) made of straw drift tubes. The four views are identified with the letters X, Y, V, U; the views are aligned respectively at 0, 90, -45 and +45 degrees and collectively covering a region with outer circular profile of diameter 2.1 m (see Figure 3.7b. The beam pipe passes through a hole in the middle of each chamber. Such layered geometry ensures at least two hits per view; this means 8-12 hits per track per chamber. With hits in chambers before and after the magnet, the track can be precisely reconstructed. The momentum resolution is $\frac{\sigma_p}{p} = 0.3\% \oplus 0.005\%$, with the momentum p measured in GeV/c.

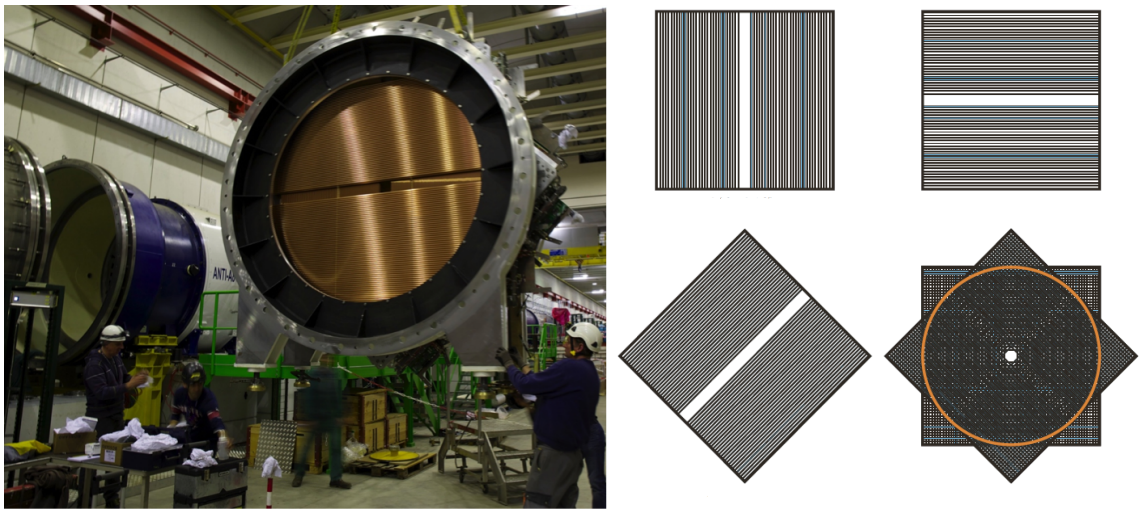

(a) (b)

Figure 3.7.: 3.7a: Picture of the STRAW detector during installation in the experimental hall. 3.7b: Sketches of the STRAW station geometry showing the arrangement of the four views. From [81].

3.2.6. Photon veto detectors

The main NA62 analysis, that is the search for the $K^+ \to \pi^+\nu\nu$ decay, needs efficient photon veto to avoid misidentifying background events from $K^+ \to \pi^+\pi^0(\pi^0 \to \gamma\gamma)$ as signal events. If the photons from the π^0 decay are not detected, separating the signal from the background becomes challenging. To detect and veto such events, a photon veto system has been designed with hermetic coverage for these photons from 0 to 50 mrad. This solid angle is covered by three detectors sets: the small angle vetos (IRC and SAC) that cover 0-1 mrad, the liquid krypton calorimeter that covers 1-8.5 mrad and the Large Angle Veto (LAV) that cover 8.5-50 mrad, as shown in Figure 3.8.

Large Angle Veto (LAV)

The Large Angle Veto system is made of 12 stations of four or five staggered layers lead-glass (75% PbO) blocks recycled from the OPAL electromagnetic calorimeter barrel [105],

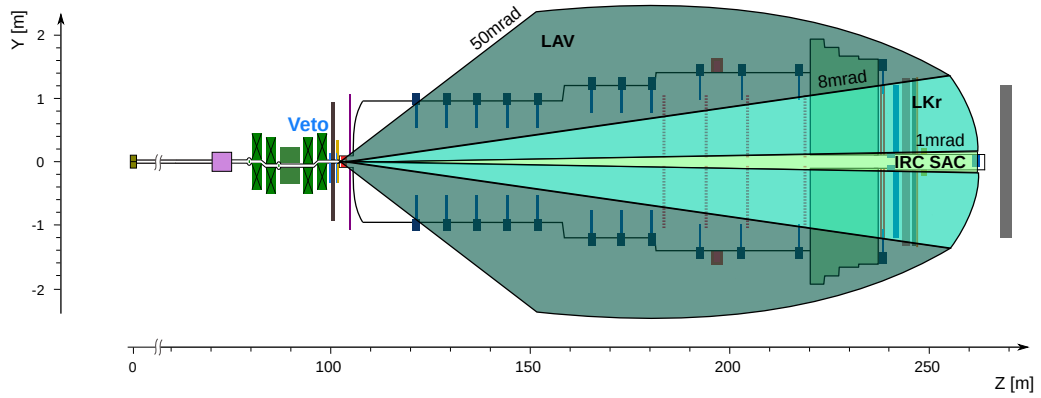

Figure 3.8.: Top view of the NA62 experiment with the angle coverage of the photon veto detectors highlighted in blue.

wrapped in a new light-tight Tyveck covering. Two LAV stations are shown in Figure 3.9. Photons detection happens thanks to the collection of the Cherenkov light produced by the charged particles of the electromagnetic shower. The blocks are arranged in rings of different radii surrounding the decay tube. Each station contains more than one ring (or layer) in order to have high detection efficiency. The first 11 stations are in vacuum while LAV 12 operates in air.

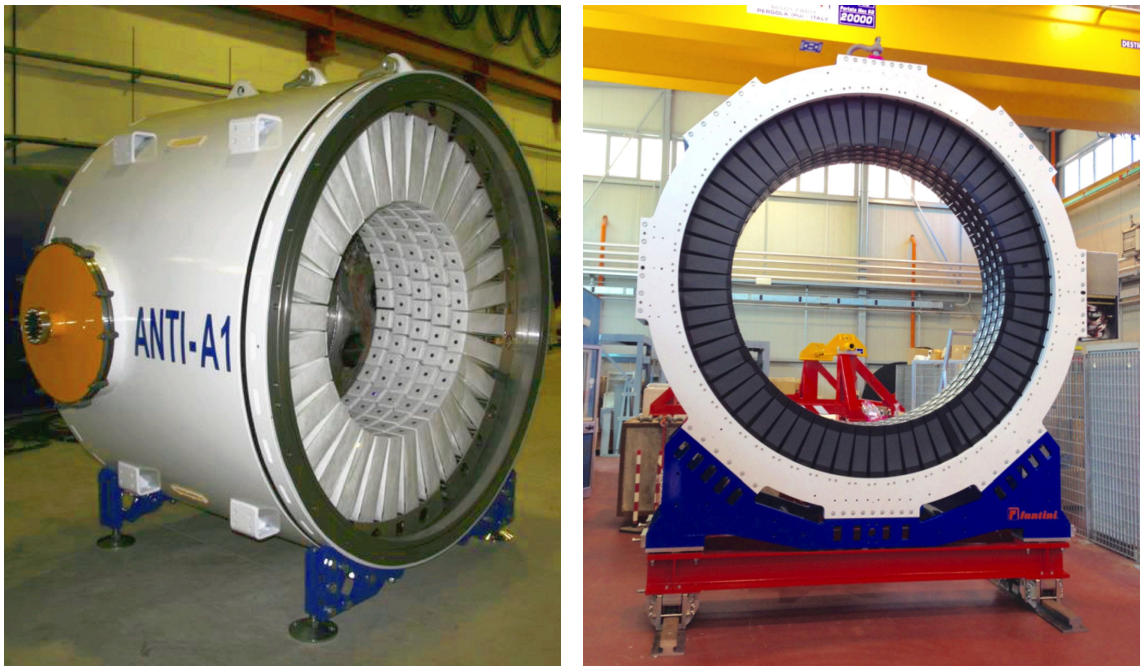

(a) (b)

Figure 3.9.: Station LAV1 (3.9a) and LAV12 (3.9b) before insertion in beam line. From [81].

Small Angle Veto (SAV)

The photons emitted at very small angles are detected by the Small Angle Veto (SAV) detector system. The SAV includes two detectors: the Intermediate Ring Calorimeter (IRC) and the Small Angle Calorimeter (SAC). Both the IRC and the SAC are sampling calorimeters with a Shashlik design, meaning that they are made of sandwiched layers of lead absorbers (thickness 1.5 mm) and of active plastic scintillator of the same thickness. IRC (Figure 3.10) has a cylindrical shape, with an outer radius of 290 mm centered around the Z axis, and an inner radius of 120 mm with the center shifted by 12 mm along the positive X axis, to take into account the displacement provided by MNP33 to beam particles. It is placed upstream the LKr and it is made of two modules, of 25 and 45 layers each. The SAC (Figure 3.11) is made out of 70 squared planes of lead and 70 squared planes of plastic scintillator, with side length 205 mm and total depth corresponding to 19 X_0. The SAV is placed downstream the LKr after the BEND dipole magnet that deflects the beam into the beam dump.

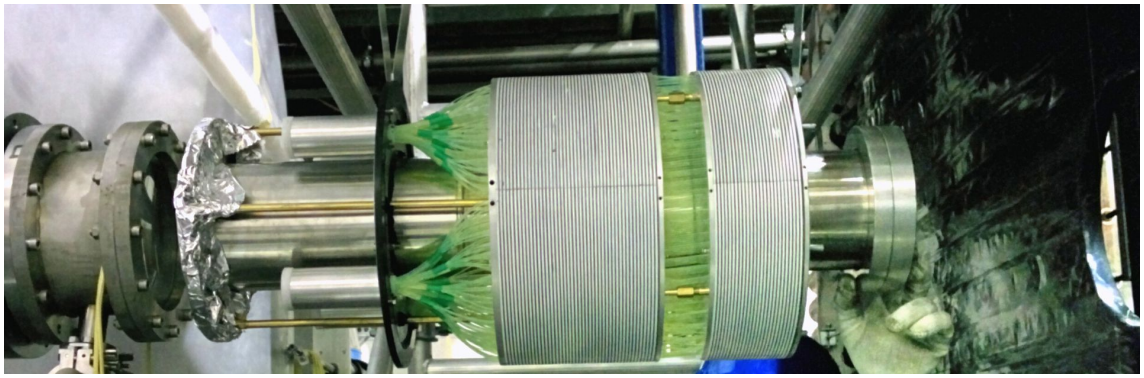

Figure 3.10.: Picture of the IRC during installations. From [81].

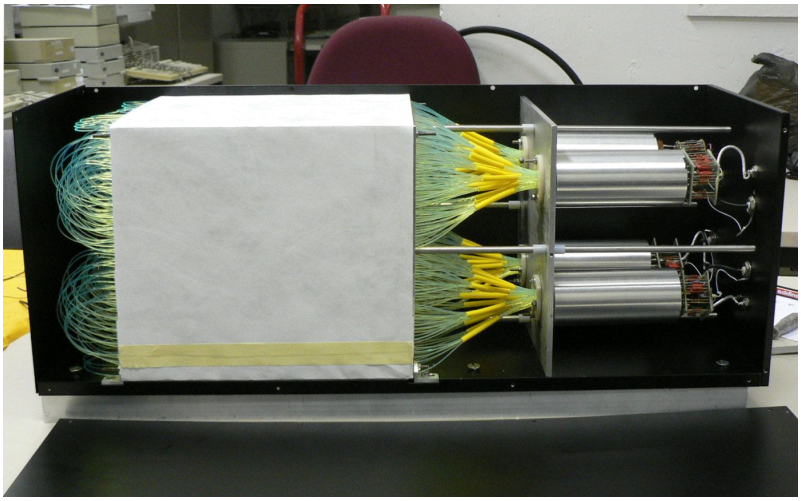

Figure 3.11.: Picture of the SAC after completion of assembly. From [81].

Liquid Krypton calorimeter (LKr)
The LKr is a quasi-homogeneous electromagnetic calorimeter, inherited from the NA48 experiment [49] but with updated readout systems to match NA62 rates. It is formed of a cryostat filled with about 9000 l of liquid krypton at 120 K. The calorimeter extends from the beam pipe (radius $\approx 8\,\text{cm}$) to a radius of 120 cm; its depth is 127 cm, corresponding to 27 X_0. The detection of electrically charged particles and photons happens thanks to the electromagnetic showers that develop when particles pass through the liquid krypton and start losing energy due to brehmsstrahlung (in the case of charged particles) or through pair production (in the case of photons). The energy lost by the particles is transferred to the calorimeter medium; the energy deposition in the calorimeter is measured thanks to the charge produced in the electromagnetic shower that is collected by the preamplifiers directly attached to the calorimeter cells that compose the calorimeter. The cells are made of Cu-Be electrodes and have a cross section of 2x2 cm^2, and are aligned to the longitudinal axis of the experiment. The LKr has an active fiducial volume with a regular octagon cross-section, with apothem 1130 m.
The depth of 27 X_0 contains effectively the electromagnetic showers, that develop logarithmically. However, hadronic showers such as those created by the positively charged pions that cross the LKr are unlikely to by fully contained [25]. Finally, muons act as minimum ionizing particles (MIPs), losing a small amount of energy as they cross the detector. For this reason, the LKr can also be used as tool for particles identification thanks to the ratio between the energy deposited in the calorimeter and the momentum of the particle measured by the STRAW spectrometer (see Section 3.2.5), E/p. The energy resolution is:

$$\frac{\sigma_E}{E} = \frac{4.8\%}{\sqrt{E}} \oplus \frac{11\%}{E} \oplus 0.9\% \tag{3.1}$$

where E is measured in GeV, and the time resolution is ~ 600 ps.

3.2.7. Ring Imaging CHerenkov detector (RICH)

As the main goal of the NA62 experiment is to collect $K^+ \to \pi^+\nu\bar{\nu}$ decays, the experiment needs good particle identification, in particular to distinguish between π^+ and μ^+. The Ring Imaging CHerenkov (RICH) detector is designed for particle identification (PID). The efficiencies for π^+ identification and μ^+ rejection are measured for particles of momentum $15 - 35\,\text{GeV/c}$ and are respectively $\mathcal{O}(80-60)\%$ and $\mathcal{O}(10^{-3} - 10^{-2})$ [82]. The RICH detector has a time resolution of $\mathcal{O}(100)$ ps. The detector is made of a cylindrical vessel of 17.5 m length, filled with neon gas kept at a constant pressure of 990 mbar. The vessel includes four sections of decreasing diameter (from 4.2 m upstream to 3.2 m downstream) and is traversed by the beam pipe. The detection of particles happens with the same physical principle as in the KTAG detector: charged particles pass through a gas medium and emit Cherenkov photons at an angle determined by their mass and momentum. By measuring this angle and using the momentum measurement provided by the STRAW spectrometer the mass of a particle can be derived. The Cherenkov ring as function of the particle momentum is shown in Figure 3.12. The last downstream vessel contains a mosaic of 20 spherical mirrors (18 hexagonal and 2 half-mirrors, that are used in the center

and have a central opening to accommodate the beam pipe) that reflect and focus the Cherenkov light cone into a ring on two PM array. A schematic of the RICH detector is shown in Figure 3.13.

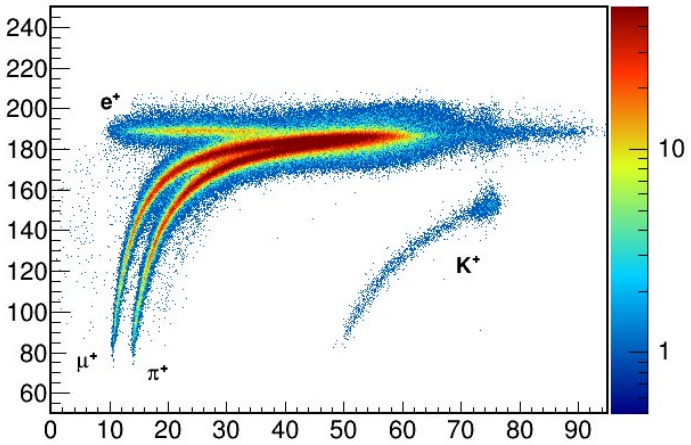

Figure 3.12.: Cherenkov ring radius as a function of particle momentum; electrons, muons, charged pions and scattered beam kaons can be clearly seen. Particles with momentum higher than 75 GeV/c are due to halo muons. From [81].

3.2.8. Charged Particle Hodoscopes (CHODs)

Further downstream in the beamline, there are two charged particles hodoscopes (CHODs). One of them was used in the NA48 experiment and hence they are called CHOD and NA48-CHOD. Their active area covers radii between the IRC outer radius (145 mm) and the LAV12 inner radius (1070 mm). The second hodoscope was introduced in NA62 in order to sustain the higher rate NA62 operates with.

The NA48-CHOD is made of two consecutive planes, respectively of 64 vertical and 64 horizontal 2 cm thick plastic scintillator slabs, read out by PMs. The slabs are organized in four quadrants, and form an octagon of 1210 mm apothem, with a hole in the center of 128 mm radius. Slabs widths vary from 65 mm in the central region to 99 mm at the edges of the detector as the detector illumination is larger close to the beam. The NA48-CHOD provides two time measurements, one per plane (reducing tails in time distributions) and a position measurement. A time resolution of 270 ps is measured in 2017 and 2018 data. A schematic of the NA48-CHOD is shown in Figure 3.14a.

The CHOD has been installed on the front plane of the LAV12 station; it is made of a mosaic of 152 plastic scintillator tiles covering an annular region between radii of 0.140 m and 1.070 m. The tiles are 30 mm thick, and the scintillator light is read out by SiPM pairs. The tiles slightly overlap with their neighbours, to ensure there are no dead zones. A schematic of the CHOD is shown in Figure 3.14b.

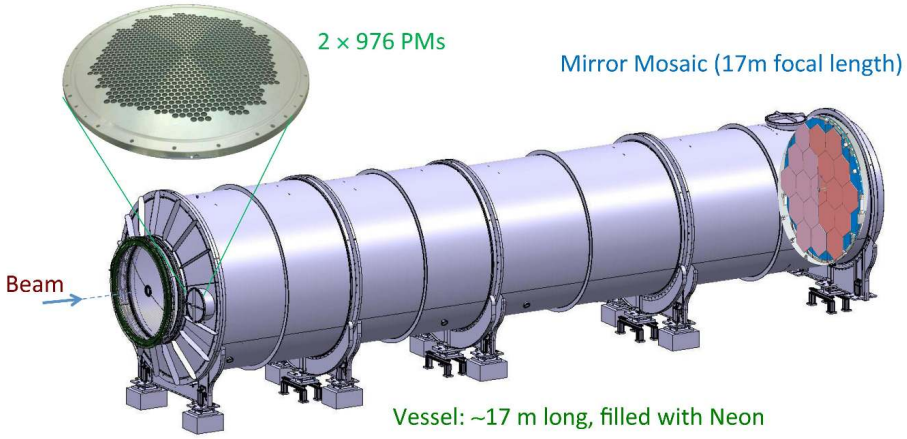

Figure 3.13.: Schematic view of the RICH detector. A zoom on one of the two disks accommodating the light sensors (PMs) is shown on the left; the mirror mosaic is made visible through the neon container (vessel) on the right. From [81].

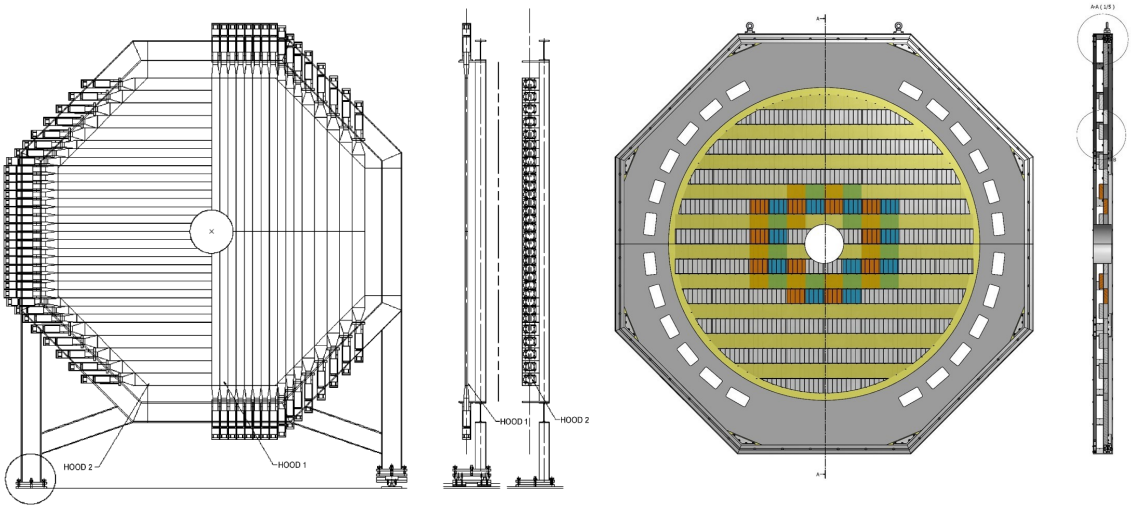

(a) (b)

Figure 3.14.: Charged hodoscopes used by NA62: the NA48-CHOD (left) and the CHOD (right). Adapted from [81].

3.2.9. Hadronic Calorimeters

Further muon identification is provided by an hadronic calorimeter s , made of two detectors called MUon Veto: MUV1, built for the NA62 experiment, and MUV2, inherited from the NA48 experiment [49]. Both detectors modules are Shashlick calorimeters, made from sandwiched layers of iron and scintillator.
The MUV1 detector is made of 24 layers of 26.8 mm thick steel plates. The distance between consecutive iron layers is 12 mm, and they are interlayered with 9 mm thick scintillator strips, that are 60 mm in width and 2.620 m long. Consecutive layers of scintillators are alternately aligned in the horizontal and vertical direction, providing x and y measurements, making 12 layers with horizontal and 11 layers with vertical strip direction. The scintillator strips are read out at both ends by WLS fibers coupled to PMs.
The MUV2 detectors, used in a reversed position with respect to the NA48 experiment, uses the same technology as MUV1 but with larger tiles. It is made of 24 steel plates of 25 mm thickness, interlayered with plastic scintillators tiles. Each scintillator tile consists of 44 scintillating strips; each strip spans half the calorimeter and is 1300 mm long, 119 mm wide, and 4.5 mm thick.
Hadronic showers are caused by hadrons such as π^+; these particles interact with a nucleus, inducing the production of secondary hadrons such as p, n, $\pi^\pm$ and π^0. In turn, these particles further interact, logarithmically creating more secondaries until their energy is not sufficient for the interaction to happen. The development of such hadronic shower is characterized by the nuclear interaction length, λ_I, that is in general larger than the radiation length X_0. The MUV1 and MUV2 calorimeters cover a total of 8 interaction lengths, respectively 4.1 and 3.7. Hadronic showers are usually accompanied by an electromagnetic component, generated by high energy photons in the neutral pion decay $\pi^0 \to \gamma\gamma$. The fact that hadronic showers have two components and have a larger transversal development is used to distinguish between electrons and pions in NA62: electrons instigate electromagnetic showers that start in LKr and rarely reach MUV1 and MUV2, while pions may begin to shower in LKr, and the shower often continues in MUV1 and MUV2.
The whole hadronic calorimeter system makes up for 66 ton of steel. It has a 0.9 ns time resolution, and the energy resolution, measured with 2015 data, is:

$$\frac{\sigma(E)}{E} = 0.115 \oplus \frac{0.38}{\sqrt{E}} \oplus \frac{1.37}{E} \tag{3.2}$$

where E is measured in GeV. The two detectors MUV1 and MUV2 are shown in the picture in Figure 3.16, respectively in red and dark blue color.

3.2.10. Fast MUon Veto (MUV3)

The MUV3 detector is placed downstream after the hadron calorimeter, after the iron wall (in light blue in Figure 3.16) that constitutes another 4.7 interaction length, so that the only charged particles that can reach it are the muons. Indeed, electrons and positrons are absorbed by the LKr, and pions showers are contained in the hadronic calorimeter system; muons on the other hand act as MIP and can reach the MUV3. The MUV3 is

hence an efficient detector to veto or identify muons. The MUV3 is a square plane, of side length 2.640 m and it is made of an array of 148 scintillator tiles, that are 50 mm thick. 140 tiles are classified as "outer tiles", have a size of 200 mm x 200 mm, while the remaining 8 tiles are smaller and are called "inner tiles", as they surround the central beam pipe as shown in Figure 3.15. The signal produced by muons crossing the tiles is read out by two photomultipliers placed on its backside. There is an 8% probability that a muon passes through a PM window; in this case, some Cherenkov photons are generated, which arrive before the scintillation photons. This mechanism affects the time reconstruction; nonetheless, a time resolution of 0.5 ns is obtained. For $\mu^{\pm}$ of momenta over 15 GeV/c, the measured identification efficiency is larger than 99.5%.

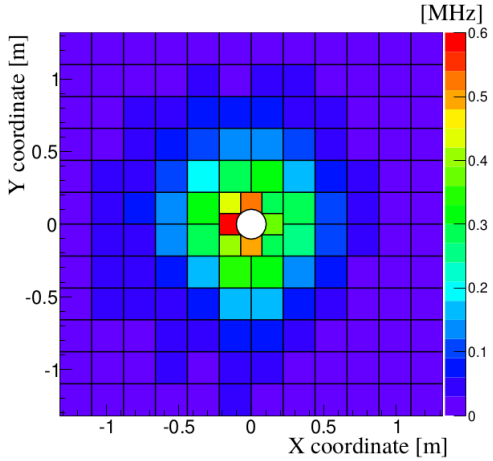

Figure 3.15.: MUV3 illumination from [81].

3.2.11. Additional veto detectors

The MUV0 (peripheral muon veto) and the HASC (hadronic sampling calorimeter) are additional veto detectors that are employed to detect $\pi^{\pm}$ from $K^+ \to \pi^+\pi^+\pi^-$ decays that are outside the lateral acceptance of the STRAW chambers. The MUV0 is a scintillator hodoscope, placed on the downstream flange of the RICH, only on one side as shown in Figure 3.1; it is designed to detect π^- with momenta below 10 GeV/c that are deflected by the magnet in this region. The HASC is made of 9 modules, each made of a sandwich of 60 pairs of lead plates and 60 plates of scintillator. It is placed downstream of MUV3; it is used to detect π^+ of momentum larger than 50 GeV/c that pass though the holes at the centres of the STRAW chambers.

3.3. Trigger and Data Acquisition system (TDAQ)

The NA62's Trigger and Data Acquisition system (TDAQ) has been designed considering the high particles and data flux and hence the need of high performance triggering and

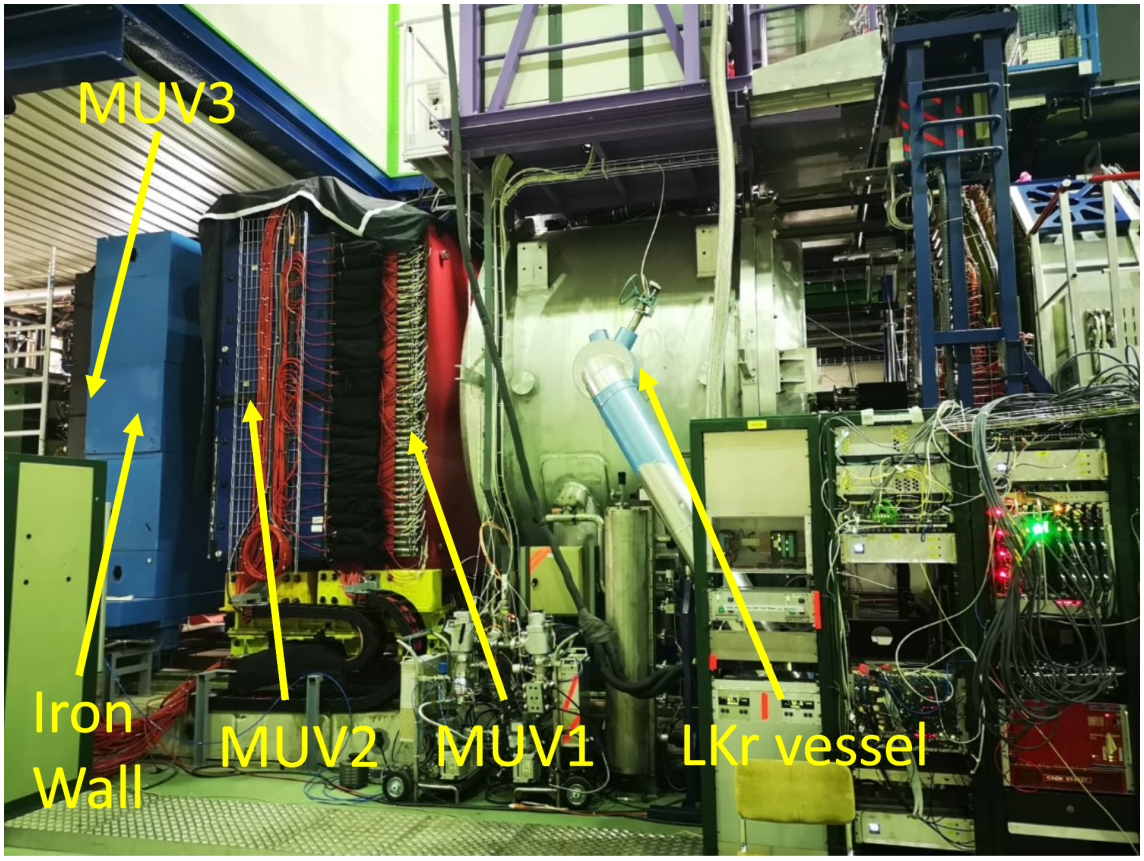

Figure 3.16.: Annotated picture of the calorimetric system of the NA62 experiment. The LKr vessel is visible on the right, followed by the MUV1 in red, the MUV2 in dark blue and the iron wall to stop all the particles in lighter blue. MUV3 is placed just after the iron wall. The beam comes from the right. Picture taken in NA62 experimental hall.

data acquisition, that should minimize dead times while ensuring efficient data collection. The TDAQ system involves three trigger levels: hardware (low) level trigger L0, software (high) level triggers L1 and L2. The L0 trigger has the role to reduce the event rate from 10 MHz produced at nominal intensity to 1 MHz. The L1 and L2 trigger further reduce the event rate to 10 kHz; the dedicated NA62 PC Farm and the merger PCs then ensure data storage to tape.

L0 trigger

The L0 trigger works thanks to the inputs from a set of fast detectors, with a maximum latency of 1 ms. The L0 Trigger Processor (L0TP) receives the packets of information, called *primitives*, from the NA48-CHOD, CHOD, RICH, LKr and MUV3 detector readout boards. The primitives contain information regarding which pre-defined conditions (trigger bits) are satisfied independently in each system. The L0TP sorts the primitives in time, and compares the received primitives to the trigger *masks*. A trigger mask is a predefined set of conditions that result in an event being accepted (if the conditions are satisfied) or discarded (if the conditions are not satisfied). Each trigger mask (there can be up to ten

masks) can have a downscaling factor, which can be applied if a trigger mask is satisfied. After a positive L0 trigger verdict, the recorded data is sent to a PC farm to be processed and reduced by the high level triggers L1 and L2.

High Level Triggers (HLT: L1 and L2)
To match the available bandwidth for permanent storage ($\mathcal{O}(10)$ kHz), data rates needs further reduction. This is done thanks to two levels of software triggers, L1 and L2. The L1 trigger uses information from KTAG, STRAW and LAV to reduce data rate by a factor 10. The L2 trigger further reduces the data rate by another factor 10; it is based on partially reconstructed events, and uses correlated information between several detectors. Both L1 and L2 triggers run on the NA62 PC farm.

Data acquisition
The data taking relies on the SPS beam delivery structure, that is expected to be uniform over bursts of 3 seconds. The bursts are separated by some variable time, and they constitute the unit of data taking. The electronic devices run in a synchronized way during the burst, and they reset to the initial state outside the burst. This happens thanks to the Timing, Trigger and Control (TTC) system, that deals with clock and trigger distribution. The TTC is a unidirectional optical fiber based transmission system with two multiplexed channels. One channels transmits the L0 trigger signal only, while the other carries encoded information concerning resets and trigger types. All the elements of NA62 TDAQ system run on the TCC clock, that distributes the Start of Burst (SoB) command, sent about 1 s before the burst, that corresponds to the start time of the measurements of the current burst. Similarly, the TCC clock delivers the End Of Burst (EOB) signal, that signals all system to stop the data taking. A schematic of NA62 TDAQ logic is shown in Figure 3.17.

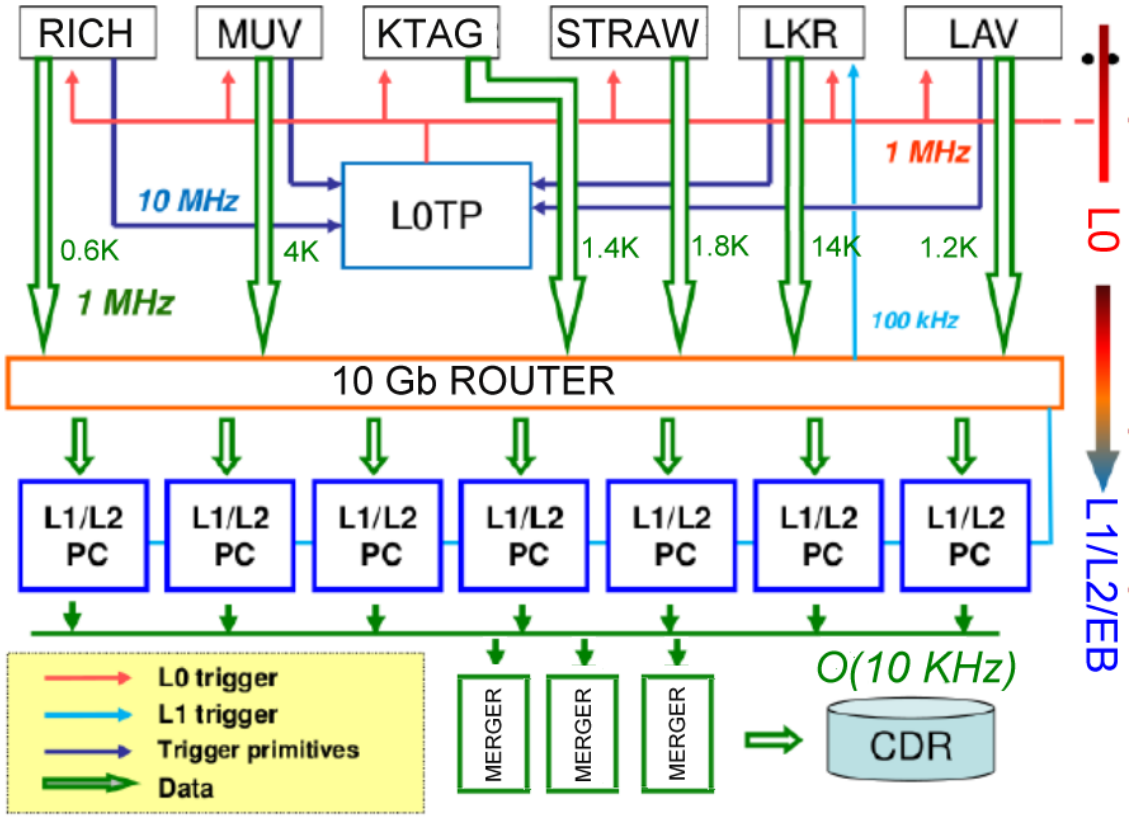

Figure 3.17.: Overview of the NA62 Trigger and Data Acquisition system. Numbers near the data arrows correspond to the average data size in byte. Only a few detectors are displayed for the sake of simplicity. From [81].

All of NA62 detectors except the trackers and the calorimeters use a TDC-based TADQ system, called TEL62, that was redesigned from the TEL1 board developed for the LHCb experiment. For NA62, a high-precision TDC has been developed: the TDCBoard (TDCB), which is a mezzanine card for the TEL62 which can digitise leading and trailing edge time signals of 128 channels, with a time resolution of 100 ps. The TEL62 sends the detector data to the the PC farm after receiving an L0 trigger

The GTK readout system is made of custom-made modules, the GTK-RO boards, that interface the on-chip readout TDCPix to the TTC clock and trigger. The GTK-RO temporarily stores in memory the data provided by the TDCPix and transferred via four 200 m long optical fibres. The total data bandwidth is 12.8 Gb/s for each chip, that corresponds to 128 Gb/s per station. The arrival of a L0 trigger with a fixed latency allows to identify the time slot of interest; three time slots centered around L0 time and corresponding to 75 ns time window are read out from memory, and are then transmitted to six PCs, through Gigabit Ethernet switches. Each PC serves five read out cards (one row of chips in each station); the PCs identifies and organizes the data by L0 triggers, and sends them to the PC farm, after receiving the L1 trigger information.

The STRAW spectrometer is read out by eight-channel front-end chip, serving eight straws and a TDC; for the readout of the STRAW, the CARIOCA readout chip [79], originally

developed for LHCb muon chambers, is used. The STRAW readout sends the data to the PC farm after receiving the L0 trigger information.
The calorimeters (LKr, MUV1, MUV2, SAV) use the CREAM (Calorimeter REAdout Module) readout system [30], that was developed specifically for the LKr. They are 6U VME 64 boards, equipped with a large memory for storing data of an entire SPS burst. The information from CREAMs cannot be fully exploited to take a L0 trigger decision, because the bandwidth required to move the corresponding data would be too large. Since the information from the calorimeters is crucial to reach the veto power required by the main NA62 analysis, every 25 ns the sum of digitized signals is sent from CREAM to the L0Calo system,which reconstructs clusters from the calorimeters, computing their positions, times and energies.

4. Tagging proof of principle at NA62

Summary

As mentioned in Chapter 2, the feasibility of the neutrino tagging technique can be studied on data from the NA62 experiment, described in detail in Chapter 3. This chapter presents

the analysis of the $K^+ \to \mu^+\nu_\mu$decay with tagged neutrino at NA62: Section 4.1 presents the analysis strategy and the expected event topology; Section 4.2 details the choice of the L0 and L1 trigger mask for tagged neutrino events; Section 4.3 describes the MC simulation used to build a signal selection, to assess the offline selection acceptances, and to assess the systematic uncertainties. The description of the offline event selection is presented in Section 4.4, and the background assessment is described in Section 4.5, followed by the estimate of the necessary trigger efficiencies in Section 4.6. Finally, an estimate of the event yield is presented in Section 4.7, and the observed signal candidates are presented in Section 4.8.

4.1. Tagging at NA62

NA62 high intensity kaon beam and its detectors can be exploited to demonstrate the feasibility of the neutrino tagging technique. Indeed, as the K^+'s dominantly decay as $K^+ \to \mu^+\nu_\mu$(called $K\mu\nu$ in the following), they naturally produce a neutrino beam. The mean energy of these neutrinos is about 40 GeV. At these energies, the probability for a neutrino to interact in the 20 tons of krypton contained in the LKr electromagnetic calorimeter is:

$$\begin{aligned} P &= \frac{M^{\mathrm{Kr}}}{m_m^{\mathrm{Kr}}} \times \mathcal{N}_A \times A_{\mathrm{Kr}} \times E \times \sigma \times \frac{1}{\mathcal{S}_{\mathrm{LKr}}} \\ &= \frac{16.24 \cdot 10^6\ g}{84\ g/mol} \times 6 \cdot 10^{23}\ mol^{-1} \times 84\ \times 40\ GeV \times 0.68 \cdot 10^{-38}\ cm^2/GeV \times \frac{1}{5.3 \cdot 10^4\ cm^2} \\ P &= 5.0 \cdot 10^{-11}, \end{aligned} \tag{4.1}$$

where: M^{Kr} is the active volume mass of the LKr calorimeter, m_m^{Kr} is the molar mass of the Krypton, $\mathcal{N}_A$ is the Avogadro number, A_{Kr} is the number of nucleons in a Krypton atom, E is the interacting neutrino energy in GeV, σ is the interaction cross-section and $\mathcal{S}_{LKr}$ the surface of the active region of the LKr calorimeter. Such interaction probability is of the same order of magnitude than the measured branching fraction of the $K^+ \to \pi^+\nu\overline{\nu}$ decay [82]. The analysis of the $K^+ \to \mu^+\nu_\mu$ decay with interacting neutrino (denoted as $K\mu\nu*$ in the following) hence requires a similar number of K^+ decays and background rejection as the $K^+ \to \pi^+\nu\overline{\nu}$ analysis.
Given the annual collected K^+ decays at NA62, $\mathcal{O}(10^{12})$, few hundred of neutrino interactions could be observed at NA62. To demonstrate the feasibility of the tagging technique, these interactions could individually be associated with their tagged neutrino obtained from the $K\mu\nu$ decay kinematically reconstructed using the GTK and STRAW.
In the energy range of NA62, the neutrino cross-section is dominated by the deep inelastic scattering (DIS) process, as shown in Figure 1.3a. In this regime, the identification of NC interaction at the trigger level is not possible, as their experimental signature only consists of a hadronic shower in the LKr[56]. However, the neutrino CC interaction induces the production of a hadronic shower and of a charged lepton of corresponding flavour (μ^-) in the DIS process, as shown in the diagram in Figure 1.4 [51]. The presence of both a hadronic shower in LKr and of a μ^- in the final state can efficiently be exploited in a trigger

strategy including the MUV3. For such a strategy to work, the μ^- created in the neutrino interaction must be inside the MUV3 geometrical acceptance.

4.1.1. Event topology

The signature of the $K\mu\nu$ decay for which the neutrino interacted is a single muon track up to LKr, with a hadronic shower appearing in LKr and MUVs at positions consistent with the neutrino extrapolated one, and two well separated muons in the MUV3 detector, as shown in Figure 4.1. The signal events feature a squared missing mass m^2_{miss} compatible with 0, where $m^2_{\text{miss}} = (P_K - P_{\mu^+})^2$, and P_K and P_{μ^+} are the 4-momenta of the K^+ and of the μ^+. Moreover, the signal events are expected to feature small values of the distance between the LKr cluster associated to the neutrino interaction and the neutrino extrapolated position at the LKr front plane, denoted $d_{\text{LKr}\nu}$. Backgroud events are expected to originate from two sources. The first background source consists of $K\mu\nu$ with extra accidental activity in the LKr, MUV1/2, and MUV3, called in the following *overlaid* $K\mu\nu$. The second background source consists of other K^+ decays (such as $K^+ \to \pi^+\pi^0$ and $K^+ \to \pi^+\pi^+\pi^-$) with activity in the calorimeters and in MUV3, and with one of the final state particles incorrectly identified as a μ^+. Such background is referred to in the following as *mis-reconstructed* K^+ *decays*.

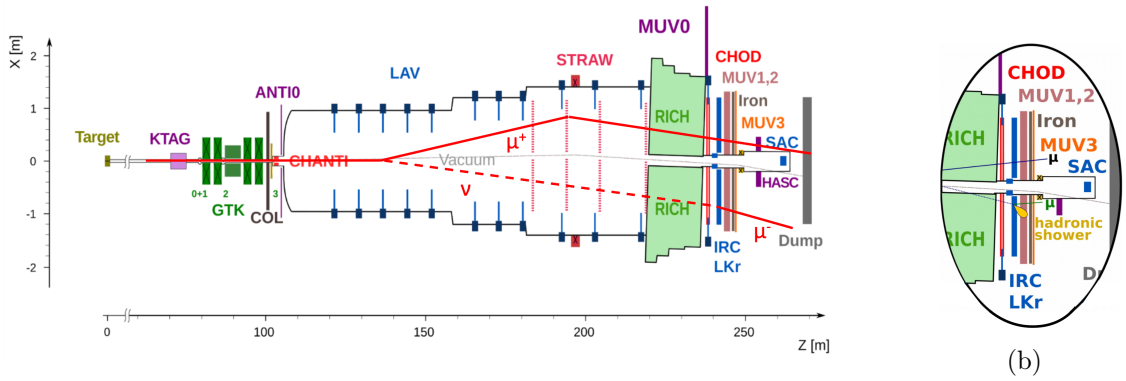

(a) (b)

Figure 4.1.: The $K\mu\nu$ with tagged neutrino decay outline overlaid with the NA62 experiment's schematic top view (4.1a) and a zoom on the downstream subdetectors that contribute to detect the neutrino interaction (4.1b).

4.1.2. Analysis strategy

The signal event topology allows defining regions of the phase space dominantly populated by signal or background. The event selection is optimized using data in the background regions and simulated signal data. The content of signal region for data is kept blind during the analysis development to avoid any potential bias.
The signal region is defined as $|m^2_{\text{miss}}| < 0.006\,\text{GeV}^2/\text{c}^4$ and $d_{\text{LKr}\nu} < 60\,\text{mm}$. The first criteria ensure that the candidates are indeed $K\mu\nu$ decays and the second one imposes that

the energy deposition in the LKr originates from the interaction of the neutrino from the $K\mu\nu*$ process. The size of the signal region is chosen to match the experimental resolution on these two parameters. The distribution of these parameters for the simulated signal is shown in Figure 4.2.

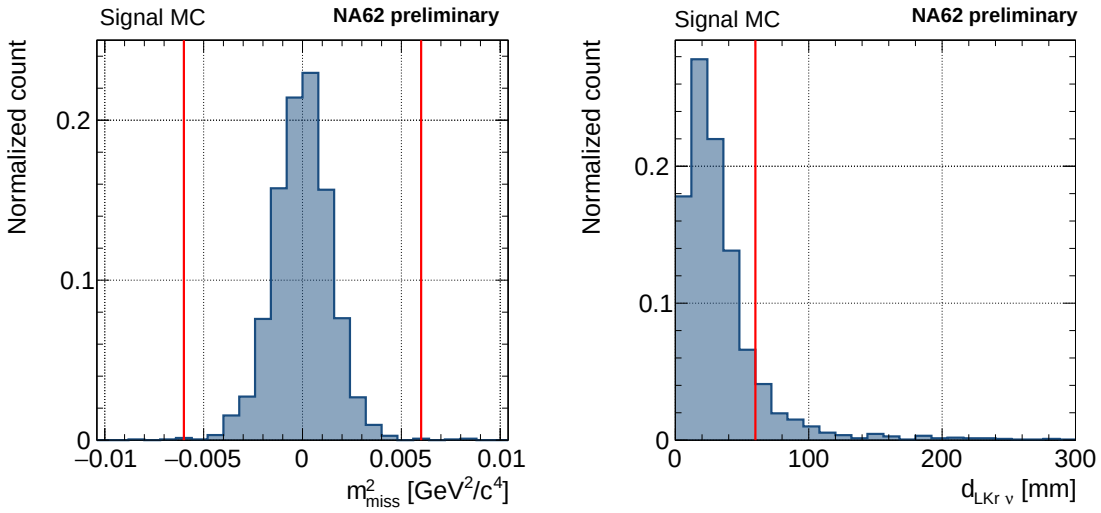

(a) (b)

Figure 4.2.: Distribution of m^2_{miss} (4.2a) and of $d_{\text{LKr}\nu}$ (4.2b) for the simulated signal. The red solid lines represent the cuts separating the signal region from the control region.

The background originating from overlaid $K\mu\nu$ decays is studied in the m^2_{miss} signal region but on the side bands of the $d_{\text{LKr}\nu}$ signal region, while the background originating from mis-reconstructed kaon decays is studied on the side bands of the m^2_{miss} signal region. The background pollution in the signal region is assessed using a data-driven method separately for the two background sources.
The number of expected tagged neutrino events can be estimated thanks to the following elements:

- the number of effective K^+ decays in a given fiducial region, N_K
- the branching fraction of the $K\mu\nu$ decay, $\mathcal{B}(K^+ \to \mu^+\nu_\mu)$
- the interaction probability for a neutrino of a given energy to interact in the LKr, $P_{\text{int,LKr}}$
- the efficiency to detect and reconstruct a tagged neutrino event, $\epsilon_{K\mu\nu*}$.

The number of expected tagged events in a given fiducial region can hence be written as:

$$N^{exp}_{K\mu\nu*} = N_K \cdot \mathcal{B}(K^+ \to \mu^+\nu_\mu) \cdot P_{\text{int,LKr}} \cdot \epsilon_{K\mu\nu*} \tag{4.2}$$

The efficiency $\epsilon_{K\mu\nu*}$ takes into account several effects, such as geometric and kinematic acceptances, and selection criteria to identify the tagged $K\mu\nu$ decay. The interaction

probability $P_{\text{int,LKr}}$, that can be calculated with the simple computation in Equation 4.1, or can be estimated more precisely thanks to simulations.
A sample of standard $K\mu\nu$ decays, called normalization sample, provides an estimate for the number of total effective K^+ decays (N_K) in a given fiducial region:

$$N_K = \frac{N_{K\mu\nu}}{\epsilon_{K\mu\nu} \cdot \mathcal{B}(K^+ \to \mu^+\nu_\mu)}, \tag{4.3}$$

where $N_{K\mu\nu}$ is the number of $K\mu\nu$ normalization events in the chosen fiducial region, $\epsilon_{K\mu\nu}$ is the efficiency to select the normalization $K\mu\nu$ events, and $\mathcal{B}(K^+ \to \mu^+\nu_\mu)$ is the branching fraction of the $K\mu\nu$ decay. The signal and normalization sample can be selected using the same criteria (common selection) up to the point where the topology of the normalization and signal events diverge due to the neutrino interaction. This strategy allows to cancel out may common terms of Equation 4.2, obtaining a simpler equation with fewer items to be estimated, as will be shown later.

4.2. Data sets, trigger and data filtering

Data has been collected using a dedicated trigger line, called `mask10`, which has been commissioned and deployed since 2018. The hardware trigger (L0), contains logical signals from RICH, CHOD, NA48CHOD, LKr, MUV3; a software trigger (L1) exploits information from KTAG, LAV and STRAW reconstruction to reduce and select the data before writing them to disk [82]. The data set analyzed has been collected during the 2022 data taking, precisely from run number 011923 to run number 012578.

4.2.1. Signal trigger and filtering

The neutrino L0 trigger definition requires a RICH signal compatible with a single μ^+. The time of the RICH signal, called trigger time, is used as reference to define coincidence time windows of 6.25 ns in NA48-CHOD, CHOD, MUV3 and LKr. The current L0 definition of mask10 is: `!RICH16-UTMC-!Q2-MOQX-E5`, where:

- `!RICH16` requires RICH signal that fires less than 16 supercells (which are groups of 8 adjacent PMs) [81];
- `UTMC` requires a signal in less than five CHOD tiles;
- `!Q2` requires no signals in opposite CHOD quadrants, to suppress background coming from $K^+ \to \pi^+\pi^+\pi^-$ decays [82];
- `MOQX` requires at least two candidates in outer opposite quadrants in MUV3;
- `E5` requires more than 5 GeV energy deposit in LKr, without constraints on the number of clusters.

At L1, three algorithms, `KTAG5`, `!LAV` and `STRAW_1TRK`, are sequentially applied, where,

- `KTAG5` requires that more than four KTAG sectors have at least one detected Cherenkov photon within 5 ns of the L0 trigger time;
- `!LAV` requires less than 3 hits in LAV stations 2 to 11 within 6 ns of the L0 trigger time;
- `STRAW_1TRK` requires at least one STRAW track corresponding to a positively charged particle with momentum below 65 GeV/c, forming a vertex between 100 m and 180 m from the primary target in the z direction, with a closest distance of approach (CDA) between the downstream track and the beam track smaller than 200 mm.

The definition of `mask10` has changed through the years; the definition of mask10 in the analysed period is stable. The trigger rates during the 2022 data taking are 11 kHz after L0 trigger, and 3 kHz after L1 trigger for the nominal beam intensity of 3.5 10^{11} POT on T10. Data is further reduced by a filter, called Muon Neutrino (`MUONNU`) filter, which enforces the MUV3 trigger condition, demanding that, for at least one pair of MUV3 candidates, the product between the two x coordinates and the product of the two y coordinates of the two signals are both negative. Furthermore, the time difference between the MUV3 reconstructed candidates is required to be smaller than 2 ns. No downscaling is applied neither to this trigger mask nor to the filtering. The first few runs of 2022 are not used for the scope of this analysis, as the L0 trigger definition did not have the correct LKr L0 trigger condition. The instantaneous beam intensity, obtained by measuring the GTK signal rate for each event, for the analyzed runs, is shown in Figure 4.3.

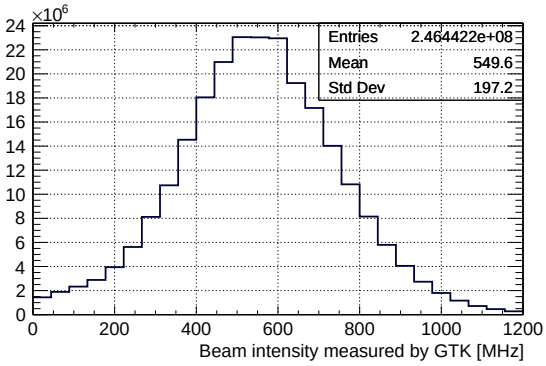

Figure 4.3.: Instantaneous beam intensity measured by the GTK.

4.2.2. Normalization trigger and filtering

The normalization sample is obtained from minimum-bias data. The minimum-bias trigger (called `mask2`) is based on RICH and CHOD information downscaled by a factor of 600. Its L0 definition is `RICH-Q1`. Data used for normalization are further reduced by a filter, called Restricted Muon (`RESMU`) filter, that selects events recorded with the control (just NA48-CHOD information) or `mask2` trigger, that have positively charged tracks in STRAW and

LKr acceptance, satisfying minimal geometric and kinematic criteria and with a spatially associated MUV3 candidate. In addition, in order to have the signal and normalization channels selections as similar as possible, three extra L0 conditions from `mask10` (`!RICH16, !Q2, UTMC`), are required offline for normalization events.
The number of bursts processed is shown as a function of the Run number ID in Figure 4.4a. For one run (12575), the number of `MUONNU` processed bursts exceeds the number of `RESMU` processed bursts by 150 bursts. The number of normalization events is under-estimated by a factor $\sim 0.046\%$.

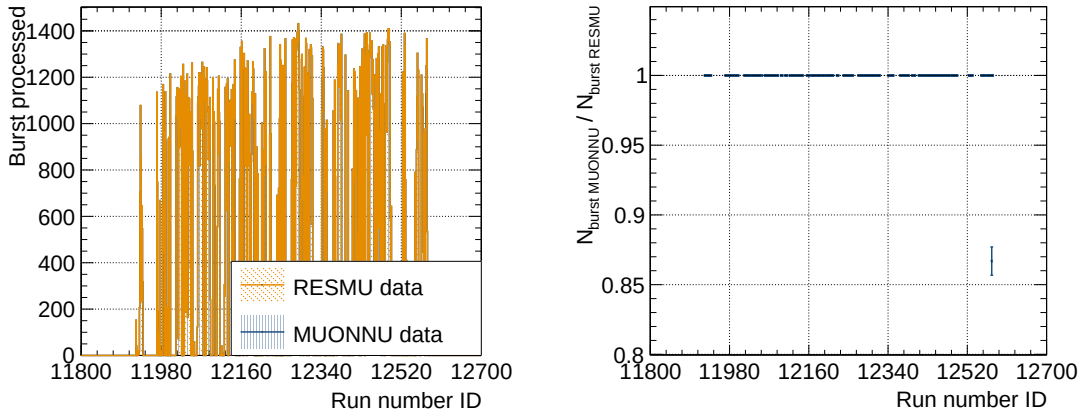

(a) (b)

Figure 4.4.: 4.4a: Number of processed bursts per run for `RESMU` data and `MUONNU` data. 4.4b: Ratio between the number of bursts per run processed for `MUONNU` data and for `RESMU` data.

4.3. Monte Carlo simulation

A Monte Carlo simulation of the signal events has been used to estimate the selection acceptance. The native NA62MC package is based on GEANT4 which is not able to simulate neutrino interactions. NA62MC was thus interfaced with GENIE v3.02.00 [18] which is among the reference software to simulate neutrino interactions. A simplified detector geometry is produced based on the one available in NA62. This geometry contains only the Kr volume. The neutrino cross-section on Kr atoms has been computed for the purpose of this analysis by the GENIE collaboration using flavour `G18_10a_02_11b`. The CC interaction processes considered are quasi-elastic (including charm and lambda production), resonant and deep inelastic (including charm production).
The simulation follows the standard NA62 process, but when a neutrino is produced it is passed to GENIE. GENIE checks if the neutrino is in the LKr acceptance and, in that case, makes it interact using one of the process above-mentioned. It returns the interaction final state, generated using Pythia6, as well as the interaction probability computed based on the geometry and cross-section. The final state particles are collected and passed back to GEANT4 for their subsequent tracking in the detector volume. The interaction probability

is stored in the event weight. The interfacing of NA62MC with GENIE was performed using NA62MC v3.1.7. As a result, the software only allows simulating data taken in Run1 conditions. The main consequence of this feature for this data analysis is that during Run 1 the number of GTK stations was 3 instead of 4.
A MC sample containing $50 \cdot 10^3$ K^+'s was produced in which the K^+'s are forced to decay in μ^+ and in ν_μ in the decay volume (102.425 – 180.0 m from the target). The distribution of the event weight (i.e. interaction probability) is shown in Figure 4.5a. Note that the mean interaction probability, for the events in which the neutrino is inside the LKr acceptance, is about $7 \cdot 10^{-11}$ which is compatible with the simple estimate provided in Equation 4.1. The neutrino interaction z coordinate from the Monte Carlo is shown in Figure 4.5b.
Out of the $50 \cdot 10^3$ K^+'s, 1.7% do not decay, because they undergo scattering in KTAG and in GTK, which causes them to exit the beam pipe. Out of the K^+ that decay, 86% decay in the fiducial volume defined for $105m < Z_{end} < 180m$, where Z_{end} is the Z coordinate of the true end position from the primary target, provided by the MC. In 20% of events out of the K^+ that decay in the fiducial volume, the ν_μ originating from the decay are outside the LKr acceptance, as shown in Figure 4.6. Table 4.1 summarizes the event losses for the Monte Carlo sample, up to the first step of the offline selection.
Additional existing Monte Carlo samples have been used for background studies, which simulate overlaid $K^+ \to \pi^+\pi^0$ decays as well as $K^+ \to \pi^+\pi^+\pi^-$ decays, both from Run1 and Run2.

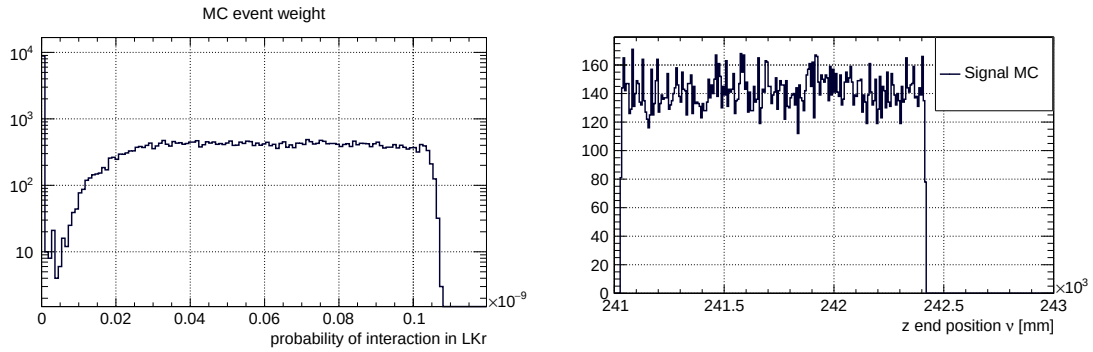

(a) (b)

Figure 4.5.: 4.5a: Event weight distribution of the Monte Carlo sample in log scale. 4.5b: True end position z coordinate of the Monte Carlo events.

Type of event	Event fraction
K^+ decays	98%
K^+ decays in FV	86%
with interacting ν in LKr	80%

Table 4.1.: Event loss for MC for basic requirements. The events fractions are estimated with respect to the number of events satisfying the previous condition.

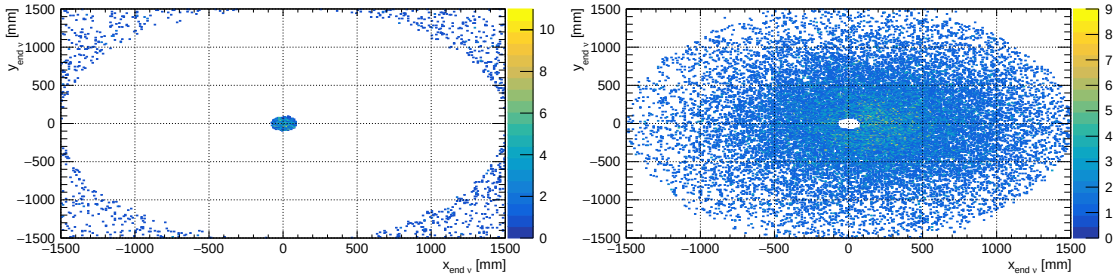

(a) (b)

Figure 4.6.: True neutrino position at LKr front plane for events with weight = 0 (4.6a) and for events with weight $\neq 0$ (4.6b).

4.4. Event selection

This section is dedicated to the description of the signal and normalization selections. A qualitative description of the selection and its logic is presented, followed by a fully detailed description of all applied criteria.
The signal and normalization selections have been built following a PNN-like signal selection. The first step in the offline selection consists in a preselection that enforces some quality criteria on data, associates the STRAW tracks to activity in the downstream detectors, and matches it to a parent K^+ reconstructed by the GTK and the KTAG. The details of the preselection and of the single track kaon decay are specified in Appendix B.
After this preselection, the event selection is divided in two stages: a selection common to signal and normalization, called in the following "common selection" and abbreviated CS, followed by signal selection to identify the neutrino interaction. The analysis procedure for both signal and normalization is shown in the flowchart in Figure 4.7. The details of the selection criteria established in the common $K\mu\nu$ selection and in the neutrino interaction selection are specified respectively in Section 4.4.1 and in Section 4.4.2. A schematic representation of the whole signal selection is shown in Figure 4.8.

4.4.1. Common selection

The common selection for $K\mu\nu$ decays, that is represented by the second gray square in the flowchart in Figure 4.7, requires the identification of the downstream charged particle as a μ^+. The μ^+ must be inside the downstream detector acceptance, and not too close to the beam pipe. In addition, the neutrino, reconstructed using the decay kinematics (in particular, measuring the muon and the kaon 4-momenta), is required to be in the LKr acceptance, not too close from the beam pipe and well separated from the μ^+. The details of the selection criteria performed are detailed in Section 4.4.1.1.

4.4.1.1. Single muon track identification

Charged kaons decaying into muons are already selected at trigger level, by requiring at least two muons within the trigger time window in outer opposite quadrants in MUV3.

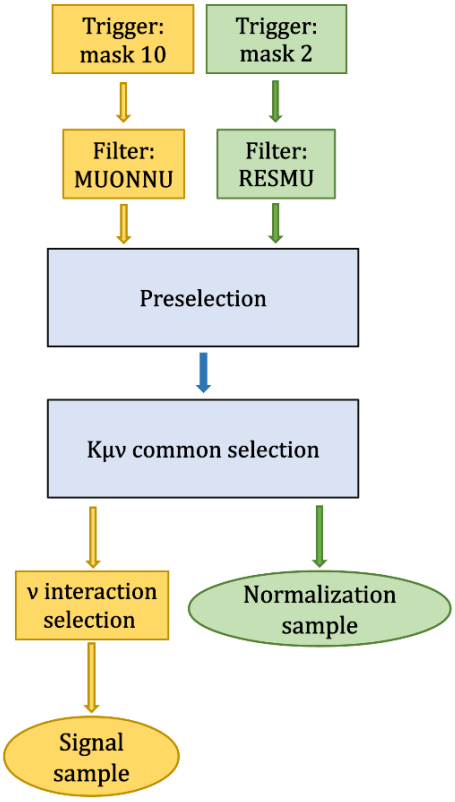

Figure 4.7.: Flowchart of the analysis pipeline for signal and normalization samples.

However, some further requirements, described in this section, are applied in the offline selection to reinforce the muon identification. An event with a single muon track must satisfy the following criteria:

- the z coordinate of the reconstructed decay vertex, defined as the mid-point between the beam and downstream track at the closest distance of approach, must fall inside the fiducial volume defined in $105m < Z_{vtx} < 180m$,
- STRAW multiplicity rejection based on the identification of events with STRAW hits compatible with partial (not reconstructed) muon tracks originating from the decay vertex (called *segments*),
- closest distance of approach (CDA) between the downstream track and the beam track reconstructed by GTK and KTAG must be $< 4\,\text{mm}$,
- the μ^+ track momentum must be smaller than $65\,\text{GeV/c}$,
- exactly one candidate in NA48CHOD within 6 ns of the RICH track time,
- exactly one candidate in CHOD within 6 ns of the RICH track time,
- track extrapolated position matched to a LKr cluster or cell candidate,

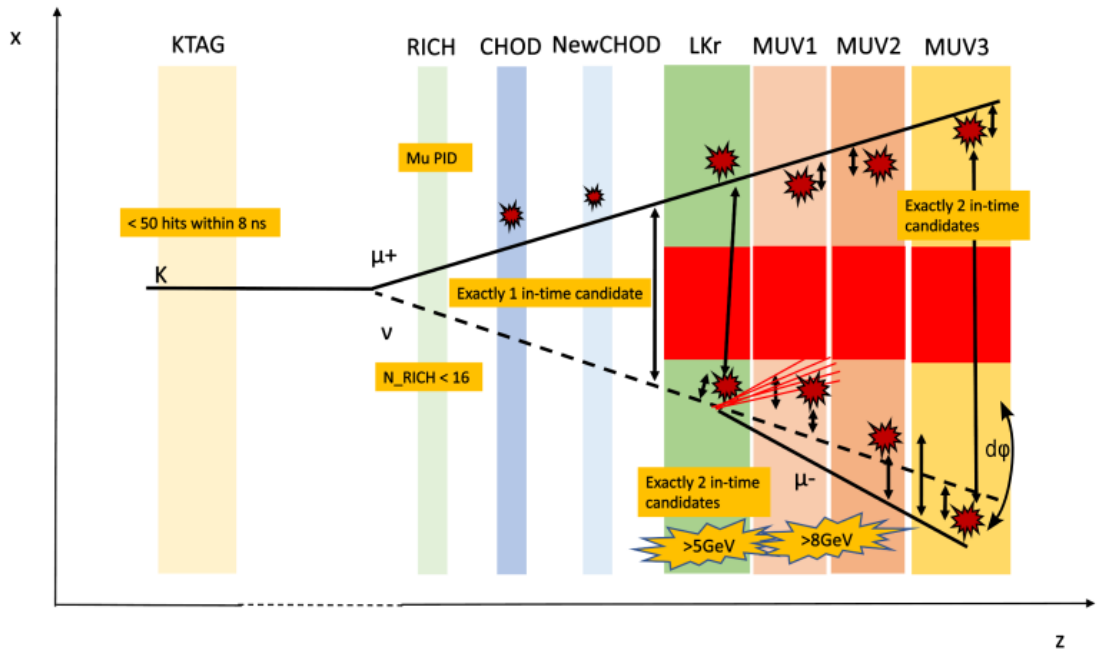

Figure 4.8.: Not-to-scale schematic representation of the signal selection in the main detectors used in the analysis, from the top view of the experiment.

- at least one geometrically associated MUV3 candidate in-time within 7 ns of the RICH track time,
- time difference between RICH and KTAG time $\Delta T(RICH - KTAG) < 0.5$ ns,
- time difference between GTK and KTAG time $\Delta T(GTK - KTAG) < 0.5$ ns,
- time difference between RICH and GTK time $\Delta T(RICH - GTK) < 0.5$ ns,
- rejection of events with candidates in SAC, IRC, SAV in the full event time window,
- rejection of events with any activity downstream the vertex z coordinate within 3 ns from the RICH trigger time in the LAVs,
- hit multiplicity rejection combining in-time activity in CHOD, NA48CHOD and LKr. The details of the algorithm performing the hit multiplicity rejection are given in Appendix C;
- satisfy the RICH μ^+ PID criteria:
  - RICH most likely hypothesis, that returns the particle specie that is more probable to belong to the track crossing the RICH,
  - the particle mass, computed thanks to the RICH using the Cherenkov angle, must be 0.08 GeV $< m_{RICH} <$ 0.125 GeV ;
- rejection of events with more than 5 GTK tracks, within 0.6 ns of the RICH track time,

- time and spatial match in both MUV1 and MUV2:
  - at least one MUV1 and at least one MUV2 candidate must be found within 10 ns of the RICH track time;
  - separation between the muon extrapolated position at MUV1 and its closest associated candidate must be < 100 mm;
  - separation between the muon extrapolated position at MUV2 and its closest associated candidate must be < 170 mm;
- distance between the neutrino extrapolated position and the muon track extrapolated position at the LKr plane larger than 200 mm,
- neutrino extrapolated position at LKr front plane in the LKr geometrical acceptance (octagon with apothem of 1130 mm),
- distance between the neutrino extrapolated position at LKr front plane and the center of the beam pipe larger than 250 mm,
- distance between the muon extrapolated position at LKr front plane and the center of the beam pipe larger than 250 mm,
- distance between the neutrino extrapolated position at MUV3 and the center of the beam pipe larger than 300 mm,
- distance between the muon extrapolated position at MUV3 and the center of the beam pipe larger than 300 mm,
- distance between the muon track position extrapolated at MUV3 and its associated MUV3 candidate smaller than 220 mm,

The μ^+ and the K^+ must then satisfy the squared missing mass condition discussed in Section 4.1.2: $|m^2_{miss}| < 0.006\,\mathrm{GeV}^2/\mathrm{c}^4$. Finally, to make the signal and normalization selection as similar are possible, the common selection requires a positive `Q1` L0 trigger condition (i.e. at least one hit in a CHOD tile) which is part of `mask2` but not `mask10`.

4.4.2. Signal selection

On top of this common selection, extra requirements aiming to identify the neutrino interaction are applied to selected the signal events. The signal selection, identified by the bottom yellow rectangle in Figure 4.7, proceeds through four steps, presented in the following.

4.4.2.1. Interaction association

The first step consists in matching the neutrino interaction activity in the relevant subdetectors. The activity from the neutrino is expected to appear in the LKr, where an energy deposit from the hadronic shower originating from the CC interaction of the neutrino with

the Kr nucleons is expected. The hadronic shower is expected to continue through the MUV1 hadronic calorimeter, leaving an energy deposit that sums with the MIP energy deposit of the positively charged muon from the kaon. The neutrino CC interaction also generates a negatively charged muon. The μ^- would be detected by the MUV3 detector and shall also leave a MIP energy deposit in MUV1 and MUV2. The offline signal selection hence requires, in addition to the μ^+ LKr cluster (see Sec.4.4.1.1), to have a LKr cluster matched to the neutrino in a time window of ± 6 ns with the μ^+ track RICH time.
The standard cluster reconstruction in LKr is performed by grouping cells within 110 mm from a seed, where a seed is a cell with at least 250 MeV deposited and an energy greater than the average energy of the 3x3 (5x5 in case of dead cells) surrounding cells. The energy of the cluster is the sum of the energy of the cells; the cluster time is the time of the seed; the position of the clusters is the barycenter of the cells weighted with the energy in the cells. As in this analysis the highest LKr efficiency is required, a second reconstruction algorithm is used when no standard cluster matches the μ^+, or the shower. In this reconstruction, energy depositions of at least 40 MeV are clustered geometrically by looking at adjacent cells, where two cells are defined adjacent if separated by less than 100 mm. The energy, time and position of clusters are defined as in the standard reconstruction [33]. Clusters from this latter reconstruction are referred to as "auxiliary clusters".
The signal selection imposes a constraint on the number of standard clusters in time with the μ^+ track in the LKr calorimeter. When both the μ^+ and the neutrino are matched to standard clusters in the LKr, the number of LKr standard clusters is constrained to be exactly two. If the μ^+ is matched to an auxiliary cluster and the neutrino candidate is found to be in the standard clusters, or vice versa, the number of standard clusters is constrained to be exactly one. If both the μ^+ and the neutrino associated clusters are matched to auxiliary clusters, it implies there were no standard clusters to match it to. This condition is proved very powerful in removing background originating mis-reconstructed K^+ decays and from overlaid $K\mu\nu$. No condition is applied on the number of reconstructed auxiliary clusters.
The effect of this selection on the signal is studied with a simulation. The simulation shows that a neutrino interacting with an LKr nucleon can produce a shower that doesn't leave energy deposit in a continuous way. This type of event leads to a fragmented shower, resulting in more than one LKr cluster. Fragmented showers are more frequent for neutrinos interacting early in the LKr volume, as shown in Figure 4.9. The signal loss due to such effect is included in the signal acceptance. The constraint on a number of standard clusters is a source of random veto (see Section 4.7.2.2).
The selection further requires the neutrino interaction to have at least one matched candidate in the MUV1 and MUV2 calorimeters within 6 ns of the RICH track time. In addition, at MUV3, there must be one candidate matched to the μ^- from the neutrino. The selection hence requires having exactly 2 candidates in MUV3 (one from the μ^+ and one from the μ^-) within 7ns of the μ^+ track RICH time.
The details of the time and spatial matching in LKr, MUV1, MUV2, MUV3 are:

- separation of the LKr cluster associated to the neutrino and the μ^+ track extrapolated at the LKr front plane smaller than 200 mm,

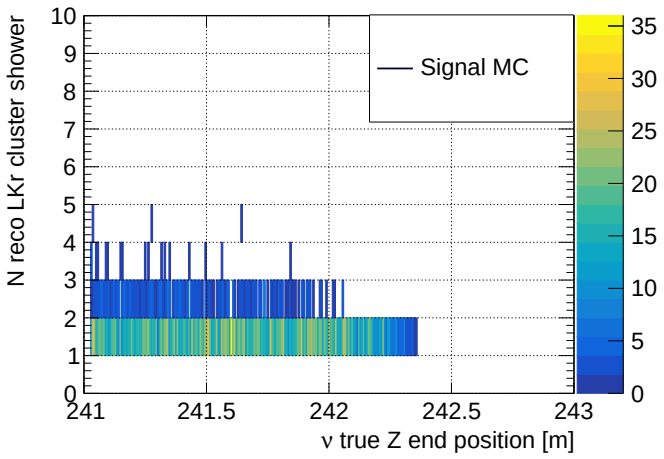

Figure 4.9.: Number of reconstructed LKr standard cluster associated to the hadronic shower as function of the z coordinate of the true interaction position, for shower candidates reconstructed by the standard LKr reconstruction.

- time difference between the muon and the neutrino LKr clusters smaller than 6 ns,
- time difference between the neutrino associated LKr cluster and the muon RICH time smaller than 6 ns,
- distance between the neutrino associated LKr cluster and the extrapolated neutrino position at the front LKr plane smaller than 60 mm (Figure 4.2b),
- distance between the neutrino associated MUV1 candidate and the extrapolated neutrino position at the front MUV1 plane smaller than 350 mm,
- distance between the neutrino associated MUV2 candidate and the extrapolated neutrino position at the MUV2 front plane smaller than 700 mm,
- distance between the two μ^+ and μ^- MUV3 candidates larger than 440 mm,
- μ^+ and μ^- MUV3 candidates in opposite outer quadrants of the detector,
- time difference between the μ^+ and μ^- MUV3 candidates smaller than 2 ns.

4.4.2.2. Extra activity rejection

The signal selection also enforces conditions to veto background from K^+ and π^+ decaying late in the beam line, in-time with the $K\mu\nu$ event. Such background sources are likely to leave some energy deposit in the inner parts of the LKr and MUVs calorimeters. For this reason, events are vetoed if they feature the presence of activity in-time with the μ^+ track in the inner regions of the LKr, MUV1 and MUV2 calorimeters. The inner regions of the three calorimeters are defined as:

- a radius from the beam center smaller than 250 mm for LKr,

- a radius from the beam center smaller than 200 mm for MUV1,
- a radius from the beam center smaller than 300 mm for MUV2.

In addition, an upstream veto condition is applied to KTAG, to reduce the number of events that may contain more than one K^+ decay. The distribution of the number of KTAG hits, shown for normalization events in Figure 4.10, features 3 peaks, corresponding respectively to one, two and three kaons detected in KTAG. The average number of hits per K^+ is 20. The number of KTAG hits, in a time window of 8 ns from the track RICH time, is constrained to be smaller than 50. Such veto causes a 4% signal loss, estimated using the normalization sample, as quantified in Section 4.7.2.2. The distribution of the number of KTAG hits can be fitted with three Gaussians, corresponding to the three components of the distribution. The integral of each of these distributions between 0 and 50 allows estimating the percentage of selected events with one, two or three K^+'s:

- 6% events with 3 K^+'s,
- 28% events with 2 K^+'s,
- 66% events with 1 K^+.

Despite 35% of the events have more than one K^+, the percentage of events in which more than one K^+ decay is only about 3.5%, as on average only 10% of the K^+'s decay in the fiducial volume.
The extra activity rejection conditions introduce some random veto that are estimated with a data-driven method (see Section 4.7.2.2), as the Monte Carlo signal simulation features clean events without overlay with background sources.

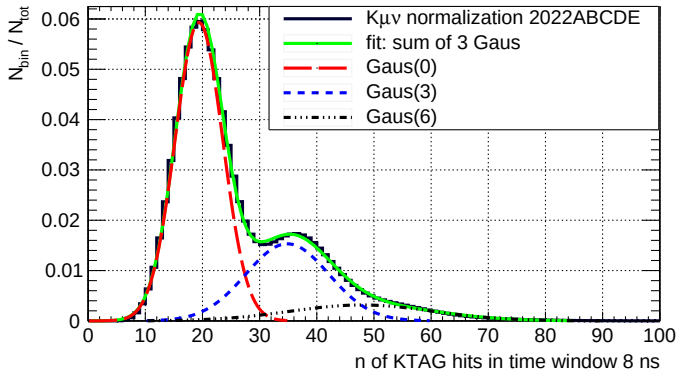

Figure 4.10.: Normalized distribution of number of KTAG hits within 8ns from the track RICH time for normalization $K\mu\nu$. The distribution is fitted with the sum of three Gaussian (green continuous curve). The three curves are also shown separately, with the dashed red, blue and black lines.

4.4.2.3. Interaction energy requirements

The neutrino interaction is identified using the energy deposit from the hadronic shower in the calorimeters. For this reason, some additional requirements constrain the signal in the calorimeters:

- the sum of the energy deposits from the μ^+ and the shower LKr cluster associated to the neutrino interaction must be larger or equal than 5 GeV (complementing the E5 trigger condition),
- a total in-time energy deposit of at least 8 GeV must be observed in the MUV1 and MUV2 together,
- the sum of the energies of the LKr, MUV1 and MUV2 candidates matched to the neutrino has to be smaller or equal to the neutrino energy reconstructed from the K^+ decay.

In addition, simulation shows that, for signal events, the interaction products release only a small part of their energy in the MUV2 calorimeter. Indeed, as the hadronic shower starts in the LKr, it runs out before reaching the MUV2 calorimeter. Hence, the only interaction product that survives up to MUV2 is the μ^-. The energy deposit associated to the neutrino interaction in MUV2 is thus only a MIP and is nearly always smaller than 10% of the total calorimetric energy deposit, as shown in Figure 4.12. The ratio between MUV2 energy deposit associated to the neutrino and the total energy deposit is thus required to be smaller than 0.1.
Finally, the ratio between the LKr reconstructed interaction energy and the neutrino energy, estimated from the K^+ decay, is required to be larger than 0.05 and smaller than 0.5. In order to be detected and trigger the LKr E5 condition, it is necessary for the neutrinos to deposit a portion of their energy in the LKr. However, this energy deposition in the LKr must not exceed 50% since it is crucial for the μ^- produced in the neutrino interaction to be sufficiently energetic to fall inside the MUV3 geometrical acceptance. Additionally, the shower shall leave some energy in the MUV1 calorimeter to pass the offline signal selection. Figure 4.11 shows the distribution of the ratio between the LKr reconstructed shower energy and the neutrino energy for signal MC and background from data side bands.

4.4.2.4. Interaction topology selection

The last part of the selection applies cuts related to the kinematics of the K^+ decay and neutrino interaction.
First, to ensure that the LKr and MUV1 shower candidates, and the MUV2 and MUV3 μ^- candidates associated to the interaction products of the neutrino are indeed coming from the same object, their transverse positions $(x_{\mathrm{LKr,MUV1,MUV2,MUV3}}, y_{\mathrm{LKr,MUV1,MUV2,MUV3}})$ have to be close to each other:

- $dr_{\mathrm{LKr-MUV1}} = \sqrt{(x_{\mathrm{LKr}} - x_{\mathrm{MUV1}})^2 + (y_{\mathrm{LKr}} - y_{\mathrm{MUV1}})^2} < 350\,\mathrm{mm}$,
- $dr_{\mathrm{MUV2-MUV3}} = \sqrt{(x_{\mathrm{MUV2}} - x_{\mathrm{MUV3}})^2 + (y_{\mathrm{MUV2}} - y_{\mathrm{MUV3}})^2} < 500\,\mathrm{mm}$.

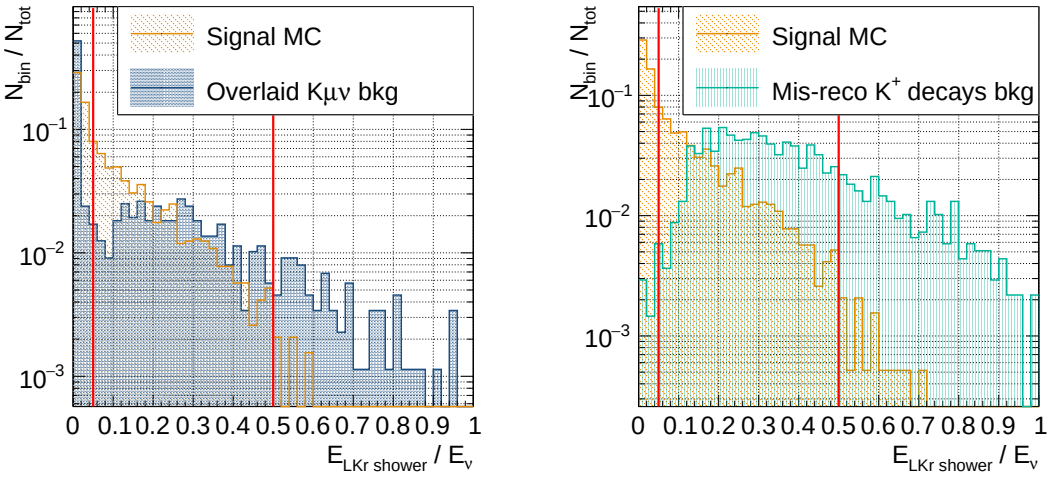

(a) (b)

Figure 4.11.: Normalized distribution of the ratio between the energy deposit in LKr and the kinematically reconstructed neutrino energy in logarithmic scale, for signal and background of overlaid $K\mu\nu$ (4.11a), and for signal and background of mis-reconstructed K^+ decays (4.11b). The red solid lines represent the cuts.

The distributions of $dr_{\mathrm{LKr-MUV1}}$ and $dr_{\mathrm{MUV1-MUV2}}$ are shown respectively in Figure 4.13 and in Figure 4.14 for signal and background.
In addition, the correlation between the interaction inelasticity, defined as the ratio between the μ^- and the initial neutrino energies, and the opening angle between the shower and the μ^- can be exploited to further reduce the background. Indeed, in CC interactions of a given neutrino energy, high energy μ^-'s tend to be produced more collinear to the neutrino direction than low energy ones. A proxy for this opening angle is the transverse distance between the MUV3 candidate associated to the μ^- and the extrapolated neutrino position at MUV3, dr_{MUV3}. The interaction inelasticity can be estimated as

$$\frac{E_{\mu^-}}{E_\nu} = \frac{E_\nu - E_{\mathrm{LKr}\nu} - E_{\mathrm{MUV1}\nu}}{E_\nu} \tag{4.4}$$

where $E_{\mathrm{LKr}\nu}$, $E_{\mathrm{MUV1}\nu}$ are the energies of the candidates associated to the hadronic shower in the calorimeters and E_ν the neutrino energy reconstructed from the decay kinematics. Figure 4.15 shows the variable $dr_{\mathrm{MUV3}\mu^-}$ as a function of the inelasticity of the interaction for both backgrounds (Figure 4.15a, Figure 4.15b) and signal from MC (Figure 4.15c). Thanks to the signal MC sample, it is possible to identify the signal region, shown in Figure 4.15c and identified by the two parallel lines:

- $dr_{MUV3\mu^-} > (800 - 880 \cdot E_{\mu^-}/E_\nu)\,\mathrm{mm}$
- $dr_{MUV3\mu^-} < (1300 - 880 \cdot E_{\mu^-}/E_\nu)\,\mathrm{mm}$

Furthermore, the neutrino and its interaction products, the hadronic shower and the μ^-, should belong to the same plane. Hence, in a cylindrical coordinates reference frame in

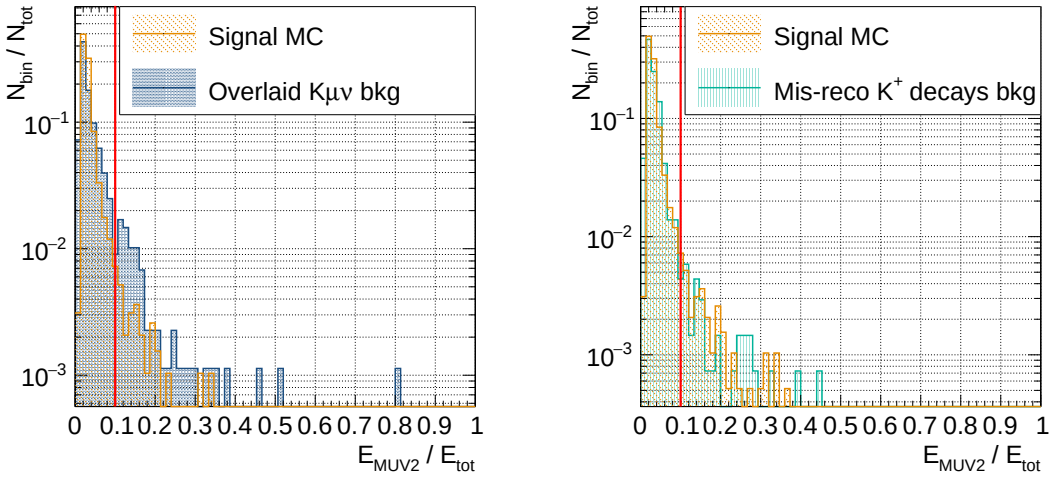

(a) (b)

Figure 4.12.: Normalized distribution of the ratio between the energy deposit in MUV2 and the total energy deposit associated to the neutrino interaction, in logarithmic scale, for signal (orange) and background of overlaid $K\mu\nu$ (4.12a) (blue), and for signal (orange) and background of mis-reconstructed K^+ decays (4.12b) (green). The red solid lines represent the cuts.

which the z axis corresponds to the neutrino direction, shown in the schematic in Figure 4.17, the azimuthal angle between the two candidates should be of π radians. This variable, called $d\phi_{LKr-MUV3}$, is shown for signal from simulations and for data in Figure 4.16, and is constrained in the signal selection to be larger than 1.7 radians and smaller than 4 radians. An additional condition is enforced to help reduce the background: if the x coordinate of the LKr candidate associated to the neutrino is negative, the neutrino candidate LKr radius must be larger than 250 mm. If the x coordinate of the LKr candidate associated to the neutrino is positive, then the x, y coordinates of the LKr candidate must follow a half-ellipse cut. The half ellipse has a major axis of 900 mm along x and a minor axis of 500 mm along y.

Indeed, events for which the μ^+ is emitted at large angle on the Salève side (x negative) are likely to be discarded, as the magnet (MPN33) further deviates the μ^+ on the Salève side, outside the LKr acceptance. The neutrinos corresponding to these events are emitted on the Jura side (x positive) and at low angle, as shown in Figure 4.19. Hence, this acceptance effect naturally induces a depletion in the neutrino spatial distribution at the LKr near the beam pipe on the Jura side. This depletion can be observed on MC signal in Figure 4.20c. The same distribution but for background events in shown in Figure 4.20a for background on the side bands of $d_{\mathrm{LKr}\nu}$ and in Figure 4.20b for background in the side bands of m^2_{miss}. A schematic of the neutrino interaction topology and of the variables used in the *interaction topology* selection is provided in Figure 4.18.

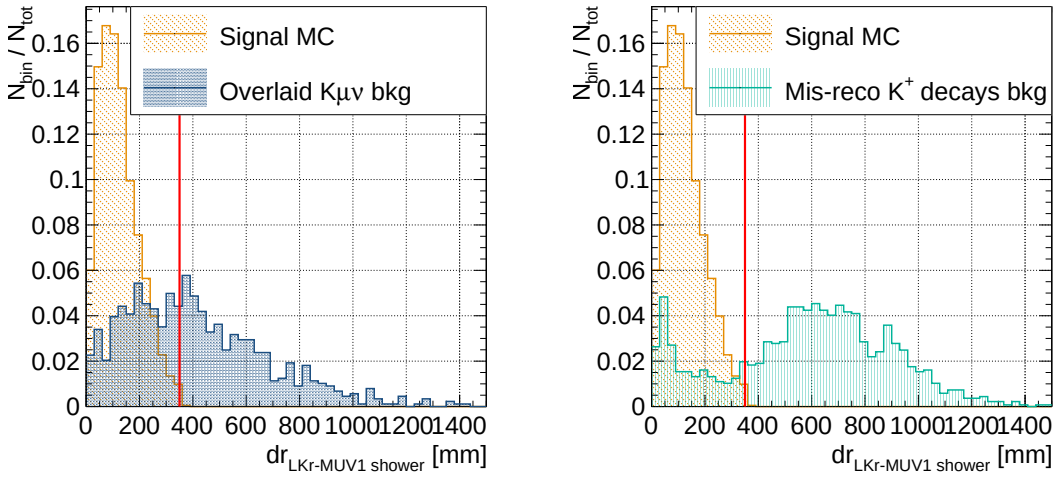

(a) (b)

Figure 4.13.: Normalized distribution of the distance between the x, y coordinates of the LKr closest cluster and the MUV1 closest candidate associated to the neutrino interaction for signal (orange) and background of overlaid $K\mu\nu$ (4.13a) (blue), and for signal (orange) and background of mis-reconstructed K^+ decays (4.13b) (green). The red solid lines represent the cuts.

4.4.3. Summary

The neutrino interaction selection acceptance, estimated on MC signal events, is 4.2% and is discussed in detail in Section 4.7.2.1. The acceptance budget contributions from the different steps in the signal selection are shown in Table 4.2 for signal from the MC, and for the two background sources: overlaid $K\mu\nu$ and mis-reconstructed K^+ decays, respectively on the entire ranges of $d_{\mathrm{LKr}\nu}$ and of m^2_{miss}.

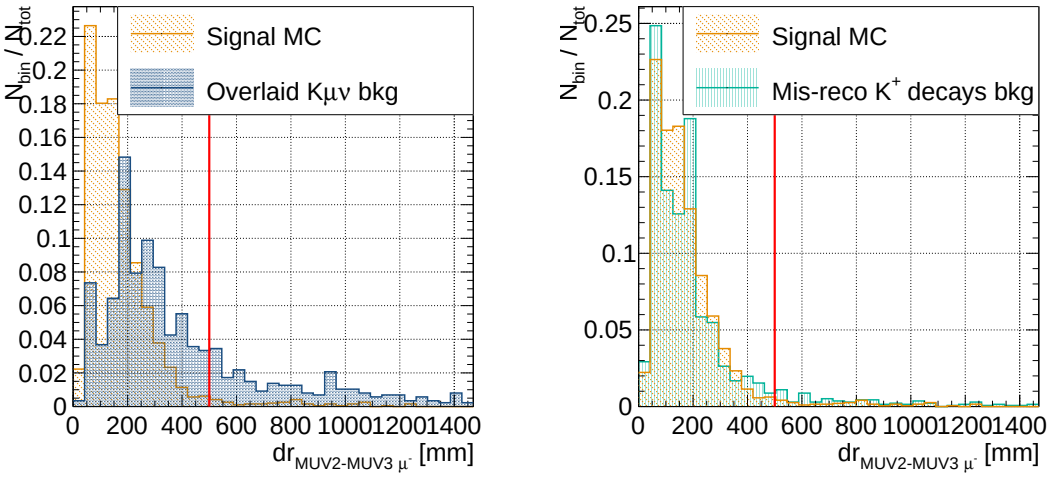

(a) (b)

Figure 4.14.: Normalized distribution of the distance between the x, y coordinates of the MUV2 closest candidate associated to the neutrino interaction and the MUV3 candidate associated to the μ^- for signal (orange) and background of overlaid $K\mu\nu$ (4.14a) (blue), and for signal (orange) and background of mis-reconstructed K^+ decays (4.14b) (green). The red solid lines represent the cuts.

Selection step	**Overlaid $K\mu\nu$ ϵ**	**Mis-reco K^+ decays ϵ**	**Signal acc**
Interaction association	0.05%	0.06%	28%
Extra activity rejection	44%	63%	93%
Energy requirements	23%	51%	30%
Interaction topology selection	1%	$< 0.2\%$	53%

Table 4.2.: Offline neutrino selection step efficiencies for background and MC acceptance for signal. The background suppression factors are computed on the full range of the sidebands of m^2_{miss} (for mis-recontructed K^+ decays) and of $d_{\text{LKr}\nu}$ (for overlaid $K\mu\nu$). *Caveat*: the values of background and signal are not to be directly compared, as the background data includes the trigger conditions, while the MC sample does not. For this reason, the interaction association acceptance (that contains the offline MOQX condition) and the energy requirements acceptance (that contains the E5 offline condition) are overestimated for background. Likewise, the extra activity rejection efficiency is not as meaningful for the signal, because the MC simulation features clean events with no overlay, and is hence not relevant for signal.

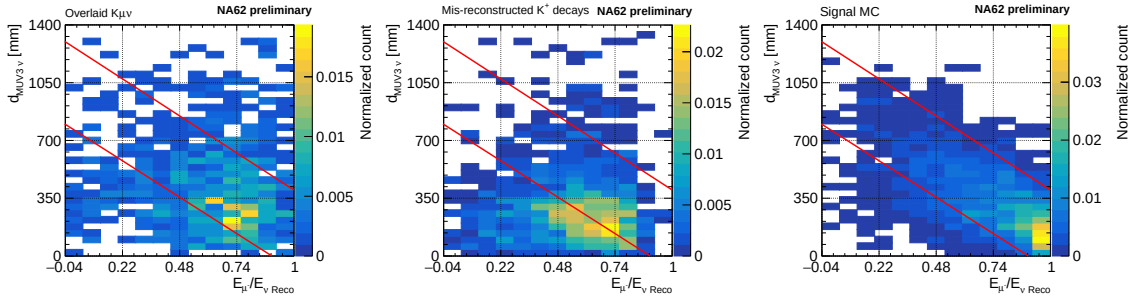

(a) (b) (c)

Figure 4.15.: Distance between the μ^- MUV3 candidate and the neutrino extrapolated position at MUV3 as function of the inelasticity of the interaction for background of overlaid $K\mu\nu$ (4.15a), for background mis-reconstructed K^+ decays without the $d_{\mathrm{LKr}\nu}$ cut (4.15b), and for MC signal events (4.15c). The red solid lines represent the cuts.

4.5. Background assessment

The background to the signal events is studied with a data driven method. The signal selection is applied on the entire 2022 data sample from run number 011923 to run number 012578, and background events in control regions are studied. An extrapolation of the expected number of background events in the signal region is then performed. As mentioned in Section 4.1.1, the most relevant features of the signal event topology are the squared missing mass and the distance between the reconstructed LKr cluster associated to the neutrino shower and the neutrino extrapolated position to the LKr front plane. The background pollution in the signal region is assessed separately for the two background sources.

4.5.1. Mis-reconstructed K^+ decays

The first background source are mis-reconstructed K^+ decays. This background is studied in the signal region m^2_{miss} side bands, $|m^2_{miss}| > 0.006\,\mathrm{GeV}^2/\mathrm{c}^4$. No data events are present in the side bands of the squared missing mass variable after applying the full selection.
In order to estimate the expected background pollution in the signal region, a quadratic fit in the m^2_{miss} side bands is performed on data in a control region; the fitted distribution is obtained by applying the selection on data up to the extra activity rejection (included), but excluding the $d_{\mathrm{LKr}\nu}$ cut from the Interaction association (see Table 4.2). The control region is defined by values of m^2_{miss} between -0.015 and $0.006\,\mathrm{GeV}^2/\mathrm{c}^4$ and between 0.006 and $0.03\,\mathrm{GeV}^2/\mathrm{c}^4$, and is represented by the blue rectangles in Figure 4.21. The distribution of these events and the quadratic fit is shown in Figure 4.22. By integrating the fitted function in the signal region, the extrapolated number of background events inside the $m^2_{\mathrm{miss}} < 0.006\,\mathrm{GeV}^2/\mathrm{c}^4$ range before applying further suppression is found to be $11.6 \pm 0.3_{stat}$. This number must be scaled by the acceptance of the remaining selection cuts, i.e. the $d_{\mathrm{LKr}\nu}$ cut, the energy requirements and the kinematics selection.
The acceptance of the energy requirements and kinematics selection is obtained on the

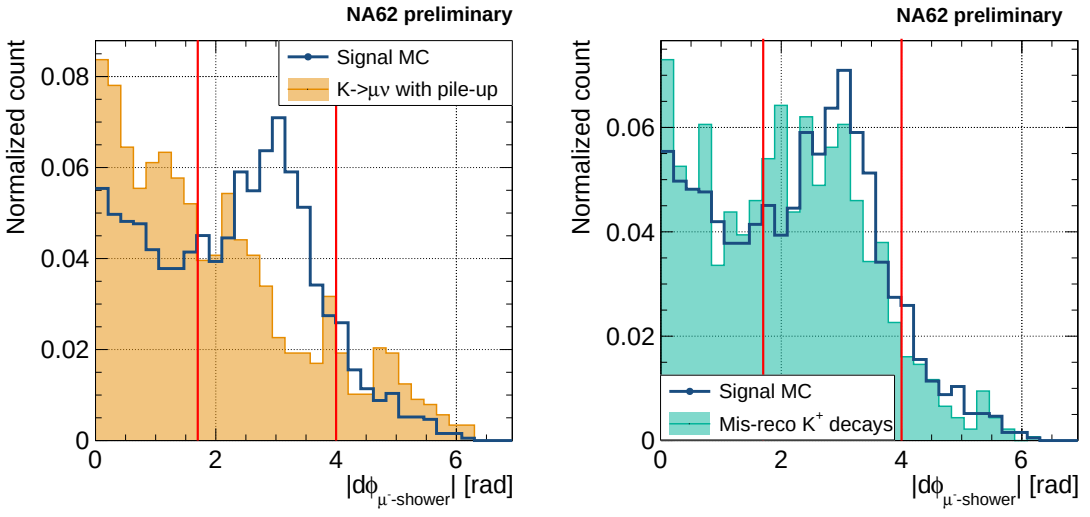

(a) (b)

Figure 4.16.: Normalized distributions of the variable $d\phi_{LKr-MUV3}$ for signal (blue line) and background of overlaid $K\mu\nu$ (4.16a) (orange fill), and for signal (blue line) and background of mis-reconstructed K^+ decays (4.16b) (green fill). The red solid lines represent the cuts.

m^2_{miss} side bands before applying the $d_{\text{LKr}\nu}$ cut and is found to be $(2.4 \pm 0.5_{stat})\%$. The distribution of events passing all the selection but the $d_{\text{LKr}\nu}$ cut is shown in 4.23b in the m^2_{miss} region.

The acceptance of the $d_{\text{LKr}\nu}$ cut is assumed to be independent of the other cuts, and thus is estimated before applying those cuts, on the m^2_{miss} side bands shown in Figure 4.23a. This assumption is verified by performing the quadratic fit of the m^2_{miss} plot on two different halves of the $d_{\text{LKr}\nu}$ range. The difference between the resulting integrals of the fits in the signal region performed on the two $d_{\text{LKr}\nu}$ slices, weighted by the number of entries in each of the two slices, is accounted for as a systematic uncertainty on the number of expected background events in the signal region. The $d_{\text{LKr}\nu}$ cut acceptance is found to be $(0.5 \pm 0.2_{stat})\%$.

The acceptance of the entire selection is thus the product of the $d_{\text{LKr}\nu}$ acceptance and the energy requirements and kinematics selection acceptance; the total number of background events is the product between the selection acceptance and the extrapolated number of background events inside the signal region before further suppression:

$$\mathbf{N^{exp}_{bkg}(Mis-reco\ K^+) = 0.0014 \pm 0.0007_{stat} \pm 0.0002_{syst}}.$$

An attempt to verify the background assessment has been performed by running the signal selection on MC samples simulating overlaid $K^+ \to \pi^+\pi^0$ decays and $K^+ \to \pi^+\pi^+\pi^-$ decays, from Run1 and Run2. The size of the MC samples is of $\mathcal{O}(10^8)$ events, and no events were found to survive the interaction association selection (see Section 4.4.2.1).

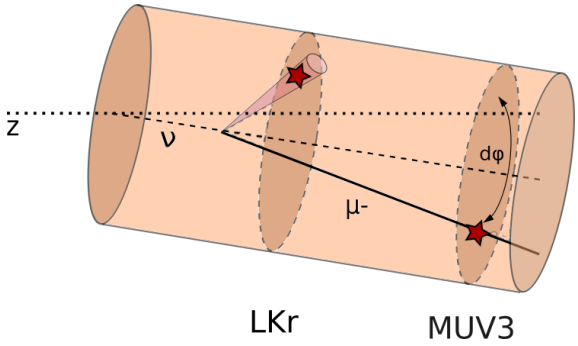

Figure 4.17.: Schematic of the implementation of the $d\phi_{LKr-MUV3}$ cut. The direction of the neutrino allows building a cylindrical coordinates reference frame in which the ν_μ direction is the z axis.

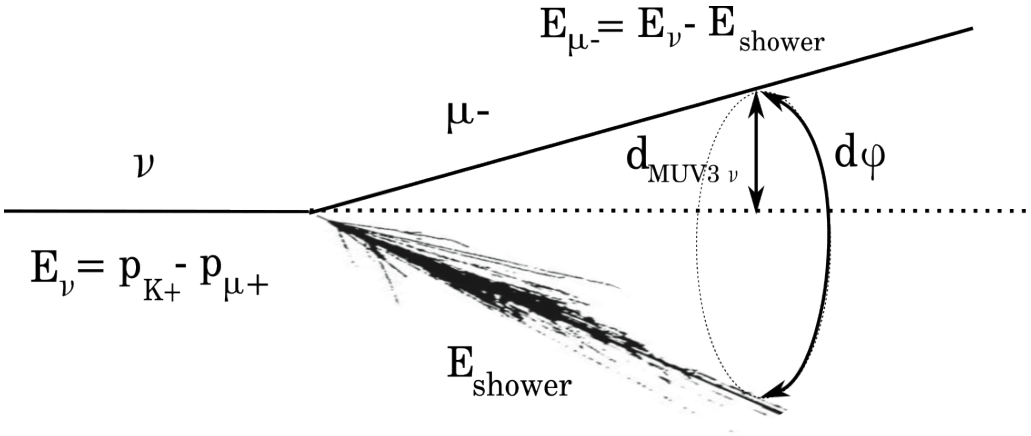

Figure 4.18.: Schematic of the interaction topology in the LKr, with all the variables concerned. The neutrino energy is derived from the momenta of the parent K^+ and of the charged daughter μ^+; the μ^- energy is derived subtracting the energy deposit from the hadronic shower to the neutrino energy. $d_{MUV3\mu^-}$ is the distance between the MUV3 μ^- candidate and the neutrino extrapolated position at MUV3.

4.5.2. Overlaid $K\mu\nu$

Another background source stems from genuine $K\mu\nu$ decays overlaid with accidental activity that mimics the activity associated to the neutrino interaction in the calorimeters. The second background region is hence defined in the $d_{\mathrm{LKr}\nu}$ side band of the signal region, $d_{\mathrm{LKr}\nu} > 60\,\mathrm{mm}$; the pollution from this background source is assessed in a control region defined by $d_{\mathrm{LKr}\nu}$ range [60, 300] mm. As the extra activity is unrelated to the $K\mu\nu$ decay, one can assume that the amount of background events scales with the surface over which the LKr cluster from the neutrino is searched. Hence, the $d_{\mathrm{LKr}\nu}$ distribution of the background events is expected to be proportional to $d_{\mathrm{LKr}\nu}$ (each $d_{\mathrm{LKr}\nu}$ bin corresponds to a ring of the search surface). A linear fit to the $d_{\mathrm{LKr}\nu}$ distribution in the control region can be thus used to estimate the expected background pollution in the signal region.
One background event survives the entire selection, and it falls outside the control region

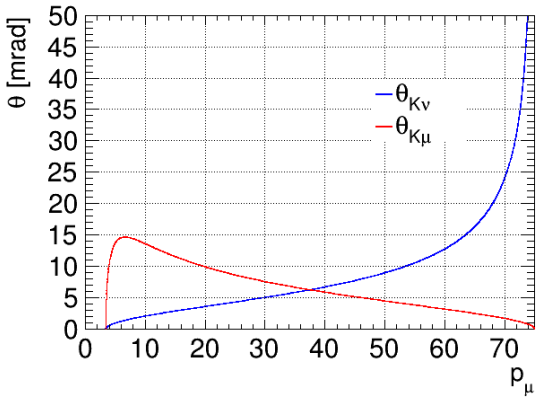

Figure 4.19.: Opening angle between the parent beam K^+ and the daughters μ^+ in red and ν_μ in blue, as function of the μ^+ momentum from a toy simulation.

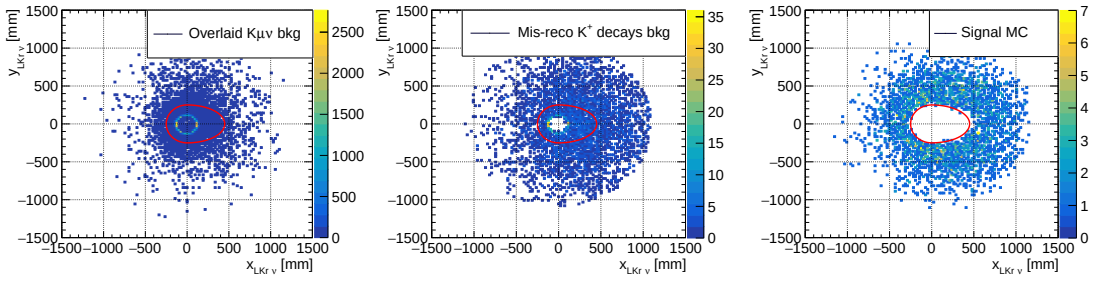

(a) (b) (c)

Figure 4.20.: x-y coordinates of the LKr cluster matched to the neutrino for background on the side band of $d_{\mathrm{LKr}\nu}$ (4.20a), for background on the side bands of m^2_{miss} (4.20b), and for MC signal events (4.20c). The cut removing the central part of the LKr for the cluster associated to the shower (a circle of radius 250 mm on the negative x side and a half-ellipse of major axis of 900 mm along x and minor axis of 500 mm along y) is shown as a solid red line.

as shown in Figure 4.24a. For this reason, a method similar to the one explained in Section 4.5.1 has been implemented to estimate the number of expected background events in the signal region. For this purpose, two cuts, uncorrelated with each other, have been removed from the selection: the $d\phi_{LKr-MUV3}$ cut and the $d_{MUV3\mu^-}$ cut. The distribution of the $d_{\mathrm{LKr}\nu}$ variable is shown in Figure 4.24b for the background events, in the side band of $d_{\mathrm{LKr}\nu}$, passing the signal selection except for the $d\phi_{LKr-MUV3}$ cut and the $d_{MUV3\mu^-}$ cut. Such distribution is fitted with a linear fit, also shown in Figure 4.24b. An extrapolation can be done to the signal region, and the integral of the fit function in the signal region returns $1.08 \pm 0.02_{stat} \pm 0.34_{syst}$ events. The systematic uncertainty reflects the difference of the integral values obtained by varying the fit range, using the range [60, 200] mm. The number of expected background events in the signal region can hence be derived by scaling the integral of the fit function in the signal region by the acceptances of the $d\phi_{LKr-MUV3}$

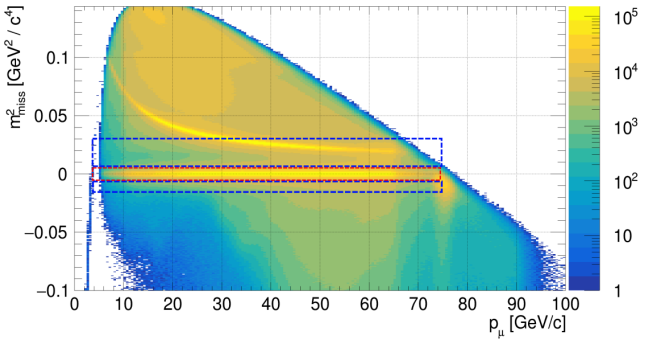

Figure 4.21.: Squared missing mass as function of the muon track momentum for the 2022ABCDE sample from MUONNU filter passing the pre-selection and quality cuts, with logarithmic scale on the z axis. The blue rectangles identify the control region where the fit is performed, while the red rectangle corresponds to the signal region.

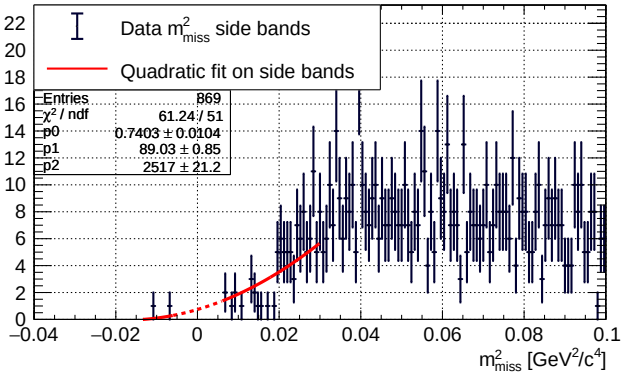

Figure 4.22.: Squared missing mass distribution for background events surviving the selection up to and including the anti-pileup cuts, fitted with a quadratic function. The fit line is dashed in the signal region and solid in control regions, where the fit is performed.

cut and the $d_{MUV3\mu^-}$ cut in the control region, respectively 0.15 ± 0.07 and 0.23 ± 0.08. The statistical uncertainty on the background is obtained with error propagation. The accuracy of the result obtained with such method is limited by the size of the background sample. The expected number of background events in the signal region is hence:

$$\mathbf{N^{exp}_{bkg}(OV\ K\mu\nu) = 0.04 \pm 0.02_{stat} \pm 0.01_{syst}.}$$

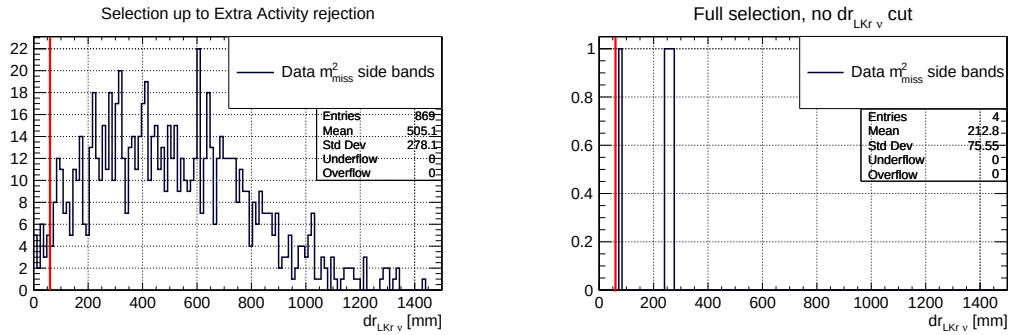

(a) (b)

Figure 4.23.: $d_{\mathrm{LKr}\nu}$ distribution for background events on the side bands of m^2_{miss} after the anti-pileup selection step (4.23a) and after the entire interaction selection except for the $d_{\mathrm{LKr}\nu}$ cut (4.23b).

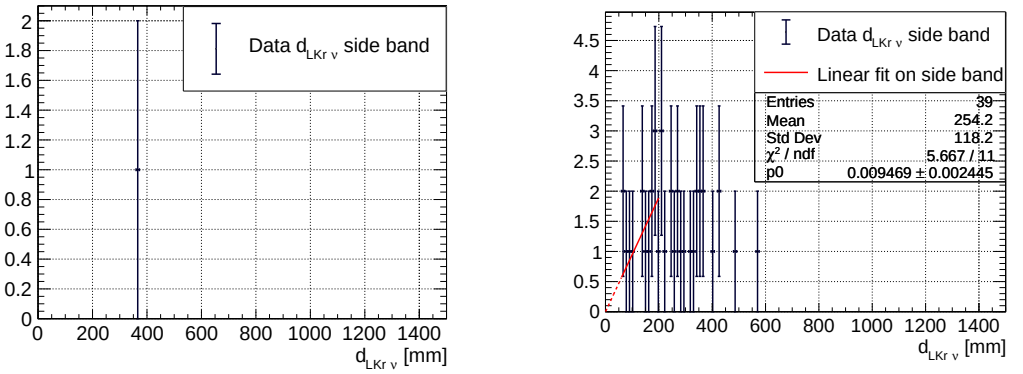

(a) (b)

Figure 4.24.: 4.24a: Surviving background entry in the side band of $d_{\mathrm{LKr}\nu}$. 4.24b: Distribution of the background in the side band of $dr_{LKr\nu}$ after the selection, except for the $d\phi_{LKr-MUV3}$ cut.

4.6. Trigger efficiency

The aim of this section is to compute the trigger efficiency for the events passing the offline selection. As the selection enforces offline the trigger selection, the trigger efficiency after selection is expected to be close to 100%. Furthermore, all trigger conditions which are applied to both the signal and normalization sample are cancelling in the normalization procedure and thus do not need to be estimated. Hence, the only efficiencies to be estimated are those of the `MOQX`, `E5`, and the `mask10` L1 trigger which are only applied to the neutrino trigger line. The following sections are dedicated to the estimate of these trigger efficiencies.

4.6.1. MUV3 L0 trigger condition

The MUV3 L0 trigger condition, called in the following `MOQX`, was made for the neutrino trigger line; its performances have been tested for the first time for the purposes of this analysis. The `MOQX` condition definition is: at least two MUV3 candidates in opposite outer quadrants. This means that the inner tiles - the eight smallest and most illuminated tiles in Figure 3.15 - are excluded from the trigger condition, preventing collecting background of beam π^+'s that decay into muons and hence reducing the rate of data collected. Indeed, the $\pi^+ \to \mu^+\nu_\mu$ decay kinematics is very forward, contrary to $K\mu\nu$ which happens at larger angles as shown in Figure 4.25.

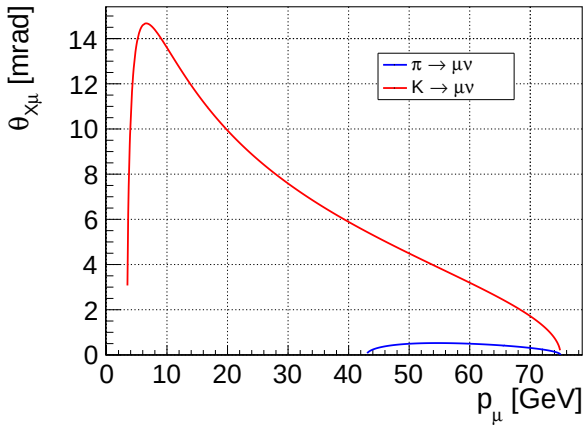

Figure 4.25.: Opening angle between muon daughter and mother for $K^+ \to \mu^+\nu_\mu$ decay (red) and for $\pi^+ \to \mu^+\nu_\mu$ decay (blue) as function of the μ^+ momentum from simulation.

A sample of $K^+ \to \pi^+\pi^+\pi^-$ ($K\pi\pi\pi$) with one of the positive and the negative pions decaying into muon and neutrino was used to estimate the efficiency of `MOQX`. Requiring two pions of opposite charge implies that the two spectrometer tracks are bent in opposite direction and ensures a good spatial separation of the two final state muons, as required by the signal selection. The $K\pi\pi\pi$ sample is selected from the multi-track trigger (`mask5`), that requires more than 8 RICH supercells fired, hits in opposite CHOD quadrants and at least 3 hits in CHOD, with a down-scaling of 100. The data from `mask5` are further filtered, requiring decays with three track vertex, with at least two MUV3 candidates (`2MU3TV` filter stream).

The `MOQX` efficiency has been estimated on data sample 2022B. For the purpose of this measurement, in the offline analysis the MUV3 detector surface has been divided into 12 bins along x and y, following the outer tiles division; the bins are identified with a unique identification number (UID) that depends on the x and y position and on the quadrant. The numbering scheme is shown in Fig 4.26a. The expected UID of the two muons is obtained from the propagation of the tracks of the μ originating from the charged π to the MUV3 z position. The efficiency of the `MOQX` condition is then computed in the plane $\mu^-_{\mathrm{UID}} \times \mu^+_{\mathrm{UID}}$. In this plane, represented in Figure 4.26b, the events supposed to pass `MOQX` – i.e. with muons intercepting the MUV3 in opposite outer quadrants – populate the 36-bin wide orange

shaded regions located on the diagonal. The efficiency is obtained by computing the fraction of these events that indeed passed MOQX. The efficiency map is shown in Figure 4.27a, and it shows that two of the four diagonal squares (μ^+ on Q2 with μ^- on Q4 and μ^+ on Q3 with μ^- on Q1) are less populated. Indeed, the magnet (MNP33) deviates the π^+ towards the Salève side (x negative), and the π^- towards the Jura side (x positive), resulting in the μ^+ populating mostly quadrants Q1 and Q4 and the μ^- populating mostly quadrants Q2 and Q3, as shown in Figure 4.28. In order to compute an average efficiency, such efficiency map has been weighted by the spatial distribution of the MC signal events that pass the selection, shown in Figure 4.27b. The average MOQX efficiency is $\epsilon^{MOQX} = 0.976 \pm 0.007_{stat} \pm 0.001_{syst}$ and is stable across the MUV3 tiles. The statistical uncertainty is obtained with error propagation. The systematic uncertainty is estimated by weighting the MOQX efficiency map obtained from data by the spatial distributions of surviving MC signal events from two additional signal MC samples. In these two additional signal MC samples the true neutrino energy is biased, respectively, by +10% and −10%, to account for uncertainties in the modelling of the final state interaction. Since the neutrino cross-section depends linearly on the energy, the interaction probability is biased by the opposite amount. The magnitude of the bias has been conservatively chosen by using the estimate of the MINOS collaboration on the energy scale uncertainty induced by the modelling of the final state interaction [7].

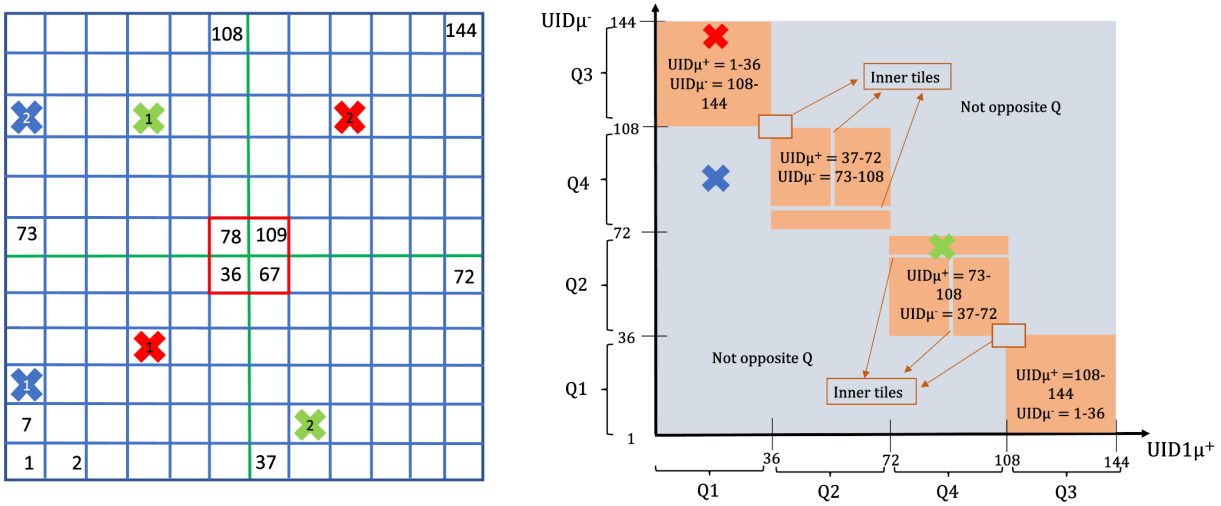

Figure 4.26.: 4.26a: Numbering scheme of the unique identification number of the bins the MUV3 detector area is divided in. The events satisfying the MOQX conditions, such as the ones represented by the green and red crosses in 4.26a, result in entries in the orange squares on the diagonal of the plot of UID_{μ^-} as function of UID_{μ^+} shown in 4.26b. On the other hand, the events not satisfying the MOQX condition, such as the ones represented by a blue cross in 4.26a result in entries in the grey area outside the diagonal in the plot in 4.26b. The empty areas in the orange diagonal squares correspond to the inner tiles of MUV3. The quadrant numbers displayed on the x and y axis of 4.26b are obtained by defining the first quadrant as the bottom left, and then proceeding in the numbering counterclockwise.

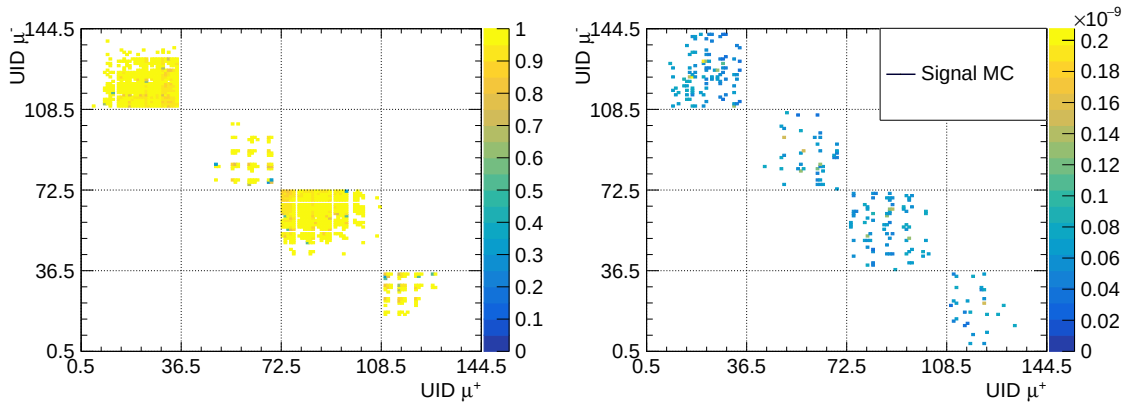

(a) (b)

Figure 4.27.: 4.27a: Efficiency map of the `MOQX` condition. 4.27b: Spatial distribution of signal events from the MC passing the signal selection.

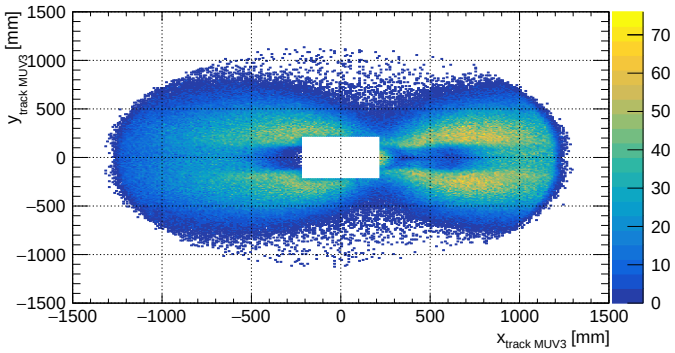

Figure 4.28.: Hit map of the MUV3 detector for $K\pi\pi\pi$ events. The two shapes visible on the positive and negative x coordinate sides correspond, respectively, to the μ^- and to the μ^+ from the π^- and the π^+. The central empty square corresponds to the MUV3 inner tiles.

4.6.2. LKr L0 trigger condition

The LKr L0 trigger condition, called in the following `E5`, is crucial to trigger on signal events. As mentioned above, the LKr is the only calorimeter in NA62 that has an integrated L0 trigger system. For this reason, `E5` is the condition that, together with the `MOQX` condition, allows identifying the neutrino interactions. The `E5` condition requires a total energy deposit larger than 5 GeV in LKr within the trigger time window (6.25 ns), without any constraint on the number of clusters. The efficiency of this trigger condition can be estimated with a sample of $K^+ \to \pi^+\pi^0$ ($K\pi\pi$) from a trigger mask that does not require any LKr condition. Such a sample has been obtained from data that pass: the `control` trigger, that contains only CHOD information downscaled by a factor 2000; `mask2`; `mask0`, that

contains information from RICH, CHOD with a veto condition on MUV3, downscaled by a factor 400. The $K\pi\pi$ sample is selected offline. The selection requires a single-track vertex with basic requirements on pion PID using information from the RICH detector and calorimeters, vetoing events with a matched candidate in MUV3, with the m^2_{miss} computed assuming the mass of the π^+ between 0.013 and 0.023 $\mathrm{GeV}^2/\mathrm{c}^4$. Events with activity in IRC or SAV or SAC or photon-like activity in LKr are discarded. The two photons from the π^0 must be detected in the LAV stations. Moreover, exactly one LKr candidate in time with the RICH track time is requested, so that the energy deposit in the LKr is purely hadronic and associated to the π^+ track. Events that feature activity in the inner regions of LKr (radius < 250 mm) are rejected. Finally, events are also required to have a reconstructed in-time energy larger than 5 GeV. The efficiency of the LKr trigger condition is the fraction of these events that fired the trigger condition. The efficiency as a function of the in-time energy deposit from K$\pi\pi$ events, shown in Figure 4.29a, is weighted by the in-time energy deposit distribution from Monte Carlo signal event shown in Figure 4.29b, weighted by the probability of interaction of the associated ν_μ each event. The obtained value for the efficiency of the `E5` trigger condition, measured on samples 2022B, C, D and E, is $\epsilon^{E5}_{K\mu\nu*} = 0.82 \pm 0.01_{stat} \pm 0.01_{syst}$. The statistical uncertainty is obtained with error propagation. The systematic uncertainty is estimated comparing the result to the ones obtained by weighting the `E5` efficiency distribution from data by the in-time energy deposit distribution obtained from the two additional signal MC described in Section 4.6.1.

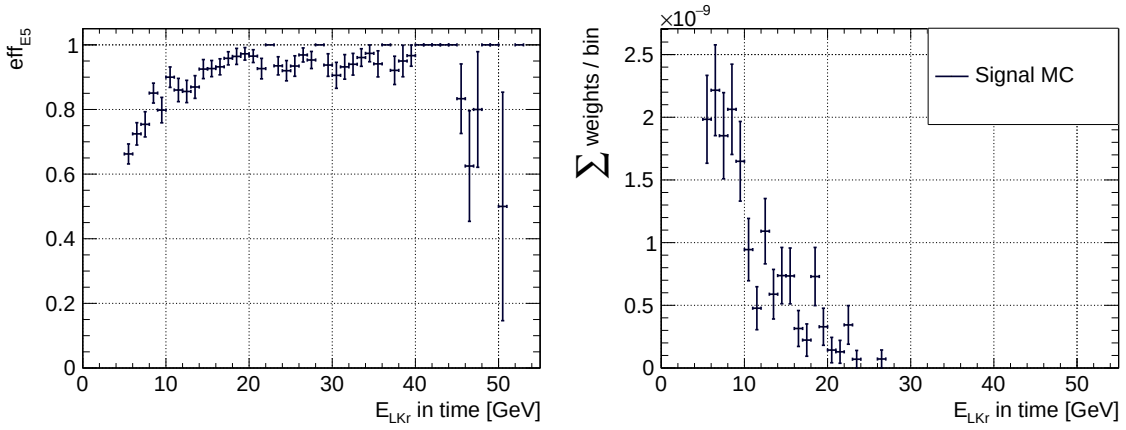

(a) (b)

Figure 4.29.: 4.29a: Efficiency of the LKr L0 trigger condition E(5) in bins of reconstructed in-time energy deposit in the calorimeter. 4.29b: Distribution of total LKr in-time energy deposit of MC signal events that pass the signal selection, weighted by the probability of interaction of the associated ν_μ for each event.

4.6.3. L1 trigger efficiency

The L1 trigger efficiency can be estimated with events satisfying `mask10` requirements at L0 and passing the $K\mu\nu$ common selection, but skipping L1 selection. Such events, called

"autopass", make up 0.3% of the sample of `mask10` data passing the common selection. Note, that despite the L1 selection is not applied to these events, the outputs of the L1 algorithms are stored for offline analysis. Hence, using the autopass events which, given the offline reconstruction, should have passed the L1 selection, the L1 efficiency can be computed as the fraction of these events that indeed passed the L1 algorithms.
The L1 trigger is applied online sequentially. Hence, the efficiency of each algorithm is computed with respect to the event sample that passed the previous algorithm and is reported in Table 4.3. Since the `STRAW_1TRK` algorithm depends on the momentum of the muon track, the efficiency of this algorithm is estimated in bins of muon momentum and weighted by the MC muon momentum distribution of the events that pass the full signal selection, shown in Figure 4.30b. The `STRAW_1TRK` algorithm efficiency is shown as a function of the reconstructed muon momentum in Figure 4.30a.
The total L1 efficiency, measured on `MUONNU` filtered data on samples 2022A, B, C, D, E, is the product of the three algorithms efficiencies [99]:

$$\epsilon^{L1}_{mask10} = \epsilon^{KTAG} \cdot \epsilon^{nLAV} \cdot \epsilon^{STRAW\_1TRK} = 0.932 \pm 0.002_{stat}.$$

The results obtained from autopass data have been compared to the results from the simulated HLT trigger on the same autopass sample, with identical results up to 10^{-5}. The assigned uncertainty is hence statistical.

L1 algo	**Efficiency**
`KTAG` | ($K\mu\nu$ sel)	0.998 ± 0.001
`nLAV` | ($K\mu\nu$ sel) & `KTAG`	0.996 ± 0.001
`STRAW_1TRK` | ($K\mu\nu$ sel) & `nLAV` & `KTAG`	0.938 ± 0.001

Table 4.3.: L1 trigger algorithms' efficiency. Each component's verdict is only evaluated in the presence of a positive verdict from the previous algorithms in the chain.

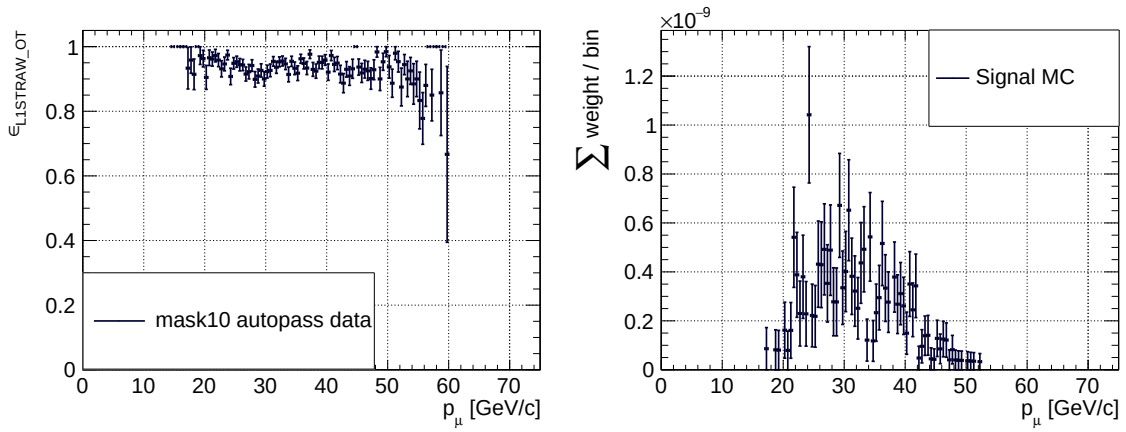

(a) (b)

Figure 4.30.: 4.30a: Distribution of the STRAW_1TRK efficiency as a function of the reconstructed track momentum for mask10 autopass events. 4.30b: Muon momentum distribution for MC signal events surviving the offline selection, weighted by the interaction probability of each event.

4.7. Signal Yield estimate

The expected signal yield $N^{exp}_{K\mu\nu*}$ for a year run in the signal region is derived with the relation in Equation 4.2:

$$N^{exp}_{K\mu\nu*} = N_K \cdot \mathcal{B}(K^+ \to \mu^+\nu_\mu) \cdot P_{\text{int,LKr}} \cdot \epsilon_{K\mu\nu*} \tag{4.5}$$

where:

- N_K is the number of kaon decays in the fiducial volume,
- $\mathcal{B}(K^+ \to \mu^+\nu_\mu)$ is the branching ratio of the decay,
- $P_{\text{int, LKr}} = (6.0 \pm 0.1) \cdot 10^{-11}$ is the average interaction probability of the neutrino in the LKr calorimeter for events that pass the common selection, whose distribution is shown in Figure 4.31. A 2% uncertainty corresponding to the uncertainty on the ν_μ^{CC} cross-section (see Fig.28 in [51]) is assigned to this value.
- $\epsilon_{K\mu\nu*}$ is the overall signal efficiency.

The item $\epsilon_{K\mu\nu*}$ includes the contributions from the common offline selection, from the interaction offline selection and from the trigger efficiency. It can be written as:

$$\epsilon_{K\mu\nu*} = \epsilon^{common}_{K\mu\nu} \cdot \epsilon^{int}_{K\mu\nu*} \cdot \epsilon^{mask10/sel}_{K\mu\nu*} \tag{4.6}$$

The contributions from each of these factors is assessed in the following.

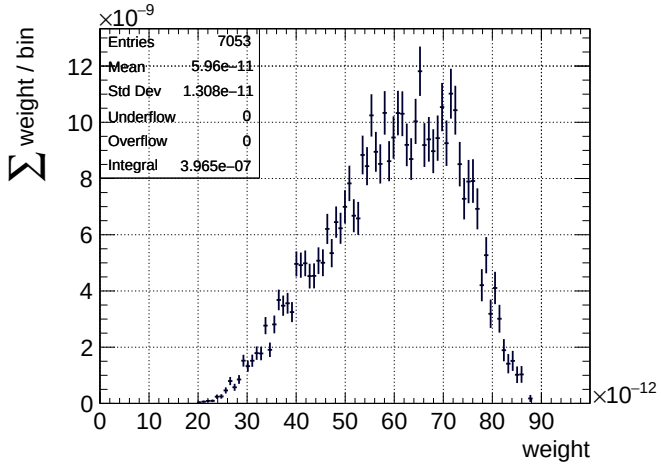

Figure 4.31.: MC weight distribution for events passing the common selection.

4.7.1. Normalization $K\mu\nu$

The number of expected events can be normalized with respect to the total number of normalization K$\mu\nu$ that pass the common selection. The number of kaon decays can be estimated from the relation:

$$N_K = \frac{N_{K\mu\nu}}{\epsilon_{K\mu\nu} \cdot \mathcal{B}(K^+ \to \mu^+\nu_\mu)} \tag{4.7}$$

where $N_{K\mu\nu}$ is the total number of normalization events collected with the mask2 trigger $N^{mask2}_{K\mu\nu}$, multiplied by the downscaling factor $D^{mask2} = 600$, and $\epsilon_{K\mu\nu}$ the overall normalization acceptance.
The overall normalization acceptance is the product between the acceptance of the common selection and the mask2 trigger efficiency. The expression in Eq 4.5 can hence be written as:

$$\begin{aligned} N^{exp}_{K\mu\nu*} &= N^{mask2-ext}_{K\mu\nu} \cdot D^{mask2} \cdot \frac{\epsilon_{K\mu\nu*}}{\epsilon_{K\mu\nu}} \cdot P_{\text{int,LKr}} = \\ &= N^{mask2-ext}_{K\mu\nu} \cdot D^{mask2} \cdot \frac{\epsilon^{common}_{K\mu\nu} \cdot \epsilon^{int}_{K\mu\nu*} \cdot \epsilon^{mask10/sel}_{K\mu\nu*}}{\epsilon^{common}_{K\mu\nu} \cdot \epsilon^{mask2-ext/sel}_{K\mu\nu}} \cdot P_{\text{int,LKr}} = \\ &= N^{mask2-ext}_{K\mu\nu} \cdot D^{mask2} \cdot \frac{\epsilon^{int}_{K\mu\nu*} \cdot \epsilon^{mask10/sel}_{K\mu\nu*}}{\epsilon^{mask2-ext/sel}_{K\mu\nu}} \cdot P_{\text{int,LKr}} \end{aligned} \tag{4.8}$$

where:

- $N^{mask2-ext}_{K\mu\nu}$ is the number of normalization events from minimum bias data (`mask2`) extended by the `!RICH16, !Q2, UTMC` conditions from `mask10` (see Section 4.2.2) in 2022 year run passing the common selection, downscaled by 600,
- $\epsilon^{common}_{K\mu\nu}$ is the common part of offline selection that cancels out in the ratio,

- $\epsilon^{int}_{K\mu\nu*}$ is the acceptance of signal event selection with respect to the events that satisfy the common $K\mu\nu$ selection, and is the product of the selection acceptance $A^{int}_{K\mu\nu*}$ with the random veto efficiency ϵ^{RV},
- $\epsilon^{mask10/sel}_{K\mu\nu*}$ is the trigger efficiency of `mask10` on selected signal events,
- $\epsilon^{mask2-ext/sel}_{K\mu\nu}$ is the trigger efficiency of the `mask2` extended by the `!RICH16, !Q2, UTMC` conditions from `mask10` evaluated on selected normalization events.

The number of observed normalization events is $N_{K\mu\nu} = N^{mask2-ext}_{K\mu\nu} \cdot D^{mask2}_{min-bias} = 1.4873 \cdot 10^{11}$, where $N^{mask2-ext}_{K\mu\nu}$ is the integral of the normalization m^2_{miss} distribution in Figure 4.32. The number of observed normalization events in Figure 4.32 is a proxy for the number of effective $K\mu\nu$ decays. The number of effective $K\mu\nu$ decays can also be computed by fitting the m^2_{miss} distribution in Figure 4.32 with the m^2_{miss} distribution obtained from running the common selection on a $K\mu\nu$ MC sample. The difference between the integrals of the two histograms is taken into account as a systematic uncertainty on the variable $N_{K\mu\nu}$, and it is 1.4%. The rest of the items listed above are estimated in the following.

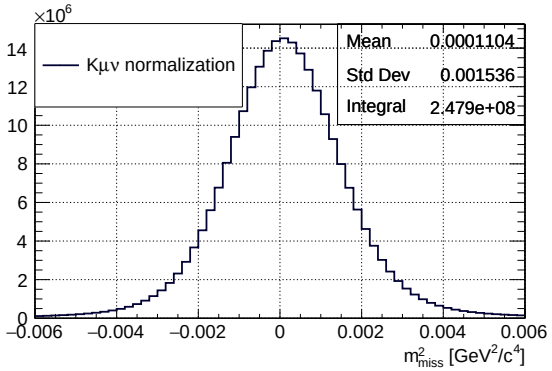

Figure 4.32.: Squared missing mass distribution for normalization $K\mu\nu$ from mask2, surviving the entire common selection. The integral of this histogram has to be multiplied by the downscaling factor of mask2 in order to get the number of $K\mu\nu$ decays in the 2022 run.

4.7.2. Signal selection efficiency

The signal offline selection efficiency is defined with the following relation:

$$\epsilon^{int}_{K\mu\nu*} = A^{int}_{K\mu\nu*} \cdot \epsilon^{RV} \tag{4.9}$$

where $A^{int}_{K\mu\nu*}$ is the interaction selection acceptance, evaluated on MC, and ϵ^{RV} is the probability for a signal event to pass the interaction selection without being rejected by additional random activity in the detectors.

4.7.2.1. Selection acceptance

The signal selection acceptance is computed on the signal MC sample with the following relation:

$$A^{int}_{K\mu\nu*} = \frac{\sum^{selected} p_i}{\sum^{all} p_i} = 0.0421 \pm 0.0025_{stat} \pm 0.0015_{syst} \tag{4.10}$$

where $\sum^{all} p_i$ and $\sum^{selected} p_i$ are the sums of the interaction probability, p_i, for the events passing the common selection and for the events passing the common and the interaction selection. These two sums are reported as the integral of the neutrino energy distributions weighted by the interaction probabilities shown in Figure 4.33. The systematic uncertainty is computed by comparing the obtained acceptance to the ones obtained from the two signal MC samples described in Section 4.6.1.

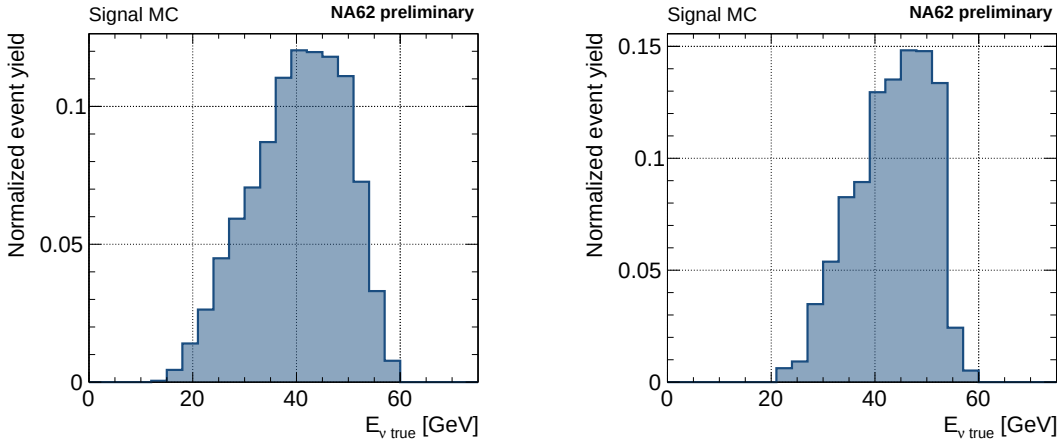

(a) (b)

Figure 4.33.: True ν energy distribution from the MC after the common selection (4.33a) and after the entire interaction selection (4.33b).

The MC used to compute the interaction selection acceptance does not include overlaid activity in the detector. Such extra activities could lead to the rejection of some events that would fail the extra activity selection, described in Section 4.4.2.2. Hence, the acceptance should be corrected for this effect. The estimation of the random veto correction factor, ϵ^{RV}, is presented in the next section.

4.7.2.2. Random Veto

The source of random veto for the present analysis is any accidental random activity that would result in a signal event being discarded. The item ϵ^{RV} represents the acceptance of anti-pileup veto conditions, and is computed as the ratio between the number of normalization events before and after the extra activity rejection. Since ϵ^{RV} is computed on normalization events in absence of the neutrino interaction, the veto conditions are modified with respect to those described in Section 4.4.2.2. The veto conditions applied to normalization for the purpose of estimating the item ϵ^{RV} are:

- no extra activity in the inner regions of MUV1 (radius of 200 mm) and of MUV2 (radius of 300 mm),
- no additional LKr standard clusters and no extra activity in the inner regions of LKr (radius of 250 mm),
- no extra candidates at MUV3,
- number of KTAG hits within 8 ns of the RICH track time < 50.

The acceptance of the anti-pileup veto estimated with the normalization sample is $\epsilon^{RV} = 0.816 \pm 0.014_{syst}$. Its contributions are listed in Table 4.4. The uncertainty on the random veto efficiency is dominated by the systematic ones, that we assume to be similar to the one provided in [82], which is 1.4%.

RV source	**Relative acceptance**
additional activity in MUV1 and MUV2 inner regions	0.982
additional LKr clusters or extra activity in LKr inner region	0.989
additional activity in MUV3	0.877
number of KTAG hits in 16ns time window < 50	0.958

Table 4.4.: Acceptance of the anti-pileup veto conditions estimated on normalization sample.

4.7.3. Trigger efficiency

The trigger efficiency $\epsilon^{mask10/sel}_{K\mu\nu*}$ is the product of the efficiencies of the L0 and L1 trigger of the neutrino trigger mask on selected events for signal. For normalization, the term $\epsilon^{mask2-ext/sel}_{K\mu\nu}$ represents the product of the efficiency of `mask2` and of the trigger conditions applied offline (`!RICH16, !Q2, UTMC`) to the normalization selection. Their ratio can be written as:

$$\frac{\epsilon^{mask10/sel}_{K\mu\nu*}}{\epsilon^{mask2-ext/sel}_{K\mu\nu}} = \frac{\epsilon^{!RICH16}_{K\mu\nu*} \cdot \epsilon^{UTMC}_{K\mu\nu*} \cdot \epsilon^{MOQX}_{K\mu\nu*} \cdot \epsilon^{Q1}_{K\mu\nu*} \cdot \epsilon^{!Q2}_{K\mu\nu*} \cdot \epsilon^{E5}_{K\mu\nu*} \cdot \epsilon^{L1}_{K\mu\nu*}}{\epsilon^{!RICH16}_{K\mu\nu} \cdot \epsilon^{UTMC}_{K\mu\nu} \cdot \epsilon^{Q1}_{K\mu\nu} \cdot \epsilon^{!Q2}_{K\mu\nu}} \tag{4.11}$$

After cancellation of the common terms, the trigger ratio is:

$$\frac{\epsilon^{mask10/sel}_{K\mu\nu*}}{\epsilon^{mask2-ext/sel}_{K\mu\nu}} = \epsilon^{MOQX/sel}_{K\mu\nu*} \cdot \epsilon^{E5/sel}_{K\mu\nu*} \cdot \epsilon^{L1/sel}_{K\mu\nu*} \tag{4.12}$$

As the `mask10` L1 algorithms (`STRAW_1TRK`, `nLAV` and `KTAG`) do not exploit the neutrino interaction, one can assume that the L1 efficiency is the same for events passing the common selection and for events passing the full selection consisting of the common selection and the neutrino interaction selection. Hence, the efficiency derived in 4.6.3 can be used in Equation 4.12.
The results for the trigger efficiencies contributions in Equation 4.12 are summed up below:

- $\epsilon^{MOQX}_{K\mu\nu*} = 0.976 \pm 0.007_{stat} \pm 0.001_{syst}$ estimated in Section 4.6.1,
- $\epsilon^{E5}_{K\mu\nu*} = 0.82 \pm 0.01_{stat} \pm 0.01_{syst}$ estimated in Section 4.6.2,
- $\epsilon^{L1/sel}_{K\mu\nu*} = 0.932 \pm 0.002_{stat}$ estimated in Section 4.6.3.

The contributions to the signal yield estimate are summarized and reported in Table 4.5.

Contribution	Value and uncertainty
$P_{\text{int,LKr}}$	$(6.0 \pm 0.1_{syst}) \cdot 10^{-11}$
$N_{K\mu\nu}$	$(1.48 \pm 0.02_{syst}) \cdot 10^{11}$
$A^{int}_{K\mu\nu*}$	$0.0421 \pm 0.0025_{stat} \pm 0.0015_{syst}$
ϵ^{RV}	$0.816 \pm 0.014_{syst}$
$\epsilon^{MOQX}_{K\mu\nu*}$	$0.976 \pm 0.007_{stat} \pm 0.001_{syst}$
$\epsilon^{E5}_{K\mu\nu*}$	$0.82 \pm 0.01_{stat} \pm 0.01_{syst}$
$\epsilon^{L1/sel}_{K\mu\nu*}$	$0.932 \pm 0.002_{stat}$

Table 4.5.: Contributions to the signal yield and their uncertainty.

4.7.4. Event Yield

Having now estimated all the contributions in Equation 4.8, it is possible to estimate the signal yield and its uncertainty, obtained with error propagation:

$$\begin{aligned} N^{exp}_{K\mu\nu*} &= N_{K\mu\nu} \cdot A^{int}_{K\mu\nu*} \cdot \epsilon^{RV} \cdot \epsilon^{sel}_{E5} \cdot \epsilon^{sel}_{MOQX} \cdot \epsilon^{sel}_{L1} \cdot P_{\text{int,LKr}} \\ &= \mathbf{0.228 \pm 0.014_{stat} \pm 0.011_{syst}} \end{aligned} \tag{4.13}$$

This expected number of signal event is to be compared with the ones for background, which are:

$$\begin{aligned} \mathbf{N^{exp}_{bkg}(Mis - reco\ K^+) = 0.0014 \pm 0.0007_{stat} \pm 0.0002_{syst}}, \\ \mathbf{N^{exp}_{bkg}(OV\ K\mu\nu) = 0.04 \pm 0.02_{stat} \pm 0.01_{syst}}. \end{aligned} \tag{4.14}$$

The signal to background ratio of the analysis is thus about 5.5/1.
To assess the significance of future findings in the signal region, we compute the p-values for signal and background for observing 0, 1, and 2 events, assuming that the signal and background processes follow a Poisson distribution,using the results in Equation 4.13 and Equation 4.14 as λ values for the Poisson distribution:

Probability for signal $\mathbf{N^{exp}_{K\mu\nu*} = 0.228}$

- for 0 data events p = 0.7961

- for 1 data event p = 0.1815
- for 2 data events p = 0.0207

Probability for background $N^{exp}_{bkg} = 0.0414$

- for 0 data events p = 0.9595
- for 1 data event p = 0.0397
- for 2 data events p = 0.00082

Probability for total event yield $N^{exp}_{events} = 0.2694$

- for 0 data events p = 0.7638
- for 1 data event p = 0.2058
- for 2 data events p = 0.0277.

Figure 4.34 represents the expected number of events per m^2_{miss} and $d_{LKr\nu}$ bin, for background (left) and signal (right).

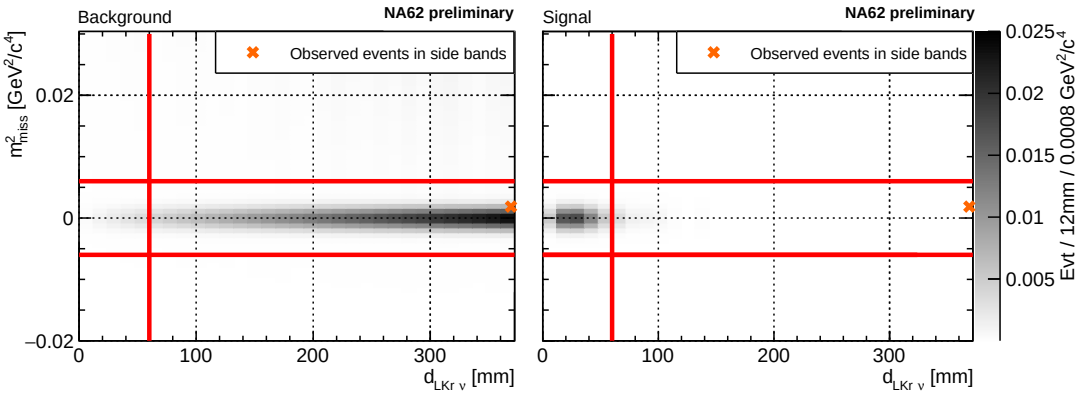

Figure 4.34.: Number of expected events for background (left) and signal (right). The grey scale reflects the number of expected events per bin of $0.0008\,\mathrm{Gev}^2/\mathrm{c}^4 \times 12\,\mathrm{mm}$. The red lines represent the cuts that locate the signal region. Events in the side bands of the signal region are indicated with orange cross-shaped markers.

4.8. Opening the box on the signal region

Upon revealing the content of the signal region, **two tagged neutrinos candidates have been found**. Their main properties are summed up in Table 4.6; their position in the signal region is reported with orange-shaded crosses in Figure 4.35.

Considerations

Statistical significance tests have been performed to compare the number of events found in the signal region to the expected number of signal events computed in Section section 4.7. The expected signal yield is 2.3σ away from the number of found events, while the expected background yield is 3.3σ away; these two events are hence compatible with being signal candidates. However, a caveat imposes: it can be misleading to talk about statistical significance with respect to these results, as this analysis only aimed to prove the feasibility of the tagging technique with data. No new physics or new measurements evidences are being claimed; for this reason, the statistical significance provided must be taken and shared *cum grano salis*.

Nonetheless, the finding of two signal candidates is a remarkable achievement, and a crucial first step towards the development of full scale tagged experiments, that is, hopefully, not too far in the future. These two events are the first tagged neutrino candidates detected in physics history.

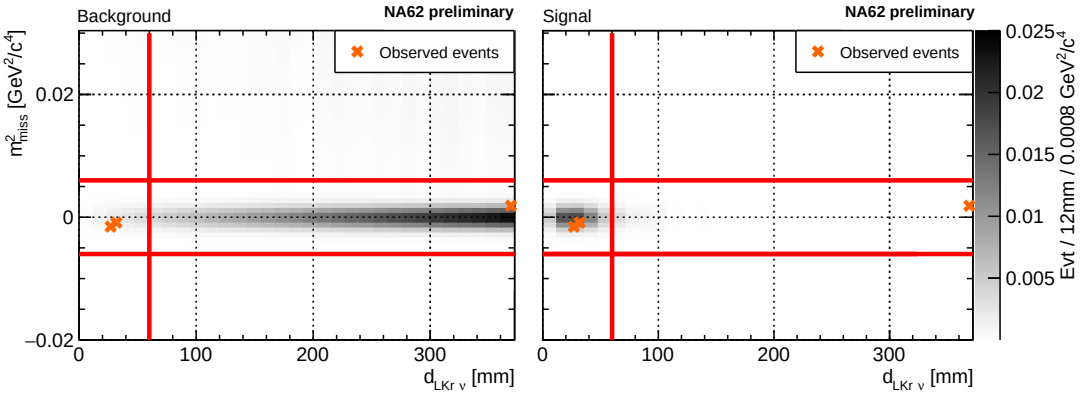

Figure 4.35.: Number of expected events for background (left) and signal (right). The grey scale reflects the number of expected events per bin of $0.0008\,\mathrm{Gev}^2/\mathrm{c}^4 \times 12\,\mathrm{mm}$. The red lines represent the cuts that locate the signal region. The orange cross-shaped markers represent the data events upon opening the box.

4.8.1. Event display

The downstream activity of the two events is shown in the event displays in Figure 4.36 for Event A and in Figure 4.37 for Event B. The two event displays show the muon track ad the neutrino track, kinematically reconstructed from the measured properties of the K^+ and of the μ^+. Moreover, the associated activity in CHOD, LKr, MUV1, MUV2 and MUV3 is shown in the form of red boxes. The length of the red boxes in the three calorimeters is proportional to the energy deposit in the calorimeter. The two events look very similar, with a very high energy neutrino appearing at the LKr in correspondence to the neutrino direction kinematically reconstructed, and in a 6 ns time window with respect to the RICH μ^+ track time. The hadronic shower then continues in MUV1, while in MUV2 and MUV3 the only interaction product visible is the μ^-; for this reason,

Variable	**Event A**	**Event B**
$d_{\mathrm{LKr}\nu}$	31.9 mm	27.0 mm
m^2_{miss}	$-0.00088\,\mathrm{GeV}^2/\mathrm{c}^4$	$-0.0015\,\mathrm{GeV}^2/\mathrm{c}^4$
$d\phi_{LKr-MUV3}$	3.29 rad	3.24 rad
E_ν	52.1 GeV	57.5 GeV
p_{μ^+}	25.25 GeV/c	18.74 GeV/c
p_{K^+}	77.3 GeV/c	76.2107 GeV/c
$E_{LKr\ in\ time}$	13.36 GeV	7.67 GeV
$E_{MUV1\ in\ time}$	9.85 GeV	10.90 GeV
$E_{MUV2\ in\ time}$	2.48 GeV	2.80 GeV
E_{μ^-}/E_ν	0.68	0.78
n_{KTAG}	28	17
z_{vtx}	161.2 m	157.7 m
$r_{LKr\nu}$	335.0 mm	304.2 mm
x, y at MUV3 μ^-	(550, 770) mm	(330, 770) mm
x, y at MUV3 μ^+	(-330, -770) mm	(-550, -990) mm
Run ID	12477	11986
Burst ID	336	41
Event Nb	2333361	1662909

Table 4.6.: Features of the two signal candidates found in the signal region.

the activity in MUV2 and 3 is expected to be slightly misaligned with the neutrino trajectory.

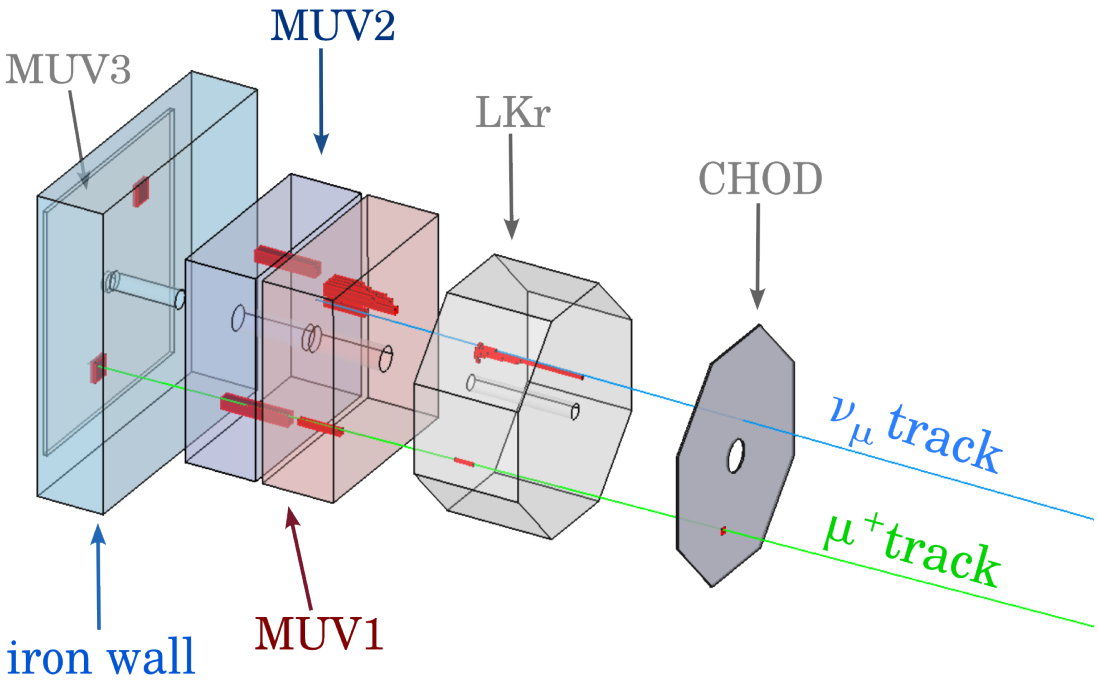

Figure 4.36.: Annotated event display for Event A. The 3-dimensional volumes represent the active volumes of the downstream detectors. The green line is the track of the μ^+; the blue line represents the neutrino trajectory reconstructed from the K^+ and μ^+. The red boxes represent the activity in the detector. For the LKr, MUV1 and 2 the length of the box is the normalized energy deposit in each cell.

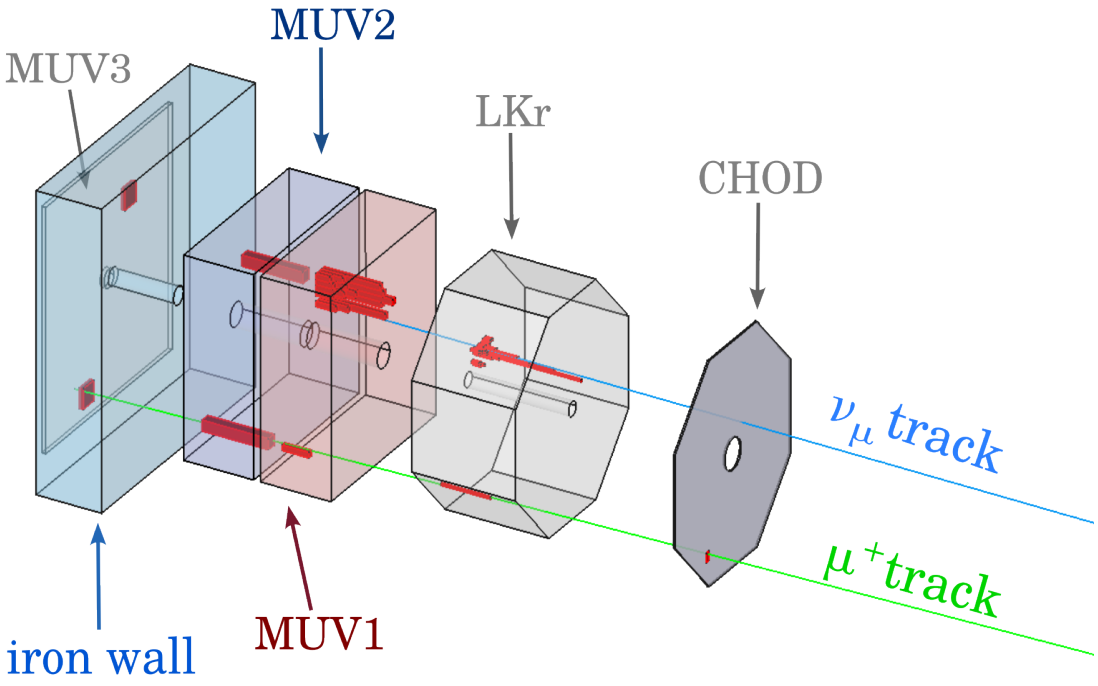

Figure 4.37.: Annotated event display for Event B. The 3-dimensional volumes represent the active volumes of the downstream detectors. The green line is the track of the μ^+; the blue line represents the neutrino trajectory reconstructed from the K^+ and μ^+. The red boxes represent the activity in the detector. For the LKr, MUV1 and 2 the length of the box is the normalized energy deposit in each cell. Apart from the neutrino cluster, some extra low energy hits have been found in LKr.

5. Towards a full scale tagged neutrino experiment

Summary

The neutrino tagging technique holds promises for the future of neutrino physics; the implementation of a full scaled tagged neutrino experiment is foreseeable under some assumptions. As mentioned in Chapter 2, the tagging heavily relies on the performances of the beam spectrometer, that should be a state-of-the-art silicon tracker. In particular, the extreme particle rate at the tracker imposes some constraints on the time resolution of the detector: being able to separate all the particles is a crucial requirement to be able to perform the tagging. For this reason, in the framework of this project, a study on the time resolution budget of time-tagged silicon detectors has been performed. For this study, the state-of-the-art NA62's GigaTracKer detector have been used in a beam test, with the goal of studying in detail the factors that contribute to the time resolution budget of planar silicon sensors. The upcoming sections are dedicated to an introduction to the physics of semiconductors and to the working principles of silicon detectors, followed by a description of the experimental setup of the beam test, and of analysis of the data taken during such beam test.

5.1. Silicon detectors

Silicon sensors have found a large use in the field of experimental particle physics: they have desirable features that make them versatile in many applications. Silicon sensors are

typically characterized by fast charge collection time and high signal-to-noise ratio. They are used for tracking purposes, because of their high precision in position measurements and their low material budget, that allows to reduce the scattering. Silicon detectors' functioning principle is based on semiconductor physics and on the p-n junction operated at reverse bias.

5.1.1. Basics of semiconductor physics

This section is dedicated to a brief introduction to semiconductor physics. An extensive and much more exhaustive description of this subject can be found in textbooks such as [80] and [73].
Semiconductors are crystalline solids, with atoms arranged in a three-dimensional periodic lattice. Examples of semiconductors are silicon (Si) and germanium (GeAs); in the following sections we will talk about silicon, but the same considerations are also valid for germanium. Each atom in a three-dimensional periodic lattice is surrounded by four close neighbors. Each atom has four electrons in the outer orbit; these valence electrons [1] are shared with the four neighbouring atoms. This sharing of electrons is known as covalent bonding; each electron pair constitutes a covalent bond. Single atom electrons have discrete energy levels that are eigenstates of the Schroedinger's equation. When two identical atoms are far apart, the allowed energy levels consist of one doubly degenerate level, meaning that their electrons have identical energy levels. However, when two identical atoms are close by, the degenerate energy levels split into two levels, due to the bonding between the atoms. This splitting happens because of the Pauli exclusion principle, that states that no more than two electrons in a given system can be in the same energy state at the same time. If this consideration is extended to a crystalline lattice, where N identical atoms are close, there is an overlap of the orbits of the valence electrons of different atoms, and the valence electrons interact with each other. This interaction causes a shift in the energy levels, creating N separate but closely spaced levels. If N is large, the splitting of energy levels results in continuous "allowed" energy bands for the valence electrons.

[1] Valence electrons are electrons in the outer shell of an atom, that can participate in chemical bonds.

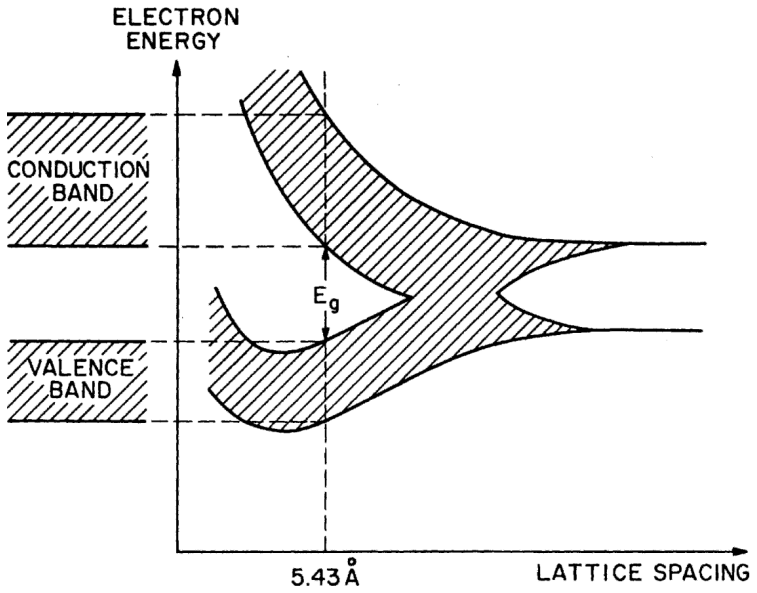

Figure 5.1.: Energy levels of silicon atoms arranged in a diamond structure, as a function of lattice spacing. From [80].

The band gap energy between the bottom of the conduction band and the top of the valence band is the width of the forbidden energy gap, as shown at in Figure 5.1. Physically, the energy gap is the energy required to break a bond in the semiconductor to free an electron to the conduction band and leave a hole in the valence band. The energy band gaps of silicon and germanium are 1.1 eV and 0.7 eV respectively.
At a temperature of absolute zero, all electrons occupy the lowest energy states (valence band) and are bound to their tetrahedron lattice; the upper energy band (the conduction band) will be empty. At higher temperatures, the covalent bonds can break, and a valence electron may become a free electron, leaving behind a vacating place or *hole*[73]. Both the electron and the hole (to be filled by a neighboring electron) are available for conduction, the hole behaving like a positively charged particle. This creates a weak conductivity. Electrons and holes are called charge carriers.
In the intrinsic (pure) semiconductor case, the concentration of electrons in conduction band and holes in valence band is equal: $n = p = n_i$, where n (p) indicates the number of electrons (holes) in the conduction (valence) band, and n_i is the intrinsic carrier density. Indeed, each hole in the valence band is produced by an electron jumping to the conduction band.

Doping

Electronic devices are typically obtained by adding impurities (*dopants*) to the crystalline lattice of silicon, to control its conductivity. The doped silicon is called *extrinsic*. Doping can be either *n-type*, if silicon atoms are replaced by pentavalent or *donor* atoms (such as arsenic, phosphorus); or *p-type*, if silicon atoms are replaced with a trivalent or *acceptor* atom such as boron. Donor atoms have one more valence electron: this creates an additional

energy level close to the conduction band. Acceptor atoms have three electrons in the valence band, creating a hole near the valence band of the silicon and working as a trap for electrons in the valence band. In n-type silicon, electrons are called majority charge carriers; vice versa, in p-type silicon holes are majority and electrons minority carriers. Charge motion in semiconductors is mainly due to two mechanisms: drift and diffusion. The first is due to the application of an external electric field, while the second to a gradient in the carrier concentration distribution.
When no external field of intensity E is applied, the average displacement of the charge carriers is null. The introduction of an electric field causes the carriers to move parallel to the field in opposite directions for the two polarities, and to acquire a drift velocity given by:

$$\begin{aligned} v_n &= -\mu_n E \\ v_p &= \mu_p E \end{aligned} \tag{5.1}$$

where v_n and v_p are the drift velocities of electrons and holes, μ_n and μ_p the respective mobilities that depend on dopant, charge carrier concentration, temperature and electric field:

$$\begin{aligned} \mu_n &= \frac{e \cdot \tau_n}{m_n} \\ \mu_p &= \frac{e \cdot \tau_p}{m_p} \end{aligned} \tag{5.2}$$

where $\tau_{n,p}$ is the mean free time between successive collisions, e the electron charge, $m_{n,p}$ is the effective mass of electrons or holes. For electric field values below 1 kV/cm, mobilities in silicon can be considered constant with values μ_n =1350 $\mathrm{cm^2\,V^{-1}\,s^{-1}}$ and μ_p =450 $\mathrm{cm^2\,V^{-1}\,s^{-1}}$ at room temperature. When the electric field increases, the mobility becomes gradually more field-dependent and drift velocity tends to saturate [65]. Drift velocities reach a saturation value that is different for the two charge carriers [31], as shown in Figure 5.2. Electrons' drift velocity saturation value is about 10^7 cm/s under an applied electric field of about 300 kV/cm, while holes saturation require much higher fields and reach a slightly lower velocity of about 9.5 10^6 cm/s.

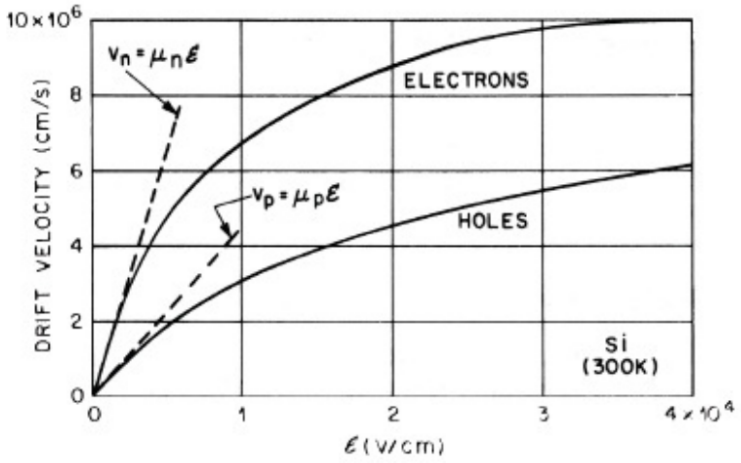

Figure 5.2.: Drift velocity of electrons and hole as a function of the external electric field for a temperature of 300K. From [80].

Diffusion, on the other hand, happens when the distribution of free charge carriers is inhomogeneous. The charge carriers incur in a motion that takes carriers from the region with higher concentration to flow toward the region with lower concentration. Such motion depends on the carrier gradient and temperature and causes a recombination mechanism at thermal equilibrium.

5.1.2. Silicon sensors working principle

The properties of silicon detectors can be understood thanks to the most basic structure that can be formed with doped silicon, the p-n junction. The p-n junction is formed by a p-doped and an n-doped region joined together; an electronic element formed by a p-n junction is called a diode. In a p-n junction, if no external voltage is applied, electrons near the p-n interface are likely to diffuse into the p-region leaving positively charged ions in the n-region behind, while the holes diffuse towards the n-region. This mechanism creates a charge free region in the area around the p-n interface, the *depletion zone* (represented by the white region in Figure 5.4). If the p-type region is connected to a negative and the n-type region to a positive terminal (reverse bias voltage) as shown in Figure 5.3, the holes and the electrons will travel to the electrodes, and consequently, the depletion region will broaden. Because of this, the diode forms a high resistance to current flow. The depletion width increases with the square root of the applied bias voltage; increasing the voltage bias will therefore make the depletion region (or bulk) grow.

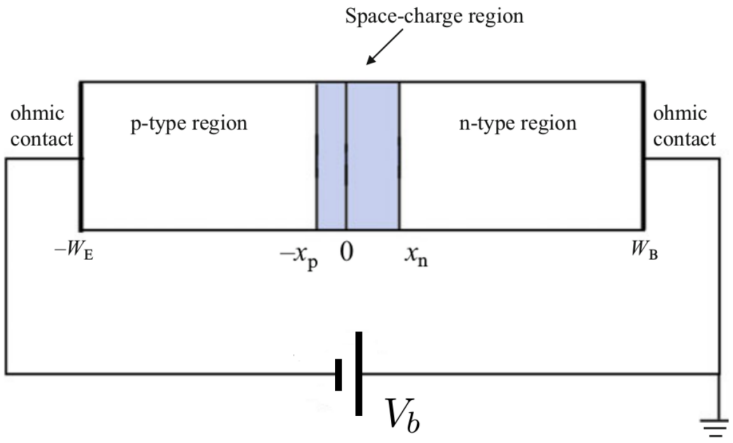

Figure 5.3.: p-n junction at reverse bias. From [31].

The simplest silicon sensor unit is formed by two thin layers of highly doped semiconductor (p- and n-type), separated by a lightly doped, nearly intrinsic bulk, operated under reverse bias. The electrodes are placed in correspondence to the highly doped semiconductor layers. The signal is induced by the drift motions of electrons and holes produced by the ionizing particle crossing the sensor inside the depletion region electric field and towards the electrodes, giving place to the particle detection [107]. The voltage bias affects not only the width of the depletion region in the p-n junction, but also the drift velocity of the charge carriers:

$$\begin{aligned} v_n &= -\mu_n E = -\mu_n \frac{V_b}{d} \\ v_p &= \mu_p E = \mu_p \frac{V_b}{d}. \end{aligned} \tag{5.3}$$

Signal formation and detection

If an ionizing particle traverses the detector, an equal number of free electrons and holes is produced; the charge carriers formed in the bulk of the sensor drift towards the electrode thanks to the electric field developed in the sensor due to the bias voltage. The current induced on an electrode by a moving charge is described by [93] and [103] and summarized by the Ramo-Shockley theorem:

$$i(t) = -q\vec{v}(t) \cdot \vec{E_W} \tag{5.4}$$

where $\vec{v}$ is the charge velocity and E_W is the *weighting field*. The weighting field, which should not be confused with the electric field, is obtained by applying unit potential to an electrode while grounding the neighbouring electrodes. More practically, the weighting field describes the coupling between the charge and the electrodes. It depends only on the geometry of the sensors: on the distance from the pixel electrode to the backplane electrode, on the pixel implant width and on the distance to the neighbouring electrodes. Ramo's theorem shows that charge carriers drifting in the high field regions contribute more to the

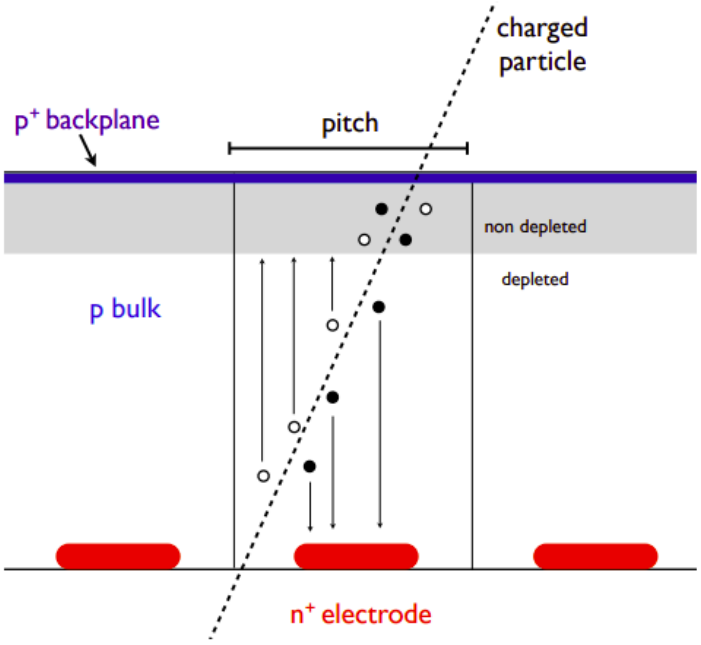

Figure 5.4.: Cross section of a partially under depleted n-on-p sensor. A charged particle (dashed line) traverses the sensor. The electrons (full circles) and holes (open circles) liberated in the depleted region (white background) will drift towards the n+ and p+ electrodes respectively, contributing to the signal formation in contrast to the charge carriers liberated in the non-depleted region (grey background). From [107].

current pulse. By integrating the current in Equation 5.4 over time, one can obtain the total charge collected.
In the simplest case of a detector with parallel plates geometry, if the bias voltage is much larger than the depletion voltage (i.e. the minimum voltage at which the bulk of the sensor is fully depleted, that depends on doping, thickness of the sensor and material resistivity), the electric field can be considered uniform:

$$E = \frac{V_b}{d} \tag{5.5}$$

[31], where E is the intensity of the electric field across the sensor, V_b is the bias voltage and d is the electrode distance (or sensor thickness). A charge carrier moves in the sensor with drift velocity described by Equation 5.3, and couples to the collection electrode by the weighting field $E_W = \frac{1}{d}$; according to Ramo's theorem the current induced in the electrodes by a charge carrier c is:

$$i_c = e\vec{E_W} \cdot \vec{v_c} = \mu_c e\vec{E_W} \cdot \vec{E} = e\mu_c \frac{V_b}{d^2} \tag{5.6}$$

where e is the electron charge, $\vec{E_W}$ is the weighting field intensity and $\vec{E}$ is the electric field induced by the bias voltage in the sensor and μ_c is the mobility of the charge carrier considered (holes or electrons). The time needed by a charge to cross the bulk is called

collection time and is:

$$t_c = \frac{d}{v} = \frac{d^2}{\mu_c V_b}. \tag{5.7}$$

If one compares the collection time for an electron and a hole produced at the same point $x = \frac{d}{2}$ in the middle of the two electrodes, the electrons will be collected in a time that is about 3 times shorter than the time needed to collect the holes. This is due to the different mobility values: $\mu_e \sim 3\mu_h$. When the electrons are fully collected, the holes keep inducing current longer.
There are different types of sensors, that differ for the doping of the pixel electrode, bulk and backplane electrode. The most commonly used sensor is the p-on-n type. In this type of sensor, the depletion region starts from the p^+ pixel electrode and grows towards the backplane as a function of reverse bias voltage, and the holes are collected in the p^+. These kinds of sensors are usually prone to radiation damage. On the other hand, the n-on-p type sensors are usually defined as "radiation hard", as their performance are not worsened after heavy radiation doses [10].

5.1.3. Radiation damage

Radiation damage is a term that refers to detector defects caused by exposure to a flux of particles. These defects can be divided into bulk damage and surface damage. Bulk damage occurs when a high energy particle displaces a primary knock-on atom out of its lattice position [70], creating point-like or cluster-like defects, depending on the energy and the type of the particle. The main consequence of bulk damage is the change in effective doping concentration: the defects cause donor removal and generation of acceptor-like states in the bulk. In n-type bulk (p-on-n sensors), the doping concentration changes such that the initially n-type silicon bulk becomes intrinsic and, after more particle fluence, can turn to p-type with the acceptor concentration growing as the fluence increases. This effect is most commonly known as type-inversion. The effect of the type inversion on an n bulk is that after it occurs, the depletion region grows from the backplane. After the inversion, full depletion cannot be accomplished: drifting charges will induce signal to multiple pixels electrodes, resulting in a degradation of the sensor resolution.
The second type of radiation damage, the surface damage, affects the oxide (such as SiO2) and the silicon-oxide interface. Since the oxide is an insulator, charges cannot be removed and form local concentrations. The oxide is used on the surface of most silicon devices as insulating layer on both wafer surfaces in detectors. Since the crystal structure of the SiO2-Si surface is irregular, the displacement of single atoms does not cause the effects that occur in the bulk. Ionization on the other hand can cause permanent defects [63].

5.1.4. Time tagging silicon detectors

Including time information in the tracking process brings considerable advantages. Depending on how the timing information is included, it is possible to obtain simpler track reconstruction algorithms, if the timing information is included to each hit, or an optimized power consumption, if the timing information is assigned to each event[28]. In addition,

thanks to the algorithm simplification, it is possible to reduce the number of tracking planes, that means reducing the material budget. mptI think that Fig 5.5 has no ref in the text The time resolution σ_t can be expressed as the sum of several terms [28]:

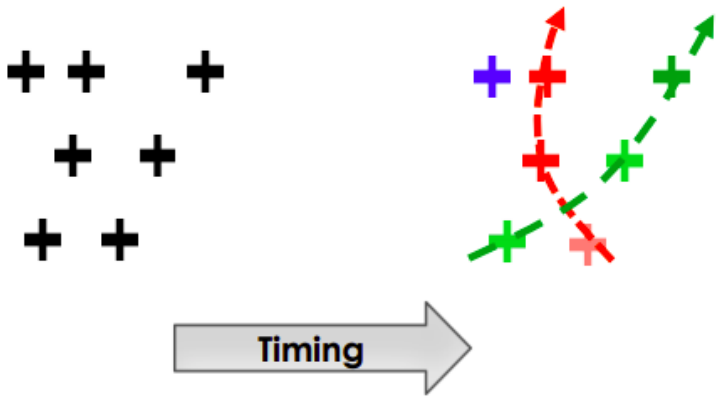

Figure 5.5.: The effect of including time information in tracking algorithms.

$$\sigma_{\mathrm{t}}^2 = \sigma_{\mathrm{jitter}}^2 + \sigma_{\mathrm{straggling}}^2 + \sigma_{\mathrm{distortion}}^2 + \sigma_{\text{Time Walk}}^2 \tag{5.8}$$

where:

- the term σ_{jitter} represents the time resolution contribution induced by the early or late firing of the comparator, due to the presence of noise. It is proportional to the inverse of the slope of the signal around the threshold value, as shown in Figure 5.6:

  $$\sigma_j = \frac{\sigma_{noise}}{dV/dt} \tag{5.9}$$

  where σ_{noise} is the uncertainty on the signal induced by the noise. The way to reduce it is with low noise sensors, low electronics noise and fast slew rates.

- the term $\sigma_{\mathrm{straggling}}$ represents the time resolution contribution induced by the variation of charge deposit created by a crossing ionizing particle through the sensor, on an event-by-event basis. This produces an irregular signal shape, that ultimately degrades the resolution.

- the term $\sigma_{\mathrm{distortion}}$ originates from the non-uniformity of the weighting potential, whose shape is shown in Figure 5.7 for a GTK pixel. The weighting field (WF) is the opposite of the gradient of the weighting potential (WP), and as mentioned in the previous sections, only depends on the geometry of the pixel. As a result, the current induced by the charge carriers, that is proportional to the drift velocity and to the weighting field, induces signal shapes that differ at the center and at the edges of a pixel. This mechanism spoils the time resolution.

- $\sigma_{\text{Time Walk}}$ is a term that represents the time walk (TW), that affects the output of discriminators generating a delay on the firing of the discriminator. This effect is

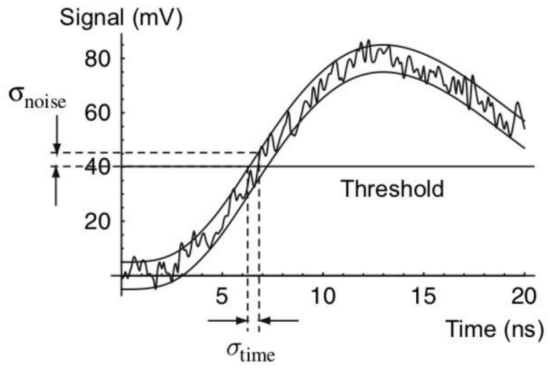

$$\sigma_{time} = \frac{\sigma_{noise}}{k} \qquad k = \frac{\Delta v}{\Delta t}$$

Figure 5.6.: Schematic representation of the noise effect on the time measurement in silicon sensors. Credits [95]

shown in Figure 5.8. This delay of detection depends on the signal amplitude: for signals arriving simultaneously, the time needed to cross the threshold is shorter for signals with larger amplitudes than for signals with smaller ones. This effect can be taken into account thanks to the electronics, or corrected offline, thanks to the Time over Threshold (ToT), defined as the difference between the trailing time (the time at which the signal falls below the threshold) and the leading time (the time at which the signal rises above the threshold).

After these considerations, assuming that the time walk is corrected, it is possible to summarize the key features that a planar silicon sensors should have in order to optimize the time resolution. The requirements to have a detector that has a good time resolution, are to be able to produce fast, steep and uniform signals. This can be obtained first by reducing the sensor thickness: indeed, the current induced by the motion of the charge carriers is inversely proportional to the square of the sensor thickness, as shown in Equation 5.4. However, by reducing the sensor thickness, the amplitude of the signal also reduces; this exposes to a larger sensitivity to noise. For this reason, the thickness of a sensor must be chosen to compromise between these two effects. In addition, the electric field across the sensor should be intense, in order to move the carriers with saturated drift velocity; this would uniform the drift velocities of the carriers and reduce the distortion factor. Furthermore, the geometry of the pixel should be taken into account in order to obtain a weighting field that is uniform across the sensor. However, the ratio between the pixel size and the sensor thickness is very relevant in the estimate of the time resolution [96]; there must hence be a trade-off between these requirements in order to minimize the distortion contribution due to the weighting field, and to maximize the intensity of the current signal pulse. Finally, a p-doped bulk in which the main charge carriers are the electrons is an advantage, as the mobility of the electrons is larger than the one of the holes, guaranteeing a faster signal (c.f. Equation 5.7). In order to study how these factors affect the time

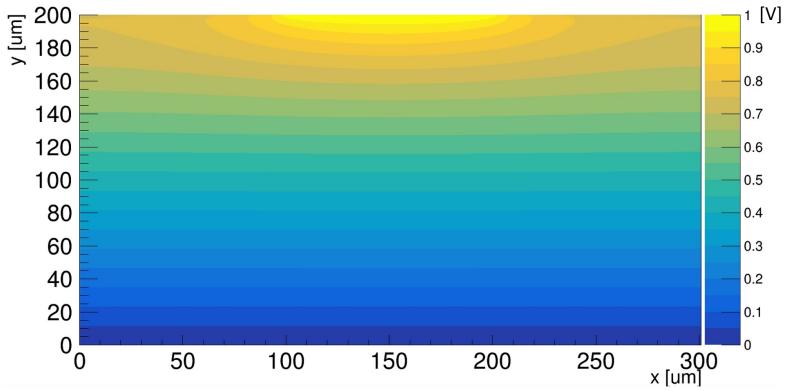

Figure 5.7.: The weighting potential on the cross section of a p-in-n sensor on a $300\mu m \times 300\mu m \times 200\mu m$ pixel (such as the ones of the GTK) in a simulation from the software WeightField2 [32]. The potential is more intense at the center than at the edges, and more uniform at the bottom than at the top.

resolution of silicon pixel detectors a beam test was performed with planar silicon sensors (n-on-p and p-on-n) readout out with the TDCPix chip, developed for the need of the NA62's GigaTracker[53].

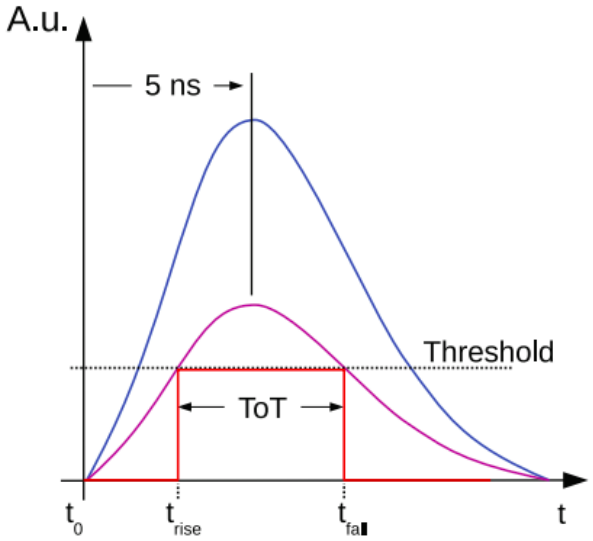

Figure 5.8.: Signal amplitude as a function of time. For the same time of arrival, signals with larger amplitudes cross the threshold earlier when rising and later when falling than signals with smaller amplitudes. This translates in a larger ToT.

5.1.5. The NA62 GigaTracKer: sensor and ASIC

The NA62 GigaTracKer (GTK), briefly introduced in Section 3.2.2 is the experiment beam spectrometer.

Silicon sensor

The GigaTracker silicon sensor has a size of 27.0×60.8 mm and is 200 µm thick. The most probable charge released by a 75 GeV/c charged hadron in such sensors is about 2.4 fC. The silicon sensor cross section is shown in Figure 5.9. The sensor is covered on both sides with aluminium to improve the electric field uniformity over the sensor area; it is typically operated with bias voltages between 150 and 300 V to optimize the charge drift velocities. The readout ASIC is compatible with p-in-n and n-in-p type sensors; both have been produced.

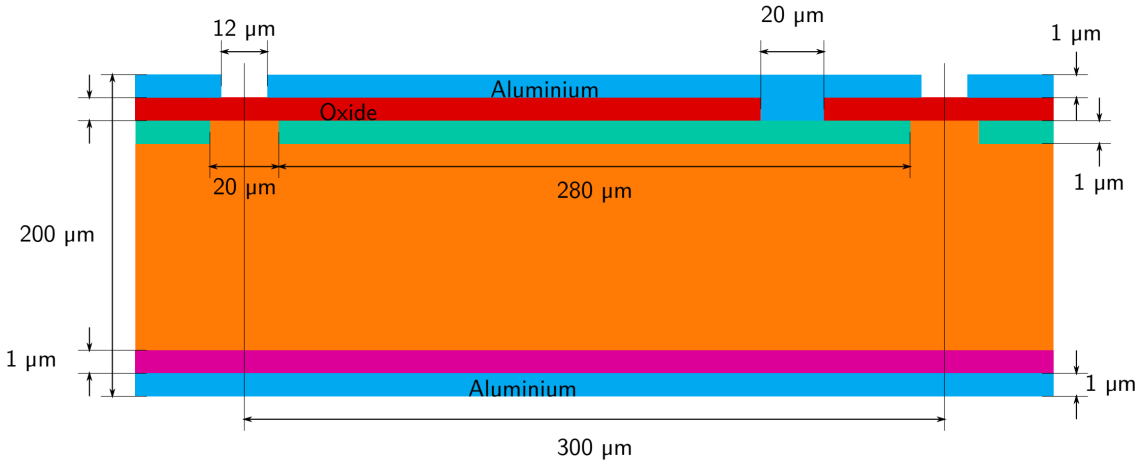

Figure 5.9.: Cross-section of the GigaTracker sensor. One pixel implant and its corresponding aluminium contact is represented. From [109].

Readout electronics

The readout ASIC, the TDCPix, is bump bonded to the sensor. The ASIC is 100 µm thick, and reads out 1800 pixels, distributed on a matrix of 40×45, and its layout is shown in Figure 5.10. The power and signal connection are placed at the chip periphery (end of column, EoC) (the orange part in Figure 5.10) and equip the entire GTK detector. Data registering and transfer do not depend on a trigger word: all the hits are processed and transferred. This corresponds to a chip output up to 7.6 Gbit/s at the full NA62 beam intensity, considering that the hit words are 48 bits wide. The main information contained in the hit are the leading and trailing time, that allow to compute the ToT that is used as a proxy for the signal amplitude, and its pixel address. The TDCPix is made of four *quarter chips* that read out ten columns of 45 pixels; analogue signals are propagated though the pixel columns via transfer lines. Five pixels are connected to a *hit arbiter* at the EoC; the hit arbiter processes the signal of only one pixel hit at a time, masking the signals from the four other pixels in the meantime. The hit arbiter is connected to a TDC, where the time and address of the hit pixel are recorded, and then transferred to a buffer with a header and a trailer word. Data are then sent off chip with a 3.2 Gbit/s serial link, one per quarter chip.

The TDCPix chips are connected via a carrier card and optical fibres to a custom FPGA [2] card, that receives and buffers the data and, after receiving L0 trigger signals, transmits the relevant hits to the PC farm for processing.

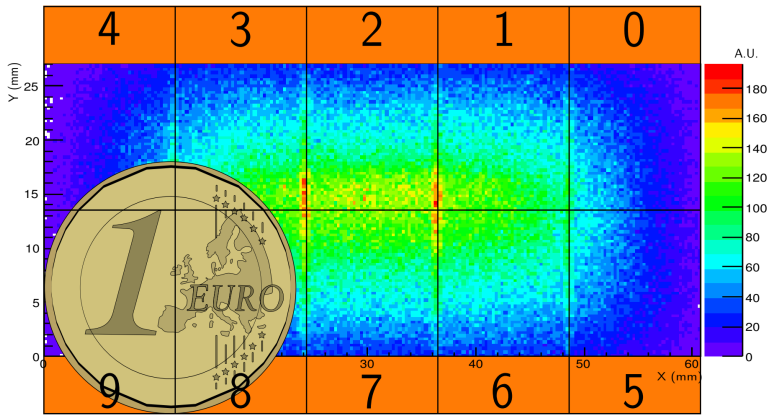

Figure 5.10.: GigaTracker readout ASIC numbering scheme superimposed on the simulated illumination of the sensor. The orange areas represent the end of column regions of the readout chips where most of the TDCpix digital logic is implanted. The higher rates in the inter-chip regions is due to the larger pixel size. From [109]

5.1.6. Previous tests on the NA62 GigaTracKer

The time resolution of the TDCPix has been tested in several campaigns, described in details in [83].
A first test that has been performed is the charge injection: a known charge has been injected directly in the pixel for 10000 times, without a sensor, allowing to measure the contribution σ_{jitter}; the obtained contribution to the time resolution from the noise is, for a charge of 2.4 fC and including the time walk correction, ~ 72 ps.
Later, some laser pulse tests have been carried out, using p-on-n sensor, with a bias voltage of 300 V; at first the laser was injected at the center of the pixel. The resolution obtained with this method was ~ 80 ps. In addition, the laser has been injected at different positions across the pixels; the changing of the current shape due to the variation of the injection position induced a degradation of the resolution of ~ 85 ps. A test campaign measuring the charge straggling contribution to the time resolution is still missing; however, from simulations, the charge straggling contribution seems to worsen the resolution of 100 ps. The time resolution budget for the GTK using p-on-n sensors is then:

$$\sigma = \sqrt{\sigma^2_{\text{jitter}} + \sigma^2_{\text{distortion}} + \sigma^2_{\text{straggling}}} = \sqrt{80^2 + 85^2 + 100^2} = 150ps. \qquad (5.10)$$

However, studies to measure the effects of radiations and temperature on the ASIC, an experimental confirmation of the charge straggling effect, and a study on how the pixel geometry affects the time resolution in the case of Minimum Ionizing Particles crossing

[2] Field Programmable Gate Arrays

the sensor are still missing. The data collected during the beam test that is the subject of this analysis have the purpose of testing the performances of two sensors types (p-on-n and n-on-p), as function of bias voltage, with data taken in the same conditions; moreover, the second objective is the study of the effect of the pixel geometry on the time resolution, using MIPs instead of laser pulse.

5.2. Beam test data analysis

The beam test that has been analyzed has been performed at CERN SPS in 2017 with a π^+ beam at 180 GeV/c, with the aim of studying the different contributions to the time resolution. The experimental setup includes three tracking planes made of planar sensors readout with TDCPix chips (the devices under test, DUT), and the LHCb VELO TimePix3 telescope, whose characteristics are detailed in [15]. The TimePix3 telescope has a high spatial resolution which allows to precisely determine the position at which the particle crossed the DUT. The data was collected with the two sensors types and with different bias voltages applied to them. The main challenges for the analysis of the data set produced during the beam test, is that the entire test has been performed without an external time reference, and that the record of the relative and absolute positions of the DUT stations have been lost. These features influenced the entire methodology of the beam test data analysis, as it will become clear in the later sections.

5.2.1. Data sets

Data are divided into runs; each run has been taken at a different voltage bias, and contains different data files for each detector plane and for different voltage bias settings. Stations 1 and 2 of DUT were positioned close together and inside a box, shown in Figure 5.11a, while the third plane was placed outside the box (Figure 5.11b), at a larger distance, followed by the 8 stations of TimePix3 telescope. For the purposes of the analysis, only runs that present files for every device station have been considered.
A set of 6 samples with sensor biases of 100, 150, 200, 250, 300 V for n-on-p sensor, and a set of 5 samples with sensor biases of 100, 200, 300 V were selected based on simple quality criteria for this analysis

Data quality
The beam is in general very well collimated, and the chips of the three planes are fairly well aligned. There are same time offsets between the planes, mostly due to non-equal delays in the cables and electronics.
Another characteristic of the data set worth mentioning is the bad quality of the data taken by the third station (the one outside the box), for both the sensor types: the n-on-p plane 3 presented a malfunctioning row, while the p-on-n plane 3 showed some noisy or disconnected pixels.

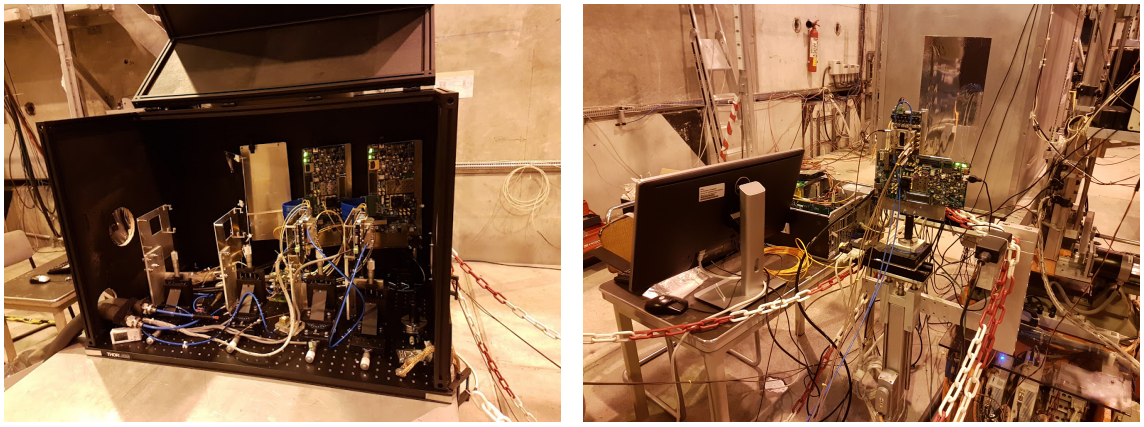

(a) (b)

Figure 5.11.: 5.11a: The box with planes 1 and 2 of TDCPix, close together. Picture taken during the test beam in 2017. 5.11b: The TimePix3 telescope (gray box) and plane 3 of TDCPix ("L" structure in front of it). Picture taken during the test beam in 2017.

5.2.2. Time walk correction

A first coarse estimate of the TW corrections of each DUT was determined by using another DUT as time reference as no external time reference is available. Few iterations were performed, in which the TW corrections were used to improve the precision of the time reference thus allowing to refine the TW correction of the DUT as function of the ToT. Indeed, as shown in Figure 5.8, larger amplitudes correspond to larger ToT and a shorter delay of detection. The delay of detection as a function of the ToT is derived for each ToT bin thanks to the plots of $\Delta t_{ij} = t_i - t_j$ (shown in Figure 5.13), where $i, j \in [1, 2, 3]$ are the indices of the DUT stations and t_i is the rising times respectively of the i$^{\text{th}}$ plane, as function of ToT. These plots are shown in Figure 5.12 before (Figure 5.12a) and after (Figure 5.12b) the iterated correction. The visible effect of the correction is to shrink and flatten the distribution of Figure 5.12, and to shrink the Δt distributions in **??**.
For the purposes of this analysis, the time walk correction for each run is computed using all the hits from all the pixels selected with the procedure described in section E, and correcting for pixel to pixel time offsets.

5.2.3. Time resolution as function of bias voltage and sensor type

The time resolution is obtained by fitting a Gaussian to the $\Delta t = t_i - t_j$ distribution obtained after the three rounds of correction, where t_i and t_j are the rising times of the two selected DUT modules. Assuming that the width of the Gaussian, σ_{i-j}, is the sum in quadrature of the two resolutions, σ_i and σ_j, the resolution of a single module can be extracted as:

$$\sigma_i = \sqrt{\frac{1}{2}(\sigma^2_{i-j} + \sigma^2_{i-k} - \sigma^2_{j-k})}. \tag{5.11}$$

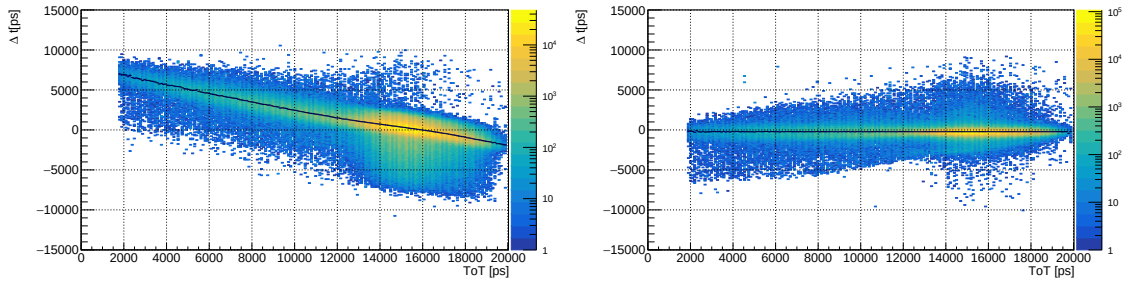

(a) (b)

Figure 5.12.: The Δt as function of ToT plot (colors) with the mean values of Δt for each ToT bin (black dots), for planes 2 and 1, before (5.12a) and after (5.12b) the three rounds of iterations.

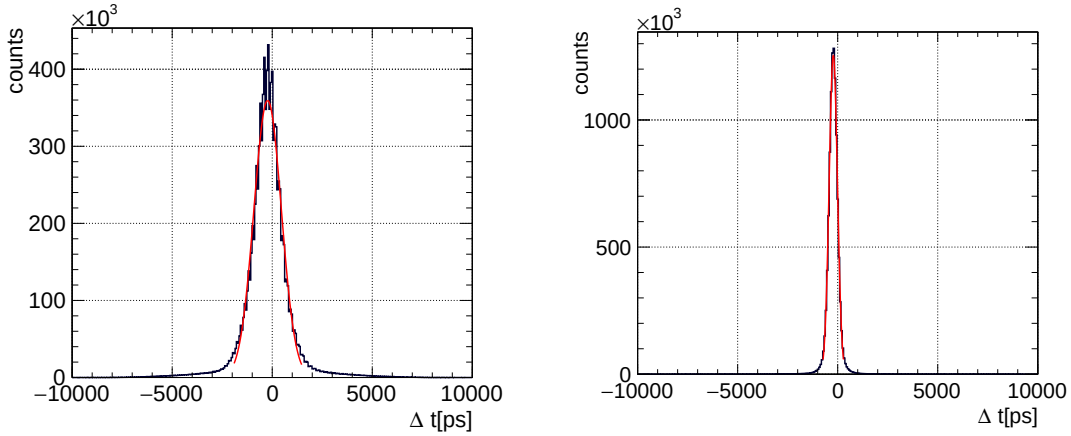

(a) (b)

Figure 5.13.: The time difference $\Delta t = t_2 - t_1$ for DUT stations 2 and 1, before (5.13a) and after (5.13b) the three rounds of iterations.

Figure 5.14 shows the time resolution as a function of the voltage bias. The theoretical resolution points shown in Figure 5.14 with the solid and the dashed black line have been obtained using the model of [96], in particular with Equation 4.52, using the drift velocities of electrons and holes, considering a width (w) of the square pixel of w =300 µm and a thickness d = 200 µm, and exploiting the coefficients of Table 1 and Table 2, considering a width over thickness ratio $w/d = 1.5$ and a $w(d) = 0.14$ (c.f. [96] Figure 4a, PAI sigma curve). The n-on-p sensor time resolution, shown in Figure 5.14b, appears to be significantly better than the one of p-in-n, shown in Figure 5.14a. This can be explained with the following considerations.

Considerations

There are three main facts that need to be considered. First, the signal induced by a particle crossing the sensor is made of two parts, the electrons-induced and the holes-induced signal.

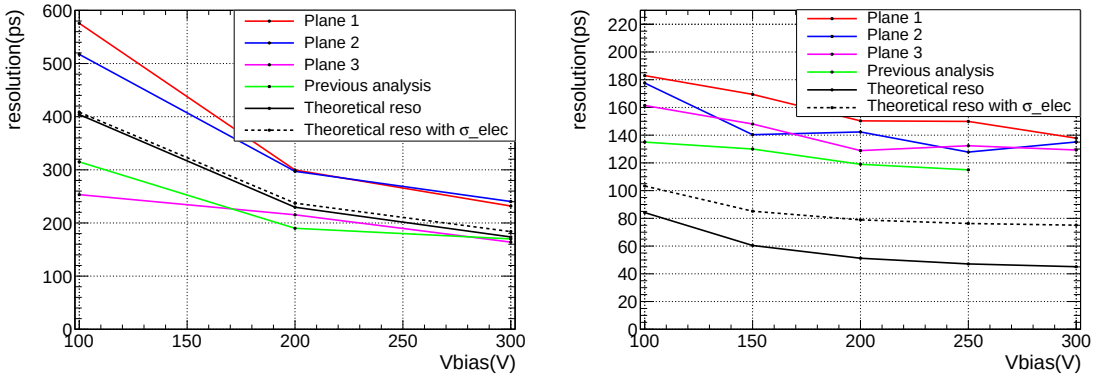

(a) (b)

Figure 5.14.: Resolution as a function of voltage bias for p-on-n (Figure 5.14a) and n-on-p (Figure 5.14b sensors: plane 1 is in red, plane 2 in blue and plane 3 in pink. The green line shows the results from previous tests [83]. The solid black line corresponds to the theoretical time resolution computed thanks to the formula provided in [96], that corresponds to the resolution of the sensor. The dashed black line corresponds to the theoretical time resolution computed by taking into account the intrinsic resolution of the TDCPix due to the electronics, which is 60 ps [97].

Second, according to Equation 5.6, the intensity of the current induced by the carrier is larger for large weighting fields, and is hence larger for the charged collected by the pixel electrode, where the WF is larger (cf Figure 5.7). Last, as mentioned in Section 5.1.4, the contribution to the time resolution from the noise is inversely proportional to the time needed to collect the charge. These three observations translate to the fact that, in general, faster and more intense signal correspond to a better time resolution. Holes, which have a smaller mobility than the electrons', induce a slow signal, that is hence less steep and that has a small signal-to-noise ratio compared to the signal induced by the electrons. On the other hand, the signal induced by electrons is ~ 3 times faster and is less affected by the noise contribution. This fact is illustrated in Figure 5.15, in which the green line shows the theoretical time resolution for a square pixel with $d = 200\,\mu\text{m}$, as function of the ratio w/d, for n-on-p sensors (electrons moving towards the pixel: 5.15a) and for p-on-n sensors (holes moving towards the pixel: 5.15b).
Furthermore, according to Equation 5.7, the electrons are the fastest (and hence the main) contribution to the total induced current. Having discussed these facts, it becomes clear that the time resolution in n-on-p sensors is in general better than in p-on-n sensors. Indeed, in n-on-p sensors, electrons derive towards the pixel electrode where the WF is more intense [96], as shown in the sketch in Figure 5.16a; here, the product of the WF and the electric field is maximum, making their contribution larger than in p-on-n sensors [107]. On the other hand, in p-on-n sensors, electrons are collected in the part of the sensor where the weighting is less intense. As stated in [96], the charges moving towards the part where the WP falls to zero will not contribute to the signal, making the electrons' contribution in

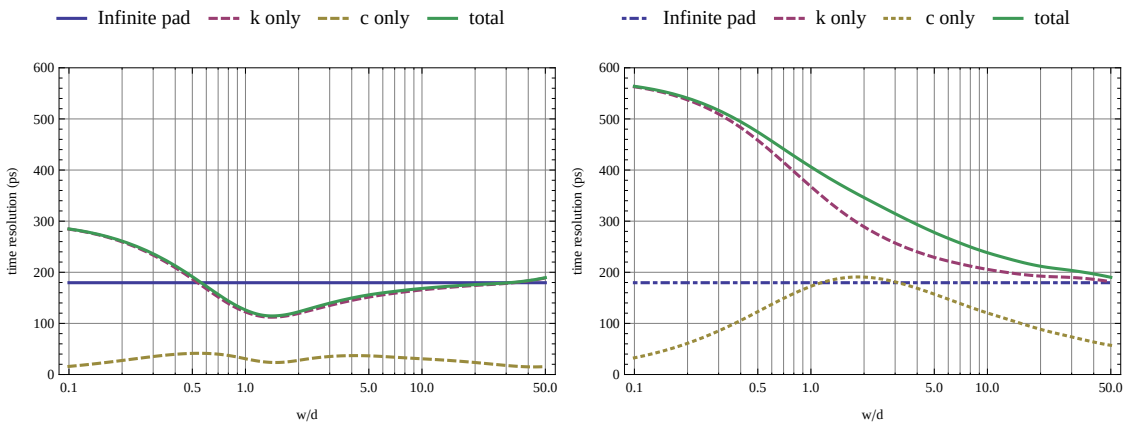

(a) (b)

Figure 5.15.: Time resolution for values of$d = 200\,\mu m$ and V = 200 V as a function of the pixel size w assuming the Landau theory for the charge deposit. The "c only" curve refers to the effect from a uniform line charge. In 5.15a the electrons move towards the pixel while in 5.15b the holes move towards the pixel. From [96].

p-on-n less intense (c.f. Figure 5.16b). A schematic of charge motion in n-on-p (Figure 5.16a) and in p-on-n (Figure 5.16b) sensors is shown in Figure 5.16.
In addition, the results show that the time resolution improves with a higher voltage bias, which is expected. The drift velocity of the charge carriers is directly proportional to the intensity of the drift electric field (c.f. Equation 5.4). However, the results obtained in the present analysis are worse than the ones from the previous analysis [83] [98]; this difference is of around $\sim$ 20 ps in the case of n-on-p sensors, while it is in average much larger in the case of p-on-n sensors. The hypothesis is that in this test beam, the noise contribution was somehow larger. The origin of this discrepancy is not understood, a possible explanation could be the presence of an additional jitter in the clock when it is distributed to the three devices. This extra contribution to the time resolution could compromise the ability to measure the weighting field effect; nonetheless, an attempt was made to measure it, and the analysis of the collected data is presented in Section 5.2.4.

5.2.4. Resolution as function of position inside the pixel

By measuring the time resolution in the sensor as function of the pixel position, it is in principle possible to quantify the weighting field contribution to the time resolution budget. For this purpose, the TimePix3 (TPX) telescope has been used to reconstruct the particles trajectory and determine the position at which they cross the pixels of the DUT. The TPX data and the tracking are handled by the software Kepler, based on the Gaudi event-processing framework [39]. Kepler handles the stations alignment, and performs the tracking with the eight planes of TPX and with one plane of TDCPix. The positions of the DUT stations were not noted in the logbook of the beam test, and it is impossible to retrieve them from data. Hence, it is derived the best (x,y) position of the planes for some

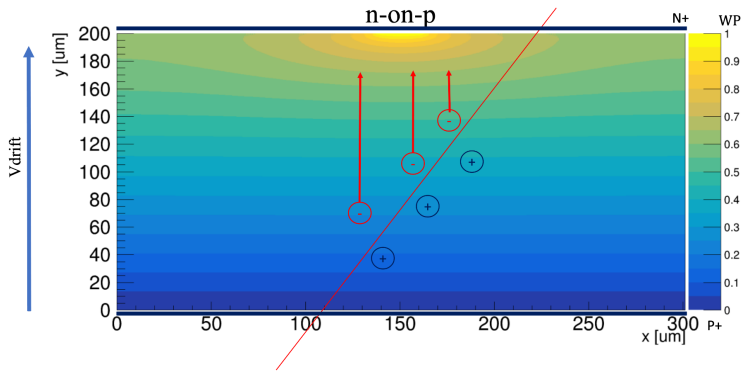

(a)

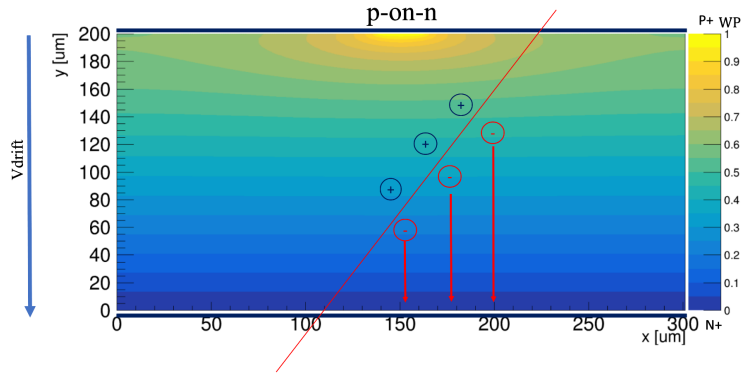

(b)

Figure 5.16.: A sketch of how the positive and negative induced charges drift towards the electrodes for n-on-p (top) and p-on-n (bottom) sensors; the density lines represent the weighting potential and are obtained with the software WeightField2 for the GTK sensor specifics.

supposed z position.

The alignment parameters are used not only by Kepler, but also in the following step of the analysis.

Kepler provides a list of track with their position, slope, residuals and timing. After having determined the offset in space and time between the DUTs and the TimePix3 telescope, the hits in the DUTs were associated to the tracks reconstructed with the telescope and aligned in time and space. The spatial resolution to determine the particle position at the DUT has been computed using hits that fire two adjacent pixels in the DUT. The firing of two adjacent pixels happens when a particle pass through the DUT pixel within 5μm from the edge. [3] Using these hits to compute the residual (that is the difference between the track coordinate and the hit coordinate) has the advantage of eliminating the main

[3]Also δ rays can fire two adjacent pixels. δ rays are not MIPs: they present large ToTs, which makes it possible to eliminate their contribution to the spatial resolution.

contribution to the spatial resolution given by the size of the DUT pixels. The residuals for these selected hits (i.e. the difference between the track position and its associated hit position at the DUT) are shown in Figure 5.17a for the X coordinate, and in Figure 5.17b for the Y coordinate. From Figure 5.17a, two contributions are visible. By plotting the residuals for each coordinate as a function as the ToT of the hit associated to the track (shown in Figure 5.18), it is clear that the two contributions stem from hits that have different ToT. The narrower part of the distribution is due to actual particles that cross the detector plane, while wider contribution to the residual distribution can be attributed to δ rays. δ rays have indeed larger ToT, as they are not MIPs. By fitting the two plots of Figure 5.17 with the sum of two gaussian (one wider and one narrower), one can deduce the resolution of the tracker, which is given by the width of the narrower distribution. The spatial resolution is found to be $\sim 50\mu$m on the y coordinate and $\sim 30\mu$m on the x coordinate;

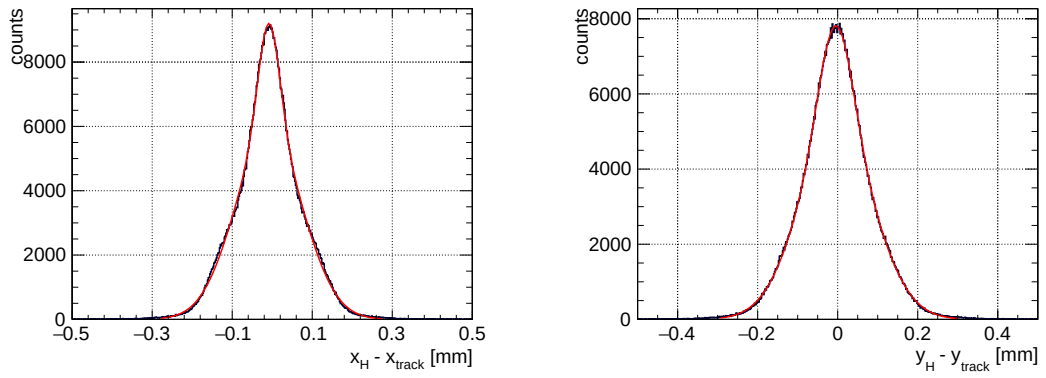

(a) (b)

Figure 5.17.: Residual plots for hits that fire two pixels, in X (5.17a) and Y (5.17b), fitted with the sums of two gaussian distributions with the same mean.

The pixel area of the DUT were divided in 3 regions along the y coordinate and in 10 regions along the x coordinate, as shown in Figure Figure 5.19. Only the central sample in y has been considered for the time being, as shown in Figure 5.19. The region to which a hit belongs is determined thanks to the position of the intercept at the DUT plane of the track associated to the hit. The time resolution in a given region was derived using the hits associated to the tracks intercepting this region on the DUT. The distribution of the time difference between these hits and the ones on the reference time DUT was fitted with a Gaussian. From the width of the Gaussian, σ_s, and the reference time resolution, σ_r, the time resolution for the region was estimate as:

$$\sigma_{1S} = \sqrt{\sigma_s^2 - \sigma_r^2} \tag{5.12}$$

The time resolution is expected to improve when moving from the pixel edges towards the center, because at the center, the weighting field is more intense. From the data of the 2017 test beam campaign, no significant variation of the time resolution was found, but

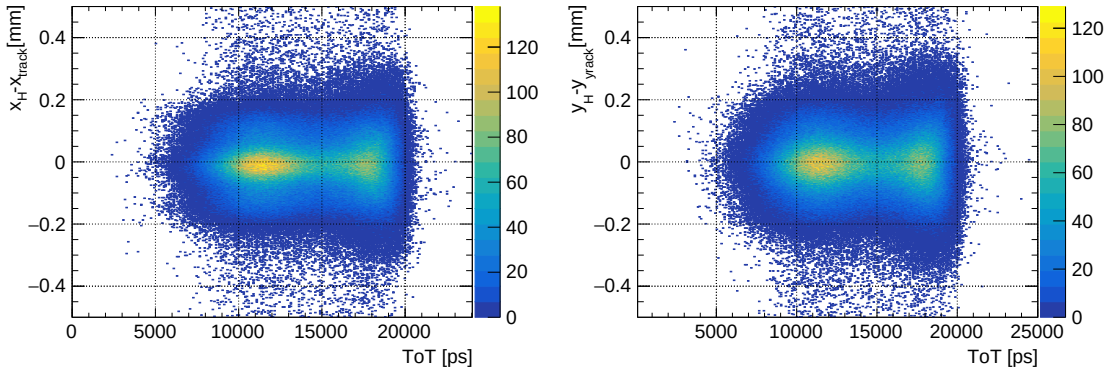

(a) (b)

Figure 5.18.: Residual plots for hits that fire two pixels, in X (5.18a) and Y (5.18b) respectively, as function of the ToT of the hits associated to the track.

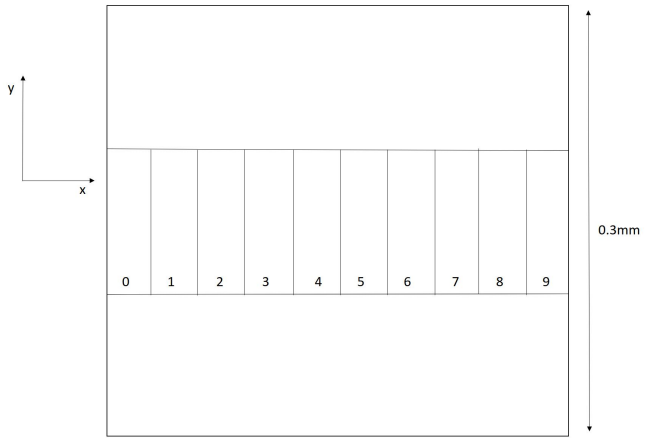

Figure 5.19.: Sketch of slicing of one pixel.

the precision of our results do not exclude it and calls for extra beam test campaign. In such test, extra care should be taken in controlling the clock distribution jitter as well and in measuring the relative position of the devices. Moreover, the code developed for this analysis is versatile, and can be used to perform the same analysis on future beam tests that aim to probe the weighting field contribution in silicon pixel detectors.

5.3. State of the art and future silicon sensors

Further beam tests with an external time reference are foreseen in the near future, on planar sensors at different thicknesses and on new technologies such as LGADs. Such tests are expected to provide quantitative results as far as the WF effect is concerned.
Apart from the silicon planar sensors, other sensor technologies are currently being devel-

oped, or already used. An example of more recent sensors are the Low-Gain Avalanche Detectors (LGAD), that merge the desirable characteristics of standard silicon detectors to the advantages (high gain and therefore very good time resolution) of the Avalanche PhotDiode (APD). LGADs operation principles are based on the avalanche effect, where a single photon can trigger a cascade of electron-hole pairs through impact ionization, resulting in significant signal amplification. With electric fields of the order of 300 kV/m, the electrons (and holes, but to a lesser extent) acquire enough kinetic energy to generate more electron-hole pairs. This is called charge multiplication; under these conditions, there is a gain factor in the sensor that has an exponential dependence on the electric field, proviging signals that are a factor of 10 higher than those of standard sensors [28]. The LGADs optimised for time stamping are also called Ultra-Fast Silicon Detector (UFSD) ([28]). The advantage of using such technology is that these sensors can produce very large amplitude signals, hence the noise contribution to the time resolution would be drastically reduced, while using very thin sensors, that reduces the charge straggling contribution to the time resolution. A schematic of the design of a LGAD sensor is shown in Figure 5.20.

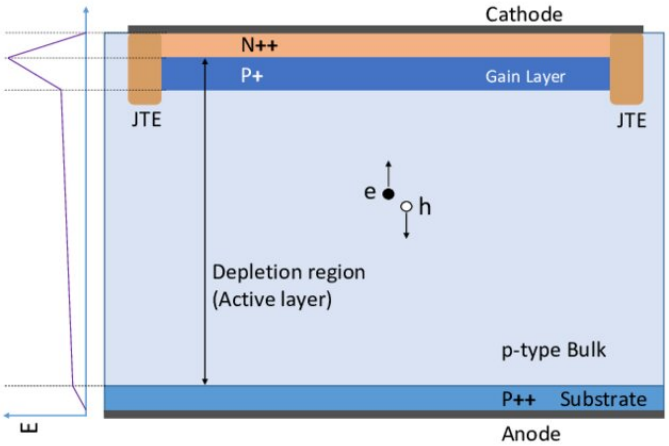

Figure 5.20.: Schematic for the LGAD sensors. From [69].

One of the most recent technologies in the field of time-stamping silicon detectors is the TimeSpot 3D ([26]): they are three-dimensional silicon sensors whose electrodes are vertically etched into the wafer. This allows to shorten the distance that the signal has to travel before being collected without reducing the sensor thickness and so the signal amplitudes, lowering the percentage of signal loss and allowing to have good results even at lower depletion voltages. A schematic of the TimeSpot 3D sensor is shown in Figure 5.21.

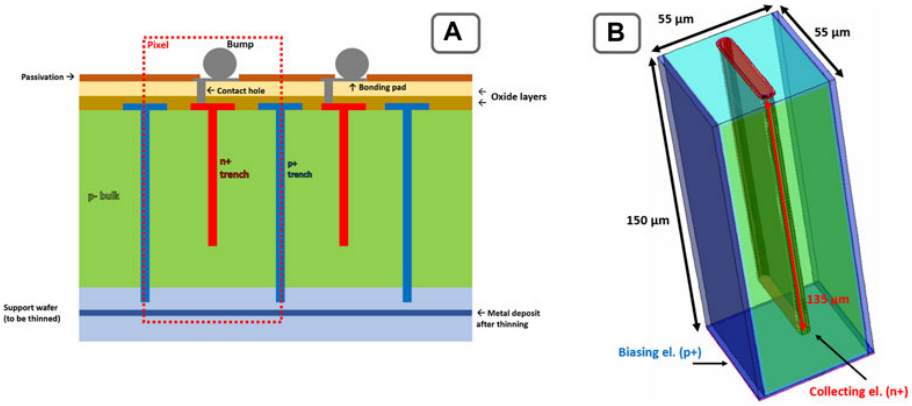

Figure 5.21.: Geometry of a 3D trench-type silicon pixel. (A) Structure of a sensor and its doping profiles (red for n+ doping, green for p- doping and blue for p+ doping). (B) TimeSPOT pixel rendering with physical dimensions. From [26].

6. Conclusions

Neutrino physics is a developing and exciting branch of particle physics; the study of neutrinos and of their properties will lead to a better understanding of the fundamentals laws of nature. One of the most compelling proof of beyond the Standard Model physics are neutrino oscillations, and its discovery has created a new branch in particle physics. The three-flavour paradigm still has some unknown variables, such as the octant of θ_{23} and the CP-violating phase δ_{CP}, a fundamental parameter in the PMNS matrix that quantifies the CP violation in the lepton sector. In addition, the neutrino mass hierarchy and the value of neutrino masses are still unknown. Present and future experiments are dedicated to measure these parameters to clarify the mechanism of neutrino oscillations. In particular, accelerator based experiments aim to measure these unknown variables; new long baseline experiments are under construction, and will use powerful beams to have a larger statistics. However, the measurements at present and future LBNEs are limited by the systematic uncertainties, in particular by the limited knowledge of the neutrino cross-sections and of the interaction models.

In this thesis, a new paradigm for short- and long baseline experiments has been studied: the neutrino tagging. This method proposes the use of spectrometers located along the hadron beam line and along the decay region of a neutrino beam line; these spectrometers are used to reconstruct the charged mother and daughters of neutrino-creating decays. Furthermore, a unique pairing between the tagged neutrino and the interacting neutrino at the far detector is possible using time and angular coincidences. The technological challenges of operating silicon trackers in a very harsh radiation environment such as the one of neutrino-creating beam can be overcome by using a narrowband, slowly extracted beam. The neutrino tagging technique vastly reduces the systematic uncertainties that affect neutrino oscillation studies. If used at a short baseline experiment, the tagging will allow measuring ν_e and ν_μ cross-sections with a precision below 1%. This will then improve the precision in oscillation measurements at tagged long baseline experiments, in particular on the δ_{CP} parameter.

The feasibility of this technique has been proved for the very first time on data. For this purpose, the NA62 experiment has been used. NA62, a kaon physics experiment located in the North Area at CERN SPS, provides an intense 75 GeV/c K^+ beam. Most of these K^+ decay in muon and neutrino, naturally producing a neutrino beam. NA62 is equipped of a beam spectrometer, a downstream particle spectrometer, an electromagnetic calorimeter, a hadron calorimeter and a muon detector. The goal of this thesis has been to search for $K^+ \to \mu^+\nu_\mu$ decays with the neutrino interacting in the calorimeters. Finding such fully reconstructed event proves the feasibility of the technique. The downstream detectors allow designing a triggering strategy and an offline signal selection based on the expected

signal topology. A blind analysis has been performed; a signal region has been chosen using the two main variables that define the signal. The background pollution in the signal region has been evaluated with a data driven method on the sidebands of the signal region. The signal acceptance has been evaluated thanks to a Monte Carlo simulation; the trigger efficiencies have been computed by measuring the detector response with data, and by convoluting the detector response with the simulated signal properties. Upon unmasking the signal region, two tagged neutrino candidates have been found; considering the Poissonian statistics, this number remains compatible with the expected number of signal events $N^{exp}_{K\mu\nu*} = 0.228 \pm 0.014_{stat} \pm 0.011_{syst}$. The proof of principle of the neutrino tagging technique has been demonstrated with this data analysis. This is a crucial first step towards the implementation of a full scale tagged neutrino experiments.
Moreover, a study of the factors that impact the time resolution in silicon pixel detector has been performed. The time resolution of the spectrometers used in the tagging is indeed of great importance: the tracker must be able to distinguish tracks from each other, in a harsh radiation environment. For this purpose, a beam test performed with a telescope using single chips based on the technology of the NA62 GigaTracKer, has been analysed. Thanks to this analysis, the difference between the performances of n-on-p and of p-on-n sensor types has been highlighted. However, due to additional contributions to the time resolution, it was not possible to measure the weighting field effect across the device's pixels. This test beam campaign calls for further testing of the state-of-the-art devices.
The neutrino tagging technique holds promises for future neutrino physics analyses by improving the precision on the measurement of the neutrino properties. The work presented in this thesis is a major step towards the establishment of this method as an effective paradigm.

Bibliography

[1] J. N. Abdurashitov, E. P. Veretenkin, V. M. Vermul, et al. "Solar neutrino flux measurements by the Soviet-American gallium experiment (SAGE) for half the 22-year solar cycle". In: *Journal of Experimental and Theoretical Physics* 95.2 (2002), pp. 181–193. ISSN: 1090-6509. DOI: 10.1134/1.1506424. URL: https://doi.org/10.1134/1.1506424 (cit. on p. 9).

[2] K. Abe et al. "The T2K Experiment". In: *Nucl. Instrum. Meth. A* 659 (2011), pp. 106–135. DOI: 10.1016/j.nima.2011.06.067. arXiv: 1106.1238 [physics.ins-det] (cit. on pp. 22, 26).

[3] K. Abe, N. Abgrall, H. Aihara, et al. "T2K neutrino flux prediction". In: *Physical Review D* 87.1 (Jan. 2013). DOI: 10.1103/physrevd.87.012001. URL: https://doi.org/10.1103%5C%2Fphysrevd.87.012001 (cit. on p. 25).

[4] K. Abe, J. Amey, C. Andreopoulos, et al. "Combined Analysis of Neutrino and Antineutrino Oscillations at T2K". In: *Phys. Rev. Lett.* 118 (15 Apr. 2017), p. 151801. DOI: 10.1103/PhysRevLett.118.151801. URL: https://link.aps.org/doi/10.1103/PhysRevLett.118.151801 (cit. on p. 29).

[5] B. Abi, R. Acciarri, M.A. Acero, et al. "Volume I. Introduction to DUNE". In: *Journal of Instrumentation* 15.08 (Aug. 2020), T08008. DOI: 10.1088/1748-0221/15/08/T08008. URL: https://dx.doi.org/10.1088/1748-0221/15/08/T08008 (cit. on p. 27).

[6] R. Acciarri, M. A. Acero, M. Adamowski, et al. "Long-Baseline Neutrino Facility (LBNF) and Deep Underground Neutrino Experiment (DUNE) Conceptual Design Report Volume 1: The LBNF and DUNE Projects". In: (2016). arXiv: 1601.05471 [physics.ins-det] (cit. on pp. 22, 23, 26).

[7] P. Adamson, C. Andreopoulos, K. E. Arms, et al. "Neutrino and antineutrino inclusive charged-current cross section measurements with the MINOS near detector". In: *Phys. Rev. D* 81 (7 Apr. 2010), p. 072002. DOI: 10.1103/PhysRevD.81.072002. URL: https://link.aps.org/doi/10.1103/PhysRevD.81.072002 (cit. on p. 86).

[8] P. Adamson, I. Anghel, C. Backhouse, et al. "Measurement of Neutrino and Antineutrino Oscillations Using Beam and Atmospheric Data in MINOS". In: *Phys. Rev. Lett.* 110 (25 June 2013), p. 251801. DOI: 10.1103/PhysRevLett.110.251801. URL: https://link.aps.org/doi/10.1103/PhysRevLett.110.251801 (cit. on p. 22).

[9] S. Adrián-Martínez, M. Ageron, F. Aharonian, et al. "Letter of Intent for KM3NeT 2.0". In: *Journal of Physics G: Nuclear and Particle Physics, 43 (8), 084001, 2016* 43.8 (Jan. 27, 2016), p. 084001. DOI: 10.1088/0954-3899/43/8/084001. arXiv: 1601.07459 [astro-ph.IM] (cit. on pp. 15, 17–19, 33).

[10] Anthony Affolder, Phil Allport, and Gianluigi Casse. "Collected charge of planar silicon detectors after pion and proton irradiations up to $2.2 \cdot 10^{16}$ n_{eq} cm^{-2}". In: *Nuclear Instruments and Methods in Physics Research Section A: Accelerators, Spectrometers, Detectors and Associated Equipment* 623.1 (2010). 1st International Conference on Technology and Instrumentation in Particle Physics, pp. 177–179. ISSN: 0168-9002. DOI: https://doi.org/10.1016/j.nima.2010.02.187. URL: https://www.sciencedirect.com/science/article/pii/S0168900210004547 (cit. on p. 108).

[11] N Agafonova, A Aleksandrov, O Altinok, et al. "Momentum measurement by the multiple Coulomb scattering method in the OPERA lead-emulsion target". In: *New Journal of Physics* 14.1 (Jan. 2012), p. 013026. DOI: 10.1088/1367-2630/14/1/013026. URL: https://dx.doi.org/10.1088/1367-2630/14/1/013026 (cit. on p. 33).

[12] A. Aguilar, L. B. Auerbach, R. L. Burman, et al. "Evidence for neutrino oscillations from the observation of $\overline{\nu}_e$ appearance in a $\overline{\nu}_\mu$ beam". In: *Phys. Rev. D* 64 (11 Nov. 2001), p. 112007. DOI: 10.1103/PhysRevD.64.112007. URL: https://link.aps.org/doi/10.1103/PhysRevD.64.112007 (cit. on p. 36).

[13] Q. R. Ahmad, R. C. Allen, T. C. Andersen, et al. "Direct Evidence for Neutrino Flavor Transformation from Neutral-Current Interactions in the Sudbury Neutrino Observatory". In: *Phys. Rev. Lett.* 89 (1 June 2002), p. 011301. DOI: 10.1103/PhysRevLett.89.011301. URL: https://link.aps.org/doi/10.1103/PhysRevLett.89.011301 (cit. on p. 9).

[14] M. H. Ahn, E. Aliu, S. Andringa, et al. "Measurement of neutrino oscillation by the K2K experiment". In: *Phys. Rev. D* 74 (7 Oct. 2006), p. 072003. DOI: 10.1103/PhysRevD.74.072003. URL: https://link.aps.org/doi/10.1103/PhysRevD.74.072003 (cit. on p. 22).

[15] K. Akiba, M. van Beuzekom, H. Boterenbrood, et al. "LHCb VELO Timepix3 telescope". In: *Journal of Instrumentation* 14.05 (May 2019), P05026–P05026. DOI: 10.1088/1748-0221/14/05/p05026. URL: https://doi.org/10.1088%2F1748-0221%2F14%2F05%2Fp05026 (cit. on p. 114).

[16] A Akindinov, E Anassontzis, G Anton, et al. "Letter of interest for a neutrino beam from Protvino to KM3NeT/ORCA". In: *The European Physical Journal C* 79.9 (Sept. 2019), p. 758. DOI: 10.1140/epjc/s10052-019-7259-5 (cit. on pp. 20, 22).

[17] Guido ALTARELLI. *The Standard Model of Particle Physics*. 2005. arXiv: hep-ph/0510281 [hep-ph] (cit. on p. 4).

[18] Luis Alvarez-Ruso, Costas Andreopoulos, Adi Ashkenazi, et al. "Recent highlights from GENIE v3". In: *The European Physical Journal Special Topics* 230 (Dec. 2021). DOI: 10.1140/epjs/s11734-021-00295-7 (cit. on p. 65).

[19] G. Backenstoss, B. D. Hyams, G. Knop, et al. "Helicity of μ^- Mesons from π-Meson Decay". In: *Phys. Rev. Lett.* 6 (8 Apr. 1961), pp. 415–416. DOI: 10.1103/PhysRevLett.6.415. URL: https://link.aps.org/doi/10.1103/PhysRevLett.6.415 (cit. on p. 8).

[20] A.E. Ball, S. Katsanevas, and N. Vassilopoulos. "Design studies for a long baseline neutrino beam". In: *Nuclear Instruments and Methods in Physics Research Section A: Accelerators, Spectrometers, Detectors and Associated Equipment* 383.2 (1996), pp. 277–290. ISSN: 0168-9002. DOI: https://doi.org/10.1016/S0168-9002(96)00711-5. URL: https://www.sciencedirect.com/science/article/pii/S0168900296007115 (cit. on p. 22).

[21] V. Barger, K. Whisnant, and R. J. N. Phillips. "CP Nonconservation in Three-Neutrino Oscillations". In: *Phys. Rev. Lett.* 45 (26 Dec. 1980), pp. 2084–2088. DOI: 10.1103/PhysRevLett.45.2084. URL: https://link.aps.org/doi/10.1103/PhysRevLett.45.2084 (cit. on p. 14).

[22] D Beavis, A Carroll, and I Chiang. "Long baseline neutrino oscillation experiment at the AGS. Physics design report". In: (Apr. 1, 1995). DOI: 10.2172/52878 (cit. on p. 25).

[23] R. Becker-Szendy, R.M. Bionta, C.B. Bratton, et al. "IMB-3: a large water Cherenkov detector for nucleon decay and neutrino interactions". In: *Nuclear Instruments and Methods in Physics Research Section A: Accelerators, Spectrometers, Detectors and Associated Equipment* 324.1 (1993), pp. 363–382. ISSN: 0168-9002. DOI: https://doi.org/10.1016/0168-9002(93)90998-W. URL: https://www.sciencedirect.com/science/article/pii/016890029390998W (cit. on p. 9).

[24] H. Bethe and R. Peierls. "The neutrino". In: *Nature* 133 (1934), p. 532. DOI: 10.1038/133532a0 (cit. on p. 2).

[25] R.K. Bock, T. Hansl-Kozanecka, and T.P. Shah. "Parametrization of the longitudinal development of hadronic showers in sampling calorimeters". In: *Nuclear Instruments and Methods in Physics Research* 186.3 (1981), pp. 533–539. ISSN: 0167-5087. DOI: https://doi.org/10.1016/0029-554X(81)90232-9. URL: https://www.sciencedirect.com/science/article/pii/0029554X81902329 (cit. on p. 50).

[26] F. Borgato et al. "Charged-particle timing with 10 ps accuracy using TimeSPOT 3D trench-type silicon pixels". In: *Front. in Phys.* 11 (2023), p. 1117575. DOI: 10.3389/fphy.2023.1117575 (cit. on pp. 122, 123).

[27] C. Bovet, R. Maleyran, L. Piemontese, et al. "The Cedar Counters for Particle Identification in the SPS Secondary Beams: A Description and an Operation Manual". In: (Dec. 1982). DOI: 10.5170/CERN-1982-013 (cit. on p. 43).

[28] Nicolo Cartiglia, R. Arcidiacono, B. Baldassarri, et al. "Tracking in 4 Dimensions". In: *Nuclear Instruments and Methods in Physics Research Section A: Accelerators, Spectrometers, Detectors and Associated Equipment* (June 2016), pp. -. DOI: 10.1016/j.nima.2016.05.078 (cit. on pp. 108, 109, 122).

[29] Christian Cavata. "Neutrinos: Summary of new results". In: *eConf* C030603 (2003). Ed. by P. Perret, VEN03 (cit. on p. 9).

[30] A Ceccucci, R Fantechi, P Farthouat, et al. "The NA62 Liquid Krypton calorimeter readout module". In: *Journal of Instrumentation* 6.12 (Dec. 2011), p. C12017. DOI: 10.1088/1748-0221/6/12/C12017. URL: https://dx.doi.org/10.1088/1748-0221/6/12/C12017 (cit. on p. 58).

[31] F. Cenna. "Design and Test of Sensors and Front-EndElectronics for Fast Timing in High EnergyPhysics". PhD thesis. Universitá degli Studi di Torino, 2018 (cit. on pp. 104, 106, 107).

[32] Francesca Cenna, Nicolo Cartiglia, M. Friedl, et al. "Weightfield2: A fast simulator for silicon and diamond solid state detector". In: *Nuclear Instruments and Methods in Physics Research Section A Accelerators Spectrometers Detectors and Associated Equipment* 796 (Apr. 2015). DOI: 10.1016/j.nima.2015.04.015 (cit. on p. 111).

[33] CERN-SPSC-2017-013 / SPSC-SR-208, ed. *2017 NA62 Status Report to the CERN SPSC* (cit. on p. 71).

[34] CERN-SPSC-2022-012 / SPSC-SR-306, ed. *2022 NA62 Status Report to the CERN SPSC* (cit. on p. 42).

[35] J Chadwick. "Intensitätsverteilung im magnetischen Spectrum der β-Strahlen von radium B + C". In: *Verhandl. Dtsc. Phys. Ges.* 16 (1914), p. 383. URL: http://cds.cern.ch/record/262756 (cit. on p. 2).

[36] J. Chadwick. "Possible Existence of a Neutron". In: *Nature* 129 (1932), p. 312. DOI: 10.1038/129312a0 (cit. on p. 2).

[37] Nikolaos Charitonidis, Andrea Longhin, Michelangelo Pari, et al. "Design and Diagnostics of High-Precision Accelerator Neutrino Beams". In: *Appl. Sciences* 11.4 (2021). 43 pages, 17 figures, to appear in Applied Science, p. 1644. DOI: 10.3390/app11041644. arXiv: 2103.07726. URL: https://cds.cern.ch/record/2777351 (cit. on pp. ix, 24, 31).

[38] J. H. Christenson, J. W. Cronin, V. L. Fitch, et al. "Evidence for the 2π Decay of the K_2^0 Meson". In: *Phys. Rev. Lett.* 13 (4 July 1964), pp. 138–140. DOI: 10.1103/PhysRevLett.13.138. URL: https://link.aps.org/doi/10.1103/PhysRevLett.13.138 (cit. on p. 8).

[39] M Clemencic, H Degaudenzi, P Mato, et al. "Recent developments in the LHCb software framework gaudi". In: *J. Phys.: Conf. Ser.* 219 (2010), p. 042006. DOI: 10.1088/1742-6596/219/4/042006. URL: https://cds.cern.ch/record/1269669 (cit. on p. 118).

[40] The NUSEK Collaboration, (M. Aglietta, G. Battistoni, et al. "Experimental Study of Atmospheric Neutrino Flux in the NUSEX Experiment". In: *Europhysics Letters* 8.7 (Apr. 1989), p. 611. DOI: 10.1209/0295-5075/8/7/005. URL: https://dx.doi.org/10.1209/0295-5075/8/7/005 (cit. on p. 9).

[41] Janet M. Conrad, Michael H. Shaevitz, and Tim Bolton. "Precision measurements with high-energy neutrino beams". In: *Reviews of Modern Physics* 70.4 (Oct. 1998), pp. 1341–1392. DOI: 10.1103/revmodphys.70.1341 (cit. on pp. vii, 7).

[42] G. Danby, J-M. Gaillard, K. Goulianos, et al. "Observation of High-Energy Neutrino Reactions and the Existence of Two Kinds of Neutrinos". In: *Phys. Rev. Lett.* 9 (1 July 1962), pp. 36–44. DOI: 10.1103/PhysRevLett.9.36. URL: https://link.aps.org/doi/10.1103/PhysRevLett.9.36 (cit. on p. 3).

[43] H. Danielsson, O. Gavrishchuk, P. A. Giudici, et al. "New veto hodoscope ANTI-0 for the NA62 experiment at CERN". In: *Journal of Instrumentation* 15.07 (July 2020), pp. C07007–C07007. DOI: 10.1088/1748-0221/15/07/c07007. URL: https://doi.org/10.1088%2F1748-0221%2F15%2F07%2Fc07007 (cit. on p. 46).

[44] Gavin S. Davies. *NOvA: Present and Future*. 2011. arXiv: 1110.0112 [hep-ex] (cit. on p. 22).

[45] Raymond Davis Jr., Don S. Harmer, and Kenneth C. Hoffman. "Search for neutrinos from the sun". In: *Phys. Rev. Lett.* 20 (1968), pp. 1205–1209. DOI: 10.1103/PhysRevLett.20.1205 (cit. on p. 9).

[46] Peter B. Denton, Megan Friend, Mark D. Messier, et al. "Snowmass Neutrino Frontier: NF01 Topical Group Report on Three-Flavor Neutrino Oscillations". In: (Dec. 1, 2022). DOI: 10.48550/ARXIV.2212.00809. arXiv: 2212.00809 [hep-ph] (cit. on p. 17).

[47] DUNE Collaboration. "Long-baseline neutrino oscillation physics potential of the DUNE experiment". In: *Eur. Phys. J. C 80, 978 (2020)* 80.10 (June 26, 2020). DOI: 10.1140/epjc/s10052-020-08456-z. arXiv: 2006.16043 [hep-ex] (cit. on pp. x, 28, 30).

[48] Ivan Esteban, M.C. Gonzalez-Garcia, Michele Maltoni, et al. "The fate of hints: updated global analysis of three-flavor neutrino oscillations". In: *Journal of High Energy Physics* 2020.9 (Sept. 2020). DOI: 10.1007/jhep09(2020)178. URL: https://doi.org/10.1007%5C%2Fjhep09%5C%282020%5C%29178 (cit. on p. 16).

[49] V. Fanti, A. Lai, D. Marras, et al. "The beam and detector for the NA48 neutral kaon CP violation experiment at CERN". In: *Nuclear Instruments and Methods in Physics Research Section A: Accelerators, Spectrometers, Detectors and Associated Equipment* 574.3 (2007), pp. 433–471. ISSN: 0168-9002. DOI: https://doi.org/10.1016/j.nima.2007.01.178. URL: https://www.sciencedirect.com/science/article/pii/S0168900207002719 (cit. on pp. 50, 53).

[50] E. Fermi. "Versuch einer Theorie der β-Strahlen. I". In: *Zeitschrift fur Physik* 88.3-4 (Mar. 1934), pp. 161–177. DOI: 10.1007/BF01351864 (cit. on p. 2).

[51] J. A. Formaggio and G. P. Zeller. "From eV to EeV: Neutrino Cross Sections Across Energy Scales". In: *Rev. Mod. Phys. 84, 1307 (2012)* 84.3 (May 31, 2013), pp. 1307–1341. DOI: 10.1103/revmodphys.84.1307. arXiv: 1305.7513 [hep-ex] (cit. on pp. xi, 5, 7, 60, 90).

[52] Y. Fukuda, T. Hayakawa, E. Ichihara, et al. "Evidence for Oscillation of Atmospheric Neutrinos". In: *Phys. Rev. Lett.* 81 (8 Aug. 1998), pp. 1562–1567. DOI: 10.1103/PhysRevLett.81.1562. URL: https://link.aps.org/doi/10.1103/PhysRevLett.81.1562 (cit. on pp. 9, 10).

[53] G. Aglieri Rinella et al. "The NA62 GigaTracKer: a low mass high intensity beam 4D tracker with 65 ps time resolution on tracks". In: *Journal of Instrumentation* 14.07 (July 2019), P07010. DOI: 10.1088/1748-0221/14/07/P07010. URL: https://dx.doi.org/10.1088/1748-0221/14/07/P07010 (cit. on pp. ix, 30, 36, 111).

[54] Claudio Giganti, Stéphane Lavignac, and Marco Zito. "Neutrino oscillations: The rise of the PMNS paradigm". In: *Prog. Part. Nucl. Phys.* 98 (2018), pp. 1–54. DOI: 10.1016/j.ppnp.2017.10.001. arXiv: 1710.00715 [hep-ex] (cit. on pp. 15, 29).

[55] E. Cortina Gil et al. "The beam and Detector of the NA62 experiment at CERN". In: *Journal of Instrumentation* 12.5 (May 2017). DOI: 10.1088/1748-0221/12/05/P05025 (cit. on p. 44).

[56] Carlotta Giusti and Martin V. Ivanov. "Neutral Current Neutrino-Nucleus Scattering Theory". In: *Journal of Physics G: Nuclear and Particle Physics* 47.2 (Aug. 22, 2019), p. 024001. DOI: 10.1088/1361-6471/ab5251. arXiv: 1908.08603 [hep-ph] (cit. on pp. xi, 4, 60).

[57] Evgueni Goudzovski, Marian Krivda, Cristina Lazzeroni, et al. "Development of the kaon tagging system for the NA62 experiment at CERN". In: *Nuclear Instruments and Methods in Physics Research Section A: Accelerators, Spectrometers, Detectors and Associated Equipment* 801 (2015), pp. 86–94. ISSN: 0168-9002. DOI: https://doi.org/10.1016/j.nima.2015.08.015. URL: https://www.sciencedirect.com/science/article/pii/S0168900215009493 (cit. on p. 44).

[58] Jack Henshaw and John Fry, eds. *Design of a hydrogen filled Cedar. NA62 Internal Note NA62- 2021-03.* 2021 (cit. on p. 43).

[59] K. S. Hirata, T. Kajita, T. Kifune, et al. "Observation of ^{8}B solar neutrinos in the Kamiokande-II detector". In: *Phys. Rev. Lett.* 63 (1 July 1989), pp. 16–19. DOI: 10.1103/PhysRevLett.63.16. URL: https://link.aps.org/doi/10.1103/PhysRevLett.63.16 (cit. on p. 9).

[60] Dario Hrupec. "Extragalactic sources of rapidly variable high energy gamma radiation". PhD thesis. Zagreb U., Phys. Dept., 2008 (cit. on p. 19).

[61] Patrick Huber, Mauro Mezzetto, and Thomas Schwetz. "On the impact of systematical uncertainties for the CP violation measurement in superbeam experiments". In: *Journal of High Energy Physics* 2008.03 (Mar. 2008), p. 021. DOI: 10.1088/1126-6708/2008/03/021. URL: https://dx.doi.org/10.1088/1126-6708/2008/03/021 (cit. on p. 28).

[62] L. Iconomidou-Fayard and Daniel Fournier. "The Discovery of Direct CP Violation". In: *Adv. Ser. Direct. High Energy Phys.* 23 (2015), pp. 205–235. DOI: 10.1142/9789814644150_0009 (cit. on p. 8).

[63] K. Iniewsky. *Radiation Effects in Semiconductors*. Ed. by CRC Press. 2011. DOI: https://doi.org/10.1201/9781315217864, (cit. on p. 108).

[64] Bahcall J N, Fowler W A, Jr. I Iben, et al. "Solar neutrino flux". In: *Astrophys. J.* 137 (1963), pp. 344–346. DOI: 10.1002/andp.201600097 (cit. on p. 9).

[65] C. Jacoboni, C. Canali, G. Ottaviani, et al. "A review of some charge transport properties of silicon". In: *Solid-State Electronics* 20.2 (1977), pp. 77–89. ISSN: 0038-1101. DOI: https://doi.org/10.1016/0038-1101(77)90054-5. URL: https://www.sciencedirect.com/science/article/pii/0038110177900545 (cit. on p. 104).

[66] K. Kodama, N. Ushida, C. Andreopoulos, et al. "Observation of tau neutrino interactions". In: *Physics Letters B* 504.3 (2001), pp. 218–224. ISSN: 0370-2693. DOI: https://doi.org/10.1016/S0370-2693(01)00307-0. URL: https://www.sciencedirect.com/science/article/pii/S0370269301003070 (cit. on p. 3).

[67] Sacha E. Kopp. "Accelerator Neutrino Beams". In: *Phys.Rept.439:101-159,2007* 439.3 (Sept. 14, 2006), pp. 101–159. DOI: 10.1016/j.physrep.2006.11.004. arXiv: physics/0609129 [physics.acc-ph] (cit. on pp. 23, 26, 28).

[68] T. D. Lee and C. N. Yang. "Question of Parity Conservation in Weak Interactions". In: *Phys. Rev.* 104 (1 Oct. 1956), pp. 254–258. DOI: 10.1103/PhysRev.104.254. URL: https://link.aps.org/doi/10.1103/PhysRev.104.254 (cit. on p. 8).

[69] Mengzhao Li, Yunyun Fan, Xuewei Jia, et al. *Effects of shallow carbon and deep N++ layer on the radiation hardness of IHEP-IME LGAD sensors*. Oct. 2021 (cit. on p. 122).

[70] Gunnar Lindström. "Radiation damage in silicon detectors". In: *Nuclear Instruments and Methods in Physics Research Section A: Accelerators, Spectrometers, Detectors and Associated Equipment* 512.1 (2003). Proceedings of the 9th European Symposium on Semiconductor Detectors: New Developments on Radiation Detectors, pp. 30–43. ISSN: 0168-9002. DOI: https://doi.org/10.1016/S0168-9002(03)01874-6. URL: https://www.sciencedirect.com/science/article/pii/S0168900203018746 (cit. on p. 108).

[71] Francesca Lodovico. "The Hyper-Kamiokande Experiment". In: *Journal of Physics: Conference Series* 888 (Sept. 2017), p. 012020. DOI: 10.1088/1742-6596/888/1/012020 (cit. on p. 22).

[72] L. Ludovici and P. Zucchelli. *Conceptual Study of an "Anti-Tagged" Experiment Searching for muon-neutrino –> electron-neutrino Oscillation*. 1997. arXiv: hep-ex/9701007 [hep-ex] (cit. on p. 36).

[73] G. Lutz. *Semiconductor Radiation Detectors*. Springer-Verlag, Berlin. 1999 (cit. on pp. 102, 103).

[74] Ziro Maki, Masami Nakagawa, and Shoichi Sakata. "Remarks on the unified model of elementary particles". In: *Prog. Theor. Phys.* 28 (1962), pp. 870–880. DOI: 10.1143/PTP.28.870 (cit. on p. 10).

[75] R. Marchevski and G. Ruggiero. *NA62 internal Note 18-04* (cit. on pp. 142–144).

[76] S van der Meer. *A directive device for charged particles and its use in an enhanced neutrino beam.* CERN Yellow Reports: Monographs. Geneva: CERN, 1961. DOI: 10.5170/CERN-1961-007. URL: https://cds.cern.ch/record/278088 (cit. on p. 23).

[77] A. Meregaglia. "ENUBET: Enhanced NeUtrino BEams from kaon Tagging". In: *Journal of Instrumentation* 11.12 (Dec. 2016), p. C12040. DOI: 10.1088/1748-0221/11/12/C12040. URL: https://dx.doi.org/10.1088/1748-0221/11/12/C12040 (cit. on p. 28).

[78] P. Mermod. *Hidden sector searches with SHiP and NA62.* 2017. arXiv: 1712.01768 [hep-ex] (cit. on p. 46).

[79] D Moraes, W Bonivento, Nicolas Pelloux, et al. *The CARIOCA Front End Chip for the LHCb muon chambers.* Tech. rep. Geneva: CERN, 2003. URL: http://cds.cern.ch/record/691709 (cit. on p. 57).

[80] Sze M. N. and Lee M. K. *Semiconductor Devices. Physics and Technology.* 1985 (cit. on pp. 102, 103, 105).

[81] NA62 Collaboration. "The Beam and detector of the NA62 experiment at CERN". In: *Journal of Instrumentation* 12.05 (Mar. 24, 2017), P05025–P05025. DOI: 10.1088/1748-0221/12/05/p05025. arXiv: 1703.08501 [physics.ins-det] (cit. on pp. 42, 45–49, 51, 52, 54, 57, 63).

[82] NA62 Collaboration. "An investigation of the very rare $K^+ \to \pi^+\nu\bar{\nu}$ decay". In: *Journal of High Energy Physics* 2020.11 (July 16, 2020). DOI: 10.1007/jhep11(2020)042. arXiv: 2007.08218 [hep-ex] (cit. on pp. 50, 60, 63, 94, 142, 143).

[83] M Noy, G Aglieri Rinella, A Cotta Ramusino, et al. "Characterisation of the NA62 GigaTracker End of Column Demonstrator Hybrid Pixel Detector". In: *Journal of Instrumentation* 6.11 (Nov. 2011), p. C11025. DOI: 10.1088/1748-0221/6/11/C11025. URL: https://dx.doi.org/10.1088/1748-0221/6/11/C11025 (cit. on pp. 113, 117, 118).

[84] Wolfgang Pauli. "Pauli letter collection: letter to Lise Meitner". Typed copy. URL: https://cds.cern.ch/record/83282 (cit. on p. 2).

[85] Z Pavlovic. *Studies of the Neutrino Flux for the NuMI Beam at FNAL.* Tech. rep. (cit. on p. 32).

[86] M. L. Perl, G. S. Abrams, A. M. Boyarski, et al. "Evidence for Anomalous Lepton Production in $e^+ - e^-$ Annihilation". In: *Phys. Rev. Lett.* 35 (22 Dec. 1975), pp. 1489–1492. DOI: 10.1103/PhysRevLett.35.1489. URL: https://link.aps.org/doi/10.1103/PhysRevLett.35.1489 (cit. on p. 3).

[87] M. Perrin-Terrin. *Tagged Neutrino Beams*. Feb. 9, 2023. URL: https://indico.in2p3.fr/event/28691/sessions/18313/attachments/75711/109587/2023-02-09_KM3NeTFr_Tagging.pdf (cit. on p. 22).

[88] Mathieu Perrin-Terrin. "Neutrino Tagging, a new tool for accelerator based neutrino experiments". In: *Eur. Phys. J. C (2022) 82:465* 82.5 (Dec. 23, 2021). DOI: 10.1140/epjc/s10052-022-10397-8. arXiv: 2112.12848 [hep-ex] (cit. on pp. x, 23, 28, 32, 34, 36).

[89] B. Pontecorvo. "Inverse beta processes and nonconservation of lepton charge". In: *Zh. Eksp. Teor. Fiz.* 34 (1957), p. 247 (cit. on p. 9).

[90] B. Pontecorvo. "Neutrino Experiments and the Problem of Conservation of Leptonic Charge". In: *Zh. Eksp. Teor. Fiz.* 53 (1967), pp. 1717–1725 (cit. on p. 9).

[91] B. Pontecorvo. "Tagging direct neutrinos. A first step to neutrino tagging". In: *Lettere al Nuovo Cimento* 25.9 (June 1979), pp. 257–259. DOI: 10.1007/bf02813638 (cit. on p. 29).

[92] Hyper-Kamiokande Proto-Collaboration. "Hyper-Kamiokande Design Report". In: (May 2018). DOI: 10.48550/ARXIV.1805.04163. arXiv: 1805.04163 [physics.ins-det] (cit. on p. x).

[93] S. Ramo. "Currents Induced by Electron Motion". In: *Proceedings of the IRE* 27.9 (1939), pp. 584–585. DOI: 10.1109/JRPROC.1939.228757 (cit. on p. 106).

[94] F. Reines and C. L. Cowan. "Detection of the Free Neutrino". In: *Phys. Rev.* 92 (3 Nov. 1953), pp. 830–831. DOI: 10.1103/PhysRev.92.830. URL: https://link.aps.org/doi/10.1103/PhysRev.92.830 (cit. on p. 3).

[95] W. Riegler. *Time resolution of silicon sensors*. URL: %5Curl%7Bhttps://indico.cern.ch/event/1083146/attachments/2328724/3975380/detector_seminar_oct_15_2021_timing_riegler_v2.pdf%7D (cit. on p. 110).

[96] W. Riegler and G. Aglieri Rinella. "Time resolution of silicon pixel sensors". In: *Journal of Instrumentation* 12.11 (Nov. 2017), P11017. DOI: 10.1088/1748-0221/12/11/P11017. URL: https://dx.doi.org/10.1088/1748-0221/12/11/P11017 (cit. on pp. 110, 116–118).

[97] G. Aglieri Rinella, S. Bonacini, P. Jarron, et al. "TDCpix pixel detector ASIC with 100 ps time stamping". In: *Nuclear Instruments and Methods in Physics Research Section A: Accelerators, Spectrometers, Detectors and Associated Equipment* 1053 (2023), p. 168331. ISSN: 0168-9002. DOI: https://doi.org/10.1016/j.nima.2023.168331. URL: https://www.sciencedirect.com/science/article/pii/S0168900223003212 (cit. on pp. 117, 145).

[98] G. Aglieri Rinella, M. Fiorini, P. Jarron, et al. "The TDCpix Readout ASIC: A 75 ps Resolution Timing Front-End for the Gigatrackerof theNA62 Experiment". In: *Physics Procedia* 37 (2012). Proceedings of the 2nd International Conference on Technology and Instrumentation in Particle Physics (TIPP 2011), pp. 1608–1617. ISSN: 1875-3892. DOI: https://doi.org/10.1016/j.phpro.2012.04.106. URL: https://www.sciencedirect.com/science/article/pii/S1875389212018779 (cit. on p. 118).

[99] A. Romano. *Pinunu Analysis Meeting, 18/10/2017, https://indico.cern.ch/event/674013/contributions/2757487/attachments/1542957/2420473/L1Trigger_PNNWKG_181017.pdf* (cit. on p. 89).

[100] A. D. Sakharov. "Violation of CP Invariance, C asymmetry, and baryon asymmetry of the universe". In: *Pisma Zh. Eksp. Teor. Fiz.* 5 (1967), pp. 32–35. DOI: 10.1070/PU1991v034n05ABEH002497 (cit. on p. 8).

[101] Enrico Scantamburlo. "Measurement of the Water to Scintillator Charged-Current Cross-Section Ratio for Muon Neutrinos at the T2K Near Detector". In: 2017 (cit. on p. 6).

[102] F. A. Scott. "Energy Spectrum of the Beta-Rays of Radium E". In: *Phys. Rev., vol. 48, pp. 391– 395* () (cit. on p. 2).

[103] W. Shockley. "Currents to conductors induced by a moving point charge". In: *J. Appl. Phys.* 9.10 (1938), pp. 635–636. DOI: 10.1063/1.1710367 (cit. on p. 106).

[104] and T. Adam, N. Agafonova, A. Aleksandrov, et al. "Measurement of the neutrino velocity with the OPERA detector in the CNGS beam". In: *Journal of High Energy Physics* 2012.10 (Oct. 2012). DOI: 10.1007/jhep10(2012)093. URL: https://doi.org/10.1007%2Fjhep10%282012%29093 (cit. on p. 22).

[105] "The OPAL detector at LEP". In: *Nuclear Instruments and Methods in Physics Research Section A: Accelerators, Spectrometers, Detectors and Associated Equipment* 305.2 (1991), pp. 275–319. ISSN: 0168-9002. DOI: https://doi.org/10.1016/0168-9002(91)90547-4. URL: https://www.sciencedirect.com/science/article/pii/0168900291905474 (cit. on p. 47).

[106] M. Torti, F. Acerbi, A. Berra, et al. "A high precision narrow-band neutrino beam: The ENUBET project". In: *International Journal of Modern Physics A* 35.34n35 (2020), p. 2044017. DOI: 10.1142/S0217751X20440170. eprint: https://doi.org/10.1142/S0217751X20440170. URL: https://doi.org/10.1142/S0217751X20440170 (cit. on pp. ix, 31).

[107] Panagiotis Tsopelas. "A silicon pixel detector for LHCb". presented 21 Nov 2016. 2016. URL: https://cds.cern.ch/record/2238509 (cit. on pp. 106, 107, 117).

[108] Martin Van Beuzekom. "Vertex Detector for LHCb Upgrade-II". In: *Proceedings of the 29th International Workshop on Vertex Detectors (VERTEX2020)*. Vol. 34. Journal of the Physical Society of Japan, June 9, 2021, p. 10014. DOI: 10.7566/jpscp.34.010014 (cit. on pp. ix, 30).

[109] Bob Velghe. "Development and Commissioning of the Silicon Pixel GigaTracker for the NA62 Experiment at CERN". PhD thesis. UCL Louvain (cit. on pp. 112, 113).

[110] L. Wolfenstein. "Neutrino oscillations in matter". In: *Phys. Rev. D* 17 (9 May 1978), pp. 2369–2374. DOI: 10.1103/PhysRevD.17.2369. URL: https://link.aps.org/doi/10.1103/PhysRevD.17.2369 (cit. on pp. 14, 15).

[111] C. S. Wu, E. Ambler, R. W. Hayward, et al. "Experimental Test of Parity Conservation in Beta Decay". In: *Phys. Rev.* 105 (4 Feb. 1957), pp. 1413–1415. DOI: 10.1103/PhysRev.105.1413. URL: https://link.aps.org/doi/10.1103/PhysRev.105.1413 (cit. on p. 8).

ANNEXES

A. Intitulés des doctorats AMU

- Discipline
  - Spécialité

ED 62 SCIENCES DE LA VIE ET DE LA SANTE

- Biologie santé
  - Biochimie structurale
  - Génomique et Bioinformatique
  - Biologie du développement
  - Immunologie
  - Génétique
  - Microbiologie
  - Biologie végétale
  - Neurosciences
  - Oncologie
  - Maladies infectieuses
  - Pathologie vasculaire et nutrition
  - Ethique
  - Recherche clinique et Santé Publique
  - Biotechnologie

ED 67 SCIENCES JURIDIQUES ET POLITIQUES

- Droit
  - Droit Privé
  - Droit Public
  - Histoire du Droit
- Science Politique

ED 184 MATHEMATIQUES ET INFORMATIQUE

- Mathématiques
- Informatique
- Automatique

ED 250 SCIENCES CHIMIQUES DE MARSEILLE

- Sciences Chimiques

ED 251 SCIENCES DE L'ENVIRONNEMENT

- Sciences de l'Environnement
  - Anthropologie biologique
  - Ecologie
  - Géosciences
  - Génie des procédés
  - Océanographie
  - Chimie
  - Environnement et santé

ED 352 PHYSIQUE ET SCIENCES DE LA MATIERE

- Physique et Sciences de la Matière
  - Astrophysique et Cosmologie
  - Biophysique
  - Energie, Rayonnement et Plasma
  - Instrumentation
  - Optique, Photonique et Traitement d'Image
  - Physique des Particules et Astroparticules
  - Physique Théorique et Mathématique
  - Matière Condensée et Nanosciences

ED 353 SCIENCES POUR L'INGENIEUR: MECANIQUE, PHYSIQUE, MICRO ET NANOELECTRONIQUE

- Sciences pour l'Ingénieur
  - Energétique
  - Mécanique et physique des fluides
  - Acoustique
  - Mécanique des solides
  - Micro et Nanoélectronique
  - Génie civil et architecture
  - Nucléaire de fission
  - Fusion magnétique

ED 354 LANGUES, LETTRES ET ARTS

- Etudes anglophones
- Etudes germaniques
- Etudes slaves
- Langues et littératures d'Asie
  - Chinois
  - Vietnamien
  - Coréen
- Arts
  - Arts plastiques
  - Sciences de l'art
  - Musique et musicologie
  - Etudes cinématographiques et audiovisuelles
  - Arts de la scène
  - Médiation culturelle des arts
- Pratique et théorie de la création artistique et littéraire
- Langue et Littératures françaises
- Littérature générale et comparée
- Langues, littératures et civilisations romanes
  - Etudes hispaniques et latino-américaines
  - Etudes italiennes
  - Etudes roumaines

ED 355 ESPACES, CULTURES, SOCIETES

- Géographie
- Démographie
- Urbanisme et Aménagement du territoire
- Préhistoire
- Archéologie
- Histoire de l'Art

- Histoire
- Sciences de l'Antiquité
- Mondes arabe, musulman et sémitique
- Etudes romanes
- Sociologie
- Anthropologie
- Architecture
- Cultures et Sociétés d'Asie

ED 356 COGNITION, LANGAGE, EDUCATION

- Philosophie
- Psychologie
- Sciences du Langage
- Sciences de l'Information et de la Communication
- Sciences de l'Education
- Sciences Cognitives

ED 372 SCIENCES ECONOMIQUES ET DE GESTION

- Sciences de Gestion
- Sciences Economiques

ED 463 SCIENCES DU MOUVEMENT HUMAIN

- Sciences du Mouvement Humain

B. Preselection and Single Track K^+ decay selection

The selection is performed only on data coming from bursts flagged as good by the standard quality criteria, and then general conditions select events properly reconstructed [82]. To this purpose an event must have [75]:

- no global reconstruction errors in any of the detectors;
- at least one CHOD hit;
- at least one and anyway less than 2000 LKr cells with energy deposited;
- either `mask0`, minimum bias (`mask2`) or neutrino trigger (`mask10`) mask present at level 0;
- at least one and no more than 10 spectrometer track candidates reconstructed

The selection also requires that both data and Monte Carlo events satisfy some basic quality requirements.
In addition, each event must have at least one good quality reconstructed STRAW track. The criteria defining a good–quality track are detailed in the PNN internal note [75] and listed below.

- hits are present in all four chambers;
- the reconstructed χ^2 is ≤ 20
- the difference between the momentum measured before and after the fit is $<$20 GeV/c;
- the differences of the dx/dz and dy/dz slope of the track measured before and after the track fit must be respectively $<$ 0.0003 rad and 0.001 rad;
- the quality of the STRAW pattern recognition of the π^+ candidate must be ≤ 4;
- more than 15 and less than 42 hits form the track;
- no vertex is formed with any other non-fake track, where:
  - a track is considered to be fake if it is reconstructed with 3 chambers and if it has a STRAW hit in common with another track or its $\chi^2 > 30$;
  - the 2-track vertex is built if the closest distance of approach between the two (CDA) is smaller than 15 mm, the position along the z axis Z vertex between 60 and 200 m and the track time difference smaller than 50 ns. The time of the track is the average of the trailing time of the corresponding hits.

The track must be inside the geometrical acceptance of all the subdetectors. Moreover, the tracks must have activity associated in time and space in NA48-CHOD, CHOD, RICH and LKr. The LKr matching of the μ^+ track is performed with both standard and auxiliary clusters reconstruction. A MIP is not always reconstructed as a cluster in the LKr; when it is not possible to find a cluster matched to the MIP, a track-cell matching is performed.

The μ^+ cluster is also searched for in the LKr auxiliary cluster reconstruction. In order to identify the track as a muon track, a MUV3 candidate should be present within 7 ns of the CHOD track times. Finally, a KTAG candidate with at least 5 sectors must be present within 3 ns of the downstream time, which is defined as the mean of CHOD, RICH and STRAW time of the daughter track, weighted by the time resolution of the corresponding detector. The details of the matching of the single STRAW track to CHOD, NA48-CHOD, RICH and LKr are specified in [75]. A STRAW track matched to signals in NA48-CHOD, CHOD, RICH and LKr is referred to as a downstream particle.

B.1. Parent beam particle

A kaon candidate is identified thanks to the KTAG and the GigaTracKer. A parent beam particle matched in KTAG and GTK is referred to as an upstream particle. A parent beam particle that doesn't have matched candidates in either KTAG or GTK is discarded. The parent K^+ of a selected downstream charged particle is defined by: the K^+ candidate in KTAG closest in time and within ± 3 ns of the downstream particle; a beam track in GTK associated in time with the KTAG candidate and in space with the downstream track in the STRAW. Details on the association between GTK, KTAG and STRAW candidates are specified in [82]. The association between GTK, KTAG and STRAW candidates relies on a likelihood discriminant built from two variables: the time difference between the KTAG candidate and the beam track (ΔT(KTAG-GTK)); and the closest distance of approach of the beam track to the downstream charged particle (CDA) computed taking into account the bending of the particle trajectory in the stray magnetic field in the vacuum tank. The track with the largest discriminant is the best candidate. The decay vertex, defined as the mid-point between the beam and downstream track at the closest distance of approach [82], must be in the Fiducial Volume of the experiment, which is $105m < z_{vtx} < 170m$ from the target.
Muon candidates of events flagged as K decays may originate outside the NA62 vacuum decay volume, as a product of beam interactions with GTK3. Further conditions are hence applied to prevent a beam particle undergoing inelastic scattering in upstream detectors[75]:

- Time-over-Threshold(ToT) of the GTK3 hits of the K candidate to be smaller than 23 ns;
- no CHANTI candidate associated to the μ candidate, with a CHANTI candidate defined as at least one X-Y CHANTI coincidence within ± 3 ns from the track RICH time;
- no crowded events with large (>49) number of hits in any GTK station;
- any associated track in GTK, additional to the K candidate, must not form a vertex with the mu candidate in the range 100000 < Zvertex < 105000 mm.

C. Hit multiplicity rejection

All extra hits in time with time of the NA48CHOD candidate associated to the track ($T_{trackNA48CHOD}$) are collected in LKr and the two hodoscopes (CHOD, NA48-CHOD). LKr cells at coordinates (x_{hitLKr} , y_{hitLKr}), with energy E_{hitLKr} deposited at time T_{hitLKr} form extra activity in the LKr if [75]:

- $E_{hitLKr} > 0.05$ GeV;
- $|T_{trackNA48CHOD} - T_{hitLKr}| < 4$ ns for $E_{hitLKr} < 0.3$ GeV;
- -7 $< T_{trackNA48CHOD} - T_{hitLKr} <$ 10 ns for $0.3 \leq E_{hitLKr} < 2$ GeV;
- $|T_{trackNA48CHOD} - T_{hitLKr}| < 10$ ns for $E_{hitLKr} \geq 2$ GeV;
- the distance between the cell position and the track position at the LKr front face must be >100 mm.

The CHOD in-time hit pads are associated to LKr extra activity if they are:

- within a rectangle defined by 200 mm in x and 100 mm in y from the CHOD hit.

Pairs of horizontal and vertical NA48CHOD slabs are associated to extra activity in CHOD using the position of the extra in-time CHOD hits as a reference. A NA48CHOD slab pair is matched to CHOD in-time hit if it is:

- within 5 ns of the CHOD hit;
- within a rectangle defined by 200 mm in x and 100 mm in y from the CHOD hit;
- both slabs are not hit by a track;

Pairs of horizontal and vertical NA48CHOD slabs are associated to extra activity in LKr using the position of the extra in-time LKr hits as a reference. A NA48CHOD slab pair is matched to extra LKr activity is it is:

- within 5 ns of the CHOD hit;
- not more than 100 mm away from the extra hit position;
- both slabs are not hit by a track.

Furthermore, events with more than two NA48CHOD hits reconstructed within 7 ns of the track NA48CHOD time are discarded.

D. TDCPix time tagging and raw data extraction

The time tagging is performed by time stamping the hits thanks to a fine counter (ranging from 97.7 ps to 3.125 ns) and a coarse counter (with a precision of 3.125 ns), with a range of up to 6.4 µs; this time unit is called a *frame* [97]. Then, in order to extend the time stamp range, a frame word with an incrementing counter is inserted in the data every 6.4 µs. The data registered by the DUT are written in binary files that can be divided into "blocks". Each block contains a header and a payload; the latter is made of a varying number of 48 bits words, and it contains the information on the hits. In particular, the payload is composed by two frame words that contain the correspondent frame number and number of hits. Each frame word is followed by a list of hit words; each of them contains all the information about the hits contained in the frame, such as its leading and trailing time and its pixel address. However, if the hits contained in one frame are too many and the frame word (that has a higher priority) needs to be placed in order to end a frame, it can happen that some hits belonging to the frame n end up written in the frame $n+1$. In this case, the hits are corrected and placed in the right frame offline: this is possible because the Most Significant Bit (MSB) of a hit coarse time is repeated as the Least Significant Bit (LSB) of the frame counter. This way it is always possible to associate to the correct frame the hit words placed in a neighbouring frame; however, to be able to do this, it is always necessary to read the frames two by two, in order to always have the current frame and the following one kept in memory. This requirement has been the main challenge in the developing of the algorithm used to read the raw data. Each raw file contains the information of one DUT station. The size of each file is around 4 Gb each ($\sim$ 3 billions frames each), that corresponds to $\sim 10^8$ hits per plane.

The raw binary files are read thanks to an algorithm that allows to cluster all the data from 3 planes from the same run. Once the data are transformed in human-readable format and clustered, it is much faster to process and analyse them, as they are also much lighter. The clustering algorithms takes as input three files at a time, one per DUT station. The clustering is performed with a time window of 8ns (that is $\sim 3\sigma$ of the time difference distribution between planes pairs). The time offsets of planes 2 and 3 with respect to plane 1 is applied to each hit leading time, time-aligning them to station 1. The algorithm loads a number of frames ($N = 5 \cdot 10^4$) from every plane and then gradually erases the frames already used each time, until the program reaches the end of the file. These files contain frames that need to be temporally aligned between themselves before being able to start the clustering procedure: it removes a frame from the memory only if it has been used in the clustering, while constantly checking on the frame number of the current frame in order to keep the frames from the three files time aligned and without jumps that would compromise the clustering procedure.

The algorithm used is sketched in Figure 1 for clarity. At the end of the clustering procedure step, the output consists of 3 files for each run, one for each plane couple. In order to work with smaller files and reduce further the processing time, the pixel delay algorithm is applied, described in Appendix E. This algorithm gives as outputs for each plane couple some text files, where the best pixel couples are reported together with their average delay

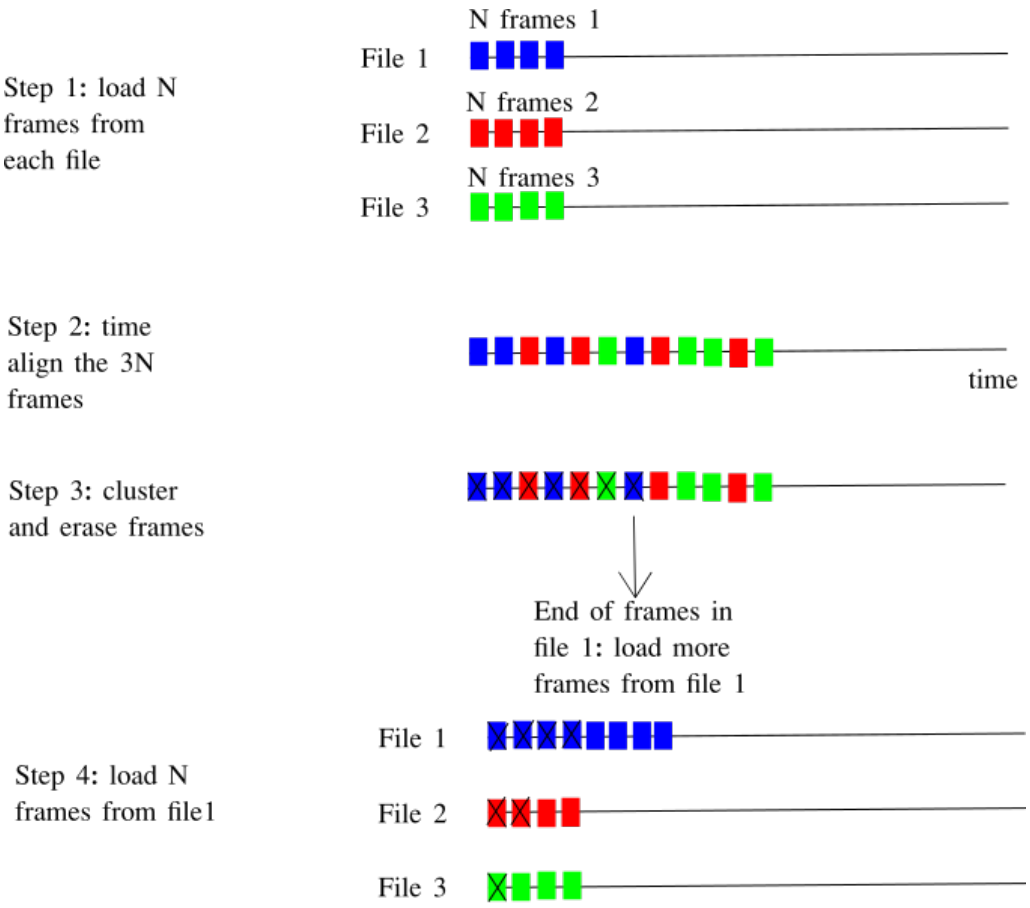

Figure 1.: The algorithm used for the data reading and clustering. This procedure allows speeding up consistently the running time and to consistently lower the memory usage.

with respect to 0. This output file is then used as input together with the correspondent clustered file for another application, creating a new clustered file that only contains the previously selected pixels in both planes.
The 3 output files per run are then merged together, giving one file per run in which there are only the hits in the selected pixels. These are the files that are used for processing and physics analysis.

E. Pixel delay

In general, the pixel output signals are delayed due to the propagation time between the pixels and the end of column (EoC) depending on the pixel position in the matrix. In addition, the digital signals at the output of the pixel discriminators degrade as they transit in the lines connecting the pixel to the EoC. Thus, the signal delay at the EoC increases

with the distance travelled by the signal from the pixel; the time walk correction obtained for a full chip is enough to get to the resolution that we wish for. This is what is called pixel delay. For the DUT it does not yet exist an algorithm that computes efficiently the pixel delay map; moreover, in absence of an external time reference, it is impossible to perfectly time-align all the pixels, as all time differences are computed between 2 planes. A custom-made algorithm has been developed during this project that found the N most populated pixel pairs between two planes thanks to a unique pixel ID (UID): the definition of the UID is the following: $UID = x + 40 * y$ where x and y are the coordinate of the pixel. The most populated N pixel couples are found by plotting the UID of the two stations under analysis, and by selecting the most populated bins. The (x,y) coordinates of the pixels of the two stations are then extracted. The algorithm subsequently computes the average time difference between the hits belonging to the most populated pixel in the first considered DUT station, and to the most populated pixel in the second considered DUT station and the 8 adjacent pixels in the second plane, in order to avoid biasing due to misalignment. For each pixel couple obtained thanks to the previous step, it computes the average time difference on limited ToT range (in the 5 bins in which the Δt as function of ToT histogram crosses the 0). This time difference is registered together with the pixel couple, and it is then applied hit by hit when computing time differences with hits coming from the selected pixels. This allows to align all pixel couples to an average time difference of 0. However, this procedure presented a bias that was spotted thanks to the hit maps of the associated intercept for each pixel of plane 1. The associated intercept is the intercept of the track reconstructed by the TPX telescope at the extrapolated plane position.

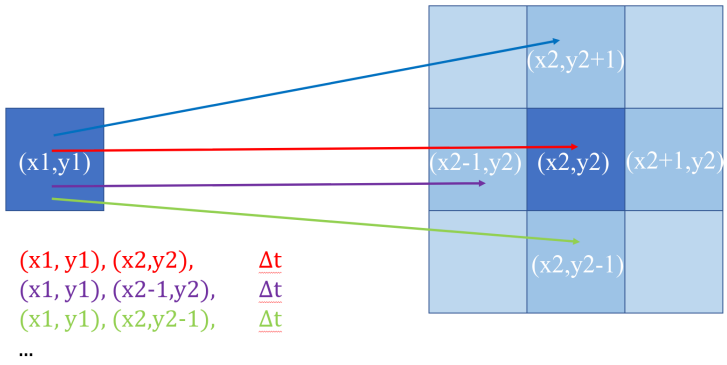

Figure 2.: Schematic representation of the pixel merging algorithm between station 1 and station 2.